

**ENTANGLED
LIGHT
IN
SILICON
WAVEGUIDES**

Joshua Wimbridge Silverstone

*A dissertation submitted to the University of Bristol
in accordance with the requirements for award of the degree of
Doctor of Philosophy, in the School of Physics of the Faculty of Science*

Submitted July 2015, in the
INTERNATIONAL YEAR OF LIGHT

Abstract

Quantum computation will unlock a new class of computational complexity, allowing us to solve previously unsolvable problems, and understand previously unconscionable phenomena. A quantum computer must exert precise control over complex quantum systems, on a truly massive scale. It must freely wield entanglement—the ethereal connection between quantum particles—to operate. Photons, particles of light, have obvious use in the *transmission* of quantum information, but could also *process* it; their manipulation is aided by a millennium of human experience with optics.

This thesis describes how to build a photonic quantum computer from the ground up, and applies today’s most scalable optical technology—silicon integrated optics—to construct the first integrated devices which can produce photons and wield their entanglement. I detail the nonlinear process used to produce photons, spontaneous four-wave mixing, as well as the silicon optical technology used to control them. I demonstrate, via four experiments, a massive scaling-up of silicon quantum photonics. Finally, I provide a glimpse of possible technological routes towards universal quantum computation with photons.

Declaration

I declare that the work in this dissertation was carried out in accordance with the requirements of the University’s Regulations and Code of Practice for Research Degree Programmes and that it has not been submitted for any other academic award. Except where indicated by specific reference in the text, the work is my own. Work done in collaboration with, or with the assistance of, others, is indicated as such. Any views expressed in the dissertation are solely my own.

SIGNED DATE

Contents

1	Introduction	1
1.1	Quantum information with photons	5
1.1.1	Qubits	5
Mixture	7	
Operations on qubits	8	
1.1.2	Photons	9
Photonic evolution	9	
Hong-Ou-Mandel interference	11	
1.1.3	Two-qubit gates	12
Optical nonlinearities as two-qubit gates	13	
The post-selected CSIGN gate	14	
1.1.4	Entanglement	14
Entangled states	15	
1.2	Quantum computation	15
1.2.1	Requirements	19
1.3	Integrated optics in silicon	19
1.3.1	Waveguides	21
The slab waveguide	22	
The strip waveguide	23	
Modal properties	23	
1.3.2	Integrated optics toolbox	25
Waveguide couplers	25	
Phase modulators	27	
Waveguide crossings	28	
Resonators	28	
Fibre-to-chip couplers	29	
1.3.3	Silicon: the optical material	29
Bandgap	30	
Thermo-optic effect	30	
Free-carrier effects	31	
Two-photon absorption	31	
Raman scattering	32	
Nonlinear optics in silicon	32	
1.4	Silicon quantum photonics	34
References	36	
2	Photon-pair sources	41
2.1	Desirable properties	43
	Brightness	43
	Indistinguishability	43

Separability	43
2.2 Spontaneous four-wave mixing	43
Resonant sources	45
2.3 Joint spectrum	46
2.4 Measuring correlated photons	47
Nonlinear loss	49
An example at high power	50
References	51
3 Experiment 1: Time-reversed Hong-Ou-Mandel interference	55
3.1 Background	56
3.1.1 Time-reversed Hong-Ou-Mandel interference	56
3.1.2 Time-reversed spontaneous four-wave mixing	56
3.2 Experiment	57
3.2.1 Effect of pairs generated in unintended places	59
3.3 Results	60
3.3.1 On-chip interference fringes	60
3.3.2 Off-chip Hong-Ou-Mandel dips	62
3.3.3 Production and interference of degenerate pairs	63
3.3.4 Brightness	64
3.4 Discussion	64
References	66
4 Experiment 2: Qubit entanglement & resonant photons	67
4.1 Experiment	67
4.1.1 Device operation	68
Device details	69
Calibration	69
4.2 Results	70
4.2.1 Resonant source overlap	70
4.2.2 Joint spectra	72
4.2.3 Bell inequality violation	73
4.2.4 Tomography	74
Model states	75
Measurements	76
4.3 Discussion	77
4.3.1 Source of entanglement	78
References	80
5 Experiments 3 & 4: Two-qubit quantum logic	81
5.1 Background	81
5.1.1 Split pairs are indistinguishable	81
Beamsplitter	81
Arbitrary interferometer	82
Experiment 3: Source & entangling gate	83
5.2 Operation	83
5.2.1 Ideal operation	83
5.2.2 Actual operation	84
5.3 Lessons	85

Experiment 4: Disentanglement	87
5.4 Design	87
5.4.1 Source	88
5.4.2 Quantum logic	89
5.4.3 Device structure	89
5.5 Results	90
5.5.1 Source performance	90
5.5.2 Tomography	91
5.6 Discussion	92
References	95
6 Conclusion	97
6.1 Retrospective	97
6.2 Un-finished business	97
6.2.1 Barriers to further progress	99
6.3 Un-started business	100
6.3.1 Cold silicon quantum photonics	100
6.3.2 Banishing nonlinear absorption, forever	101
6.4 Prospective	103
References	104
Appendices	107
A List of symbols	109
B Quantum	111
B.1 Quantum states	111
B.1.1 Pure states	111
B.1.2 Mixed states	111
B.2 Dirac matrix notation	112
B.3 Field quantisation	112
B.4 Properties of Matrices	115
B.4.1 Hermitian matrices	115
Degrees of freedom	115
B.4.2 Unitary matrices	115
B.4.3 Density matrices	116
The partial trace	117
B.4.4 Schmidt number	117
B.5 Creation and annihilation operators	118
B.5.1 Properties	118
B.5.2 Operator evolution (Heisenberg picture)	118
B.6 Hamiltonians & unitary evolution	119
B.6.1 Evolution of a photon in a single mode	120
B.7 Optical entangling gates	120
B.7.1 Cross-phase modulation	120
B.7.2 The post-selected CSIGN gate	121
Non-interfering configurations	122
Interfering configuration	123
Operator	123
Unitarity	124

References	125
C Optics	127
C.1 Electromagnetic wave equation	127
C.1.1 Linear media	127
C.1.2 Nonlinear media	128
C.2 Waveguides	128
C.2.1 Two-dimensional confinement	128
C.2.2 One-dimensional confinement	129
C.3 Evanescent couplers	131
C.4 Ring resonance	133
C.5 Quantum description of laser light	136
C.5.1 Bright light on a beamsplitter	136
References	137
D Spontaneous four-wave mixing	139
D.1 Hamiltonian	139
D.2 Squeezed vacuum	140
D.2.1 Two-mode squeezing	140
D.2.2 Single-mode squeezing	141
D.3 Pairs generated by multiple sources	143
D.4 Squeezed vacuum entanglement	144
D.5 Effect of XTPA on heralding efficiency	145
References	146
E Time-reversed Hong-Ou-Mandel interference	147
E.1 Two-photons and beamsplitters	147
E.1.1 Degenerate pairs	147
E.1.2 Non-degenerate pairs	147
E.2 Finding pairs in unexpected places	148
E.3 The Hong-Ou-Mandel dip	150
E.3.1 Application to discretely colour entangled pairs	151
E.4 Monochrome versus split photon pairs	152
References	153
F Qubit entanglement from resonant sources	155
F.1 On-chip state evolution	155
F.1.1 Imperfect overlap	157
F.2 Overlap, visibility, and multi-pair events	158
F.3 The Bell-CHSH test	159
F.4 Common-ground crosstalk correction	160
References	162
Index of figures and tables	165
Index of terms	167

Thanks

If I have seen further, it is by standing on the shoulders of giants. I have a great many people—giants—in my life to thank for their unrelenting help, support, insight, camaraderie, and love.

I am grateful to **Magnus Loutit**, **Pete Dunton**, **Josh Hugo**, and many others for their technical support at the University of Bristol, which has been excellent. I am grateful for the fun and stimulating environment provided by members of the **Centre for Quantum Photonics**. I hope the CQP carries its culture well into the future. I am especially indebted to **Raffaele Santagati**, who has been a phenomenal partner in crime, and from whom I have learned a lot. Thanks to **Jorge Barreto** for his friendship, and for his feedback on this document. Thanks also to the current and past administration (and now technical) team of the CQP—your work has allowed me to focus on the science.

Thanks, **Jeremy O'Brien**, for challenging me to shoot for the stars, and for giving me the freedom to try. Thanks, **Mark Thompson**, for demanding perfection, and for understanding that perfection is relative. I have learned enormously from both of you, and am grateful for your mentorship.

Damien Bonneau, you are honest, humble, and very talented; you are a great friend, a great colleague, and a great physicist. I look forward to many more years in your company—both inside and outside the lab.

I want to thank all **my parents** for their support, patience, and love over the years. I want to thank **Al Meldrum**, to whom I feel eternally indebted, for introducing me to optics, and for encouraging me to follow my dreams. Finally, **Liz**, thanks for making it all worthwhile.



Foreword

This year, 2015, has been designated the International Year of Light. It marks a fantastic number of base-ten anniversaries of light's development and application:

- ❶ 1000 years ago, Ibn al-Haytham finished his *Book of Optics*;
- ❷ 400 years ago, Lippershey, Janssen, and Galileo invented the telescope;
- ❸ 200 years ago, Fresnel imagined light as a wave;
- ❹ 150 years ago, Maxwell described light electromagnetically;
- ❺ 50 years ago, Börner, and Kao first used optical fibre for communication.

This list omits only a few milestones in the history of light, including: Einstein's proposal of the photoelectric effect, which cemented the idea of light as a particle, ca. 1905; and Newton's development of light's diffraction, transmission, and interaction with matter, ca. 1675. Today, the *science* of light holds an immense legacy of discovery and development.

Looking back from the future, I expect light-based *technology* to have affected humanity in unconscionable ways. Light at the very largest intensity scales promises to produce a new star on Earth, providing limitless energy via inertial-confinement fusion. At the very smallest scales—the scale of individual photons—light promises quite a different technological revolution. *This* revolution is the focus of this thesis.



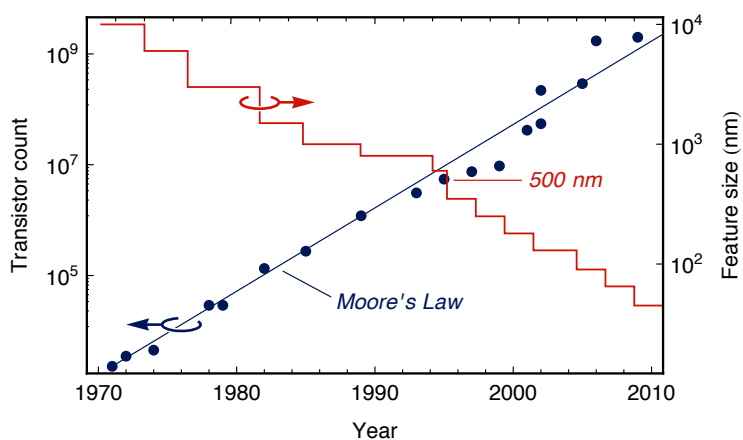
Chapter 1

Introduction

The second half of the twentieth century precipitated a technological revolution of a scale and speed like none before it: humanity started to build machines whose sole function was to process information. Information itself was a new idea, formalised in 1948 by Shannon¹ in the context of communication. The main motor of the information revolution, though, was not theoretical, but practical. Several computers were built during World War II, but the key ingredient—scalability—was not added until later. With the advent of high-purity silicon in 1956, and the electronic integrated circuit in 1958, the first integrated computer followed in 1971. From there, the applications of computation and communication exploded, transforming science, engineering, and civilisation beyond all recognition.

Computers let us understand, via simulation, the many physical, chemical, and biological systems which are beyond the reach of our analytical tools. They have transformed engineering, with improvements in computing power leading to improvements in the efficiency and functionality of humanity’s other technological pursuits. Computers have become *the* channel for human culture: literature, music, photos, film, and more are now created, distributed, and consumed digitally. Our ability to crunch data has increased exponentially since the first integrated computer. Moore’s famous observation that the complexity of the integrated circuit doubles every two years has governed the progress of microelectronics for the past half-century (see FIG. 1.1), largely through the prescription of making smaller and smaller transistors². Reviewing our information processing and communication prowess, you would be forgiven for thinking our work is done—it largely is.

FIG. 1.1: Microelectronic integration density over time. Moore’s law predicts an exponential scaling of integration density, with the transistor count doubling every two years. Transistor count data: Wolfram Alpha. Feature size data: Wikipedia.



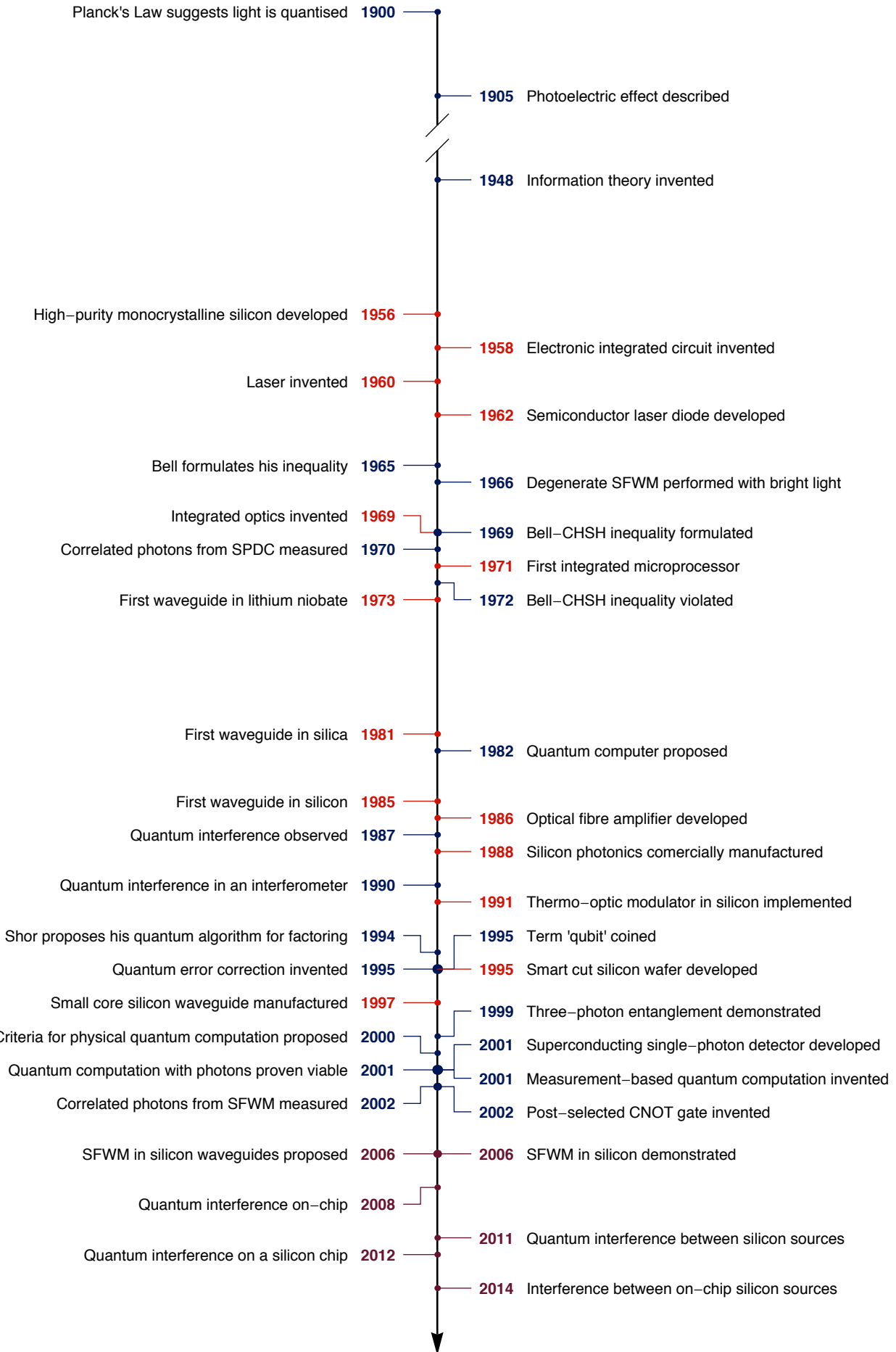
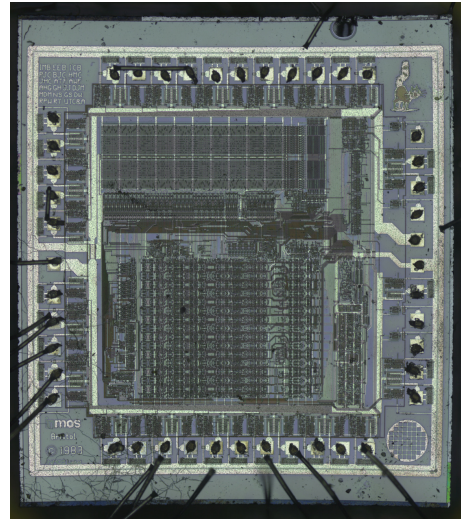


FIG. 1.2: One of the first InMOS transputer prototypes, the S42, designed in Bristol in 1983. Ca. 10 000 transistors made in $1.25\text{ }\mu\text{m}$ CMOS. This image is composed of a number of micrographs which I collected for Prof. Sir David May, one of the transputer's designers.



Despite our mastery of bits and bytes, there exist certain properties of that *classical* information, and its manipulation, which limits its usefulness. Computer scientists have classified problems into a hierarchy of complexity classes, which (among other things) dictate how hard a problem is to solve for a certain size of input: the so called 'scaling' of a problem. It turns out that if the requirement that our bits be strict 0s or 1s is relaxed, we can access different complexity classes which permit better scaling for problems we care about. For example, imagine we allow each bit to be probabilistic—call it a 'p-bit'—such that each bit has a chance p of being 0, and a chance $1 - p$ of being 1. Also notice that if $p = 0$ or $p = 1$ we recover the behaviour of our simple bits—p-bits are more general than bits. Practically, p-bits are used to search unstructured spaces, such as within Monte Carlo algorithms for optimisation, because they permit probabilistic solutions which scale much more favourably than deterministic algorithms with simple bits. In the case of p-bits, a heretofore deterministic computer is given access to the class of problems (called BPP) which are solvable efficiently by a probabilistic computer.

Now, both bits and p-bits behave classically: operations on bits yield deterministic results, and operations on p-bits yield results which follow classical probability distributions. The insight which Richard Feynman had in 1982 was that the properties of *quantum* particles may, as p-bits are able to generalise and out-perform bits in certain circumstances, give us some extra performance in an even larger class of problems (subsequently named BQP)³. He observed that simulations of quantum systems scale very badly on a classical computer (probabilistic or otherwise), but that the quantum systems have no trouble simulating themselves, at any scale. With this insight, the q-bit, and the science of quantum information was born. A quantum bit, or qubit, is a two-level quantum system, on which we can perform operations, and with which we can ultimately do computation—quantum computation.

On paper, as with many things, this looks easy: collect a few quantum systems, perform some gates between them which represent your problem, and measure them to get the answer. In practice, the challenges of this prescription are immense. DiVincenzo in 2000 came up with his famous criteria⁴ which candidate quantum systems must satisfy:

- ❶ A scalable physical system with well characterised qubits

- ② The ability to initialise the state of the qubits to a simple fiducial state
- ③ Long relevant coherence times, much longer than the gate operation time
- ④ A “universal” set of quantum gates
- ⑤ A qubit-specific measurement capability

The criteria are not perfect, but give a good perspective on the challenges of building a quantum computer. Some problems with the criteria ①-⑤ follow. The scalability ① of quantum systems can often be engineered, and if it really cannot, this is rarely known at the outset. Later in this thesis, I will show how computation can proceed without initialisation into a simple fiducial state ②, and how this non-fiducial initialisation also waives the need for a universal gate set ④. Quantum systems with very good coherence properties do not interact with the environment, nor generally with anything else. This makes our desire to perform arbitrary gates ④ (interactions), and to keep our systems coherent for long times ③ a case of trying to both eat our qubits and keep them too. In short, our requirements on the technology underpinning a quantum computer are at best challenging, and at worst in perfect conflict.

Quantum computation is the most exotic, and ambitious application of well-controlled quantum systems, but it is not the only application. Both communications and measurement can benefit from the use of quantum rather than classical information. In communications, the properties of qubits and the details of quantum measurements are used to secure a communication channel. This technology is quickly approaching commercialisation, with government, military, and financial sectors showing interest, and with short-haul quantum key distribution (QKD) networks springing up around the world. Quantum metrology, on the other hand, uses unique quantum correlations between qubits to obtain a maximum of information about a sample. Significant theoretical and practical hurdles remain before quantum metrology can compete with its classical counterpart, however.

Photons are the particles which make up light, so, unsurprisingly, they have no mass and travel at light speed, $c \approx 300\,000$ km/s. A consequence of the photon’s (lack of) mass, or alternatively of its light-speed propagation, is that single photons—perplexingly—don’t experience time. This is why, if you take two beams of light (ex. from a laser pointer) and cross them, you will find nothing happens—photons don’t interact with other photons, because neither has the time to feel the interaction. This is not to say that photons don’t interact with anything (matter, for example) but their interaction is necessarily reduced. It is for this reason that photons tend to stay coherent for long periods of time.

Speed and coherence make the photon an obvious information carrier for both quantum communication and metrology schemes. However, these same properties—continuous movement, and difficulty in interaction—seem to hinder its use in computation. For many years, this was taken as dogma, and work proceeded (and proceeds) on other candidate quantum systems: trapped ions⁵, superconducting loops⁶, and solid state systems⁷, to name the major contenders. In 2001, Knill, Laflamme, and Milburn set out to prove the impossibility of scalable computation with photons, once and for all. Instead, they came up with a scheme⁸ which doesn’t require photonic qubits to interact for computation to proceed. Their scheme (née KLM) simply requires a source of identical photons, a reconfigurable optical interferometer, and detectors able to tell how the photons scattered. With this, the field of linear optical quantum computation (LOQC) was born. Since 2001, other

proposals have improved upon the KLM scheme, to increase efficiency and better handle various quantum and classical errors. To elucidate the problem, I detail one such post-KLM scheme in §1.2.

§1.1 QUANTUM INFORMATION WITH PHOTONS

Quantum mechanics developed gradually over the first 20 years of the 20th century, and in no small part due to experimental and theoretical developments in optics. Maxwell formalised his fantastically powerful equations governing the electromagnetic field in 1861 (SC.1), but two optical measurements remained mysterious: the spectrum emitted by hot objects, and the propensity for electrons to jump off of metals only when illuminated by light above a certain frequency. In search of a description for black-body radiation, Planck in 1900 was forced to *quantise* the electromagnetic field’s energy to match his model with experiment. Though he didn’t know it, this quantisation was the first recognition that light is made up of photons. It wasn’t until 1905, when Einstein embraced this idea and used it to explain the photo-electric effect, before the idea of quantised light—and quantised *anything*—took root. It was from these ideas about light that all of quantum mechanics was born.

Subsequently, optics has been central to the exploration and test of quantum theory. After Bell formulated his inequality for local realistic theories in 1965, it was first Freedman and Clauser⁹ in 1972, then Aspect and Grangier¹⁰ in 1981, who tested it with entangled photon pairs. The first multi-partite entanglement was measured between photons¹¹, and used to directly test quantum theory¹². Photons were also forerunners, along with trapped-ion systems¹³ in 2003, in demonstrating two-qubit quantum logic gates between particles^{14,15}.

In this section, I describe some of the salient points of quantum information theory, and introduce some useful techniques for treating the behaviour of photons in that context. In the remainder of this thesis, I will use italic numerals (*0*, *1*) to represent qubit values, and roman ones (0, 1) for occupation numbers (as described in §1.1.2).

1.1.1 Qubits

Classical computers push around bits: states of voltages or currents which represent 0s or 1s. All (classical) information can be represented by bits. For example, when I enter my initials into a computer, it encodes them into the bit string 01001010 01010111 01010011. Boolean logic describes the structure of yes-or-no questions, but also, as it turns out, describes the behaviour of our 0-or-1 bits. Unlike quantum gates, which never create or destroy information, classical gates do so rampantly. Case in point: only one Boolean logic gate is needed for a classical computer to be universal—the NAND gate—and this gate has two inputs but only *one* output. Today’s computers are packed full of NAND gates, which work together to process immense numbers of bits.

If a classical bit can be in one of two states—this time call them $|0\rangle$ and $|1\rangle$ —then a quantum bit can be in any superposition of these states, $(\cos \theta)|0\rangle + (e^{i\phi} \sin \theta)|1\rangle$ for any angles θ and ϕ . This parametrisation into spherical coordinates lets us conveniently represent a qubit by a point on a sphere—the Bloch sphere—with

azimuthal coordinate ϕ and polar coordinate θ (see [FIG. 1.3](#)). In this representation, the states $|0\rangle$ and $|1\rangle$ lie at the North and South poles, respectively. [FIG. 1.3](#) highlights six cardinal states: the two poles, and four states of equal superposition on the equator. These equatorial states are written in terms of $|0\rangle$ and $|1\rangle$ as: $|\pm\rangle \equiv (|0\rangle \pm |1\rangle)/\sqrt{2}$ and $|\pm i\rangle \equiv (|0\rangle \pm i|1\rangle)/\sqrt{2}$.

Breaking the geometrical interpretation somewhat, states which are opposite one another on the Bloch sphere are orthogonal—they can be distinguished with certainty. The nearer any two states are in this picture, the lower the probability that a given measurement can distinguish them. It is for this reason that quantum information cannot be copied—no measurement gives the entire quantum state, and the state is destroyed after the first measurement. We’ll return to this in a moment.

The three axes in [FIG. 1.3](#) are labelled by the Pauli matrices, and the states which lie on each axis are eigenstates of one of these matrices. The three Pauli matrices, originally used to describe spin in three-dimensional space*, are:

$$\hat{X} \equiv \begin{pmatrix} 0 & +1 \\ +1 & 0 \end{pmatrix} \quad \hat{Y} \equiv \begin{pmatrix} 0 & -i \\ +i & 0 \end{pmatrix} \quad \hat{Z} \equiv \begin{pmatrix} +1 & 0 \\ 0 & -1 \end{pmatrix}. \quad (1.1)$$

The states $|0\rangle$ and $|1\rangle$ are eigenstates of \hat{Z} , with eigenvalues ± 1 , such that $\hat{Z}|0\rangle = +|0\rangle$ and $\hat{Z}|1\rangle = -|1\rangle$. Similarly, $|\pm\rangle$ and $|\pm i\rangle$ are the ± 1 eigenstates of \hat{X} and \hat{Z} , respectively. Notice that these lie one the x , y , and z axes of the Bloch sphere, respectively ([FIG. 1.3](#)). The Pauli matrices are both unitary and Hermitian ([SB.4](#)), but this is not generally the case for other operators.

We can probe a state by measuring an observable \hat{O} which encodes what we want to know, where \hat{O} is a Hermitian operator†. For a single qubit $|\psi\rangle$, a measurement on \hat{O} will return one of its eigenvalues‡ λ_i , and project $|\psi\rangle$ into the corresponding eigenstate $|\lambda_i\rangle$, with probability $\Pi_i = |\langle \lambda_i | \psi \rangle|^2$. Many such measurement will have an average result $\langle \psi | \hat{O} | \psi \rangle$. This means that a measurement on a qubit with observable \hat{X} , \hat{Y} , or \hat{Z} will project that qubit into that observable’s $+1$ or -1 eigenstate, depending on the result. For example, a measurement on a qubit $|\psi\rangle$ in the z -basis corresponds to a measurement of the observable \hat{Z} and can have one of two outcomes: $+1$ projecting the qubit into $|0\rangle$, and -1 projecting it into $|1\rangle$, with expectation value $\langle \psi | \hat{Z} | \psi \rangle$. Thus, a z -basis measurement can distinguish the states $|0\rangle$ and $|1\rangle$ with certainty, and the same is true of x - and y -basis measurements and their respective eigenstates.

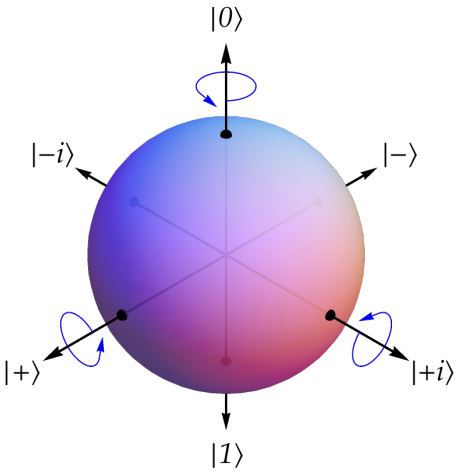
States of multiple qubits are represented like classical bit strings. For example, the four possible states of two bits can be written as $|00\rangle$, $|01\rangle$, $|10\rangle$, and $|11\rangle$. Each of these states is a tensor product of the states of two single qubits: $|ij\rangle \equiv |i\rangle \otimes |j\rangle$. Additionally, two qubits can be in any *superposition* of these states, for example $|++\rangle = (|00\rangle + |01\rangle + |10\rangle + |11\rangle)/\sqrt{4}$. Multi-qubit states which can be written as a product of single-qubit states are called separable states, while those that cannot are called entangled states. The behaviour of the component qubits in an entangled state is in some sense intertwined or connected. Separable states in superposi-

*Spin states immediately evoke the Bloch sphere ([FIG. 1.3](#)), with $|0\rangle = |\uparrow\rangle$ and $|1\rangle = |\downarrow\rangle$.

†Enforcing \hat{O} to be Hermitian ($\hat{O} = \hat{O}^\dagger$) is equivalent to asking for a *projective* measurement.

‡Since \hat{O} is Hermitian, its eigenvalues are real. If \hat{O} is a qubit observable, it has two of these.

FIG. 1.3: The standard Bloch sphere representation of a qubit, with typical cardinal states labelled. These state vectors label the $\pm x$, $\pm y$, and $\pm z$ directions ($|\pm\rangle$, $|\pm i\rangle$, and $|0/1\rangle$, respectively).



tion behave like waves, interfering constructively and destructively—quite different from the operations on bits which we are used to—but wave behaviour remains solidly part of classical physics, and can be efficiently simulated on a classical computer. The behaviour of entangled states, however, has no classical analogue, and yields some of the strangest effects in nature. It is entanglement which puts the *quantum* in quantum information, and which gives the aforementioned advantages over classical-physics-based systems. Entanglement is simultaneously the essential resource which quantum technology must harness, and the most fragile effect in nature.

Mixture

Returning briefly to our probabilistic p-bits, we can describe *both* p-bits and qubits using the compact language of density matrices¹⁶. Until now, we've dealt solely with qubit states which can be written as superpositions of $|1\rangle$ and $|0\rangle$ —these are called *pure* states. The density matrix is a more general way to represent classical or quantum states which are not pure—in general, called *mixed states*—like a p-bit which is $|0\rangle$ with chance Π and $|1\rangle$ with chance $1 - \Pi$. Density matrices are normally written as $\hat{\rho}$ and have purity \mathcal{P} :

$$\hat{\rho} \equiv \sum_i \Pi_i |\psi_i\rangle\langle\psi_i|, \quad \mathcal{P} \equiv \text{Tr}(\hat{\rho}^2) \quad (1.2)$$

where Π_i is the probability to find the system in the pure state $|\psi_i\rangle$, an eigenstate of $\hat{\rho}$. Also note the lack of modulus in the purity definition. The purity runs from $1/d$ (fully mixed) to 1 (pure), where d is the system's dimension. In the Bloch sphere picture, pure qubit states lie on the surface, with the fully mixed state lying at its centre. For $\hat{\rho}$ to be physical, it must be in *some* state, so $\sum \Pi_i = \text{Tr } \hat{\rho} = 1$.

Given $\hat{\rho}$, the chance to find it in state $|\psi\rangle$ can then simply be read from the diagonal of $\hat{\rho}$, provided $|\psi\rangle$ is one of the eigenstates $\{|\psi_i\rangle\}$. Born's rule gives the chance to find it in any general state $|\phi\rangle$:

$$\Pi_\phi = \text{Tr}(\hat{\rho} \cdot |\phi\rangle\langle\phi|). \quad (1.3)$$

We will briefly discuss operations on density matrices in the next section, then revisit them in **CH. 4**, when we look at *real* quantum states.

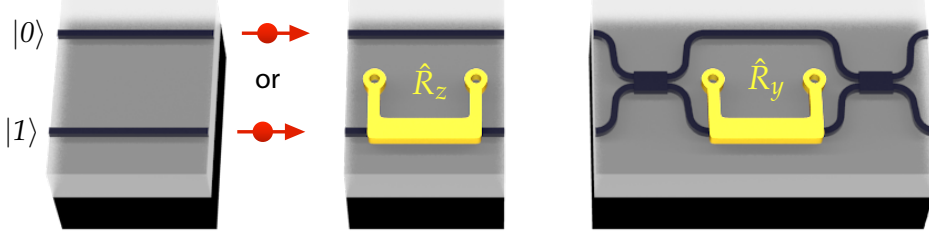


FIG. 1.4: Path encoding for photonic qubits. Path qubits are encoded in a single photon which occupies one of two waveguide modes. If the photon is in the top (bottom) mode, we call it $|0\rangle$ ($|1\rangle$). Rotations about the z - and y -axes are shown, labelled \hat{R}_z and \hat{R}_y respectively, and formed by a single phase shifter, and a Mach-Zehnder interferometer.

Operations on qubits

Since quantum mechanics is entirely time-reversible, so too are the quantum operations on qubits. This statement is equivalent to requiring quantum operations be *unitary*, i.e. for any unitary \hat{U} , applying it forwards and then backwards must be the same as doing nothing at all: $\hat{U}\hat{U}^\dagger = \hat{I}$. The many other properties of unitary operators are listed in [SB.4.2](#). In optics, this time-reversibility is intuitive, since all linear optical devices are reversible*. This intuition is no coincidence: in fact, one single photon behaves just like bright light, if we map the probability of the single photon's presence to the light's intensity. Multiple single photons, however can behave quite differently to bright light, as we will see in the next section. Unitary operators are those which preserve a vector's length (i.e. a state's normalisation). In the Bloch sphere picture, these amount to rotations and reflections about the origin. The Pauli matrices are reflections about their respective axes, and rotations can be composed of Pauli matrices in the form $\hat{R}_w(\theta) = \exp(i\theta\hat{W}/2)$ (for rotation by θ about the w -axis, with $w \in \{x, y, z\}$, and \hat{W} being the corresponding Pauli matrix from [EQ. 1.1](#)). An operation \hat{U} causes a pure state $|\psi\rangle$ and a mixed state $\hat{\rho}$ to evolve according to

$$|\psi\rangle \rightarrow \hat{U}|\psi\rangle, \quad \hat{\rho} \rightarrow \hat{U}\hat{\rho}\hat{U}^\dagger. \quad (1.4)$$

Photonic qubits encoded in the path degree of freedom have historically been referred to as dual-rail qubits. Here, I will call them simply *path* qubits. This nomenclature fits better with the widely-discussed *polarisation* and *time-bin* qubits, and allows us to freely refer to qubits stored in any photonic degree of freedom. Basic operations on path qubits are shown in [FIG. 1.4](#). A path qubit is a photon spread between two spatial modes; in our devices, these are the modes of single-mode waveguides, so a path qubit lives within a pair of these waveguides. We can manipulate path qubits with rotations around the Bloch sphere ([FIG. 1.3](#)) as shown in [FIG. 1.4](#). \hat{R}_z and \hat{R}_y rotations are realised respectively by a phase shifter, and a phase shifter between two beamsplitters—a Mach-Zehnder interferometer. An arbitrary preparation of a single qubit, starting from $|0\rangle$, is implemented using two rotations, $|\psi\rangle = \hat{R}_z(\theta_2)\hat{R}_y(\theta_1)|0\rangle$, and an arbitrary operation on a single qubit is implemented using three, $|\psi\rangle = \hat{R}_z(\theta_2)\hat{R}_y(\theta_1)\hat{R}_z(\theta_0)|\phi\rangle$, for an arbitrary $|\psi\rangle$ and $|\phi\rangle$.

*The (linear) electromagnetic wave equation is reversible, since it depends on $\frac{\partial^2 u}{\partial t^2}$ and c^2 .

1.1.2 Photons

Photons are bosons, and when they're allowed to behave naturally, they don't tend to adhere to the strict two-mode rule of path qubits. Their bosonic nature also allows more than one photon to occupy a given mode. In free space, they propagate in a vast continuum of modes with different wavevectors. Here, though, we will restrict our discussion to propagation in a discrete set of modes, such as those found in waveguides and many interferometers.

Before we discuss propagation, we must formally define what a photon is. It is convenient in the case of photons to not talk of qubits, but of excitations of the electromagnetic field. Rigorous treatment of field quantisation has been performed by many authors^{17–20}, following the first treatment, in 1927, by Dirac²¹. For completeness, I reproduce the basic results in §B.3 and summarise them below.

The number states or Fock states, denoted $|n\rangle$ with $n = 0, 1, 2, \dots$, are eigenstates of the vacuum Hamiltonian, and are indexed by the number of photonic excitations contained in their single mode. They are orthogonal ($\langle m|n\rangle = \delta_{mn}$) and form a complete basis. The creation a^\dagger and annihilation a operators respectively add and subtract one photon from the state, and preserve normalisation:

$$a^\dagger|n\rangle = \sqrt{n+1}|n+1\rangle \quad a|n\rangle = \sqrt{n}|n-1\rangle. \quad (1.5)$$

Arbitrary number states can be produced by applying the creation operator to vacuum:

$$|n\rangle = \frac{1}{\sqrt{n!}}(a^\dagger)^n|0\rangle. \quad (1.6)$$

When we don't care about the shape of our modes*, the number states and ladder operators are useful tools for modeling photonic behaviour in linear and nonlinear optics.

We can now formally write our path qubits in terms of the number states. Looking again at FIG. 1.4, the $|0\rangle$ state represents one photon occupying the top mode and zero occupying the bottom mode, with $|1\rangle$ represents the reverse. Thus, the path qubits are written

$$|0\rangle \leftrightarrow |10\rangle \quad |1\rangle \leftrightarrow |01\rangle, \quad (1.7)$$

which is known as the *qubit basis*. Photonic states which cannot be described by products of $|0\rangle$ and $|1\rangle$ (for an arbitrary set of modes) do not normally describe photonic qubits[†]

Photonic evolution

Since, as mentioned, photons don't interact, each photon propagates independently through a linear optical system, and interferes both with itself and with other indistinguishable photons, at the output. Each linear optical system is given by a unitary matrix, \hat{U} , which completely describes its mapping of input modes to output modes. Conveniently, the unitary which describes the single-photon behaviour

* Waveguide and resonator transverse and longitudinal modes are discussed in §1.3 and §C.4.

[†] States with more than $2d$ modes for d photons are referred to as qudits and are often used in experiment to simulate the behaviour of multiple qubits when multiple photons are hard to find (e.g. refs. 22,23). Some schemes encode directly in photon number (e.g. ref. 24). Multi-photon encodings are used to facilitate computation, and to detect and correct quantum errors (e.g. refs. 25,26).

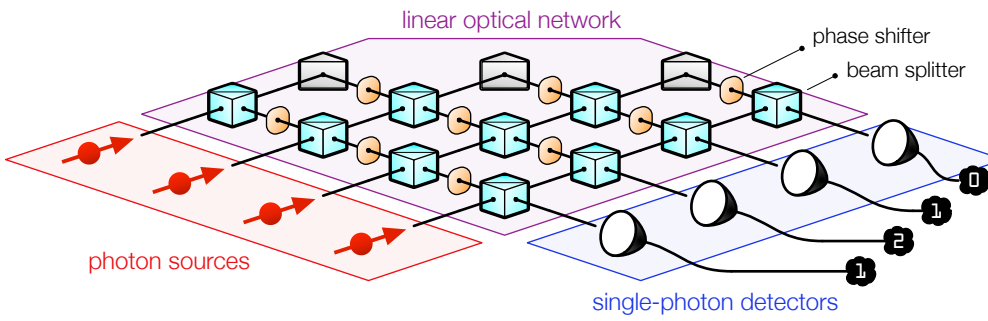


FIG. 1.5: A general linear optical quantum system.

is the same one which describes the scattering of bright light, often referred to as the scattering matrix.

In the so called Heisenberg picture of quantum mechanics, the evolution of a quantum system is lumped into the evolution of an operator on a fixed initial state. This way of describing the evolution of single photons is useful and intuitive in the context of creation operators operating on the vacuum.

Here, I'll derive in general terms how we can use the evolution of creation operators to describe the evolution of single photons through linear optical networks. Let's assume we have a set of N modes with associated annihilation (field) operators for the inputs $\{a_0, a_1 \dots a_N\}$ and outputs $\{b_0, b_1 \dots b_N\}$ which evolve according to a single-photon unitary operator \hat{U} which takes inputs to outputs, and is equivalent to the scattering matrix which acts on the classical electric field*:

$$\begin{bmatrix} E'_0 \\ \vdots \\ E'_N \end{bmatrix} = \hat{U} \begin{bmatrix} E_0 \\ \vdots \\ E_N \end{bmatrix} \rightarrow \begin{bmatrix} b_0 \\ \vdots \\ b_N \end{bmatrix} = \hat{U} \begin{bmatrix} a_0 \\ \vdots \\ a_N \end{bmatrix} \quad (1.8)$$

To obtain the rule for transforming input creation operators (a_i^\dagger) to output creation operators (b_i^\dagger), we must solve [EQ. 1.8](#) for the $\{a_i^\dagger\}$. We'll use the invertibility property of unitary matrices ($\hat{U}^{-1} = \hat{U}^\dagger$), the distributive property of the Hermitian conjugate ($(AB)^\dagger = B^\dagger A^\dagger$), and conjugate both sides to obtain relationships for the *creation* operators. Starting with [EQ. 1.8](#) we find ([§B.5.2](#)),

$$\hat{U}^T \begin{bmatrix} b_0^\dagger \\ \vdots \\ b_N^\dagger \end{bmatrix} = \begin{bmatrix} a_0^\dagger \\ \vdots \\ a_N^\dagger \end{bmatrix}. \quad (1.9)$$

Thus, the transformation of creation operators proceeds *backwards in time* compared to classical electric fields, and this makes sense considering that a^\dagger is just time-reversed a , which evolves classically according to the quantisation rule.

Now that we have the tools to propagate photons through linear optics, let's examine those optics in more detail. Linear interferometers are composed of beam-splitters, which mix optical modes together, and phase shifters, which advance or retard certain modes with respect to others. The unitary for a symmetric beamsplitter with reflectivity η , and for a phase shift of ϕ acting on the first of two modes

*The transfer matrix for the electric field is normally referred to as \hat{S} . I'll keep it as \hat{U} here to emphasise its unitarity, and to keep with the quantum optical literature.

(middle, FIG. 1.4), respectively are

$$\hat{U}_{\text{BS}} = \begin{pmatrix} \sqrt{\eta} & i\sqrt{1-\eta} \\ i\sqrt{1-\eta} & \sqrt{\eta} \end{pmatrix} \quad \hat{U}_{\text{PS}} = \begin{pmatrix} e^{i\phi} & 0 \\ 0 & 1 \end{pmatrix}. \quad (1.10)$$

In fact, it turns out that any non-trivial beamsplitter is universal for linear optical computation²⁷. A schematic of a general linear optical quantum system is shown in FIG. 1.5, composed of three principal components: a source of single photons; a linear optical network to manipulate those photons; and a set of single-photon detectors to register their behaviour. Despite the lack of interaction in this picture, it has been shown⁸ that these elements, together with feed-forward, are enough to support universal quantum computation.

Hong-Ou-Mandel interference

Quantum interference between photons was first measured by the eponymous Hong, Ou, and Mandel in 1987²⁸, almost simultaneously with Rarity and Tapster²⁹. Both teams produced a pair of indistinguishable photons, and injected one into each input of a balanced ($\eta = 50\%$) beamsplitter. Crucially, they delayed one photon by an amount τ with respect to the other, and so introduced a distinguishability in the photons' arrival time. When $\tau = 0$ the two photons were perfectly indistinguishable, and underwent so-called quantum interference—we will treat this case, below.

The two-mode input state to our system is $|11\rangle$, meaning that both modes contain one photon. As per EQ. 1.6, we can write this in terms of creation operators as $|11\rangle = a_0^\dagger a_1^\dagger |00\rangle$. We can then obtain the transformation rules for propagating this state through the beamsplitter, with unitary \hat{U}_{BS} given by EQ. 1.10, using EQ. 1.9. For now, we'll keep the beamsplitter reflectivity η general, and examine later what happens when its balanced.

$$\begin{bmatrix} b_0^\dagger & b_1^\dagger \end{bmatrix} \begin{pmatrix} \sqrt{\eta} & i\sqrt{1-\eta} \\ i\sqrt{1-\eta} & \sqrt{\eta} \end{pmatrix} = \begin{bmatrix} a_0^\dagger & a_1^\dagger \end{bmatrix} \quad (1.11)$$

$$\begin{aligned} a_0^\dagger &\rightarrow \sqrt{\eta} b_0^\dagger + i\sqrt{1-\eta} b_1^\dagger \\ a_1^\dagger &\rightarrow i\sqrt{1-\eta} b_0^\dagger + \sqrt{\eta} b_1^\dagger \end{aligned} \quad (1.12)$$

Now we can apply these rules to our input state to show Hong-Ou-Mandel interference, when $\eta = 50\%$.

$$\begin{aligned} a_0^\dagger a_1^\dagger |00\rangle &\rightarrow \left(\frac{1}{\sqrt{2}} b_0^\dagger + \frac{i}{\sqrt{2}} b_1^\dagger \right) \left(\frac{i}{\sqrt{2}} b_0^\dagger + \frac{1}{\sqrt{2}} b_1^\dagger \right) |00\rangle \\ &= \left(\frac{i}{2} b_0^\dagger b_0^\dagger + \frac{i}{2} b_1^\dagger b_1^\dagger \right) |00\rangle = i \frac{|20\rangle + |02\rangle}{\sqrt{2}} \end{aligned} \quad (1.13)$$

So, when the two photons are indistinguishable, the probability that they exit the beamsplitter separately *vanishes*. If we were to place one detector at each output, we would see no coincidences when $\tau = 0$. When they are delayed much more than their coherence length, we can distinguish them, and they behave inde-

pendently,

$$\begin{aligned}
a_0^\dagger \alpha_1^\dagger |0000\rangle &\rightarrow \left(\frac{1}{\sqrt{2}} b_0^\dagger + \frac{i}{\sqrt{2}} b_1^\dagger \right) \left(\frac{i}{\sqrt{2}} \beta_0^\dagger + \frac{1}{\sqrt{2}} \beta_1^\dagger \right) |0000\rangle \\
&= \left(\frac{i}{2} b_0^\dagger \beta_0^\dagger + \frac{i}{2} b_1^\dagger \beta_1^\dagger + \frac{1}{2} b_0^\dagger \beta_1^\dagger - \frac{1}{2} b_1^\dagger \beta_0^\dagger \right) |0000\rangle \\
&= \frac{i|1100\rangle + i|0011\rangle + |1001\rangle - |0110\rangle}{\sqrt{2}}
\end{aligned} \tag{1.14}$$

where half of the time the two photons will bunch up at the output (the final two terms).

This ‘dip’ in measured coincidences as τ approaches zero is known as a HOM dip, and has become a standard test of photon indistinguishability, with the visibility of the dip being a key figure of merit. For N_0 counts at $\tau = 0$, and N_1 for large τ , the visibility is defined as

$$V \equiv \frac{N_1 - N_0}{N_1}. \tag{1.15}$$

Ideally, if the photons are indistinguishable then there should be no coincidences in the dip ($N_0 = 0$), and the visibility approaches 100%. Furthermore, it should be noted that the interference happens in the state of each mode *inside the two detectors*, rather than somewhere inside the beamsplitter. This point was demonstrated elegantly by Pittman³⁰.

1.1.3 Two-qubit gates

The final topic of quantum information with photons is the elephant in the room—how to get one photon to change the state of another. I discussed the non-interacting nature of photons, in the context of their long coherence times, and I also mentioned that linear optics is universal for quantum computation. These two statements seem to be in opposition.

Two-qubit gates can change the amount of entanglement between qubits—they can entangle independent qubits, disentangle already entangled ones, and do everything in between. In a two-qubit controlled unitary (CU), the state of one qubit (the ‘control’) determines whether or not a certain unitary \hat{U} is applied to the second qubit (the ‘target’). If the control is $|1\rangle$, \hat{U} is applied, otherwise it’s not. Controlled unitary gates are maximally entangling—they can take a separable input to a maximally entangled output and vice versa. The most famous CU is the CNOT gate, in which $\hat{U} = \hat{X}$, such that a NOT (i.e. \hat{X}) operation is conditionally applied to the target qubit. The CNOT can be written as (see §B.2 for an explanation of Dirac matrix notation)

$$\text{CNOT} \equiv |00\rangle\langle 00| + |01\rangle\langle 01| + |10\rangle\langle 11| + |11\rangle\langle 10|, \tag{1.16}$$

from which the controlled NOT on the target can be seen in the last two terms. The CNOT entangles two qubits by their value or photonic *amplitude*.

A second important CU is the CSIGN gate, which entangles the *phase* of two input qubits. Here, $\hat{U} = \hat{Z}$, so the CSIGN is often known as ‘CZ’, and occasionally as ‘CPHASE’. It is defined as

$$\text{CSIGN} \equiv |00\rangle\langle 00| + |01\rangle\langle 01| + |10\rangle\langle 10| - |11\rangle\langle 11|, \tag{1.17}$$

from which it can be seen to act symmetrically on the control and input qubits (when both are $|1\rangle$, it applies a sign-flip). Consider its operation on the state $|++\rangle$:

$$\begin{aligned}\text{CSIGN}|++\rangle &= \text{CSIGN} \left[\frac{|00\rangle + |01\rangle + |10\rangle + |11\rangle}{2} \right] \\ &= \frac{|00\rangle + |01\rangle + |10\rangle - |11\rangle}{2} \\ &= \frac{|0+\rangle + |1-\rangle}{\sqrt{2}}.\end{aligned}\tag{1.18}$$

From a separable input, we obtain an output with maximal correlations. Incidentally, this method to generate entangled states—preparing a set of qubits in $|+\rangle$ then applying CSIGNs between them—is the prescription for obtaining cluster states, which will be discussed in §1.1.4 and applied to computation in §1.2.

In the following two sections, I show two methods to overcome photons' reluctance to interact. The first example emphasises that 'interaction' is really another way of saying 'nonlinearity', and uses *nonlinear* optics to construct a CSIGN gate; the second example gets to the heart of *linear* optics, and shows how post-selection can be used to mimic interaction.

Optical nonlinearities as two-qubit gates

If there existed a photon-photon nonlinearity, then the sum of two photons would not just be the sum of two photons, but something more. It is this something more that we would like to exploit, to implement an interaction. Nonlinear optics is a significant and well-studied field, which seeks exactly that. An example of a nonlinear optical process which we could directly use to implement a photon-photon interaction is called cross-phase modulation (XPM). See §B.7.1 for detailed calculations. XPM has an operator

$$\hat{U}_{\text{XPM}} = e^{\Phi_1 a^\dagger b^\dagger b},\tag{1.19}$$

meaning that in the presence of one photon each in modes a and b , the photons' joint phase rotates; if there is only one photon, then nothing happens. The parameter Φ_1 represents the phase precession, and depends on the interaction length and the third order $\chi^{(3)}$ nonlinearity of the medium. If we evolve a state of one or two photons over a length such that $\Phi_1 = \pi/2$, then the following maximally entangling unitary map is realised for 0 or 1 photons in two modes²⁰

$$\hat{U}_{\text{XPM}} \rightarrow |00\rangle\langle 00| + |01\rangle\langle 01| + |10\rangle\langle 10| - |11\rangle\langle 11|.\tag{1.20}$$

The XPM operation given by EQ. 1.20 is an example of a CU. If we take our two qubits to be $|0\rangle = |0\rangle$ and $|1\rangle = |1\rangle$ (where, again, italic type indicates qubit values), then a CSIGN gate (EQ. 1.17) is implemented: when the first qubit is in state $|1\rangle$, the state takes a sign-flip. If the first qubit is $|0\rangle$, then the gate does nothing.

Unfortunately for this photon-photon interaction, the crucial Φ_1 factor is very small. In a typical silicon waveguide (as detailed in §1.3.3) at a wavelength of $1.5\text{ }\mu\text{m}$, Φ_1 is at most about 2×10^{-6} radians. To obtain the necessary strength of interaction $\Phi_1 = \pi/2$, the waveguide loss must be reduced to around 0.001 dB/cm , and it must be stretched to about 200 m . The current state of the art is actually approaching this with demonstrated waveguide loss 0.0008 dB/m over 27 m ³¹. Difficult measurements of single-photon XPM were carried out by Matsuda et al. in 2009, using highly nonlinear photonic crystal fibre³², where $\Phi_1 \approx 1 \times 10^{-7}$ was achieved.

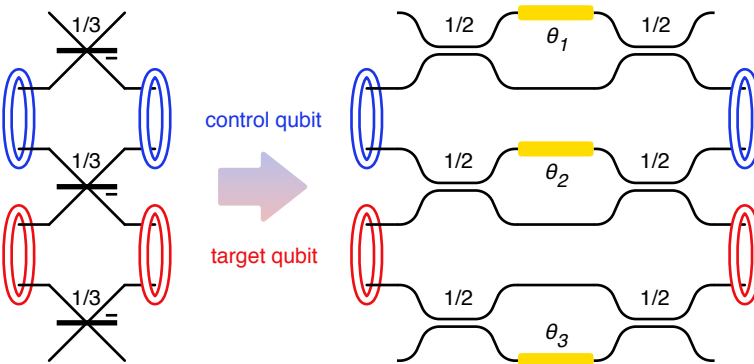


FIG. 1.6: Interferometer implementing the post-selected CSIGN operation on two path qubits, indicated in blue and red. Original proposal at left composed of $\eta = 1/3$ beamsplitters, integrated implementation with Mach-Zehnder interferometers at right. Modes carrying qubits are connected by hoops.

The post-selected CSIGN gate

Here, I'll outline the operation of a two-qubit gate which has been instrumental to many of the initial demonstrations of quantum information processing with linear optics^{14,15,33–35}. The interferometer which forms the gate (FIG. 1.6) was independently conceived by both Ralph et al.³⁶ and Hofmann and Takeuchi³⁷, in 2002, and crucially requires no ancilla (extra) resources. It was independently demonstrated by both O'Brien et al.¹⁴ and Pittman et al.¹⁵, in 2003.

The gate implements the CSIGN operation described in EQ. 1.17. Importantly, if we are happy to implement this operation *non-deterministically*, we can avoid the need for interaction. Consequently, the gate works on average once in every nine tries. When it fails, it takes the two path qubits—two photons in four modes—outside the qubit basis (EQ. 1.7), leaving only vacuum in at least one qubit.

The interferometer (FIG. 1.6) is composed of $\eta = 1/3$ asymmetrical beamsplitters, each equivalent to a Mach-Zehnder interferometer (MZI, FIG. 1.4) with internal phase $\theta = 2 \arcsin \sqrt{\eta} \approx 70^\circ$. Proof that this interferometer does indeed implement the CSIGN operation is given in SB.7.2.

The gate, and indeed the rest of linear optics, works by creating a large superposition of P' photons in M' modes, then chopping out via measurement the parts of that superposition which don't reflect the desired operation, until only P photons and M modes remain. When these measurements must include the desired output state, this process is called post-selection, while if only ancilla modes and photons must be measured, it's called heralding. The great thing about the post-selected CSIGN is that $P' = P$, so no additional experimentally precious photons are needed.

1.1.4 Entanglement

I have repeatedly stated the importance of entanglement to quantum technology, but we haven't yet discussed what it actually is. In words, entanglement is the property of a coherent multi-particle state which—if present—prevents each particle from being described independently. States of independently describable particles are called ‘separable’—the opposite of ‘entangled’. Due to this somewhat backwards description—a state is entangled if it's not separable—entanglement can be very difficult to quantify. Qubits will form the basis of this discussion, but these ideas apply to any quantum state.

Entangled states

First, separability. If $|\Psi\rangle$ is a state of N particles, then $|\Psi\rangle$ is *separable* only if it can be written as a tensor product of the states of the various particles $\{|\psi_i\rangle\}$ as

$$|\Psi\rangle \stackrel{\text{sep}}{=} \bigotimes_{i=1}^N |\psi_i\rangle, \quad (1.21)$$

otherwise it is entangled to some extent—the states of some particles in $|\Psi\rangle$ depend on the states of others. The amount of entanglement in a pure state is measured by its Schmidt number, K , which counts the number of separable states required to describe $|\Psi\rangle$ (see §B.4.4). Quantifying the entanglement in a *mixed* state is much more complicated³⁸.

A few named examples of pure qubit states with *maximal* correlations—maximally entangled states—are listed below. All are normalised, but I'll omit normalisation factors for clarity.

- Bell states (2 qubits): $|\Phi^\pm\rangle \equiv |00\rangle \pm |11\rangle$ and $|\Psi^\pm\rangle \equiv |01\rangle \pm |10\rangle$
- Greenberger-Horne-Zeilinger states: $|\text{GHZ}_N\rangle \equiv |0\rangle^{\otimes N} + |1\rangle^{\otimes N}$
- W-states: $|W_N\rangle \equiv \sum_i^N |0\rangle^{\otimes(i-1)}|1\rangle|0\rangle^{\otimes(N-i)}$
- N00N-states: $|N00N\rangle \equiv |N0\rangle + |0N\rangle$

Another important class of entangled states (though not necessarily *maximally* entangled ones) are the graph states. These states are so-called because they can be represented as graphs, with qubits as nodes and entanglement between qubits as edges. A graph state is not unique to a given graph, but is part of a set related to that graph's stabilisers*. Something like the converse is also true: given only *local* operations on a graph state's qubits, it's possible to access a large set of other graphs³⁹. For example, for four qubits, there are only two unique graphs under local rotations—the star and the line—and all other graphs follow from these.

The i^{th} node in a graph is connected to a set of other nodes, \mathcal{A}_i . A graph state $|G\rangle$ of N qubits can be formed by first preparing every qubit in the state $|+\rangle$, then applying CSIGN gates between the i^{th} qubit and its neighbours in the set \mathcal{A}_i :

$$|G\rangle = \left(\bigotimes_i^N \bigotimes_{j \in \mathcal{A}_i} \text{CSIGN}(i, j) \right) |+\rangle^{\otimes N} \quad (1.22)$$

where $\text{CSIGN}(i, j)$ is a gate operating on the i^{th} and j^{th} qubits only. Graph states are fundamental to important quantum computation and quantum error correction schemes, as we shall see in the next section.

§1.2 QUANTUM COMPUTATION

The remainder of this thesis details quantum photonic tools which some day may help us build a photonic quantum computer. To put these tools in context, and to

*Formally, an N -qubit state $|\psi\rangle$ represents a given graph G if it is the simultaneous eigenstate of the N stabilisers of that graph: it must satisfy $\hat{X}_i(\bigotimes_{j \in \mathcal{A}_i} \hat{Z}_j)|\psi\rangle = \lambda|\psi\rangle$, for the i^{th} node of G where $i \in [1, N]$, and \mathcal{A}_i is the set of nodes adjacent to this one. See ref. 20 for a discussion of stabilisers.

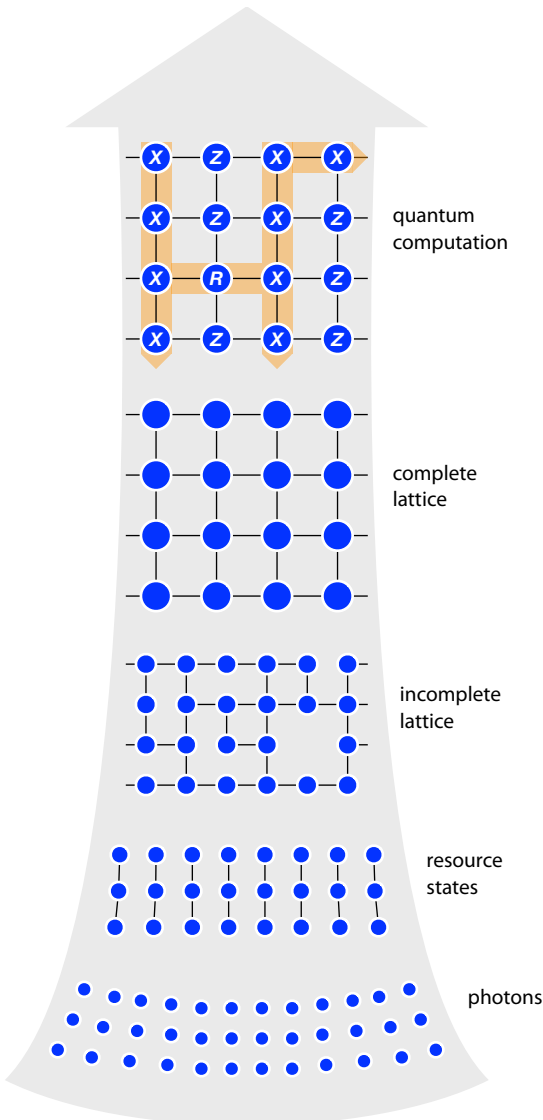


FIG. 1.7: Pictorial summary of MBQC with photons. Single photons at the bottom of the stack are entangled into resource states; those resource states are entangled into an incomplete lattice cluster; percolation on that lattice makes it complete; and finally quantum computation (potentially including error correction) is performed on that complete cluster state lattice.

understand how they relate to their target machine, we must first have some idea of what that machine might look like.

There has been much discussion of the requirements for construction of a quantum computer, from the strict criteria we discussed⁴, to what quantum gates must be implemented to make it universal^{27,40}, to what errors can be tolerated for it to work. Much of this prior literature has assumed that quantum computation would proceed via *gates* in quantum circuits. Though it has been shown that the circuit model of computation is feasible with optics⁸, these gates remain an acute problem for us, since they only work some of the time (cf. §1.1.3). On top of this, unlike other quantum information carriers, photonic qubits sometimes just get lost in the wider world, with their state unknown to us. For these reasons, together with recent developments in correcting quantum errors, and new approaches for tolerating our flaky gates and qubits, we are lead naturally into the arms of an altogether different computational paradigm.

In measurement-based quantum computation (MBQC) a large, entangled resource state is prepared, and computation proceeds by making various measurements on the qubits of that resource state. The resource state is known as a cluster

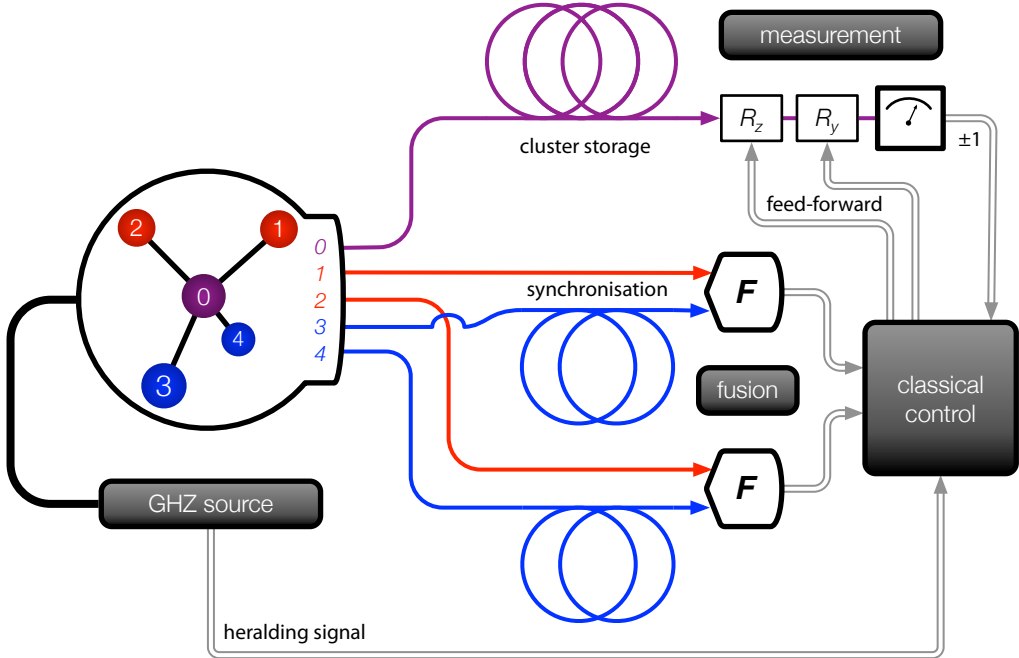


FIG. 1.8: Outline of a linear optical quantum computer, based on the measurement-based model of computation. In this model, the measurements performed on a cluster state encode the quantum algorithm to be performed. GHZ states ($|0\rangle^{\otimes N} + |1\rangle^{\otimes N}$ with $N = 5$) are fused together into a cluster state, which is measured one qubit at a time, and the results are fed-forward to select the measurements performed later.

state, or graph state, since it can be written in the form of a graph (see §1.1.4).

MBQC was developed by Raussendorf and Briegel in 2001⁴¹, the same year as the pioneering work on LOQC by Knill Laflamme and Milburn⁸. Much literature exists on MBQC algorithms^{41–44}, their error correction^{45,46}, and their use in optics^{47–51}. I will outline here an implementation of a proposal by Brown and Rudolph in 2005⁴⁸, recently improved upon by Gimeno-Segovia et al.⁵⁰. This implementation was originally conceived between myself, Gabriel Mendoza, Nick Russell, Jacques Carolan, and Jianwei Wang. Ambitiously, we named it QNIX.

In QNIX, a large number of separable single photons evolve into a much smaller number, entangled in a cluster state. This cluster state then permits MBQC and topological error correction. This evolution is schematised in terms of graph states in FIG. 1.7. $2N$ photons are put through an interferometer which heralds N of them into a maximally entangled N -qubit Greenberger-Horne-Zeilinger (GHZ, §1.1.4) resource state with a heralded success probability of $1/2^{2N-1}$. In the case of $N = 3$ (second tier of FIG. 1.7), the success probability is $1/8$, so we must multiplex these heralded events up to an acceptable probability. As the size N of the resource state increases, considerably more switches and multiplexed events are required.

Multiplexing involves repeating a heralded event many times, and selecting one successfully heralded event from this ensemble. This selection involves detecting the heralding signal, deciding what to do, then moving a series of optical switches accordingly—all while the unheralded photon(s) are still in flight. In the case of multiplexed single photons⁵², the detection of one photon of a pair heralds the presence of the other. If enough of these heralded photon sources are

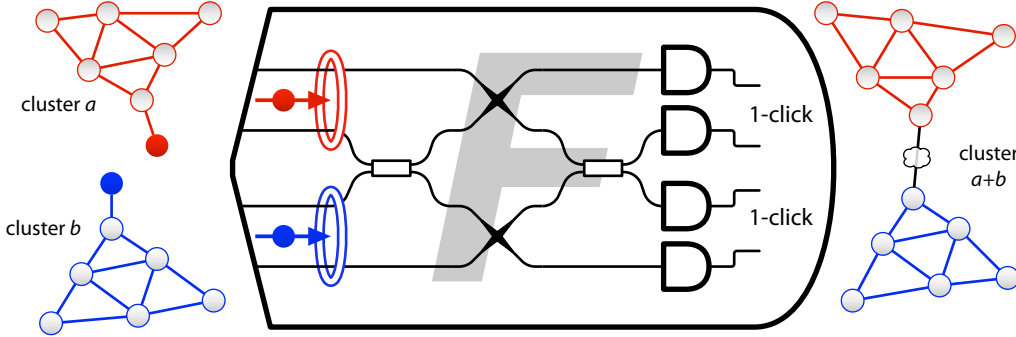


FIG. 1.9: Expanded view and operation of the fusion gate shown miniaturised in [FIG. 1.8](#). The gate joins together disconnected clusters, but destroys the input qubits (type-II fusion). It succeeds in 50% of attempts.

pumped simultaneously, each with a chance Π to produce a pair, the chance that at least one of them works is $1 - (1 - \Pi)^n$, which rapidly approaches unity for $n \approx 10$ and $\Pi \approx 10\%$. To multiplex n pair-generating events, we need a $n \times 1$ switch which can change its state in the time-of-flight of the unmeasured photon. For m output modes, m such switches are required. Each of our GHZ sources has $m = 2N = 6$ output modes, so requires around $n = 32$ multiplexed events to obtain near-deterministic production—around $6 \times (32 \times 1)$ switches (or $192 \times 2 \times 1$ switches).

These GHZ resource states are next used to construct a large, highly entangled cluster state, via an operation called fusion⁴⁸, outlined in [FIG. 1.9](#). The non-unitary fusion gate takes two qubits and performs a Bell-like measurement on them, with operator $|01\rangle\langle 01| + |10\rangle\langle 10|$. When this measurement comes up positive, we know that the qubits were correlated, and that any larger entangled states they were part of are now also correlated. When two qubits, each part of a larger cluster state, are input, the fusion operation has a 50% chance to work. Gimeno-Segovia showed that this operation can be boosted to 75% by using an ancilla entangled pair⁵⁰ via the Bell-measurement scheme of Grice⁵³, and Ewert showed this same success probability was possible using four separable ancilla photons⁵⁴.

This cluster state is now suitable for quantum computation, provided suitable quantum information paths across it can be formed. This path-finding task is made easier by the theory of percolation, which tells us the maximum acceptable chance that a site or bond might be missing, above which a path across a given lattice can be formed (for an infinite lattice of a given shape). This maximum chance is known as the percolation threshold, which is generally different for sites and bonds. One-dimensional lattices aren't of great interest⁴⁴ (they're classically simulable), and two-dimensional lattices necessarily have worse percolation thresholds than three-dimensional ones. For this reason, we identified the three-dimensional diamond lattice as a good candidate, as it has high site- and bond-percolation thresholds*, with a coordination of just 4—meaning a small GHZ state can be used (5-qubits).

*Site and bond thresholds are 0.39 and 0.43, respectively. See ref. 55 for a list of thresholds for various lattices.

These can either be created ballistically, or constructed using smaller (e.g. 3-qubit) GHZ states. The full scheme, for constructing a cluster from resource states, and performing percolation and computation on that cluster is shown in **FIG. 1.8**.

1.2.1 Requirements

From this discussion, it may be evident that we need just a few modular components, repeated many times, to build a quantum computer from linear optics and photons. Some of these needs are addressed in this thesis. Altogether then, they are:

- ❶ Photon-pair sources, producing indistinguishable photons
- ❷ Large interferometers, reconfigurable and functioning with high fidelity
- ❸ High-efficiency single-photon detectors
- ❹ Fast and low-loss optical switches
- ❺ Control and feed-forward electronics

These components, taken together, would allow a photonic quantum computer to wield entanglement—the delicate link between photons—on an unprecedented scale. Above all else, I hope you have seen that the real dynamo at the heart of a quantum computer, and indeed at the heart of any quantum machine, is that entanglement. The remainder of this thesis focusses on assembling the tools and techniques to harness photonic entanglement on the large scale.

§1.3 INTEGRATED OPTICS IN SILICON

To integrate a technology is to take all the disparate parts of that technology and put them together on a common platform. Electronic circuits were busy becoming integrated from 1958, so one might think it just a matter of time before optics did the same. However, for electronics, the benefits and applications of integrated circuits were undeniable—speed, complexity, and reliability followed integration—and were applicable to a range of already identified devices. This pre-existing application and utility was just not there for optics, certainly not initially.

In 1960, Maiman observed the first laser oscillations in ruby, and kicked off a renaissance in optical research based on this new source of bright, single-moded, coherent light. It wasn't until the invention of the gallium arsenide laser diode in 1962⁵⁶, however, that the idea of communicating with light came to the fore. In 1966 the first intensity-modulated fibre-optic communication system was set up⁵⁷, though it wasn't until the fibre amplifier was developed in 1986⁵⁸ that optical fibre communications gained the range necessary to be useful. With an application in hand, and a precedent set in the semiconductor-based optics of the laser diode, the integration of optics found its legs. Miller's futuristic proposal published in 1969^{59–62} launched the new discipline of integrated optics.

The first semiconductor-based waveguides provided optical confinement in only one dimension (slab waveguides), but the development of two-dimensionally confined waveguides—those which can route light in all three dimensions—progressed rapidly. Development started with traditional optical materials, such as

glasses and acousto- and electro-optic crystals, then moved to direct-bandgap (III-V) semiconductors, and finally into silicon. These developments all were tightly focussed on the infrared telecommunications bands around $1.3\text{ }\mu\text{m}$ and $1.55\text{ }\mu\text{m}$ in wavelength, about which silica fibre has dispersion and loss minima, respectively.

Lithium niobate, due to its strong electro-optic effect, was the first integrated host of a two-dimensional waveguide, in 1973. In 1981 the first silica strip waveguide was manufactured, with a size and guided mode very similar to that of optical fibre, easing fibre-chip coupling. Indium phosphide, a III-V semiconductor sharing a crystal structure with gallium arsenide, was used to make lasers⁶³ and other optics⁶⁴ in the early 1980s, with immediate applications to telecommunications base stations and repeaters. Of the main integrated optical technologies, silicon bloomed relatively late, with the first “rib waveguide” in silicon demonstrated in 1985 by Soref and Lorenzo⁶⁵. These waveguides are in the so-called weak confinement (or low index contrast) regime, with dimensions $\gg \lambda/n$, with all wavevectors pointing roughly in the direction of travel, with concomitant large bend radii, and with similar propagation speeds for both polarisations (i.e. low birefringence). I’ll call this original rib-waveguide-based silicon photonics *large core* silicon photonics*.

Large core silicon photonics was commercially pioneered by Bookham Technology (now Oclaro) starting in 1988, targeting the telecommunications market. Telecommunications, however, with its low volumes and high performance requirements, largely opted for more functional (if expensive) photonic devices⁶⁷. As of 2001, the integrated optics market was dominated by high-speed lithium niobate modulators (30%) and III-V electro-optics and sources (42%), with silica the preferred platform for low-loss passives (11%), and silicon hanging on, with 3% of sales⁶⁸. Ironically, the silicon pioneer Oclaro is now a market leader—but no longer makes silicon photonics—with primary interests in indium phosphide and lithium niobate devices.

Like silicon electronics before it, silicon photonics has been revolutionised by improvements in fabrication technology. In the early 1990s, it was well-known that a single-mode, high index contrast silicon waveguide clad in silica required dimensions of about $200 \times 500\text{ nm}^2$, with at least 700 nm of lower cladding⁶⁹. However, it was also clear at the time that the available substrates (SIMOX, BESOI) could not simultaneously provide the cladding thickness (SIMOX was restricted to $0.5\text{ }\mu\text{m}$ lower oxide) and silicon uniformity (BESOI was unsuitable for the precise and small $h = 0.2\text{ }\mu\text{m}$ layer) which were needed⁷⁰. Furthermore, state-of-the-art lithography simply couldn’t produce the required 500-nm features (see FIG. 1.1).

In 1995, however, the puzzle pieces fell into place, and small-core silicon photonics became possible: LETI developed a new wafer-processing technique called Smart Cut, which allowed the production of silicon-on-insulator wafers with an unlimited buried oxide thickness, beneath a precise, crystalline silicon slab⁷¹; and that same year the microelectronics industry serendipitously moved from 600 to 350 nm feature sizes (FIG. 1.1). These two developments set the stage for modern small-core silicon photonics, with diffraction limited, high-confinement waveguides, and high integration density, and for new applications which could leverage these properties. The first small-core silicon waveguide was fabricated at MIT, in

*Despite their size, large rib waveguides can be designed to be monomode, with higher order modes leaking out through the slab—see ref. 66.

1997 by Foresi, Agarwal, Kimerling et al.⁷².

For some time, electronic engineers have been worrying about the fundamental limits in scaling their systems by simply shrinking the transistor, in their never-ending pursuit of Moore's law. Communications bandwidth between electronic components has been identified as a bottleneck in increasingly distributed micro-electronic systems, and the engineers started thinking about how to replace the $1/RC$ bandwidth of electrical currents and voltages with the theoretical 200 THz bandwidth of light⁷³. The new silicon photonics was a natural fit, both in size, in material, and in cost; this so-called optical interconnect problem has strongly motivated silicon photonics development ever since.

1.3.1 Waveguides

At this point, we have referred to waveguides and waveguiding many times; in this section I will make these ideas precise. Perhaps not surprisingly, a waveguide is a structure which guides waves. Though many types of waves and waveguides exist throughout physics, we will focus here on the art and science of guiding infrared *light waves* through silicon structures.

Put simply, a waveguide is a structure in which a light beam can propagate without a change in its shape—without diffraction. Light in a given waveguide can propagate in one or more modes, travelling at different characteristic speeds, and without loss of intensity due to spreading. These characteristic speeds are defined by effective indices of refraction n_{eff} , which reduce the phase speed of light from that in vacuum to c/n_{eff} . In dielectric total-internal-reflection waveguides, light is guided by a high-refractive-index core surrounded by a lower-refractive-index cladding. In silicon photonics, the core is always silicon, but the cladding can be silica, air, polymer, or more exotic materials. For a waveguide with core index n_{core} and cladding index n_{clad} , the effective index of a guided mode always lies between them: $n_{\text{clad}} < n_{\text{eff}} < n_{\text{core}}$. A wave with effective index n_{eff} propagates with a wavenumber $k_z = \beta$, where β is called the propagation constant and is related to the frequency of oscillation by $\beta = \omega c / n_{\text{eff}}$.

Several common waveguide shapes are shown in [FIG. 1.10](#). The simplest, the slab waveguide, confines light in only one dimension, such that guided light can freely propagate in a plane. More complicated—and more useful—structures, such as the rib and strip waveguides, confine light in two dimensions, so it can be guided along an arbitrary path.

Light in linear media obeys the two electromagnetic wave equations, which stem directly from Maxwell's equations ([SC.1.1](#)); for $\mathbf{F} \in \{\mathbf{E}, \mathbf{B}\}$ they read:

$$\nabla^2 \mathbf{F} = \mu_0 \epsilon \ddot{\mathbf{F}}. \quad (1.23)$$

These equations describe \mathbf{E} and \mathbf{B} plane waves propagating at the speed of light in the medium, $v = 1/\sqrt{\mu_0 \epsilon} = c/n$, but will also describe the propagation of our not-plane-waves, though with a modified phase speed, $c/n_{\text{eff}} = \omega/\beta$. We seek waveguided solutions which propagate in z , but don't change their shape in x and y , i.e. $\mathbf{F} = \mathcal{F}(x, y) e^{i\beta z - i\omega t}$. Inserting this back into [EQ. 1.23](#), we obtain an eigenvalue problem based on the vector Helmholtz equation, with eigenvalue β (from [EQ. C.15](#)):

$$\nabla^2 \mathcal{F} = (\beta^2 - k^2) \mathcal{F}. \quad (1.24)$$

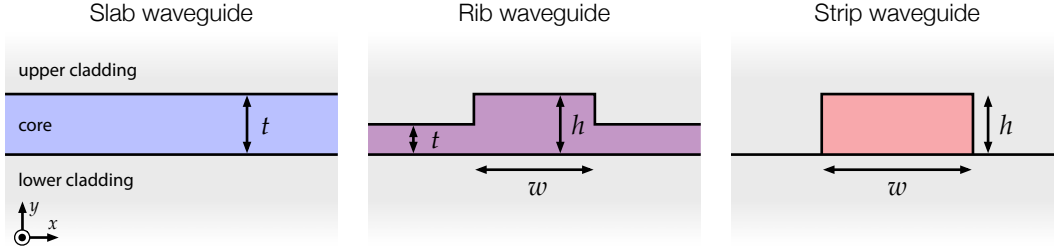


FIG. 1.10: Types of waveguides. Light propagates in the (shaded) core layer, whose refractive index is greater than that in the upper and lower cladding layers. A slab waveguide confines light in one dimension, in a film of thickness t , while rib and strip waveguides confine light to a $w \times h$ core. Rib waveguides have a partially etched core layer (remaining thickness t) which decreases index contrast, while strip waveguides are fully etched to maximise confinement and yield a symmetrical guided mode. The x - y plane is shown, such that guided modes propagate outwards, in the $+z$ direction.

This is known as the transverse vector Helmholtz equation, and it implicitly describes waveguide modes of any polarisation. Solutions of [EQ. 1.24](#) are discussed in the following sections, for two important classes of waveguides, the slab and the strip, both depicted in [FIG. 1.10](#).

The slab waveguide

In this section, I will briefly describe the origin of waveguiding in the simplest possible structure—the slab waveguide. Detailed calculations are listed in [§C.2.2](#).

We can postulate a field vector which depends not on both x and y , as the general case of [EQ. 1.24](#), but just on y , due to the infinite extent in x (see [FIG. 1.10](#)). Our new slab-mode transverse field profile then looks like

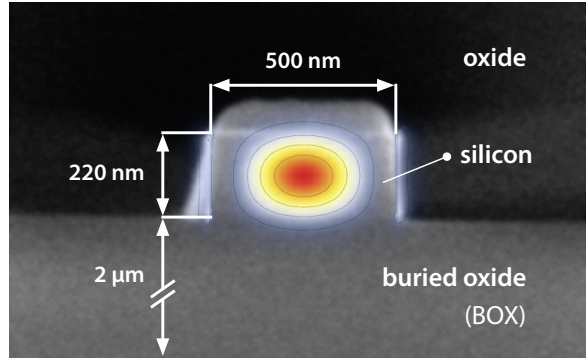
$$\mathcal{F}(x, y) = \mathcal{F}_x(y) \mathbf{x}, \quad (1.25)$$

where we have chosen to polarise the field in the x direction. If $\mathbf{F} = \mathbf{E}$, we call this mode TE and if $\mathbf{F} = \mathbf{B}$, we call it TM, standing for transverse electric and magnetic, respectively, since \mathbf{F} lies solely in the transverse plane of propagation.

To find the modes of propagation (and their propagation constants), we work out the boundary conditions at the two interfaces— E_x , E'_x , and B_x are continuous, while B'_x is not—substitute our trial solution [EQ. 1.25](#) into the Helmholtz equation [EQ. 1.24](#), and solve for β . This calculation is carried out in [§C.2.2](#). We find a transcendental eigenvalue equation for β , for both TE and TM modes ([Eqs. C.25](#) and [C.28](#)). These equations show us two things: the TE mode is much more confined to the waveguide core than the TM one; and if the upper and lower cladding are different, there exists a regime in which not even the fundamental mode propagates*. We will revisit this first point in our discussion of the strip waveguide ([§1.3.1](#)). Regarding the second, I'll just note that due to the massive index contrast in silicon waveguides, this situation is rarely encountered. Field profiles for the fundamental (and only) TE and TM modes in a silicon slab with silica upper and lower cladding are shown in [FIG. C.1](#).

*See §2.4.3 of [74](#).

FIG. 1.11: Electron micrograph showing the typical geometry of a silicon strip waveguide. The highly confined fundamental TE₀₀ mode, polarised horizontally, is superimposed. Microscopy courtesy Michael Strain.



The strip waveguide

In this thesis, waveguides of the geometry labelled *strip* in FIG. 1.10 are primarily used. There is, however, some debate about the name of this type of waveguide: they are variously referred to as ‘photonic wire’, ‘nano wire’, ‘rib’, ‘ridge’, ‘strip’, ‘stripe’, ‘strip-loaded’, ‘buried-channel’, and ‘channel’ waveguides by different authors. Many of these names arise from fabrication methodology, some are simply descriptive, and others are disambiguating. I will continue to refer to this important structure as a *strip waveguide*.

An electron micrograph of the cross-section of a typical silicon small-core strip waveguide is shown in FIG. 1.11, superimposed with its geometry and the profile of its fundamental TE mode. The mode of a strip waveguide is determined via a similar means to that of the slab waveguide, with the important distinction that it *cannot* be obtained analytically. Two-dimensional modes such as that shown in FIG. 1.11 are found numerically, using software aptly termed a ‘mode solver’. The mode solver proceeds towards a solution analogously to how we found the modes of the slab waveguide: it numerically discretises EQ. 1.24, then solves the *matrix* eigenvalue problem for the propagation constant β (and so too the effective index $n_{\text{eff}} = \beta/k_0$) and the corresponding transverse mode profile $\mathcal{F}(x, y)$.

Modes of high-confinement strip waveguides, like their slab counterparts, come in two polarisation flavours, which we refer to as TE and TM. However, unlike TE and TM modes in slab waveguides, they are not exactly orthogonal, which is another way of saying that they are not truly transverse electric or magnetic—each mode has a small component of the other polarisation. Properly, they should be called *quasi-TE* and -TM modes, but for simplicity, I’ll continue to use the established language.

Modal properties

The amount of light propagating in the core of the waveguide has important implications for its interaction with the medium. We can quantify this using the effective mode area, A , which is often expressed as

$$\frac{\left(\iint S_z dx dy\right)^2}{\iint S_z^2 dx dy},$$

by integrating the propagating power—given by the time-averaged z -component of the Poynting vector S_z —over all cross-sectional space. This expression is useful in several situations, though not ours. Example situations are: when computing

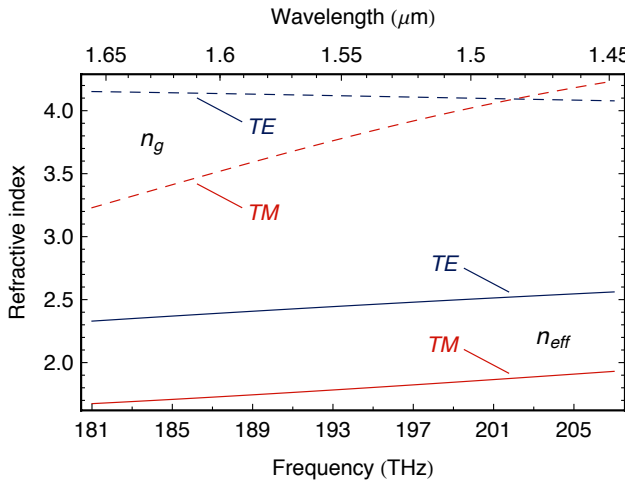


FIG. 1.12: Dispersion curves for strip waveguide geometry shown in FIG. 1.11. Effective index dispersion for the two polarisations is shown in solid lines, group index dispersion is shown in dashed lines.

mode volumes to understand cavity enhancement of emission rates, or when the index contrast is very small, such that the mode is entirely confined to the core, as is often the case in fibre optics. However, in this section about optics in *silicon*, we have quite different needs. We often seek to use the silicon core for nonlinear optical applications (discussed in detail, later) and we have very high index contrast, leading to large parts of the mode propagating in the cladding. These points motivate a new definition of the effective area, which accounts for the overlap with the medium we actually care about. We redefine it as⁷⁵

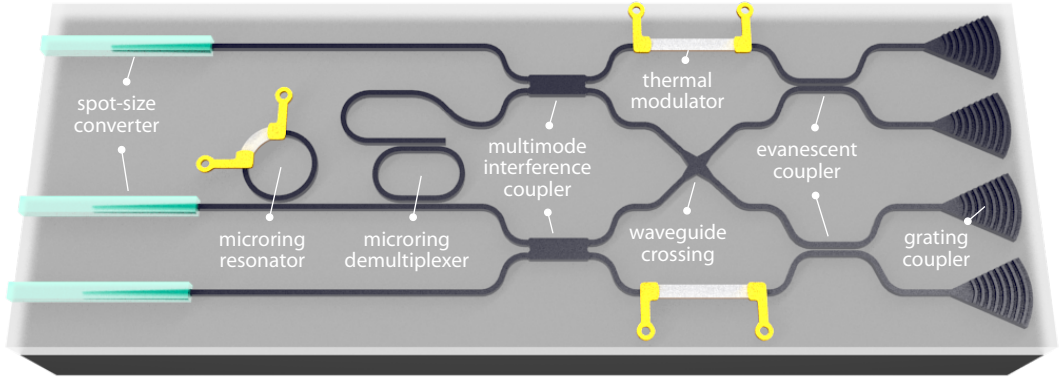
$$A \equiv \frac{\iint_{\infty} S_z dx dy \times \iint_{NL} dx dy}{\iint_{NL} S_z dx dy}. \quad (1.26)$$

The modified effective mode area A can be understood as being the area of the nonlinear medium ($\iint_{NL} dx dy$) scaled by the ratio of the total mode power ($\iint_{\infty} S_z dx dy$) to the modal power propagating in the medium ($\iint_{NL} S_z dx dy$). It can be used interchangeably with the conventional mode area, for structures where only a portion of guided modes propagate in the nonlinear medium (as in all structures discussed in this thesis). In a silicon waveguide at 1.55 μm, the fundamental TE mode has an area more than thrice the size of the TM mode (values are compiled in TABLE 1.3). Note that variations on the definition of A in EQ. 1.26 exist⁷⁶.

These highly confined modes lead to a significant overlap with the core-cladding interface. In silicon strip waveguides, scattering from this interface—especially the etched side-walls—is the primary source of propagation loss⁷⁷. For this reason, too, the TM mode tends to be less lossy than the TE, at least in straight sections⁷⁸ as it overlaps much less with the side-wall. The TE mode of a typical silicon strip waveguide today suffers around 2 dB/cm propagation loss. Several techniques have been developed to reduce this, via side-wall and cross-section engineering^{31,79–81}. The state-of-the-art for a strip waveguide (500 × 220 nm²) is now just 0.45 ± 0.12 dB/cm⁸².

Another important parameter of modal propagation is the group index. The wavefronts of a propagating mode travel at a speed c/n_{eff} . In the absence of dispersion, wavepackets, composed of many frequencies, also travel that speed. In real materials, however, the dispersion of the material index is non-zero. Indeed, for any waveguide, the effective index can have very strong modal dispersion. If the dispersion varies strictly linearly, a wavepacket will retain its shape, and travel

FIG. 1.13: Hypothetical device, showcasing the integrated optical elements used in this thesis. Not to scale.



at the so-called ‘group velocity’, $c/n_g \equiv d\omega/dk$, such that the group index is

$$n_g \equiv \frac{d(n_{\text{eff}}\nu)}{d\nu} = n_{\text{eff}} + \nu \frac{dn_{\text{eff}}}{d\nu} = n_{\text{eff}} - \lambda \frac{dn_{\text{eff}}}{d\lambda}. \quad (1.27)$$

The group index can also be obtained directly from the modal field profiles*.

Dispersion parameters describe variations in propagation speed, via Taylor expansion. The first order dispersion parameter is just $\beta_1 = c/n_g$. In general, the i^{th} order dispersion parameter is $\beta_i \equiv d^i k / d\omega^i$. Group-velocity dispersion (GVD) β_2 plays a central role in nonlinear phase matching ([§2.2](#)), and depends on the slope of n_g as $\beta_2 = 1/2\pi c \times dn_g/d\nu$ [†]. In general, the wavenumber k near ω_0 is described by

$$k(\omega) = n(\omega) \frac{\omega}{c} = \sum_{i=0}^{\infty} \frac{\beta_i}{i!} (\omega - \omega_0)^i. \quad (1.28)$$

The variation of n_{eff} and n_g for a silicon strip waveguide like that shown in [FIG. 1.11](#) is plotted against frequency and wavelength in [FIG. 1.12](#), and listed in [TABLE 1.3](#).

1.3.2 Integrated optics toolbox

Next, I’ll detail the integrated optical tools used in this thesis, and outline emerging trends in classical silicon photonics technology. I’ll start by describing the two optical structures required for linear optical quantum computation ([§1.2](#)), the on-chip beamsplitter and phase shifter, then move to on-chip optical resonators, and finally describe the spot-size converter (SSC) and grating coupler structures used to transfer light from optical fibres to microscopic silicon strip waveguides. All these elements are shown schematically in [FIG. 1.13](#).

Waveguide couplers

In this thesis, two types of on-chip beamsplitters—or waveguide couplers—are used: the evanescent coupler, and the multimode interference coupler (MMI).

The evanescent coupler couples light between two waveguides by overlapping the evanescent fields of their respective modes. There are two ways to consider

*Though this method neglects material dispersion. See §31-6 of ref. 83.

[†]It relates to the usual dispersion parameter by $D = -\frac{v^2}{c^2} \frac{dn_g}{d\nu} = -\frac{2\pi\nu^2}{c} \beta_2 = -\frac{2\pi c}{\lambda^2} \beta_2$.

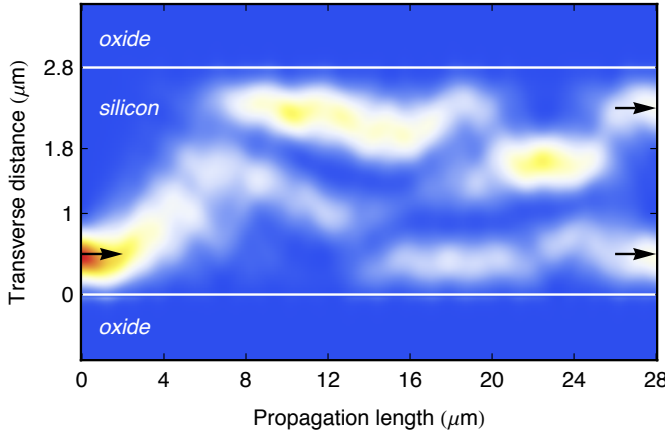


FIG. 1.14: Plan view propagation inside multi-mode region of the MMI coupler used in this thesis. The waveguide supports 9 TE modes. Simulated with a mode solver, for the MMI of ref. 85.

such a structure: to think of the field in one waveguide as changing the material polarisation of the other^{*}; or to think of the interference between the two super-modes of the combined structure. The first is the approach I take in §C.3. The second approach is a common method for modelling MMI couplers.

As the length of the evanescent coupler increases, the field in each waveguide undergoes periodic extinctions and revivals. If all light is injected in one waveguide, the length required for the first extinction in that waveguide is called the critical length, z_{crit} . Defined in terms of the cross-susceptibility χ_{ab} and alternately in terms of the effective indices of the even n_e and odd n_o super-modes, the critical length is

$$z_{\text{crit}} = \frac{n\lambda}{2\chi_{ab}} = \frac{\lambda}{2|n_o - n_e|}. \quad (1.29)$$

In terms of the critical length, the scattering matrix (Eq. 1.8) of an evanescent coupler can be written for arbitrary length z as

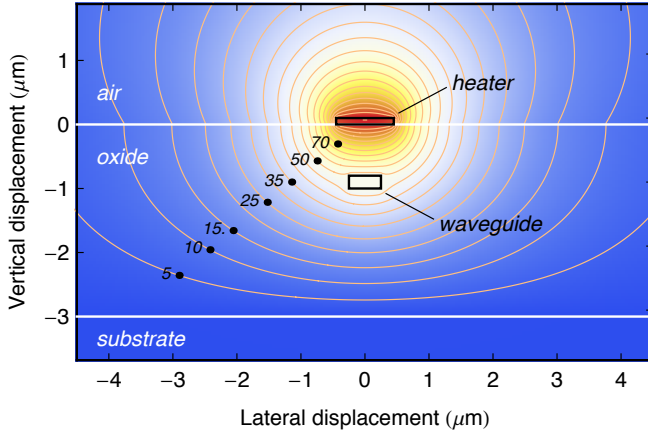
$$\hat{U}_{\text{EC}} = \begin{pmatrix} \cos(\pi z/z_{\text{crit}}) & i \sin(\pi z/z_{\text{crit}}) \\ i \sin(\pi z/z_{\text{crit}}) & \cos(\pi z/z_{\text{crit}}) \end{pmatrix} \quad (1.30)$$

which—as promised—is just a beamsplitter with reflectivity $\eta = \cos^2(\pi z/z_{\text{crit}})$ (cf. Eq. 1.10). Since the evanescent coupler acts on just two modes, there is little chance that light will leak out into non-guided or radiation modes—the evanescent coupler is intrinsically lossless. However, notice that we often want $\eta = 50\%$, and that this is the most sensitive length for an evanescent coupler. This makes evanescent couplers difficult to get right, since the length and critical length must be controlled precisely. This point motivates the *multimode* interference coupler.

At the core of an MMI lies a block which supports multiple guided modes. Monomode waveguides inject and collect light from this block, and excite many of its modes simultaneously. Each excited mode propagates with its own constant β_i , and various interferences occur between these modes as they co-propagate. If the $\{\beta_i\}$ are chosen appropriately (via the block’s width) repeated images of the input plane are formed at periodic lengths⁸⁶. In a 2×2 MMI, collection waveguides are positioned at one of these special lengths, when two images are formed, such

*Based on coupled-mode theory⁸⁴.

FIG. 1.15: Cross-section of a typical thermal phase modulator, as used in this thesis. Temperature contours are indicated in orange, and labelled with the percentage of maximum temperature: 100 indicates heater temperature, 0 indicates ambient temperature. Simulation parameters from [TABLE 1.1](#).



that the multimode field can be coupled back into monomode waveguides, and a beamsplitter operation is realised.

In this thesis, one MMI design was used⁸⁵. The light distribution inside it is shown in [FIG. 1.14](#). The input and output waveguides are tapered to a $1.0\text{ }\mu\text{m}$ width, to expand the input fundamental mode, and this mode couples into the nine propagating modes of the slab. Propagation is terminated after $28\text{ }\mu\text{m}$, at which point two single-mode copies of the input field, with half the original intensity, are imaged onto two output waveguides. In this way, the MMI coupler, like the evanescent coupler, can robustly implement a $\eta = 50\%$ beamsplitter. The trade-off in using an MMI over an evanescent coupler is loss—though low-loss MMIs have been shown^{87,88}, they are universally more lossy than evanescent couplers.

Phase modulators

The experiments in this thesis were performed at room temperature, and at very low bandwidth (to allow photon-pair integration). In this regime, we can exploit the robust and low-loss modulation offered by the thermo-optic effect, which is strong in silicon at room temperature. To modulate the phase in a waveguide, we patterned a resistive film atop it, and controlled the current flowing through that film to modulate the temperature and refractive index. This structure is variously called a ‘thermo-optic phase modulator’ (TOPM), a ‘thermal tuner’, a ‘thermal modulator’, or simply a ‘heater’. I’ll use these terms interchangeably.

Steady-state modeling of these structures is eased by the fact that the thermal field is governed by Laplace’s equation ($\nabla^2 T = 0$), i.e. the temperature has no second derivative—it’s linear⁸⁹. A simple Jacobi-method solver* can compute cross-sectional thermal fields, such as that shown in [FIG. 1.15](#). In the modulator shown there, the waveguide is roughly 50% of the heater temperature. The temperature-dependent phase due to the thermo-optic effect ([§1.3.3](#)) is

$$\Delta\phi = 2\pi \frac{\Delta n L}{\lambda} \quad \text{with} \quad \Delta n = \frac{dn_{\text{eff}}}{dT} \Delta T. \quad (1.31)$$

For a phase shift $\Delta\phi = 2\pi$, assuming the mode is entirely confined to the silicon core, and with a heater length of $50\text{ }\mu\text{m}$, a temperature change $\Delta T = 167\text{ K}$ is re-

*See §3-7 of ref. 89 for numerical method details, and 90 for material parameters.

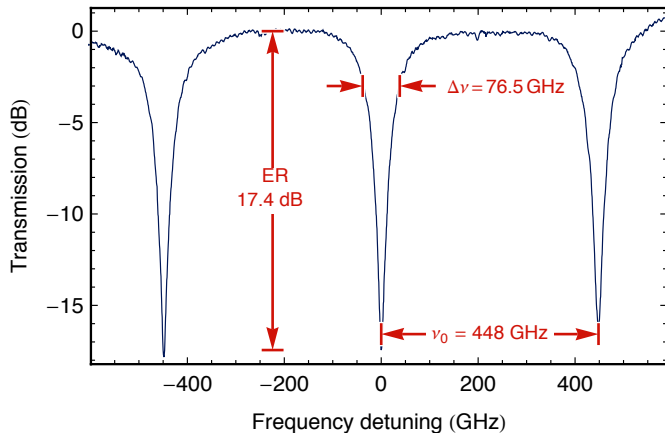


FIG. 1.16: Measured transmission spectrum of a typical add-drop ring resonator. It shows the three direct resonance parameters which can be used to obtain all others. The SFWM fluorescence of this ring versus power is shown in FIG. 2.3.

quired. This implies a required heater temperature of about 370°C. To reach this, simulation indicates we must provide 31 mW to the heater shown in FIG. 1.15, and this agrees with experience.

Waveguide crossings

Occasionally it's not possible to design an interferometer with all waveguides lying in a plane—some must cross. This is achieved by an aptly named waveguide crossing. In this work, a crossing is realised by linearly tapering the crossing waveguides to 1.5 μm (over 20 μm), then crossing them at right angles, and tapering back. The larger tapered mode reduces diffraction at the junction, and the taper length ensures low mode-conversion loss⁸⁸.

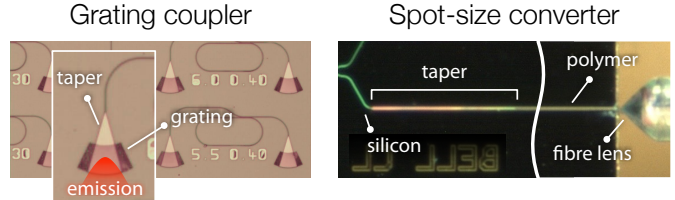
Resonators

Optical microcavities—structures in which interference causes light to build up—are used in a variety of tasks, from enhancing light-matter interactions (e.g. refs. 91, 92), to sensing environmental changes (e.g. refs. 93, 94), and implementing infinite impulse response transfer functions (e.g. 95). This work uses them for the first and last of these tasks.

Several types of resonator have been shown in silicon photonics: Fabry-Pérot⁹⁶, phase-shifted gratings^{97, 98}, photonic crystal line-defects⁹², microdisks^{99, 100}, and microrings^{100, 101}. The last of these—microrings—have several convenient properties, which motivate their use. Microrings are straightforward to manufacture, requiring no small features; they are travelling-wave resonant, meaning all fields co-propagate; and they exhibit a simple mode structure.

A ring resonator is formed of a waveguide which has been looped back on itself (see FIG. 1.13 for a schematic). Light enters and exits the loop via a bus waveguide, which is evanescently coupled to it. Light builds up inside the loop when the round-trip phase is zero. The field inside and outside a ring resonator can be understood as the solution to the set of equations which link the field in the bus waveguide to the field in the loop, and which keep track of the phase in the loop. This calculation is carried out in SC.4, where you will also find relations for various figures of merit: field enhancement (Eqs. C.42), free spectral range (FSR, ν_0 , Eq. C.47), linewidth ($\Delta\nu$, $\Delta\lambda$, Eqs. C.50), extinction ratio (Eq. C.53), and quality factor

FIG. 1.17: The two dominant methods for coupling silicon strip waveguides to optical fibre. The grating coupler emits vertically, while the spot-size converter emits from the chip edge.



(Q , [EQ. C.51](#)). Typical silicon microrings exhibit FSR from 100 GHz to 1600 GHz, and Q from 10^2 to 10^5 . The transmission spectrum of an add-drop ring resonator is shown in [FIG. 1.16](#).

A ring resonator is critically coupled when the reflectivity from the coupler equals the round-trip loss inside the loop ($r = \eta$). On resonance, a critically coupled resonator will absorb *all* incident light—all energy is transferred from the bus to the loop due to perfectly balanced interference at the coupler. When the ring is over-coupled ($r < \eta$), or under-coupled ($r > \eta$) the perfect balance between light escaping the ring and light reflecting from the coupler is lost, and some light will be transmitted on resonance.

Fibre-to-chip couplers

Silicon waveguides are square and nanoscopic ([FIG. 1.11](#)). They have $n_{\text{eff}} \approx 2.7$ and $n_g \approx 4.1$ ([FIG. 1.12](#)). On the other hand, optical fibre has a circular core 8- μm -across which weakly guides a mode with $n_{\text{eff}} \approx n_g \approx 1.5$. Light is readily coupled into optical fibre from lasers and other optics, but to get this light into a chip, significant mode conversion must occur. Two structures have been developed for this task: the spot-size converter^{[102](#)}, and the grating coupler^{[103](#)} ([FIGS. 1.13, 1.17](#)).

The spot-size converter starts by tapering a silicon waveguide down to a point, until its mode is squeezed out into the cladding, then it catches this larger mode in a lower-index-contrast polymer waveguide. The mode of this polymer waveguide (ca. 2.5 μm) can then be focussed into fibre (ca. 10 μm) using a fibre lens ([FIG. 1.17](#)).

The grating coupler, on the other hand, uses constructive interference between distributed scatterers to direct light *out-of-plane*, and straight into a fibre mode. Periodically placed teeth scatter light upwards from an enlarged waveguide, and the period determines the frequency and direction of the constructive interference and emission ([FIG. 1.17](#)).

The spot-size converter supports broadband coupling of both polarisations, but is less convenient from an integration point of view (since a chip facet is required) and is very sensitive to misalignment. The grating coupler, on the other hand, has a typical bandwidth on the order of 50 nm, supports only one polarisation, is easily integrated anywhere on the die (or wafer!), and tolerates misalignment. In general, both structures are defined in two patterning steps, though single-step versions of both exist^{[104,105](#)}. In principle, spot-size converter losses should be lower, but in practice they are about the same—between 3 and 5 dB.

1.3.3 Silicon: the optical material

Silicon, until the 1950s, was regarded as semi-metallic, and unsuitable for electronic—let alone photonic—use. Even now, a piece of silicon is pitch black to the eye, and wouldn't normally be considered as a material suitable for optics. Silicon does,

however, have a lot on its side. Many of the qualities which allowed silicon to prevail as the dominant material of electronics are the same qualities which afford it a second glance optically. Silicon is abundant, has excellent thermal conductivity, is mechanically robust, can be made unimaginably pure, can be doped, and—most importantly—has an inert oxide with which it forms high-quality interfaces. Optically, silicon has a few more tricks. It: has a strong thermo-optic effect, has a strong optical Kerr nonlinearity, is absolutely transparent from the near- to mid-IR, and its oxide forms a very convenient low-refractive-index cladding. Silicon photonics can leverage the massive manufacturing infrastructure of silicon microelectronics, and the material knowledge stemming from this industry—the most comprehensive of any material in existence—to make photonics on the large scale.

Many material properties of silicon and silica are listed in [TABLES 1.1](#) and [1.2](#), including optical, thermal, and electronic data from various sources. In the following (and prior) discussions, when I refer to ‘silicon’, I always mean ‘monocrystalline silicon’, unless otherwise stated.

Bandgap

Silicon is an indirect bandgap semiconductor, with a gap energy of about 1.11 eV (ca. 1.1 μm) at room temperature, growing to 1.17 eV at 0 K. Since *silica* is lowest loss around 1.55 μm , this part of the near-infrared dominates in telecommunications systems. Silicon’s bandgap and purity mean it’s completely transparent from 1.3 μm to well into the mid-infrared^{[106](#)}, conveniently including this 1.55 μm window.

The indirect bandgap makes light emission from bulk silicon nearly impossible with any significant efficiency. Optically pumped lasers based on stimulated Raman scattering have been shown^{[107](#)}, as well as those based on CMOS-compatible germanium^{[108](#)}, but the holy grail—an electrically pumped silicon laser—remains elusive. Much progress towards electrical pumping has been made using silicon quantum dots^{[109,110](#)}, but consensus is moving towards the use of hetero-structures with more conventional electro-luminescent materials^{[108](#)}.

Thermo-optic effect

We discussed thermo-optic modulators in [§1.3.2](#), so it won’t be surprising that silicon has a large thermo-optic coefficient at room temperature ([TABLE 1.1](#)). This can be both useful, and problematic. Phase modulation using this effect has been demonstrated with frequencies into the gigahertz^{[111](#)}, using both asymmetric Mach-Zehnder interferometers, and ring resonators. Thermo-optic modulation is also very low loss. On the other hand, the effect results in strongly temperature-dependent devices. This can be compensated with special claddings^{[112](#)}, though these require exotic materials and serialised manufacturing. The heat generated by absorption and the relaxation of carriers changes the waveguide temperature, and can cause unexpected behaviour as the optical power is increased. Finally, it should be noted that since the thermo-optic effect is caused by electronic anharmonicity, it vanishes at low temperature.

Free-carrier effects

With silicon's involvement in electronic devices, the effect of free-carriers on the optical field have been explored and strongly exploited as a modulation mechanism¹¹³. The refractive index change arising from the presence of free carriers is called free-carrier dispersion (FCD). The associated free-carrier absorption (FCA) can be problematic, however, as an additional source of linear loss.

Based on the billiard-ball Drude model for carrier behaviour, simple expressions can be developed for the change in refractive index and the absorption due to free-carriers^{114,115}

$$\Delta n_{\text{FCD}} = \frac{-e^2}{2\epsilon_0 nm^*} \frac{N_c}{\omega^2} \quad \text{and} \quad \Delta \alpha_{\text{FCA}} = \frac{e^3}{\epsilon_0 c n m^{*2}} \frac{N_c}{\omega^2}, \quad (1.32)$$

where the elementary charge, the free-carrier effective mass, and concentration are given by e , m^* , and N_c , respectively. FCD and FCA evidently increase linearly with the number of carriers, and decrease quadratically with optical frequency. These effects are particularly important at high optical powers in silicon, as free-carriers are generated by nonlinear material absorption, discussed next.

Two-photon absorption

The imaginary part of silicon's nonlinearity (discussed in the next section) gives rise to two-photon absorption, whereby a valence-band electron can be excited by *two* incident photons (TPA, see FIG. 1.18). It acts through the TPA coefficient, α_2 , which represents an intensity-dependent propagation loss. The effect of α_2 can be described by the phenomenological differential equation^{116,117} governing the decay of intensity I as light propagates through TPA media:

$$\frac{\partial I}{\partial z} = -\alpha I - \alpha_2 I^2. \quad (1.33)$$

EQ. 1.33 produces an exponentially decaying field, whose base decay rate α is enhanced by the propagating intensity, via α_2 . Thus, more nonlinear loss happens at the beginning of a waveguide than at its end. It should also be noted that when a bright field co-propagates with a single photon, TPA contributes to that photon's loss via cross-TPA (XTPA), the scaling of which is detailed in §2.4.

In the presence of a high-intensity pump, two-photon absorption provides a significant source of free carriers, which go on to cause both FCD and FCA (EQ. 1.32). These carriers thermalise and heat the waveguide, causing a further thermo-optic modulation. In a resonator, the optical path length and resonant frequency depend on the refractive index (§1.3.2). Since free carriers decrease the index (blue-shift), and temperature increases the index (red-shift), a well-documented bistability is exhibited by silicon resonators^{118–120}. This can introduce ringing in the temporal response¹²¹. The concentration of free carriers N_c excited by TPA from a mode carrying power P is^{122,123}

$$N_c(P) \approx \frac{\alpha_2 \tau P^2}{2h\nu A^2}, \quad \begin{cases} \tau = \tau_c & \text{if CW} \\ \tau = \Delta t / a & \text{if pulsed} \end{cases} \quad (1.34)$$

where τ_c is the free-carrier lifetime, Δt is the pulse duration, A is the effective area

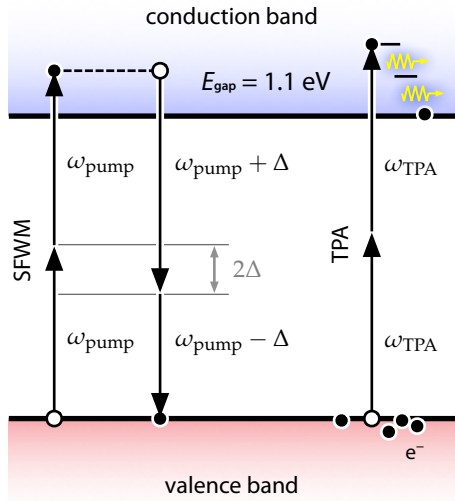


FIG. 1.18: Simplified picture of energy in silicon optics, including four-wave mixing (FWM), and two-photon absorption (TPA) effects.

(EQ. 1.26), and $a \approx 3$ for Gaussian pulses and $a = 1$ for square ones*. At room temperature, $\tau_c \approx 1.9 \text{ ns}$, but it falls rapidly with temperature¹²⁰. The total nonlinear loss resulting from TPA-coupled FCA is discussed further in §2.4 in the context of measuring correlated photons.

TPA is a major issue in silicon photonics (due to its limit on optical powers, and introduction of complicated dynamics) and in silicon quantum photonics (due to XTPA's reduction of heralding efficiency) and resolving this issue is a topic of ongoing research. Several avenues are being explored, from modifying silicon's bandgap^{124,125}, or moving to CMOS-compatible dielectrics¹²⁶, to shifting to lower optical frequencies altogether¹²⁷. Each of these approaches has drawbacks, so silicon photonics pushes on with the status quo, conscious of its limitations.

Raman scattering

When a photon scatters from an optical phonon, this is known as Raman scattering, which is inelastic. Owing to its crystallinity, silicon has a very narrow Raman resonance at $\pm 15.6 \text{ THz}$ (127 nm), the emission (and absorption) of which can be easily avoided and filtered out in practice. Spontaneous Raman scattering is a serious challenge for nonlinear systems based on amorphous materials, such as chalcogenide glasses¹²⁸, or optical fibres. As mentioned, *stimulated* Raman scattering can provide on-chip amplification¹²⁹, which has been used to show the first laser in silicon¹⁰⁷—albeit an optically pumped one. Stimulated Brillouin scattering is the acoustic-phonon cousin of stimulated Raman scattering. It has very recently been demonstrated in under-cut silicon waveguides¹³⁰.

Nonlinear optics in silicon

The polarisation \mathbf{P} of a material under the influence of an electric field \mathbf{E} describes how bound charge in that material is displaced by that field. If the field is not too great, \mathbf{P} can be described by a Taylor series in the material susceptibilities $\chi^{(n)}$,

*Pulsed approximation valid for short pulses ($\Delta t \ll \tau_c$) with low frequency ($\tau_c f \ll 1$).

$$\frac{\mathbf{P}}{\epsilon_0} = \chi^{(1)} \mathbf{E} + \chi^{(2)} \mathbf{E} \mathbf{E} + \chi^{(3)} \mathbf{E} \mathbf{E} \mathbf{E} + \dots \quad (1.35)$$

Due to the centrosymmetry of silicon's diamond structure, silicon doesn't exhibit the lowest-order $\chi^{(2)}$ optical nonlinearity. Centrosymmetry requires that, if the field is reflected, then the polarisation must also be reflected—i.e. $\mathbf{P}(-\mathbf{E}) = -\mathbf{P}(\mathbf{E})$ —but this is only possible if $\chi^{(2)}$ vanishes*. Silicon does, however, have a relatively large[†] third-order $\chi^{(3)}$ nonlinearity. This is predicated by silicon's large refractive index, since^{131,132}

$$\chi^{(m)} \approx \left(\chi^{(1)} \right)^{m+1} = (n^2 - 1)^{m+1}. \quad (1.36)$$

The $\chi^{(3)}$ nonlinear susceptibility leads to the Kerr effect, which is useful for cross-phase modulation (XPM) and frequency conversion via four-wave mixing. The imaginary part of $\chi^{(3)}$ leads to TPA.

The Kerr effect is governed by the intensity-dependent refractive index or Kerr coefficient^{131,133} n_2 , defined as

$$n(I) = n(0) + I \cdot n_2 \quad \text{with} \quad n_2 = \frac{3\chi^{(3)}}{4n^2 \epsilon_0 c}. \quad (1.37)$$

The intensity I has units [W/m²] and for a plane wave¹³⁴ is $I \equiv \frac{1}{2}n\epsilon_0 c|E|^2$, where $|E|$ is the amplitude of the electric field. However, a plane-wave suffers no waveguide dispersion, so $n_g = n$. In practice, I is simply the propagating power divided by the effective modal area: $I = P/A$ (see [EQ. 1.26](#)). This waveguided picture *does* account for waveguide dispersion, pulse shortening, etc., so a definition specifying the slowdown factor $S \equiv n_g/n_{\text{eff}}$ is not necessary. Authors working with slow-light often separate out this effect^{135–138}. The relation between the intensity-dependent refractive index and $\chi^{(3)}$ is also given in [EQ. 1.37](#), but I will treat n_2 as fundamental, as it's measured directly.

In the absence of loss, the self-phase Φ accumulated due to n_2 just depends on the propagation length and the intensity, with $\Delta n = I \cdot n_2$ being the change in index:

$$\Phi = \Delta k \cdot L = \Delta n \cdot k_0 L = (n_2 I) k_0 L = 2\pi \cdot \frac{n_2}{A\lambda} \cdot PL = \gamma PL \quad (1.38)$$

We will make Φ more precise soon, but the simple expression [EQ. 1.38](#) contains important physics. Since XPM produces a phase of 2Φ , and FWM scales with Φ^2 , the factor

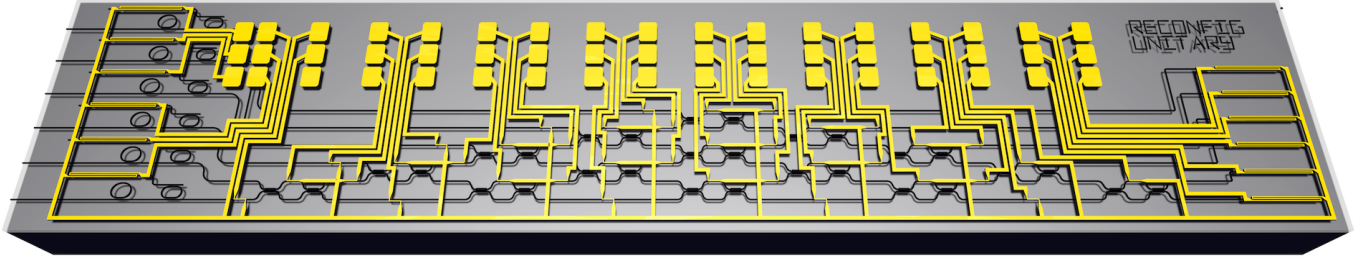
$\gamma \equiv \frac{k_0 n_2}{A},$

(1.39)

called the nonlinear parameter, is of particular importance: it determines the strength of the useful $\chi^{(3)}$ processes for guided light.

*All even orders of $\chi^{(m)}$ must also vanish. See §1.5.10 of [131](#).

[†]See Table 4.1.2 of ref. [131](#) for a list of $\chi^{(3)}$ and n_2 values for various optical materials.



§1.4 SILICON QUANTUM PHOTONICS

To build a quantum computer with photons and linear optics, we need unprecedented control of light, on an unprecedented scale (§1.1, §1.2). We need high-performance and high-yield optics, with the ability to reconfigure them on the fly, as dictated by a large classical control system. We also need a source of photons, and a way to detect them.

Silicon photonics can satisfy many of these requirements (§1.3). It provides high-density, high-yield optics. It offers methods, like XPM and carrier-based modulation, to control light on very short time scales. It also allows the direct integration of modern silicon microelectronics—for control and feed-forward—alongside silicon optics¹³⁹. These benefits drive classical interest too: silicon photonics is the most exciting growth field of integrated optics today, with huge ongoing investment from the microelectronics industry.

This work, as part of the wider effort in silicon quantum photonics, seeks to exploit the advantages, investment, and potential of silicon to achieve the large scales needed to process quantum information with photons. In silicon, photons can be: sourced from the Kerr nonlinearity, manipulated using dense optics, detected on-chip^{140,141}, and acted on by integrated electronics and fast electro-optics^{105,113}. Silicon quantum photonics is still in its infancy, but this thesis takes the first steps in identifying and assembling the necessary components, and integrating them into the first fledgling silicon quantum photonic systems.



TABLE 1.1: Silicon material data relevant to silicon photonics. All reported values are for bulk silicon, at $1.55\text{ }\mu\text{m}$.

Constant	Symbol	Value	Reference
Refractive index	n	3.478(4)	142
Nonlinear refractive index	n_2	$6.3 \times 10^{-18}\text{ m}^2\text{ W}^{-1}$	116,143,144
Nonlinear susceptibility	$\chi^{(3)}$	$2.45 \times 10^{-19}\text{ m}^2\text{ V}^{-2}$	145
Thermo-optic coefficient	$\frac{dn}{dT}$	$1.86 \times 10^{-4}\text{ K}^{-1}$	146–148
Verdet constant		$29.5\text{ rad T}^{-1}\text{ m}^{-1}$	149
Absorption coefficient	α	$\ll 0.1\text{ cm}^{-1}$	67
Two-photon absorption coefficient	α_2	$6.14 \times \text{pm W}^{-1}$	116
Free-carrier cross-section	σ_c	1.24 pm^2	116
Free-carrier lifetime	τ_c	1.9 ns	120,121
Free-carrier lifetime (10 K)		55 ps	120
Minimum direct bandgap energy		3.4 eV	116
Indirect bandgap energy	E_{gap}	1.11 eV	150
Indirect bandgap energy (0 K)		1.17 eV	150
Lattice constant	a	543 pm	150
Nearest-neighbour distance		235 pm	150
Stokes (Raman) shift		$15.6 \pm 0.1\text{ THz}$	114
Thermal conductivity (SOI)	κ	$163\text{ W m}^{-1}\text{K}^{-1}$	90
Specific heat capacity (SOI)		$703\text{ J kg}^{-1}\text{K}^{-1}$	90
Melting point		1680 K	142

TABLE 1.2: Silica material data relevant to silicon photonics. All reported values are for bulk fused silica, at $1.55\text{ }\mu\text{m}$.

Constant	Symbol	Value	Reference
Refractive index	n	1.44(4)	142
Nonlinear refractive index	n_2	$2.8 \times 10^{-20}\text{ m}^2\text{ W}^{-1}$	151
Thermo-optic coefficient	$\frac{dn}{dT}$	$9.9 \times 10^{-6}\text{ K}^{-1}$	142
Thermal conductivity (thermal)	κ	$1.38\text{ W m}^{-1}\text{K}^{-1}$	142
Thermal conductivity (PECVD)		$1.0\text{ W m}^{-1}\text{K}^{-1}$	90

TABLE 1.3: Typical data for the fundamental TE mode of a $500 \times 220\text{ nm}^2$ strip waveguide.

Constant	Symbol	Value
Effective refractive index	n_{eff}	2.446
Group refractive index	n_g	4.124
Group velocity dispersion	β_2	$-1.6\text{ ps}^2\text{ m}^{-1}\text{rad}^{-2}$
Effective modal area	A	$0.0456\text{ }\mu\text{m}^2$
Effective modal area (TM)		$0.1568\text{ }\mu\text{m}^2$
Propagation loss	α	0.46 cm^{-1}
Nonlinear parameter	γ	$220\text{ W}^{-1}\text{m}^{-1}$

REFERENCES

- [1] Shannon, C. E. A mathematical theory of communication. *Bell Sys. Tech. J.* **27**, 623–656 (1948). [\(1\)](#)
- [2] Ferain, I., Colinge, C. A. & Colinge, J.-P. Multigate transistors as the future of classical metal-oxide-semiconductor field-effect transistors. *Nature* **479**, 310–316 (2011). [\(1\)](#)
- [3] Feynman, R. P. Simulating physics with computers. *International Journal of Theoretical Physics* **21**, 467–488 (1982). [\(3\)](#)
- [4] DiVincenzo, D. P. The Physical Implementation of Quantum Computation. *arXiv.org* (2000). [quant-ph/0002077v3](#). [\(3, 16\)](#)
- [5] Monroe, C. & Kim, J. Scaling the ion trap quantum processor. *Science* **339**, 1164–1169 (2013). [\(4\)](#)
- [6] Devoret, M. H. & Schoelkopf, R. J. Superconducting circuits for quantum information: an outlook. *Science* **339**, 1169–1174 (2013). [\(4\)](#)
- [7] Awschalom, D. D., Bassett, L. C., Dzurak, A. S., Hu, E. L. & Petta, J. R. Quantum spintronics: engineering and manipulating atom-like spins in semiconductors. *Science* **339**, 1174–1179 (2013). [\(4\)](#)
- [8] Knill, E., Laflamme, R. & Milburn, G. J. A scheme for efficient quantum computation with linear optics. *Nature* **409**, 46–52 (2001). [\(4, 11, 16, 17\)](#)
- [9] Freedman, S. J. & Clauser, J. F. Experimental Test of Local Hidden-Variable Theories. *Physical Review Letters* **28**, 938–941 (1972). [\(5\)](#)
- [10] Aspect, A., Aspect, A., Grangier, P., Grangier, P. & Roger, G. Experimental Tests of Realistic Local Theories via Bell's Theorem. *Physical Review Letters* **47**, 460–463 (1981). [\(5\)](#)
- [11] Bouwmeester, D., Pan, J.-W., Daniell, M., Weinfurter, H. & Zeilinger, A. Observation of Three-Photon Greenberger-Horne-Zeilinger Entanglement. *Physical Review Letters* **82**, 1345–1349 (1999). [\(5\)](#)
- [12] Pan, J.-W., Bouwmeester, D., Daniell, M., Weinfurter, H. & Zeilinger, A. Experimental test of quantum nonlocality in three-photon Greenberger-Horne-Zeilinger entanglement. *Nature* **403**, 515–519 (2000). [\(5\)](#)
- [13] Schmidt-Kaler, F. et al. Realization of the Cirac-Zoller controlled-NOT quantum gate. *Nature* **422**, 408–411 (2003). [\(5\)](#)
- [14] O'Brien, J. L., Pryde, G. J., White, A. G., Ralph, T. C. & Branning, D. Demonstration of an all-optical quantum controlled-NOT gate. *Nature* **426**, 264–267 (2003). [\(5, 14\)](#)
- [15] Pittman, T. B., Fitch, M. J., Jacobs, B. C. & Franson, J. D. Experimental controlled-NOT logic gate for single photons in the coincidence basis. *Physical Review A* **68**, 032316 (2003). [\(5, 14\)](#)
- [16] Nielsen, M. A. & Chuang, I. L. *Quantum computation and quantum information* (Cambridge Univ. Press, Cambridge, 2010), 10th anniversary edn. [\(7\)](#)
- [17] Gerry, C. C. & Knight, P. L. *Introductory Quantum Optics*. (Cambridge University Press, Cambridge, UK, 2005), first edn. [\(9\)](#)
- [18] Sakurai, J. J. & Napolitano, J. *Modern quantum mechanics* (Addison-Wesley, San Francisco, 2011), second edn. [\(9\)](#)
- [19] Fox, M. *Quantum optics: an introduction*. Oxford Master Series in Atomic, Optical and Laser Physics (Oxford Univ. Press, Oxford, 2006). [\(9\)](#)
- [20] Kok, P. et al. Linear optical quantum computing with photonic qubits. *Reviews of Modern ...* (2007). [\(9, 13, 15\)](#)
- [21] Dirac, P. A. M. The Quantum Theory of the Emission and Absorption of Radiation. *Proceedings of the Royal Society A: Mathematical, Physical and Engineering Sciences* **114**, 243–265 (1927). [\(9\)](#)
- [22] Rossi, A., Vallone, G., Chiuri, A., De Martini, F. & Mataloni, P. Multipath Entanglement of Two Photons. *Physical Review Letters* **102**, 153902 (2009). [\(9\)](#)
- [23] Zhou, X.-Q. et al. Adding control to arbitrary unknown quantum operations. *Nature Communications* **2** (2011). [\(9\)](#)
- [24] Langford, N. K. et al. Efficient quantum computing using coherent photon conversion. *Nature* **478**, 360–363 (2011). [\(9\)](#)
- [25] Gilchrist, A., Gilchrist, A., Hayes, A., Hayes, A. J. F. & Ralph, T. C. Efficient parity-encoded optical quantum computing. *Physical Review A* (2007). [\(9\)](#)
- [26] Ralph, T. C., Hayes, A. J. F. & Gilchrist, A. Loss-Tolerant Optical Qubits. *Physical Review Letters* **95**, 100501 (2005). [\(9\)](#)
- [27] Bouland, A. & Aaronson, S. Generation of universal linear optics by any beam splitter. *Physical Review A* **89**, 062316 (2014). [\(11, 16\)](#)
- [28] Hong, C., Ou, Z. & Mandel, L. Measurement of subpicosecond time intervals between two photons by interference. *Physical Review Letters* **59**, 2044–2046 (1987). [\(11\)](#)
- [29] Rarity, J. G. & Tapster, P. R. Fourth-order interference in parametric downconversion. *Journal of the Optical Society of America B-Optical Physics* **6**, 1221 (1989). [\(11\)](#)
- [30] Pittman, T. B. et al. Can Two-Photon Interference be Considered the Interference of Two Photons? *Physical review letters* **77**, 1917–1920 (1996). [\(12\)](#)
- [31] Lee, H., Chen, T., Li, J., Painter, O. & Vahala, K. J. Ultralow-loss optical delay line on a silicon chip. *Nature Communications* **3**, 867 (2012). [\(13, 24\)](#)
- [32] Matsuda, N. et al. Observation of optical-fibre Kerr nonlinearity at the single-photon level. *Nature Photonics* **3**, 95–98 (2009). [\(13\)](#)
- [33] Kiesel, N. et al. Experimental Analysis of a Four-Qubit Photon Cluster State. *Physical Review Letters* **95**, 210502 (2005). [\(14\)](#)
- [34] Politi, A., Cryan, M. J., Rarity, J. G., Yu, S. & O'Brien, J. L. Silica-on-silicon waveguide quantum circuits. *Science* **320**, 646 (2008). [\(14\)](#)
- [35] Shadbolt, P. J. et al. Generating, manipulating and measuring entanglement and mixture with a reconfigurable photonic circuit. *Nature Photonics* **6**, 45–49 (2012). [\(14\)](#)

- [36] Ralph, T. C., Langford, N. K., Bell, T. B. & White, A. G. Linear optical controlled-NOT gate in the coincidence basis. *Physical Review A* **65** (2002). ⟨14⟩
- [37] Hofmann, H. F. & Takeuchi, S. Quantum phase gate for photonic qubits using only beam splitters and postselection. *Physical Review A* **66**, 024308 (2002). ⟨14⟩
- [38] Horodecki, R., Horodecki, P. & Horodecki, M. Quantum entanglement. *Reviews of Modern ...* (2009). ⟨15⟩
- [39] Hein, M., Eisert, J. & Briegel, H. J. Multiparty entanglement in graph states. *Physical Review A* **69**, 062311 (2004). ⟨15⟩
- [40] Barenco, A. *et al.* Elementary gates for quantum computation. *Physical Review A* **52**, 3457–3467 (1995). ⟨16⟩
- [41] Raussendorf, R. & Briegel, H. J. A one-way quantum computer. *Physical review letters* **86**, 5188 (2001). ⟨17⟩
- [42] Raussendorf, R., Browne, D. & Briegel, H. The one-way quantum computer—a non-network model of quantum computation. *Journal of Modern Optics* **49**, 1299–1306 (2002). ⟨17⟩
- [43] Briegel, H. J., Browne, D. E., Duer, W., Raussendorf, R. & Van den Nest, M. Measurement-based quantum computation. *Nature Physics* **5**, 19–26 (2009). ⟨17⟩
- [44] Nielsen, M. A. Cluster-state quantum computation. *Reports on Mathematical Physics* **57**, 147–161 (2006). ⟨17, 18⟩
- [45] Nielsen, M. & Dawson, C. Fault-tolerant quantum computation with cluster states. *Physical Review A* **71**, 042323 (2005). ⟨17⟩
- [46] Raussendorf, R., Harrington, J. & Goyal, K. Topological fault-tolerance in cluster state quantum computation. *New Journal of Physics* **9**, –199 (2007). ⟨17⟩
- [47] Barrett, S. D. & Stace, T. M. Fault Tolerant Quantum Computation with Very High Threshold for Loss Errors. *Physical Review Letters* **105**, 200502 (2010). ⟨17⟩
- [48] Browne, D. E. & Rudolph, T. Resource-efficient linear optical quantum computation. *Physical Review Letters* **95**, 010501 (2005). ⟨17, 18⟩
- [49] Kieling, K., Rudolph, T., Eisert, J. & Eisert, J. Percolation, renormalization, and quantum computing with nondeterministic gates. *Physical review letters* (2007). ⟨17⟩
- [50] Gimeno-Segovia, M., Shadbolt, P. J., Browne, D. E. & Rudolph, T. From three-photon GHZ states to universal ballistic quantum computation. *arXiv.org* (2014). [1410.3720](#). ⟨17, 18⟩
- [51] Li, Y., Humphreys, P. C. & Benjamin, S. C. Resource costs for fault-tolerant linear optical quantum computing (2015). [1504.02457](#). ⟨17⟩
- [52] Migdall, A. L., Branning, D., Castelletto, S. & Ware, M. Tailoring single-photon and multiphoton probabilities of a single-photon on-demand source. *Physical Review A* (2002). ⟨17⟩
- [53] Grice, W. P. Arbitrarily complete Bell-state measurement using only linear optical elements. *Physical Review A* **84**, 042331 (2011). ⟨18⟩
- [54] Ewert, F. & van Loock, P. 3/4-Efficient Bell Measurement with Passive Linear Optics and Unentangled Ancillae. *Physical Review Letters* **113**, 140403 (2014). ⟨18⟩
- [55] Tarasevich, Y. Y. & van der Marck, S. C. An investigation of site-bond percolation on many lattices. *International Journal of Modern Physics C* **10**, 1193–1204 (2012). ⟨18⟩
- [56] Hall, R., Fenner, G., Kingsley, J., Soltys, T. & Carlson, R. Coherent Light Emission From GaAs Junctions. *Physical Review Letters* **9**, 366–368 (1962). ⟨19⟩
- [57] Borner, M. & Patent, T. Electro-optical transmission system utilizing lasers (1966). ⟨19⟩
- [58] Mears, R. J., Reekie, L., Poole, S. B. & Payne, D. N. Low-threshold tunable CW and Q-switched fibre laser operating at 1.55 μm. *Electronics Letters* **22**, 159–160 (1986). ⟨19⟩
- [59] Miller, S. E. Integrated Optics: An Introduction. *Bell System Technical Journal* **48**, 2059–2069 (1969). ⟨19⟩
- [60] Marcatili, E. A. J. Dielectric rectangular waveguide and directional coupler for integrated optics. *Bell System Technical Journal, The* **48**, 2071–2102 (1969). ⟨19⟩
- [61] Marcatili, E. Bends in Optical Dielectric Guides. *Bell System Technical Journal* **48**, 2103–2132 (1969). ⟨19⟩
- [62] Tien, P. K. Light Waves in Thin Films and Integrated Optics. *Applied optics* **10**, 2395–2413 (1971). ⟨19⟩
- [63] Hirao, M., Tsuji, S., Mizuishi, K., Doi, A. & Nakamura, M. Long Wavelength InGaAsP/InP Lasers for Optical Fiber Communication Systems. *Journal of Optical Communications* **1** (1980). ⟨20⟩
- [64] Broberg, B., Lindgren, B. S., Öberg, M. G. & Jiang, H. A novel integrated optics wavelength filter in InGaAsP-InP. *Journal of Lightwave Technology* **4**, 196–203 (1986). ⟨20⟩
- [65] Soref, R. A. & Lorenzo, J. P. Single-crystal silicon: a new material for 1.3 and 1.6 μm integrated-optical components. *Electronics Letters* **21**, 953–954 (1985). ⟨20⟩
- [66] Soref, R. A., Schmidtchen, J. & Petermann, K. Large single-mode rib waveguides in GeSi-Si and Si-on-SiO₂. *IEEE Journal of Quantum Electronics* **27**, 1971–1974 (1991). ⟨20⟩
- [67] Soref, R. A. Silicon-based optoelectronics. *Proceedings of the IEEE* **81**, 1687–1706 (1993). ⟨20, 35⟩
- [68] From Table 1.1 of [152](#). ⟨20⟩
- [69] Lim, D. R. *Simulation of single mode si waveguides and electro-optic coupling modulators*. Ph.D. thesis, Massachusetts Institute of Technology. Dept. of Electrical Engineering (1994). ⟨20⟩
- [70] See §5.4 of ref. [74](#). ⟨20⟩
- [71] Bruel, M. Silicon on insulator material technology. *Electronics Letters* **31**, 1201–1202 (1995). ⟨20⟩
- [72] Foresi, J. S. *et al.* Small radius bends and large angle splitters in SOI waveguides. *Photonics West '97* **3007**, 112–118 (1997). ⟨21⟩
- [73] Miller, D. A. B. Optical interconnects to silicon. *IEEE Journal of Selected Topics in Quantum Electronics* **6**, 1312–1317 (2000). ⟨21⟩

- [74] Reed, G. T. & Knights, A. P. *Silicon Photonics*. An Introduction (John Wiley & Sons, Ltd, Chichester, UK, 2004). [\(22, 37\)](#)
- [75] Rukhlenko, I. D., Premaratne, M. & Agrawal, G. P. Effective mode area and its optimization in silicon-nanocrystal waveguides. *Optics Letters* **37**, 2295–2297 (2012). [\(24\)](#)
- [76] Koos, C., Jacome, L., Poulton, C., Leuthold, J. & Freude, W. Nonlinear silicon-on-insulator waveguides for all-optical signal processing. *Optics Express* **15**, 5976–5990 (2007). [\(24\)](#)
- [77] Morichetti, F. *et al.* Roughness Induced Backscattering in Optical Silicon Waveguides. *Physical Review Letters* **104**, 033902 (2010). [\(24\)](#)
- [78] Poulton, C. G. *et al.* Radiation Modes and Roughness Loss in High Index-Contrast Waveguides. *IEEE Journal of Selected Topics in Quantum Electronics* **12**, 1306–1321 (2006). [\(24\)](#)
- [79] Cardenas, J. *et al.* Low loss etchless silicon photonic waveguides. *Optics Express* **17**, 4752–4757 (2009). [\(24\)](#)
- [80] Borselli, M., Johnson, T. & Painter, O. Beyond the Rayleigh scattering limit in high-Q silicon microdisks: theory and experiment. *Optics Express* **13**, 1515–1530 (2005). [\(24\)](#)
- [81] Lee, K. K., Lim, D. R., Lim, D. R., Shin, J. & Cerrina, F. Fabrication of ultralow-loss Si/SiO₂ waveguides by roughness reduction. *Optics Letters* **26**, 1888–1890 (2001). [\(24\)](#)
- [82] Selvaraja, S. K. *et al.* Highly uniform and low-loss passive silicon photonics devices using a 300mm CMOS platform. *Optical Fiber Communication Conference (2014)*, paper Th2A.33 Th2A.33 (2014). [\(24\)](#)
- [83] Snyder, A. W. & Love, J. D. *Optical Waveguide Theory* (Springer US, Boston, MA, 1984). [\(25\)](#)
- [84] Yariv, A. Coupled-mode theory for guided-wave optics. *IEEE Journal of Quantum Electronics* **9**, 919–933 (1973). [\(26\)](#)
- [85] This MMI design, with access waveguides flush with the sidewall, is due to Mark Thompson (my advisor). It avoids the hard-to-make sharp edges common in MMI designs. It was first shown in ref. 153. [\(26, 27\)](#)
- [86] Soldano, L. B. & Pennings, E. C. M. Optical multi-mode interference devices based on self-imaging: principles and applications. *Journal of Lightwave Technology* **13**, 615–627 (1995). [\(26\)](#)
- [87] Thomson, D. J., Hu, Y., Reed, G. T. & Fédéli, J.-M. Low Loss MMI Couplers for High Performance MZI Modulators. *Photonics Technology Letters, IEEE* **22**, 1485–1487 (2010). [\(27\)](#)
- [88] Sheng, Z. *et al.* A Compact and Low-Loss MMI Coupler Fabricated With CMOS Technology. *Photonics Journal, IEEE* **4**, 2272–2277 (2012). [\(27, 28\)](#)
- [89] Holman, J. P. *Heat transfer* (McGraw-Hill, Boston, MA, 2010), tenth edn. [\(27\)](#)
- [90] Atabaki, A. H., Hosseini, E. S., Eftekhar, A. A., Yegnanarayanan, S. & Adibi, A. Optimization of metallic microheaters for high-speed reconfigurable silicon photonics. *Optics Express* **18**, 18312–18323 (2010). [\(27, 35\)](#)
- [91] Bianucci, P., Zhi, Y., Marsiglio, F., Silverstone, J. W. & Meldrum, A. F. Microcavity effects in ensembles of silicon quantum dots coupled to high-Q resonators. *Physica Status Solidi (a)* **208**, 639–645 (2010). [\(28\)](#)
- [92] Matsuda, N. *et al.* Slow light enhanced optical nonlinearity in a silicon photonic crystal coupled-resonator optical waveguide. *Optics Express* **19**, 19861 (2011). [\(28\)](#)
- [93] Silverstone, J. W., McFarlane, S., Manchee, C. P. K. & Meldrum, A. F. Ultimate resolution for refractometric sensing with whispering gallery mode microcavities. *Optics Express* **20**, 8284–8295 (2012). [\(28\)](#)
- [94] De Vos, K., Bartolozzi, I., Schacht, E., Bienstman, P. & Baets, R. Silicon-on-Insulator microring resonator for sensitive and label-free biosensing. *Optics Express* **15**, 7610–7615 (2007). [\(28\)](#)
- [95] Melloni, A. & Martinelli, M. Synthesis of direct-coupled-resonators bandpass filters for WDM systems. *Journal of Lightwave Technology* **20**, 296–303 (2002). [\(28\)](#)
- [96] Pruessner, M. W., Stievater, T. H. & Rabinovich, W. S. Integrated waveguide Fabry-Perot microcavities with silicon/air Bragg mirrors. *Optics Letters* **32**, 533–535 (2007). [\(28\)](#)
- [97] Wang, X., Grist, S., Flueckiger, J., Jaeger, N. A. F. & Chrostowski, L. Silicon photonic slot waveguide Bragg gratings and resonators. *Optics Express* **21**, 19029–19039 (2013). [\(28\)](#)
- [98] Zhang, C. *et al.* Low threshold and high speed short cavity distributed feedback hybrid silicon lasers. *Optics Express* **22**, 10202 (2014). [\(28\)](#)
- [99] Lee, H. *et al.* Chemically etched ultrahigh-Q wedge-resonator on a silicon chip. *Nature Photonics* **6**, 369–373 (2012). [\(28\)](#)
- [100] Soltani, M., Yegnanarayanan, S. & Adibi, A. Ultra-high Q planar silicon microdisk resonators for chip-scale silicon photonics. *Optics Express* **15**, 4694–4704 (2007). [\(28\)](#)
- [101] Little, B. E. *et al.* Ultra-compact Si-SiO₂ microring resonator optical channel dropping filters. *Photonics Technology Letters, IEEE* **10**, 549–551 (1998). [\(28\)](#)
- [102] Shoji, T., Tsuchizawa, T., Watanabe, T., Yamada, K. & Morita, H. Low loss mode size converter from 0.3 micrometre square Si wire waveguides to singlemode fibres. *Electronics Letters* **38**, 1669–1670 (2002). [\(29\)](#)
- [103] Taillaert, D. *et al.* An out-of-plane grating coupler for efficient butt-coupling between compact planar waveguides and single-mode fibers. *IEEE Journal of Quantum Electronics* **38**, 949–955 (2002). [\(29\)](#)
- [104] Almeida, V. R., Panepucci, R. R. & Lipson, M. Nanotaper for compact mode conversion. *Optics Letters* **28**, 1302–1304 (2003). [\(29\)](#)
- [105] Pelc, J. S. *et al.* Picosecond all-optical switching in hydrogenated amorphous silicon microring resonators. *Optics Express* (2014). [\(29, 34\)](#)
- [106] Jalali, B. *et al.* Prospects for Silicon Mid-IR Raman Lasers. *IEEE Journal of Selected Topics in Quantum Electronics* **12**, 1618–1627 (2006). [\(30\)](#)

- [107] Rong, H. *et al.* An all-silicon Raman laser. *Nature* **433**, 292–294 (2005). [\(30, 32\)](#)
- [108] Liang, D. & Bowers, J. E. Recent progress in lasers on silicon. *Nature Photonics* **4**, 511–517 (2010). [\(30\)](#)
- [109] Walters, R. J., Bourianoff, G. I. & Atwater, H. A. Field-effect electroluminescence in silicon nanocrystals. *Nature materials* **4**, 143–146 (2005). [\(30\)](#)
- [110] Maier-Flaig, F. *et al.* Multicolor Silicon Light-Emitting Diodes (SiLEDs). *Nano Letters* **13**, 475–480 (2013). [\(30\)](#)
- [111] Pernice, W. H. P. & Li, M. Gigahertz photothermal effect in silicon waveguides. *Applied Physics Letters* **93**, 213106–213106–3 (2008). [\(30\)](#)
- [112] Grillanda, S. *et al.* Post-fabrication trimming of athermal silicon waveguides **38**, 5450–5453 (2013). [\(30\)](#)
- [113] Reed, G. T., Mashanovich, G., Gardes, F. Y. & Thomson, D. J. Silicon optical modulators. *Nature Photonics* **4**, 518–526 (2010). [\(31, 34\)](#)
- [114] Lin, Q., Painter, O. J. & Agrawal, G. P. Nonlinear optical phenomena in silicon waveguides: modeling and applications. *Optics Express* **15**, 16604 (2007). [\(31, 35\)](#)
- [115] Soref, R. A., Bennett, B. & Bennett, B. R. Electrooptical effects in silicon. *IEEE Journal of Quantum Electronics* **23**, 123–129 (1987). [\(31\)](#)
- [116] Tsang, H. K. & Liu, Y. Nonlinear optical properties of silicon waveguides. *Semiconductor Science and Technology* **23**, 064007 (2008). [\(31, 35\)](#)
- [117] Liu, Y. & Tsang, H. K. Nonlinear absorption and Raman gain in helium-ion-implanted silicon waveguides. *Optics Letters* **31**, 1714 (2006). [\(31\)](#)
- [118] Almeida, V. R. & Lipson, M. Optical bistability on a silicon chip. *Optics Letters* **29**, 2387 (2004). [\(31\)](#)
- [119] Priem, G. *et al.* Optical bistability and pulsating behaviour in Silicon-On-Insulator ring resonator structures. *Optics Express* **13**, 9623–9628 (2005). [\(31\)](#)
- [120] Pernice, W. H. P. *et al.* Carrier and thermal dynamics of silicon photonic resonators at cryogenic temperatures. *Optics Express* **19**, 3290–3296 (2011). [\(31, 32, 35\)](#)
- [121] Pernice, W. H. P., Li, M. & Tang, H. X. Time-domain measurement of optical transport in silicon micro-ring resonators. *Optics Express* **18**, 18438–18452 (2010). [\(31, 35\)](#)
- [122] Boyraz, Ö., Koonath, P., Raghunathan, V. & Jalali, B. All optical switching and continuum generation in silicon waveguides. *Optics Express* **12**, 4094–4102 (2004). [\(31\)](#)
- [123] Husko, C., Colman, P., Combrie, S., De Rossi, A. & Wong, C. W. Effect of multiphoton absorption and free carriers in slow-light photonic crystal waveguides. *Optics Letters* **36**, 2239–2241 (2011). [\(31\)](#)
- [124] Healy, N. *et al.* Extreme electronic bandgap modification in laser-crystallized silicon optical fibres. *Nature materials* (2014). [\(32\)](#)
- [125] Hong, K.-H., Kim, J., Lee, S.-H. & Shin, J. K. Strain-Driven Electronic Band Structure Modulation of Si Nanowires. *Nano Letters* **8**, 1335–1340 (2008). [\(32\)](#)
- [126] Moss, D. J., Morandotti, R., Gaeta, A. L. & Lipson, M. New CMOS-compatible platforms based on silicon nitride and Hydex for nonlinear optics. *Nature Photonics* **7**, 597–607 (2013). [\(32\)](#)
- [127] Jalali, B. Silicon photonics: Nonlinear optics in the mid-infrared. *Nature Photonics* **4**, 506–508 (2010). [\(32\)](#)
- [128] Clark, A. S. *et al.* Raman scattering effects on correlated photon-pair generation in chalcogenide. *Optics Express* **20**, 16807–16814 (2012). [\(32\)](#)
- [129] Xu, Q., Almeida, V. & Lipson, M. Time-resolved study of Raman gain in highly confined silicon-on-insulator waveguides. *Optics Express* **12**, 4437–4442 (2004). [\(32\)](#)
- [130] Van Laer, R., Kuyken, B., van Thourhout, D. & Baets, R. Interaction between light and highly confined hypersound in a silicon photonic nanowire. *Nature Photonics* **9**, 199–203 (2015). [\(32\)](#)
- [131] Boyd, R. W. *Nonlinear optics* (Elsevier, Burlington, MA, 2008), third edn. [\(33, 39\)](#)
- [132] Miller, R. C. Optical second harmonic generation in piezoelectric crystals. *Applied Physics Letters* **5**, 17–19 (1964). [\(33\)](#)
- [133] Agrawal, G. P. *Nonlinear Fiber Optics* (Academic Press, San Diego, 2001), fourth edn. [\(33, 39\)](#)
- [134] See Eqs. 1.3.3 and B.1 of Agrawal ([133](#)) and Eq. 4.1.19 of Boyd ([131](#)). Boyd uses an unusual definition of $I(\text{Boyd}) = 4I$, but he compensates this in his definition of $\chi^{(3)}$. The results from both authors are consistent. [\(33\)](#)
- [135] Husko, C. A. *et al.* Multi-photon absorption limits to heralded single photon sources. *Scientific Reports* **3** (2013). [\(33\)](#)
- [136] Li, J., O’Faolain, L. & Krauss, T. F. Four-wave mixing in photonic crystal waveguides: slow light enhancement and limitations. *Optics Express* **19**, 4458–4463 (2011). [\(33\)](#)
- [137] Morichetti, F. *et al.* Travelling-wave resonant four-wave mixing breaks the limits of cavity-enhanced all-optical wavelength conversion. *Nature Communications* **2** (2011). [\(33\)](#)
- [138] Matsuda, N. *et al.* Slow light enhanced correlated photon pair generation in photonic-crystal coupled-resonator optical waveguides. *Optics Express* **21**, 8596–8604 (2013). [\(33\)](#)
- [139] Shainline, J. M. *et al.* Depletion-mode carrier-plasma optical modulator in zero-change advanced CMOS. *Optics Letters* **38**, 2657–2659 (2013). [\(34\)](#)
- [140] Pernice, W. H. P. *et al.* High-speed and high-efficiency travelling wave single-photon detectors embedded in nanophotonic circuits. *Nature Communications* **3**, 1325 (2012). [\(34\)](#)
- [141] Najafi, F. *et al.* On-chip detection of non-classical light by scalable integration of single-photon detectors. *Nature Communications* **6**, 5873 (2015). [\(34\)](#)
- [142] Weber, M. *Handbook of Optical Materials*, vol. 19 of *Laser & Optical Science & Technology* (CRC Press, 2002). [\(35\)](#)

- [143] Tsang, H. K. *et al.* Optical dispersion, two-photon absorption and self-phase modulation in silicon waveguides at 1.5 micron wavelength. *Applied Physics Letters* **80**, 416–418 (2002). [\(35\)](#)
- [144] Monat, C. *et al.* Slow Light Enhanced Nonlinear Optics in Silicon Photonic Crystal Waveguides. *IEEE Journal of Selected Topics in Quantum Electronics* **16**, 344–356 (2010). [\(35\)](#)
- [145] Hon, N. K., Soref, R. A. & Jalali, B. The third-order nonlinear optical coefficients of Si, Ge, and $\text{Si}_{1-x}\text{Ge}_x$ in the mid-wave and longwave infrared. *Journal of Applied Physics* **110**, 011301 (2011). [\(35\)](#)
- [146] Treyz, G. V. Silicon Mach-Zehnder waveguide interferometers operating at $1.3\ \mu\text{m}$. *Electronics Letters* **27**, 118 (1991). [\(35\)](#)
- [147] Cocorullo, G. & Rendina, I. Thermo-optical modulation at $1.5\mu\text{m}$ in silicon etalon. *Electronics Letters* **28**, 83–85 (1992). [\(35\)](#)
- [148] Komma, J., Schwarz, C., Hofmann, G., Heinert, D. & Nawrodt, R. Thermo-optic coefficient of silicon at 1550 nm and cryogenic temperatures. *Applied Physics Letters* **101**, 041905 (2012). [\(35\)](#)
- [149] Gabriel, C. J. & Piller, H. Determination of the optical Verdet coefficient in semiconductors and insulators. *Applied optics* **6**, 661–667 (1967). [\(35\)](#)
- [150] Kittel, C. *Introduction to Solid State Physics* (Wiley, Hoboken, NJ, 2004), eighth edition edn. [\(35\)](#)
- [151] Kato, T., Suetsugu, Y., Takagi, M., Sasaoka, E. & Nishimura, M. Measurement of the nonlinear refractive index in optical fiber by the cross-phase-modulation method with depolarized pump light. *Optics Letters* **20**, 988–990 (1995). [\(35\)](#)
- [152] Lifante, G. *Integrated Photonics. Fundamentals* (John Wiley & Sons, Ltd, Chichester, UK, 2003). [\(37\)](#)
- [153] Bonneau, D. *et al.* Quantum interference and manipulation of entanglement in silicon wire waveguide quantum circuits. *New Journal of Physics* **14**, 045003 (2012). [\(38\)](#)

Chapter 2

Photon-pair sources

How does one obtain just a single photon? A single photon carries a minuscule amount of energy: $h\nu$, given by its optical frequency ν multiplied by Planck's constant, $h = 6.626 \times 10^{-34}$ Js. A $1.55\text{ }\mu\text{m}$ (193 THz) photon carries just 1.3 attojoules. Conventional light sources—lasers, gas lamps, light bulbs—can easily produce a billion billion photons every second. The problem turns out to be one of quality.

On the microscopic scale, these photons are produced with an uncertainty in number. If a laser produces an average of N photons, for example, they have an intrinsic Poissonian uncertainty of $\pm\sqrt{N}$. Written in terms of number states, the coherent state—which describes the light in a laser pulse—with an average of $|\alpha|^2 \equiv N$ photons is¹

$$|\alpha\rangle \equiv e^{-\frac{1}{2}|\alpha|^2} \sum_{n=0}^{\infty} \frac{\alpha^n}{\sqrt{n!}} |n\rangle. \quad (2.1)$$

This represents a big superposition of different photon numbers n in the same mode, and the probability with which each state $|n\rangle$ occurs follows the Poisson distribution. Some properties of the coherent states are listed in **TABLE C.1**. What we want is just a single photon, not a superposition—a simple $|1\rangle$.

Single photons² are emitted by atom-like systems, such as rubidium or cesium atoms, solid state colour centres, or quantum dots. Early quantum optics experiments used non-resonantly excited atomic ‘cascades’, from sodium³ or calcium⁴ vapours, to produce correlated photons. Atom sources are difficult to integrate on-chip, but quantum dots integrate naturally^{5–7}, and there has also been significant recent work integrating diamond colour centres^{8,9}.

In 1970, Burnham and Weinberg observed, for the first time, correlated pairs of photons from a $\chi^{(2)}$ nonlinear crystal¹⁰—so-called *parametric* fluorescence. This source of single-mode, correlated photons proved to be bright and versatile. Parametric fluorescence powered many of the early experiments in quantum optics, despite its *intrinsically probabilistic* nature. The $\chi^{(2)}$ pair-generation process is called spontaneous parametric down-conversion² (SPDC) and involves the decay of one photon from a bright pump into two photons—conventionally referred to as *signal* and *idler* photons—conserving energy and momentum (**FIG. 2.1**). SPDC is a spontaneous version of difference frequency generation (DFG), a type of three-wave mixing. Since energy is conserved, the consumed pump photon has the same energy as the combined signal and idler photons ($h\nu_p = h\nu_s + h\nu_i$). For emission at $1.55\text{ }\mu\text{m}$, a pump at the far-detuned 775 nm is required.

SPDC requires a crystalline host with a non-zero $\chi^{(2)}$. It also requires the pump at frequency ν and the photons at $\nu/2$ to have similar effective index—they must



FIG. 2.1: Microscopic parametric fluorescence in second $\chi^{(2)}$ and third $\chi^{(3)}$ order nonlinear media. Relations between photon frequencies are indicated, for arbitrary ν and $\Delta\nu$.

be *phase matched*. This is often achieved using material birefringence. For SPDC to occur in a waveguide, that waveguide must support both ν and $\nu/2$, and satisfy the phase matching criterion, possibly for different polarisations. This is a challenging task, but recent demonstrations of waveguided SPDC in PPKTP¹¹, PPLN^{12–14}, and GaAs¹⁵ have nonetheless shown it to be possible*.

In media with no $\chi^{(2)}$, the $\chi^{(3)}$ process four-wave mixing, and its spontaneous counterpart, spontaneous four-wave mixing (SFWM) can be used to generate photon pairs. Four-wave mixing was first observed in 1966¹⁶, in the explosion of nonlinear optics which followed the invention of the laser. It was subsequently observed in (bulk) silicon in 1979¹⁷. Spontaneous four-wave mixing wasn't observed until 2002 in dispersion-shifted fibre¹⁸, a generation after the 1970s discovery and exploitation of SPDC. Silicon quantum photonics really began in 2006 with the proposal by Lin and Agrawal¹⁹ and the implementation by Sharpen et al.²⁰ of SFWM in silicon strip waveguides.

SFWM elastically scatters two pump photons (degenerate or not) into signal and idler frequencies (FIG. 2.1). This leads to the energy balance $h\nu_{p1} + h\nu_{p2} = h\nu_s + h\nu_i$, from which it's clear that all involved fields can oscillate at similar frequencies (see also FIG. 1.18). This has two important effects: it strongly eases the phase matching between fields; and it means that a waveguide need not support the ν and 2ν which SPDC must. Ultimately, SFWM affords significant flexibility in the design of waveguides for generating photon pairs.

Since 2006, the community has shown how flexible silicon-waveguided SFWM really is. It has been demonstrated in: strip waveguides^{20–25} with control over polarisation²⁶ and with glass-waveguide integration²⁷; single ring resonators^{28–34}, in a self-locking double-bus configuration³⁵, and in coupled-resonator optical waveguides^{36,37}; very high-Q microdisc resonators^{38,39}; one-dimensional photonic crystal resonators⁴⁰; photonic crystal line-defect waveguides^{41,42}, and cavities^{43,44}.

Multiplexing has been proposed to engineer true on-demand single-photon sources from probabilistic SPDC and SFWM photon-pair sources, whereby one photon from a pair is used to *herald* the presence of the other. The original space-multiplexed proposal⁴⁵ by Migdall has been elaborated on⁴⁶, and converted into time-multiplexed^{47–49}, time-frequency⁵⁰, and time-space hybrid⁵¹ architectures. Several small-scale experiments have been performed^{51,52}, including with some parts integrated^{13,42,53}.

*Periodically poled potassium titanyl phosphate (PPKTP); periodically poled lithium niobate (PPLN).

§2.1 DESIRABLE PROPERTIES

A universally useful photon-pair source has three essential properties. I list and describe them here, in order of importance*.

Brightness

The most basic requirement of a photon-pair source is that it produce a lot of photons. This property of SPDC (together with the availability of silicon SPADs) is what kicked off quantum optics in the 1970s and 1980s. Brightness is important for low-power applications, and alleviates the need for strong pump-rejection filtering.

Indistinguishability

Once a source is bright, the next concern is whether its pairs interfere with each other, or with photons from a second source. For this, they must be indistinguishable in all degrees of freedom: arrival time, transverse mode shape, temporal shape, polarisation, and frequency spectrum.

Separability

The final desirable property of a photon-pair source affects the use of *multiple* pairs simultaneously. Separability refers to the state of entanglement between the signal and idler photons of a pair. If a signal-idler pair is separable, the signal photon can be measured without giving any information on the state of the idler. If the pair is entangled, however, then this is not the case, and the state of the idler collapses when the signal is measured, ruining any subsequent interferences with photons from other pairs. For heralded and multi-pair systems, this property is fundamental. However, the separability of a photon-pair source is notoriously difficult to measure¹¹.

§2.2 SPONTANEOUS FOUR-WAVE MIXING

After making rigorous a microscopic model for the four-photon scattering of SFWM ([§D.1](#)), and expanding that model to include multiple scatterings, through squeezing ([§D.2](#)), we can describe the pair generation process quantitatively (see [§D](#)). When a bright pump pulse—with duration Δt , oscillating at ν_p , and carrying peak power P —propagates through a $\chi^{(3)}$ medium, it squeezes photon pairs from the vacuum, in sidebands at ν_s and $\nu_i = 2\nu_p - \nu_s$ above and below the pump frequency[†]. We collect the fluorescence in these sidebands, with a bandwidth of $\Delta\nu_c$. Scattering occurs only at frequencies where there is a good match between the momenta of all four fields. Exactly p pairs are produced with probability[‡]

$$\Pi_p = \operatorname{sech}^2|\xi| \times \tanh^{2p}|\xi| \times \Delta t \Delta \nu_c. \quad (2.2)$$

*I have not seen these criteria listed together elsewhere in the literature.

[†]In the time-reversed process ([CH. 3](#)), two pumps at ν_s and ν_i produce degenerate pairs at ν_p .

[‡]This is [EQ. D.9](#) including the pulse time Δt and collection bandwidth $\Delta\nu_c$.

TABLE 2.1: Derived pair generation probabilities $|\xi|^2$ from the literature. These values determine source brightness. Note: the phase of ξ is twice that of the pump field: $\arg(\xi) = \arg(\alpha^2)$. All values of $|\xi|^2$ are per unit pulse duration (Δt) and per unit collection bandwidth ($\Delta\nu_c$). For the ring resonator (**e**), $\Delta\nu_c = \Delta\nu \approx \nu_0/\pi F^2$. Pulse peak power P , interaction length L , propagation loss α , and momentum mismatch Δk .

#	Pair probability $ \xi ^2$	Reference	Notes
a	$\gamma^2 P^2 L^2 / 2$	58	No loss, phase matched
b	$\gamma^2 P^2 L^2 \Theta^2$	23,56	No loss, Θ from EQ. 2.4
c	$\gamma^2 P^2 L_{\text{eff}}^2 \Theta^2$	56	Linear loss, $L_{\text{eff}} \equiv (1 - e^{-\alpha L})/\alpha$
d	$\gamma^2 A^2 \alpha_2^{-2} \log^2(1 + \alpha_2 I L_{\text{eff}}) \Theta^2$	56	Nonlinear loss
e	$\gamma^2 P^2 L^2 F^8 \pi / 4$	40,58,59	Ring resonator, CW, F from EQ. 2.6

The parameter ξ is known as the squeeze parameter. The square of the squeeze parameter, $|\xi|^2$, represents the small-signal probability to generate a pair (per units pulse duration and bandwidth); it varies depending on the system under consideration. The phase of ξ is determined by the phase of the coherent state pump, $|\alpha\rangle$, where α is like the classical (complex) electric field amplitude:

$$\arg(\xi) = \arg(\alpha^2) = 2 \arg(\alpha). \quad (2.3)$$

TABLE 2.1 lists $|\xi|^2$ for several situations of loss and phase matching (discussed next). The hyperbolic tangent of **EQ. 2.2** accounts for the large-signal behaviour when multi-pair generation cannot be ignored (see **SD.2.1**).

Phase matching effects are included via a factor Θ , related to the classical parametric gain^{54–56} g , where

$$\Theta \equiv \text{sinc}(igL), \quad \text{and} \quad g = \sqrt{\left(\frac{\Phi}{L}\right)^2 - \left(\frac{\Phi}{L} - \frac{\Delta k}{2}\right)^2} \approx \frac{i}{2}(2\gamma P - \Delta k). \quad (2.4)$$

The momentum mismatch Δk is the difference in wavevector between the four photons, and is determined by the waveguide GVD (β_2): $\Delta k \equiv 2k_p - k_s - k_i = -\beta_2(\omega_p - \omega_s)^2$. The nonlinear phase shift is $\Phi = |\xi/\Theta|$ (see **TABLE 2.1b, c, and d**). Note that when $\beta_2 < 0$ and $\Delta k L \ll \Phi$, the cardinal sine in **EQ. 2.4** has a small imaginary argument and Θ can be (much) greater than one. In classical nonlinear optics, this is known as modulation instability^{55,57}. Θ is plotted against both the photon-pump detuning and the waveguide length in **FIG. 2.2**.

In the simplest case of just one pair ($p = 1$), the squeezing is small, so $\tanh^2|\xi| \approx |\xi|^2$ and $\Pi_1 \approx |\xi|^2$. Then, including dispersion and linear loss (**TABLE 2.1c**),

$$\Pi_1 \approx \gamma^2 P^2 L_{\text{eff}}^2 \text{sinc}^2(\gamma PL - \Delta k L / 2) \Delta t \Delta \nu_c \quad (2.5)$$

where the effective length, $L_{\text{eff}} = (1 - e^{-\alpha L})/\alpha$; Δt and $\Delta \nu_c$ are the pulse duration and collection bandwidth, respectively. This is only valid when the squeeze parameter $|\xi|^2$ is very small (see **FIG. 2.6**).

Since SFWM requires the presence of two photons, **EQ. 2.5** depends quadratically on power in the small-signal regime—this reflects the need to conserve energy. The factor $\text{sinc}^2(\Delta k L)$ on the other hand, reflects the momentum conservation. **EQ. 2.2** describes, from a complete microscopic model, the generation of photon pairs

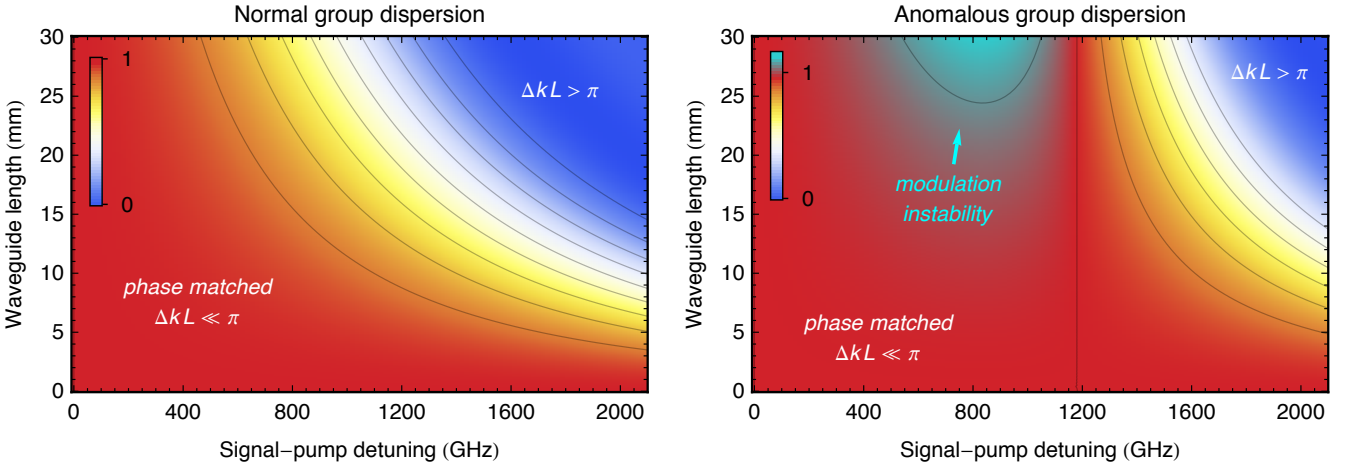


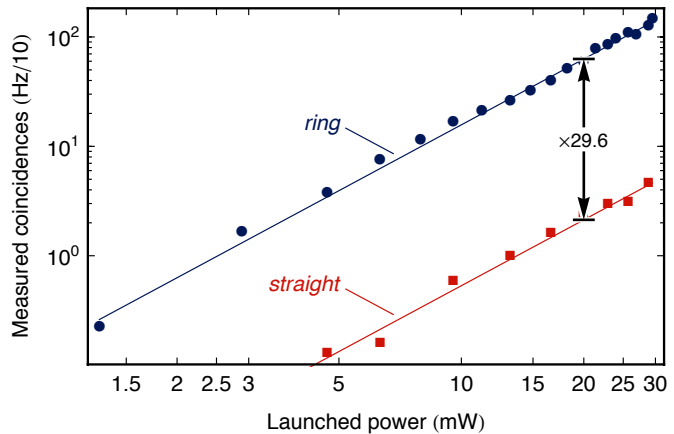
FIG. 2.2: Phase-matched SFWM efficiency for normal and anomalous GVD ($\beta_2 > 0$ and $\beta_2 < 0$, respectively). Plotting Θ (EQ. 2.4) for $\beta_2 = \pm 1.6 \text{ ps}^2/\text{m}$, as in TABLE 1.3 for $P = 100 \text{ mW}$ (peak). Modulation instability ($\Theta > 1$) occurs when the GVD is anomalous, and either P or L is large.

via SFWM. In the remainder of this chapter, I will outline some of the experimental considerations of on-chip pair-generation.

Resonant sources

Resonators present a number of advantages to SFWM sources. The quadratic power dependence of SFWM means that increases in power make the process much more efficient, and the resonant field enhancement is an appealing route to increasing efficiency further. A more efficient source requires less pump power for the same pair rate, so less pump-rejection filtering is needed. The resonator transmission characteristic aids filtering further. The resonator ring-down time can be thought of as enhancing the interaction length, such that the same length can be had in a smaller footprint. Not an advantage, per se, but the proximity of the signal, idler, and pump frequencies in SFWM makes aligning all three fields to cavity resonances much easier than in so-called ‘doubly’ resonant SPDC (e.g. refs. 60,61). Finally, the natural spectral structuring of the SFWM fluorescence has been shown to enhance spectral separability of the produced pairs⁵⁹.

FIG. 2.3: On- and off-resonance behaviour of a ring photon pair source. The ring and straight have length 162 μm , and 1.4 mm, respectively. This ring’s spectrum is plotted in FIG. 1.16. From that spectrum, we expect $|\xi_{\text{ring}}|^2 / |\xi_{\text{wg}}|^2 = 1.1$ (from $F = 1.4$), but we actually find an enhancement of $|\xi_{\text{ring}}|^2 / |\xi_{\text{wg}}|^2 = 29.6$, requiring $F \approx 2.1$, which is not unreasonably far from our estimate. Resonant source performance depends strongly on F .



On the other hand, resonators must be tuned (adding additional system complexity), their strong spectral shaping can reduce indistinguishability between different sources, and their enhanced circulating power also enhances undesired nonlinear effects.

The field enhancement F amplifies the circulating pump field, but also builds up the signal-idler probability amplitudes. From [EQS. C.44](#) and [C.52](#), F is given by

$$F \stackrel{\text{res}}{=} \frac{t}{1 - r\eta} \stackrel{\text{crit}}{=} \frac{1}{t} \quad (2.6)$$

where the first equality represents on-resonance ($\nu = mv_0$) enhancement and the second is critically coupled in addition ($r = \eta$). r is the self-coupling coefficient, $t \equiv \sqrt{1 - r^2}$ is the cross-coupling coefficient, η is the round-trip field transmission*. See [§C.4](#) for more ring resonance details.

SFWM in a ring resonator scales as F^8 ([TABLE 2.1e](#)), due equally to enhanced light circulation and to pump buildup in the cavity⁶², with each of the four fields collecting an F^2 factor—squared due to the consideration of probability (intensity) rather than amplitude (field). This enhancement becomes F^6 when *total* probability is considered over the ring linewidth, $\Delta\nu_c = \Delta\nu \approx \nu_0/\pi F^2$ —relevant when comparing to *stimulated* FWM^{59,63}.

A typical silicon microring has $Q \approx 10\,000$ with $\nu_0 \approx 400\,\text{GHz}$, giving (via [EQ. C.52](#)) $F \approx 6.5$, meaning that the typical cavity enhances the spectral brightness by a tidy factor of about $F^8 \approx 3\,000\,000$. The performance of a low- Q resonant source, in the add-drop configuration, is shown in [FIG. 2.3](#). That device—whose spectrum is plotted in [FIG. 1.16](#)—exhibits a less spectacular enhancement of $F^8 \approx 380$.

§2.3 JOINT SPECTRUM

Two photons can in general be entangled or separable in any degree of freedom, and frequency is no exception. The shared frequency state of a signal and idler photon pair is fully described by their joint spectrum, $J(\nu_s, \nu_i)$, such that their bi-photon state is

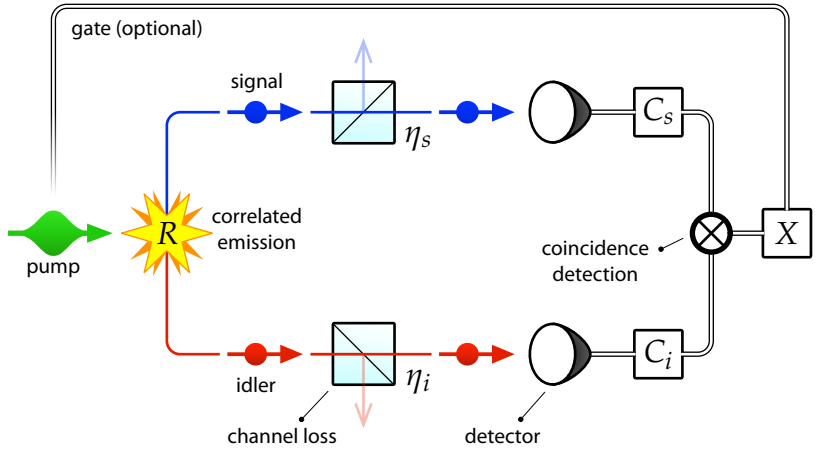
$$\sum_s \sum_i J(\nu_s, \nu_i) |1_s 1_i\rangle, \quad \text{with} \quad \sum_s \sum_i |J(\nu_s, \nu_i)|^2 = 1. \quad (2.7)$$

The sums here ease the calculation and clarify the resulting frequency superposition. They are taken over all frequency modes, indexed by s and i , with infinitesimal spacing in frequency. From [EQ. 2.7](#) we can see that if $J(\nu_s, \nu_i)$ is separable, then the pair is also separable⁶⁴.

The Schmidt number K quantifies a joint spectrum's entanglement or separability. When one photon is measured, it determines the purity ([EQ. 1.2](#)) of the other photon as $\mathcal{P} = 1/K$. Practically, \mathcal{P} is the maximum visibility of a triggered HOM dip between two pairs of spectrally entangled photons. K is roughly the number of separable states needed to describe the pair—it ranges from 1 to the dimension of

*The circulating power is reduced by a factor of η^2 per round trip.

FIG. 2.4: Coincidence detection of two photons. A pump pulse excites signal-idler photon pairs at a rate R . Each photon experiences a channel efficiency η then is collected by (perfect) single-photon detectors, yielding singles rates C_s and C_i . These detection events are correlated, leading to a coincidence count rate X .



the space*. The Schmidt number is given by (EQ. B.41)

$$\frac{1}{K} = \sum_{s,i,s',i'} J(\nu_s, \nu_i)^* J(\nu_{s'}, \nu_{i'})^* J(\nu_s, \nu_{i'}) J(\nu_{s'}, \nu_i). \quad (2.8)$$

Experimentally, we can access the magnitude of J —via the so-called joint-spectral density (JSD), $|J(\nu_s, \nu_i)|^2$ —but not yet its phase. Using, EQ. 2.8, we can put a bound on K via the triangle inequality[†],

$$K \geq 1 \sqrt{\sum_{s,i,s',i'} |J(\nu_s, \nu_i)||J(\nu_{s'}, \nu_{i'})||J(\nu_s, \nu_{i'})||J(\nu_{s'}, \nu_i)|}, \quad (2.9)$$

which is saturated if the phase of J is separable[‡] (e.g. if J is real).

A new method to access the JSD—and the joint-spectral separability—is stimulated emission tomography^{65,66} (SET), whereby a *stimulated* nonlinear optical process is used to access the efficiency of its *spontaneous* counterpart (i.e. FWM \rightarrow SFWM, DFG \rightarrow SPDC). It offers much greater speed and resolution than previous methods^{11,36,67}. Effectively, the stimulated signal is a factor of N_{stim} brighter than the spontaneous one, where N_{stim} is the number of stimulating photons. It is most valuable in sources with fine spectral features, due for example to unusual momentum mismatch⁶⁶. In addition to our own use of it in EXP. 2, SET has recently been applied to non-resonant silicon waveguide sources, alongside conventional JSD-collection methods⁶⁸.

§2.4 MEASURING CORRELATED PHOTONS

A typical pair generation experiment is pictured in FIG. 2.4, and is described in that figure's caption. Correlated photon pairs are generated at a rate R , the j^{th}

*This nebulous number is well defined for finite-dimensional systems (e.g. 2^m for m qubits), but is effectively infinite for spaces of continuous variables, like frequency.

[†]Triangle inequality: $|\sum x_i| \leq \sum |x_i|$.

[‡]Since separability is multiplicative, the phase must be separable additively: $J = e^{i\arg J} |J(s, i)| \stackrel{\text{sep}}{=} \Phi(s)\Psi(i) = e^{i(\arg \Phi + \arg \Psi)} |\Phi(s)\Psi(i)|$, so $\arg J(s, i) \stackrel{\text{sep}}{=} \arg \Phi(s) + \arg \Psi(i)$.

photon suffers a lumped loss η_j ⁶⁹, and each photon is detected by a perfectly efficient detector⁶⁹ which triggers at a singles rate C_j . In the simplest case, the binary measurement signals from the set of detectors are multiplied at each gate, and the frequency of this final signal is the coincidence rate, X . When the system has no laser-generated gate signal, a free-running detector can be used to gate the remaining detectors, or this can be done implicitly by a time interval analyser (TIA). In reality, each electro-optical path from the correlated emission must be precisely matched in time, and this becomes a challenge as the number of detectors increases (see, for example, ref. 70), making a TIA essential.

Estimating the inaccessible R from the accessible $\{C_j\}$ and X is often experimentally important. If the detectors suffer no electrical or optical background noise* then R is straightforward to calculate. Since R is the only light source for now, the singles rates in the two detectors, and the coincidences rate simply determine the generation rate and channel efficiencies⁷¹:

$$\left. \begin{aligned} C_s &= \eta_s R \\ C_i &= \eta_i R \\ X_{\text{net}} &= \eta_s \eta_i R \end{aligned} \right\} \rightarrow R = \frac{C_s C_i}{X}, \quad \eta_{s,i} = \frac{X}{C_{i,s}}. \quad (2.10)$$

The quantity X_{net} is the number of measured coincidences *excluding* the so-called accidental coincidences, X_{acc} : $X_{\text{net}} \equiv X - X_{\text{acc}}$. The accidental rate can either be experimentally measured, as the background of X , or can be estimated from the D detectors' singles:

$$X_{\text{acc}} \approx \frac{1}{\tau} \prod_j^D C_j \tau \quad (2.11)$$

where in *free-running* mode, τ is the gate window width or the integration width in the TIA; while in *pulsed* mode, $\tau = 1/f$. The ratio between coincidence signal and coincidence noise is called the coincidence to accidental ratio: $\text{CAR} \equiv X/X_{\text{acc}}$.

Noise makes the prescription of EQ. 2.10 more complicated. We trigger the SFWM with pump pulses at frequency f , include the power dependence of the generation rate $R = \Pi(P)f$, general linear noise $\mathcal{L}_j P$, and general constant noise \mathcal{C}_j , then[†]

$$\begin{aligned} C_s &= \eta_s [\Pi(P)f + \mathcal{L}_s P] + \mathcal{C}_s \\ C_i &= \eta_i [\Pi(P)f + \mathcal{L}_i P] + \mathcal{C}_i \\ X &= \eta_s \eta_i [\Pi(P)f] + X_{\text{acc}}. \end{aligned} \quad (2.12)$$

We fit the singles and coincidences to extract $\eta_s \Pi(P)f$, $\eta_i \Pi(P)f$, and $\eta_s \eta_i \Pi(P)f$, then use the ratio to compute $R = \Pi(P)f$, as in EQ. 2.10. Note that the presence of these noise sources means EQ. 2.10 always yields an inflated rate[‡].

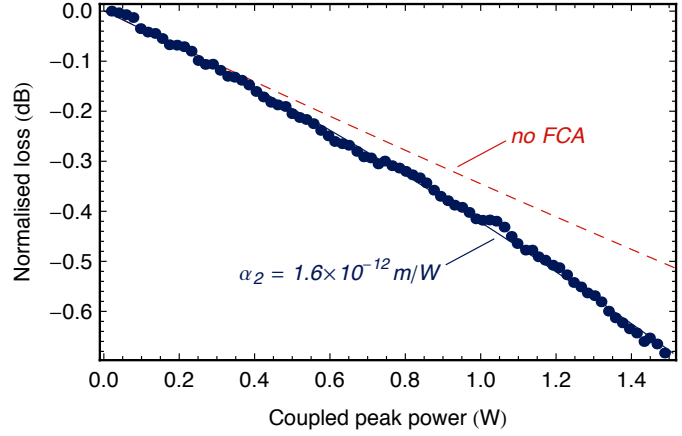
Multi-pair events add even more complexity to our picture. When measuring just two photons (as in FIG. 2.4), we must account for the increased chance of multi-pair events to cause our two detectors to click. Presented with p photons traversing

*Detector counts which occur in the absence of a photon are called dark counts. Optical background noise can come from a number of sources: leaked pump, spurious SFWM on-chip or in fibre, spontaneous Raman scattering, black-body background, etc.

[†]Recall EQ. 2.2 for the probability of pair generation, and that $\Delta t f \rightarrow 1$ for CW excitation.

[‡]The inflated rate is $R' = R + 2\bar{\mathcal{L}}P + \frac{2}{\eta} \bar{\mathcal{C}} + \frac{1}{\eta_s \eta_i R} \bar{\mathcal{C}}^2 + \frac{1}{R} \bar{\mathcal{L}}^2 P^2$.

FIG. 2.5: Nonlinear transmission with power. If the loss was linear, this curve would be flat. It plots [EQ. 2.15](#) with and without $\eta_{\text{FCA}}(P)$, and with $\eta_{\text{TPA}} = \sqrt{\eta_{\text{XTPA}}(P)}$. This data was collected synchronously with the data in **FIG. 2.6**.



a channel with efficiency η , the chance that at least one causes a click is $1 - (1 - \eta)^p$. To obtain the probability η_p of measuring at least one* signal-idler pair from p pairs, we account for the signal and idler channel efficiencies separately:

$$\eta_p \equiv (1 - (1 - \eta_s)^p)(1 - (1 - \eta_i)^p). \quad (2.13)$$

Finally, the total rate of coincidences can be worked out from [Eqs. 2.2, 2.12](#), and [2.13](#). This is the chance that p pairs are generated *and* that two of those photons survive to detection, for each p . We multiply by the number of times per second we take that chance (the pulse frequency f) to obtain the coincidence rate:

$$X = f \sum_{p=1}^{\infty} \eta_p \Pi_p + X_{\text{acc}}. \quad (2.14)$$

Nonlinear loss

Two-photon absorption (TPA) and free-carrier absorption (FCA) result in loss which depends on the pump power. TPA contributes to single-photon loss via the associated cross-TPA (XTPA), which scales as TPA squared. FCA occurs in the presence of free carriers, which make the material conductive. These carriers are normally trapped in the valence band, but they can be excited by TPA (see **FIG. 1.18**). We can account for XTPA and FCA by modifying η_s and η_i such that⁵⁶

$$\eta = \eta_L \eta_{\text{XTPA}}(P) \eta_{\text{FCA}}(P). \quad (2.15)$$

η_L encompasses coupling efficiency, propagation loss ($e^{-\alpha L}$), and detector efficiency; $\eta_{\text{XTPA}}(P)$ and $\eta_{\text{FCA}}(P)$ describe the loss due to XTPA and FCA, and explicitly depend on the injected power⁵⁶:

$$\begin{aligned} \eta_{\text{XTPA}}(P) &\equiv \frac{1}{(1 + \alpha_2 P_0 L_{\text{eff}} / A)^2} \\ \eta_{\text{FCA}}(P) &\equiv \frac{1}{\sqrt{1 + \sigma_c N_c(P) L_{\text{eff}}(2\alpha)}} \end{aligned} \quad (2.16)$$

*For the chance to measure more than one pair, multiply by a few more $1 - (1 - \eta)^p$.

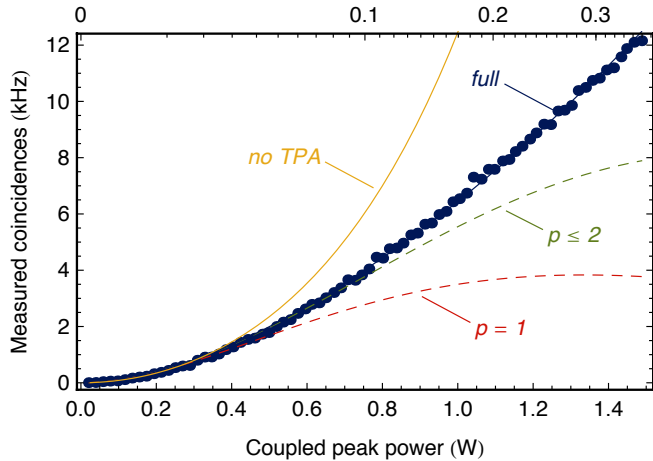


FIG. 2.6: Power dependence of SFWM in a straight waveguide. The squeeze parameter $|\xi|^2$ is shown along the top edge. Linear loss model (yellow, TABLE 2.1c), and nonlinear loss models (TABLE 2.1d) accounting for number of pairs $p = 1$, $p \leq 2$, and $p \leq 4$. Fixed: $L = 2.6$ mm, $\Delta\nu_c = 100$ GHz, $\Delta t = 0.44/\Delta\nu_c$ (Gaussian pulses), $f = 51$ MHz, $\alpha = 2.0$ dB/cm, and σ_c , A , and β_2 from TABLES 1.1, 1.3. Fit: $\gamma = 182$ /W m, $\alpha_2 = 3.1$ ps/m.

where P_0 is the power coupled to the waveguide (accounting for coupling losses, etc.), σ_c is the free-carrier cross-section^{72,73}, around 1.24×10^{-21} m⁻². These expressions arise from the phenomenological differential equation governing propagation, EQ. 1.33. $N_c(P)$, the concentration of free carriers generated by TPA, is given in EQ. 1.34.

An example at high power

In situations of high $|\xi|^2$, both squeezing and nonlinear loss are important to describe experimental results. A measurement of the power-dependence of SFWM in a grating-coupled, 2.6-mm straight waveguide is shown in FIG. 2.6, alongside several models describing multi-pair emission and nonlinear loss. These models are linear loss only (TABLE 2.1c), and nonlinear loss (TABLE 2.1d) accounting for various numbers of pairs p in the sum of EQ. 2.14. The only model which adequately describes the data includes up to $p = 4$ photon pairs, and includes both XTPA and FCA nonlinear loss.

Practically, I first estimated γ using the first few points—assuming linear loss, and single-pair emission (EQ. 2.5)—via the prescription of EQ. 2.12. I then fed this γ into the full model (TABLE 2.1d, EQ. 2.14) and performed a second fit to estimate $\alpha_2 = 3.1$ ps/m—slightly different from the one found classically (1.6 ps/m, FIG. 2.5).



REFERENCES

- [1] Gerry, C. C. & Knight, P. L. *Introductory Quantum Optics*. (Cambridge University Press, Cambridge, UK, 2005), first edn. ⟨41⟩
- [2] Eisaman, M. D., Fan, J., Migdall, A. & Polyakov, S. V. Invited Review Article: Single-photon sources and detectors. *Review of Scientific Instruments* **82**, 071101 (2011). ⟨41⟩
- [3] Kimble, H. J., Dagenais, M. & Mandel, L. Photon Anti-bunching in Resonance Fluorescence. *Physical Review Letters* **39**, 691–695 (1977). ⟨41⟩
- [4] Aspect, A., Aspect, A., Grangier, P., Grangier, P. & Roger, G. Experimental Tests of Realistic Local Theories via Bell's Theorem. *Physical Review Letters* **47**, 460–463 (1981). ⟨41⟩
- [5] Reithmaier, G. *et al.* On-chip time resolved detection of quantum dot emission using integrated superconducting single photon detectors. *Scientific Reports* **3** (2013). ⟨41⟩
- [6] Hoang, T. B. *et al.* Widely tunable, efficient on-chip single photon sources at telecommunication wavelengths. *Optics Express* **20**, 21758–21765 (2012). ⟨41⟩
- [7] Wei, Y.-J. *et al.* Deterministic and Robust Generation of Single Photons from a Single Quantum Dot with 99.5Adiabatic Rapid Passage. *Nano Letters* 141030111800004 (2014). ⟨41⟩
- [8] Burek, M. J. *et al.* High quality-factor optical nanocavities in bulk single-crystal diamond. *Nature Communications* **5**, 5718 (2014). ⟨41⟩
- [9] Chu, Y. *et al.* Coherent Optical Transitions in Implanted Nitrogen Vacancy Centers. *Nano Letters* **14**, 1982–1986 (2014). ⟨41⟩
- [10] Burnham, D. & Weinberg, D. Observation of Simultaneity in Parametric Production of Optical Photon Pairs. *Physical review letters* **25**, 84–87 (1970). ⟨41⟩
- [11] Harder, G. *et al.* An optimized photon pair source for quantum circuits. *Optics Express* **21**, 13975–13985 (2013). ⟨42, 43, 47⟩
- [12] Martin, A., Alibart, O., De Micheli, M. P., Ostrowsky, D. B. & Tanzilli, S. A quantum relay chip based on telecommunication integrated optics technology. *New Journal of Physics* **14**, 025002 (2012). ⟨42⟩
- [13] Meany, T. *et al.* Hybrid photonic circuit for multiplexed heralded single photons. *Laser & Photonics Reviews* **8**, L42–L46 (2014). ⟨42⟩
- [14] Krapick, S. *et al.* An efficient integrated two-color source for heralded single photons. *New Journal of Physics* **15**, 033010 (2013). ⟨42⟩
- [15] Horn, R. *et al.* Monolithic Source of Photon Pairs. *Physical review letters* **108**, 153605 (2012). ⟨42⟩
- [16] Carman, R., Chiao, R. & Kelley, P. Observation of Degenerate Stimulated Four-Photon Interaction and Four-Wave Parametric Amplification. *Physical Review Letters* **17**, 1281–1283 (1966). ⟨42⟩
- [17] Jain, R. K., Klein, M. B. & Lind, R. C. High-efficiency degenerate four-wave mixing of 1.06- μ m radiation in silicon. *Optics Letters* **4**, 328–330 (1979). ⟨42⟩
- [18] Fiorentino, M., Voss, P. L., Sharping, J. E. & Kumar, P. All-fiber photon-pair source for quantum communications. *Photonics Technology Letters, IEEE* **14**, 983–985 (2002). ⟨42⟩
- [19] Lin, Q. & Agrawal, G. P. Silicon waveguides for creating quantum-correlated photon pairs. *Optics Letters* **31**, 3140 (2006). ⟨42⟩
- [20] Sharping, J. E. *et al.* Generation of correlated photons in nanoscale silicon waveguides. *Optics Express* **14**, 12388–12393 (2006). ⟨42⟩
- [21] Harada, K.-i. *et al.* Indistinguishable photon pair generation using two independent silicon wire waveguides. *New Journal of Physics* **13**, 065005 (2011). ⟨42⟩
- [22] Harada, K.-i. *et al.* Generation of high-purity entangled photon pairs using silicon wire waveguide. *Optics Express* **16**, 20368–20373 (2008). ⟨42⟩
- [23] Clemmen, S. *et al.* Continuous wave photon pair generation in silicon-on-insulator waveguides and ring resonators. *Optics Express* **17**, 16558–16570 (2009). ⟨42, 44⟩
- [24] Ollislager, L. *et al.* Silicon-on-insulator integrated source of polarization-entangled photons **38**, 1960–1962 (2013). ⟨42⟩
- [25] Silverstone, J. W. *et al.* On-chip quantum interference between silicon photon-pair sources. *Nature Photonics* **8**, 104–108 (2014). ⟨42⟩
- [26] Matsuda, N. *et al.* A monolithically integrated polarization entangled photon pair source on a silicon chip. **2**, 817 (2012). ⟨42⟩
- [27] Matsuda, N. *et al.* On-chip generation and demultiplexing of quantum correlated photons using a silicon-silica monolithic photonic integration platform. *Optics Express* **22**, 22831–22840 (2014). ⟨42⟩
- [28] Azzini, S. *et al.* Ultra-low power generation of twin photons in a compact silicon ring resonator. *Optics Express* **20**, 23100–23107 (2012). ⟨42⟩
- [29] Grassani, D. *et al.* Micrometer-scale integrated silicon source of time-energy entangled photons. *Optica* **2**, 88 (2015). ⟨42⟩
- [30] Wakabayashi, R. *et al.* Time-bin entangled photon pair generation from Si micro-ring resonator. *Optics Express* **23**, 1103 (2015). ⟨42⟩
- [31] Preble, S. F. *et al.* On-Chip Quantum Interference from a Single Silicon Ring Resonator Source. *arXiv.org* (2015). [1504.04335](https://arxiv.org/abs/1504.04335). ⟨42⟩
- [32] Harris, N. C. *et al.* Integrated Source of Spectrally Filtered Correlated Photons for Large-Scale Quantum Photonic Systems. *Physical Review X* **4**, 041047 (2014). ⟨42⟩
- [33] Engin, E. *et al.* Photon pair generation in a silicon micro-ring resonator with reverse bias enhancement. *Optics Express* **21**, 27826–27834 (2013). ⟨42⟩
- [34] Silverstone, J. W. *et al.* Qubit entanglement on a silicon photonic chip. *arXiv.org* (2014). [1410.8332](https://arxiv.org/abs/1410.8332). ⟨42⟩
- [35] Reimer, C. *et al.* Integrated frequency comb source of heralded single photons. *Optics Express* **22**, 6535–6546 (2014). ⟨42⟩

- [36] Kumar, R., Ong, J. R., Savanier, M. & Mookherjea, S. Controlling the spectrum of photons generated on a silicon nanophotonic chip. *Nature Communications* **5**, 5489 (2014). [\(42\)](#) [\(47\)](#)
- [37] Davanco, M. *et al.* Telecommunications-band heralded single photons from a silicon nanophotonic chip. *Applied Physics Letters* **100** (2012). [\(42\)](#)
- [38] Jiang, W. C., Lu, X., Zhang, J., Painter, O. & Lin, Q. A silicon-chip source of bright photon-pair comb. *arXiv.org* (2012). [1210.4455](#). [\(42\)](#)
- [39] Jiang, W. C., Lu, X., Zhang, J., Painter, O. & Lin, Q. Photon-Pair Comb Generation in a Silicon Microdisk Resonator. *CLEO: 2013* (2013), paper CF2M.3 CF2M.3 (2013). [\(42\)](#)
- [40] Azzini, S. *et al.* Stimulated and spontaneous four-wave mixing in silicon-on-insulator coupled photonic wire nano-cavities. *Applied Physics Letters* **103** (2013). [\(42, 44\)](#)
- [41] Xiong, C. *et al.* Slow-light enhanced correlated photon pair generation in a silicon photonic crystal waveguide. *Optics Letters* **36**, 3413–3415 (2011). [\(42\)](#)
- [42] Collins, M. J. *et al.* Integrated spatial multiplexing of heralded single-photon sources. *Nature Communications* **4** SP - (2013). [\(42\)](#)
- [43] Matsuda, N. *et al.* Slow light enhanced correlated photon pair generation in photonic-crystal coupled-resonator optical waveguides. *Optics Express* **21**, 8596–8604 (2013). [\(42\)](#)
- [44] Takesue, H., Matsuda, N., Kuramochi, E. & Notomi, M. Entangled photons from on-chip slow light. *Scientific Reports* **4**, 3913 (2014). [\(42\)](#)
- [45] Migdall, A. L., Branning, D., Castelletto, S. & Ware, M. Tailoring single-photon and multiphoton probabilities of a single-photon on-demand source. *Physical Review A* (2002). [\(42\)](#)
- [46] Bonneau, D., Mendoza, G. J., O'Brien, J. L. & Thompson, M. G. Effect of Loss on Multiplexed Single-Photon Sources. *arXiv.org* (2014). [1409.5341](#). [\(42\)](#)
- [47] Mower, J. & Englund, D. Efficient generation of single and entangled photons on a silicon photonic integrated chip. *Physical Review A* **84** (2011). [\(42\)](#)
- [48] Rohde, P. P., Helt, L. G., Steel, M. & Gilchrist, A. Multiplexed single-photon state preparation using a fibre-loop architecture. *arXiv.org* (2015). [1503.03546](#). [\(42\)](#)
- [49] Francis-Jones, R. J. A. & Mosley, P. J. Temporal Loop Multiplexing: A resource efficient scheme for multiplexed photon-pair sources. *arXiv.org* (2015). [1503.06178](#). [\(42\)](#)
- [50] Zhang, X. *et al.* Enhancing the heralded single-photon rate from a silicon nanowire by time and wavelength division multiplexing pump pulses. *Optics Letters* **40**, 2489–2492 (2015). [\(42\)](#)
- [51] Mendoza, G. J. *et al.* Active Temporal Multiplexing of Photons. *arXiv.org* (2015). [1503.01215](#). [\(42\)](#)
- [52] Ma, X.-s., Zotter, S., Kofler, J., Jennewein, T. & Zeilinger, A. Experimental generation of single photons via active multiplexing. *Phys. Rev. A* **83**, 043814 (2011). [\(42\)](#)
- [53] Xiong, C. *et al.* Active Temporal Multiplexing of Indistinguishable Heralded Single Photons. *arXiv.org* (2015). [1508.03429v1](#). [\(42\)](#)
- [54] See §10.2, and §10.4.1 of [57](#). Ref. [55](#) discusses differences between SFWM and FWM phase matching. [\(44\)](#)
- [55] Brainis, E. Four-photon scattering in birefringent fibers. *Physical Review A* **79**, 023840 (2009). [\(44, 52\)](#)
- [56] Husko, C. A. *et al.* Multi-photon absorption limits to heralded single photon sources. *Scientific Reports* **3** (2013). [\(44, 49\)](#)
- [57] Agrawal, G. P. *Nonlinear Fiber Optics* (Academic Press, San Diego, 2001), fourth edn. [\(44, 52\)](#)
- [58] Bonneau, D. *Integrated quantum photonics at telecommunication wavelength in silicon-on-insulator and lithium niobate platforms*. Ph.D. thesis, Bristol (2013). [\(44\)](#)
- [59] Helt, L. G., Sipe, J. E., Yang, Z. & Liscidini, M. Spontaneous four-wave mixing in microring resonators. *Optics Letters* **35**, 3006–3008 (2010). [\(44, 45, 46\)](#)
- [60] Pomarico, E., Sanguinetti, B., Osorio, C. I., Herrmann, H. & Thew, R. T. Engineering integrated pure narrow-band photon sources. *New Journal of Physics* **14**, 033008 (2012). [\(45\)](#)
- [61] Scholz, M., Koch, L. & Benson, O. Statistics of Narrow-Band Single Photons for Quantum Memories Generated by Ultrabright Cavity-Enhanced Parametric Down-Conversion. *Physical Review Letters* **102**, 063603 (2009). [\(45\)](#)
- [62] Absil, P. P. *et al.* Wavelength conversion in GaAs micro-ring resonators. *Optics Letters* **25**, 554–556 (2000). [\(46\)](#)
- [63] Azzini, S. *et al.* From classical four-wave mixing to parametric fluorescence in silicon microring resonators **37**, 3807–3809 (2012). [\(46\)](#)
- [64] Law, C. K., Walmsley, I. A. & Eberly, J. H. Continuous Frequency Entanglement: Effective Finite Hilbert Space and Entropy Control. *Physical Review Letters* **84**, 5304–5307 (2000). [\(46\)](#)
- [65] Liscidini, M., Liscidini, M. & Sipe, J. E. Stimulated Emission Tomography. *Physical Review Letters* **111**, 193602 (2013). [\(47\)](#)
- [66] Eckstein, A. *et al.* High-resolution spectral characterization of two photon states via classical measurements. *Laser & Photonics Reviews* n/a–n/a (2014). [\(47\)](#)
- [67] Avenhaus, M., Eckstein, A., Mosley, P. J. & Silberhorn, C. Fiber-assisted single-photon spectrograph **34**, 2873–2875 (2009). [\(47\)](#)
- [68] Jizan, I. *et al.* Bi-photon spectral correlation measurements from a silicon nanowire in the quantum and classical regimes. *arXiv.org* (2014). [1412.0809](#). [\(47\)](#)
- [69] This loss includes on-chip propagation loss, chip-fibre coupling loss, filtering loss, and sub-unit detection efficiency, as well as any other linear or nonlinear effect which scatters or absorbs one or both correlated photons. I treat the loss on each photon to be independent for simplicity, though this stipulation can be lifted. [\(48\)](#)
- [70] Matthews, J. C. F. *et al.* Practical Quantum Metrology. *arXiv.org* (2013). [1307.4673v2](#). [\(48\)](#)

- [71] Rarity, J. G., Ridley, K. D. & Tapster, P. R. Absolute measurement of detector quantum efficiency using parametric downconversion. *Applied optics* **26**, 4616–4619 (1987). [\(48\)](#)
- [72] Pelc, J. S. *et al.* Picosecond all-optical switching in hydrogenated amorphous silicon microring resonators. *Optics Express* (2014). [\(50\)](#)
- [73] Tsang, H. K. & Liu, Y. Nonlinear optical properties of silicon waveguides. *Semiconductor Science and Technology* **23**, 064007 (2008). [\(50\)](#)

Chapter 3

Experiment 1

Time-reversed Hong-Ou-Mandel interference

The first experiment of this thesis explores two themes: indistinguishability, and integration. As I discussed in §2.1, once we have a photon pair source which is bright, the next thing to prove is that its pairs are indistinguishable—to pairs from the same source or from another. In §1.4, I talked about the aspirations of silicon quantum photonics to build *systems*. This experiment is the first step on that path—indeed, it was the strongest example of a silicon quantum photonic system when it was published, 18 months after we finished the experiment. The result garnered significant attention; my artistic impression was featured on the cover of *Nature Photonics*^{*}, we were interviewed, and I was congratulated at conferences by people I'd never met.

To show indistinguishability between silicon sources, we devised a simple experiment which integrated two sources inside an interferometer with a thermal phase shifter, as shown in FIG. 3.1. When one sets out to show indistinguishability between pairs from two sources, the most obvious way to do this is by taking a pair from source *A* and one from source *B* and interfering them on a beamsplitter. Because of the newness of on-chip phase-stable sources, I don't think anybody had thought to look at just *one* pair in superposition between *A* and *B*, and this is precisely what we did. It is essentially a trick, and flatteringly it has now been replicated in lithium niobate².

Notwithstanding the source-interference achievement, this experiment was the first one to use two on-chip sources to do anything on-chip, and certainly the first combination of sources and reconfigurable optics. While we were preparing the manuscript, Ollslager et al. (ref. 3) published their paper, showing a fully passive but similar configuration. They pumped two silicon sources, but took that light straight off the chip, encoded in polarisation. This was a nice piece of work, but I don't think they appreciated the importance of what they'd done. We pulled our draft together and got it on the Arxiv within a week of their publication.

^{*}The experiment was published in the February 2014 issue of *Nature Photonics*. See ref. 1.

§3.1 BACKGROUND

Before jumping in, I'd like to give a bit of specific background on two time-reversed effects which are used in this experiment. The first—time-reversed HOM interference ([§3.1.1](#))—underpins the quantum features of this experiment, while the second—time-reversed SFWM ([§3.1.2](#))—describes the process we used to obtain degenerate photon pairs.

3.1.1 Time-reversed Hong-Ou-Mandel interference

This effect is less spooky than it sounds. Quantum mechanics is, after all, completely reversible. This is evident from the definition of unitary evolution. Unitary operators must satisfy $\hat{U}^\dagger \hat{U} = \hat{I}$, meaning that if we first evolve a state through \hat{U} ($\hat{U}|\psi\rangle$) then evolve it back ($\hat{U}^\dagger \hat{U}|\psi\rangle$), we are always left with what we started with.

Normal, time-not-reversed HOM interference results in the ‘+’ superposition state $(|20\rangle + |02\rangle)/\sqrt{2}$ ([EQ. 1.13](#)), so it may not surprise you to find that if we take that output state and put it through another beamsplitter, we end up with $|11\rangle$ again. This may be more obvious after observing that two back-to-back beamsplitters implement a swap $\hat{U}_{\text{BS}} \cdot \hat{U}_{\text{BS}} = i\hat{X}$ —an important identity of on-chip interferometry—which does nothing to the state $|11\rangle$. So we know that,

$$\frac{|20\rangle + |02\rangle}{\sqrt{2}} \xrightarrow{\text{BS}} i|11\rangle. \quad (\text{split}) \quad (3.1)$$

This is (nearly) time-reversed Hong-Ou-Mandel interference. I say ‘nearly’ because the factor of i appears, but in practice this factor doesn’t matter. On the other hand, the ‘−’ superposition state is an eigenstate of the beamsplitter, so

$$\frac{|20\rangle - |02\rangle}{\sqrt{2}} \xrightarrow{\text{BS}} \frac{|20\rangle - |02\rangle}{\sqrt{2}}. \quad (\text{bunch}) \quad (3.2)$$

See [§E.1](#) for a bit more rigour. The moral of the story of [EQS. 3.1](#) and [3.2](#) is that if we put a superposition of two photons on a beamsplitter, the *phase* of those superpositions determines whether they bunch or split on the other side.

Counterintuitively, this result also holds for *non-degenerate* pairs—even if the two photons are *different colours*, they still interfere in this configuration (see [§E.1.2](#)). This behaviour is summarised by ([EQ. E.4](#))

$$\frac{|1_s 1_i 0_s 0_i\rangle + |0_s 0_i 1_s 1_i\rangle}{\sqrt{2}} \xrightarrow{\text{BS}} i \frac{|1_s 0_i 0_s 1_i\rangle + |0_s 1_i 1_s 0_i\rangle}{\sqrt{2}}, \quad (\text{split}) \quad (3.3a)$$

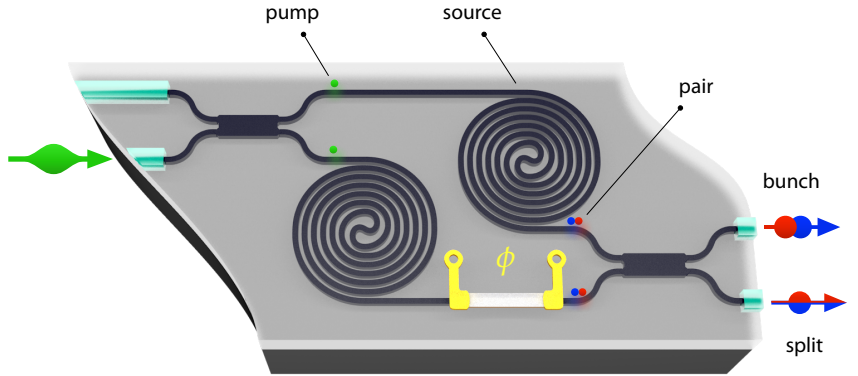
$$\frac{|1_s 1_i 0_s 0_i\rangle - |0_s 0_i 1_s 1_i\rangle}{\sqrt{2}} \xrightarrow{\text{BS}} \frac{|1_s 1_i 0_s 0_i\rangle - |0_s 0_i 1_s 1_i\rangle}{\sqrt{2}}. \quad (\text{bunch}) \quad (3.3b)$$

3.1.2 Time-reversed spontaneous four-wave mixing

In [§D](#), we derive the behaviour of SFWM where the two pump photons are the same frequency (i.e. degenerate). If instead we wish our photon pairs to emerge at the same frequency, we must use the time-reversed process. [EQ. D.1](#) states that the FWM part of the third-order Hamiltonian is

$$\hat{H} = \mathcal{E}_1 a_1^\dagger a_2 a_3 a_4^\dagger + \mathcal{E}_1^* a_1 a_2^\dagger a_3^\dagger a_4, \quad (3.4)$$

FIG. 3.1: Device detail. A bright pump laser is injected, from the left, into on-chip spot-size converters. A MMI distributes the pump between two spiralled sources. Single pairs are produced in superposition between sources, and thermally phase shifted by ϕ , then finally interfered on a second coupler. They either bunch or split at the output, depending on ϕ .



where the first term takes two photons from modes 2 and 3, and creates two photons in modes 1 and 4, and the second one does the reverse—it takes photons from 1 and 4 and creates them in 2 and 3. In the standard treatment, this second term is essentially disregarded. Instead, let's imagine we have two pump beams in modes 1 and 4, both of strength $|\bar{\alpha}|^2 \equiv |\alpha|^2/2$ (so we use the same pump energy as in the degenerate-pump case). In the low-power regime, $\hat{U} \approx \hat{I} + t\hat{H}/\hbar$. When we apply this unitary to the input—two coherent states in modes 1 and 4, and vacuum in modes 2 and 3—we get

$$\hat{U}|\bar{\alpha}00\bar{\alpha}\rangle \approx |\bar{\alpha}00\bar{\alpha}\rangle + \frac{t}{\hbar} \left(\mathcal{E}_1 a_1^\dagger a_2 a_3 a_4^\dagger + \mathcal{E}_1^* a_1 a_2^\dagger a_3^\dagger a_4 \right) |\bar{\alpha}00\bar{\alpha}\rangle \quad (3.5)$$

now remember that $a|0\rangle = 0$ (TABLE B.1) and that $a|\alpha\rangle = \alpha|\alpha\rangle$ (TABLE C.1). So the small-signal probability to generate a photon pair scales like $|\xi_d|^2 \approx |t\mathcal{E}_1/\hbar|^2 \times |\bar{\alpha}|^4 = |t\mathcal{E}_1/\hbar|^2 \times |\alpha|^4/4$, where I've added the subscript d to identify this as the *degenerate* SFWM value. In §D.1, we found $|\xi|^2 = |t\mathcal{E}_1/\hbar|^2 \times |\alpha|^4$ for non-degenerate SFWM. So, for a given input power, the time-reversed case is $\times 4$ less efficient.

If the SFWM emission is *truly* in a single mode (in space, frequency, time, polarisation, etc.) then the output is not a two-mode squeezed vacuum, but as a *single-mode* squeezed vacuum, which has different statistics—see §D.2.2. Single-mode squeezing is even less efficient than the above factor 4 would suggest. For a given value of the (naturally normalised) squeeze parameter, fewer pairs are produced; the maximum for single-pair production via single-mode squeezing is 20%, versus the two-mode version's 25%. These considerations are not important for the current experiment, however, as we pumped the device strictly in the small-signal regime (and likely in multiple frequency modes, too).

§3.2 EXPERIMENT

The experimental device is pictured in FIG. 3.1. At its heart are two 5.2-mm-long spiralled waveguides with a $470 \times 220 \text{ nm}^2$ cross-section*. These spirals are locked in an interferometer—formed by two multi-mode interference couplers—with a single thermal phase shifter. Each MMI had the geometry described in §1.3.2, and the phase shifter's heater was titanium nitride. From a cut-back measurement⁴ on the same wafer, we estimated the propagation loss at 4.1 dB/cm. We coupled the

*This cross-section was found to have the most favourable momentum mismatch (see EQ. 2.4).

device to fibre using three 2.0- μm -spot-size lensed fibres. In total, the device had an insertion loss* of about 15 dB, at best. Off-chip filters and wavelength-division multiplexers (WDM) separated the signal, idler, and pump channels. Finally, at the end of their short lives, signal and idler photons were detected by two free-running superconducting single-photon detectors, with 5% (*A*) and 8% (*B*) detection efficiency.

The device functions in essentially three stages, after the pump is divided at the device's input. ❶ Weakly pumped SFWM[†] generates at most one photon pair, split between the two spiralled sources. ❷ The pairs from the bottom source are retarded by a phase ϕ relative to those from the top source. ❸ Pair amplitudes from the two sources are mixed on a final MMI coupler, resulting in photon bunching or splitting, depending on ϕ .

Let's make this more rigorous. The pump is split between the two sources, with a power $P/2$ flowing through each. SFWM occurs in each source. Since we're only pumping weakly, we can use $|\xi|^2 = \gamma^2 P^2 L^2 \Theta^2 / 4$ (TABLE 2.1b). Since the pump in the top source crossed the first beamsplitter, it collects a $\pi/2$ phase. The squeeze parameter collects double this phase: $\arg(\xi_t)/2 = \pi/2$ (see EQ. 2.3). In the bottom source $\arg(\xi_b)/2 = 0$. Now we can use the results listed in TABLE D.1, for two pumped sources producing one pair each: $|\psi_s\rangle \approx (\xi_t a_s^\dagger a_i^\dagger + \xi_b b_s^\dagger b_i^\dagger)|0000\rangle$, where I assumed $|\xi|^2 \ll 1$, so $\zeta \approx \xi$ and $\sqrt{1 - \zeta} \approx 1$. I also labelled the top mode a and the bottom mode b . We can combine the squeeze parameters for the top and bottom sources (ξ_t and ξ_b) using the pump phase which we discussed: $\xi_t = \xi$ and $\xi_b = -\xi$, where $\xi \equiv \sqrt{|\xi|^2} = \gamma PL\Theta/2$. ❶ The state from the source is then

$$|\psi_s\rangle = (\xi a_s^\dagger a_i^\dagger - \xi b_s^\dagger b_i^\dagger)|0000\rangle \quad (3.6)$$

Next, the photons in the bottom mode pass the phase shifter, and each collect a phase ϕ : $b^\dagger \rightarrow e^{i\phi} b^\dagger$. ❷ The post-phase-shifter state $|\psi_p\rangle$ evolves from $|\psi_s\rangle$,

$$|\psi_s\rangle \rightarrow |\psi_p\rangle = (\xi a_s^\dagger a_i^\dagger - e^{i2\phi} \xi b_s^\dagger b_i^\dagger)|0000\rangle \xrightarrow{\text{norm}} \frac{|1_s 1_i 0_s 0_i\rangle - e^{i2\phi} |0_s 0_i 1_s 1_i\rangle}{\sqrt{2}}, \quad (3.7)$$

where I normalised the state in the second equality. Since all that's left for our photons is interference on the final MMI, we can now see the resemblance between EQ. 3.7 and EQ. 3.3. When $\phi = \pi/2 + m\pi$, the photons split up (EQ. 3.3a), and when $\phi = m\pi$, they bunch together in the output waveguides ($m \in \mathbb{Z}$). ❸ So in the output state $|\psi_o\rangle$, pairs either bunch or split, depending on the phase (EQ. E.4):

$$|\psi_o\rangle = \begin{cases} |bunch\rangle \equiv (|1100\rangle - |0011\rangle)/\sqrt{2}, & \text{for } \phi = m\pi \\ |split\rangle \equiv i(|1001\rangle + |0110\rangle)/\sqrt{2}, & \text{for } \phi = m\pi + \frac{\pi}{2}. \end{cases} \quad (3.8)$$

When *degenerate* pairs are created, signal-idler exchange symmetry leads to identical quantum evolution and non-classical interference as EQ. 3.8[‡]. The corresponding $|bunch\rangle$ and $|split\rangle$ states for degenerate SFWM are (EQ. E.2):

*Defined as the additional loss due to inserting the device in the lightpath.

[†]Such that $\Pi_1 \gg \Pi_2$. See EQ. 2.2 for the definition of Π_p .

[‡]Unlike most phenomena, this point is more obvious in a first-quantisation picture. The input state is $|TT\rangle - |BB\rangle/\sqrt{2}$ in *both* degenerate and non-degenerate situations (*T* and *B* mark top and bottom modes).

$$|bunch\rangle = \frac{1}{\sqrt{2}}(|20\rangle - |02\rangle), \quad \text{and} \quad |split\rangle = i|11\rangle. \quad (3.9)$$

Both degenerate and non-degenerate pairs yield two-photon $\frac{\lambda}{2}$ -like fringes—a classic signature of non-classical light^{5,6}. Writing Π_{bunch} and Π_{split} for bunching and splitting probabilities, respectively, this can be seen from the output state:

$$|\psi_o\rangle = \cos\phi|bunch\rangle + \sin\phi|split\rangle \rightarrow \begin{cases} \Pi_{\text{split}} = |\langle split|\psi_o\rangle|^2 = \sin^2\phi \\ \Pi_{\text{bunch}} = |\langle bunch|\psi_o\rangle|^2 = \cos^2\phi, \end{cases} \quad (3.10)$$

3.2.1 Effect of pairs generated in unintended places

Bright light sees our device as a simple Mach-Zehnder interferometer (MZI), and is steered accordingly. When we input a power P in input A of a MZI, the resulting output power in each arm A and B is

$$P_A = P \cos^2(\phi/2) \quad P_B = P \sin^2(\phi/2). \quad (3.11)$$

Thus, when $\phi = 0$ all the pump is deposited in output B , and when $\phi = \pi$ its all in output A . Now, *all* waveguides in this device are the same shape, size, and composition—all waveguides in this device generate pairs.

Pairs generated in the input (independent of ϕ) are steered between outputs A and B . When we measure the rate of pair splitting (with one photon measured in A , and one in B), we would see peaks in ‘input photon’ coincidences when the MZI is configured as a beamsplitter: $\phi = (2m+1)\pi/2$, with $m \in \mathbb{Z}$. Measuring in bunching, however, we see peaks in A and B when the input pairs are steered to that output: peaks in A should occur at $\phi = 2m\pi$, and peaks in B should be at $\phi = (2m+1)\pi$. Looking at the previously expected two-photon fringes (EQ. 3.10), we see that input-generated pairs match exactly with the previously expected splitting behaviour, but contrast in the case of bunching—input pair peaks match up with every *other* source pair peak.

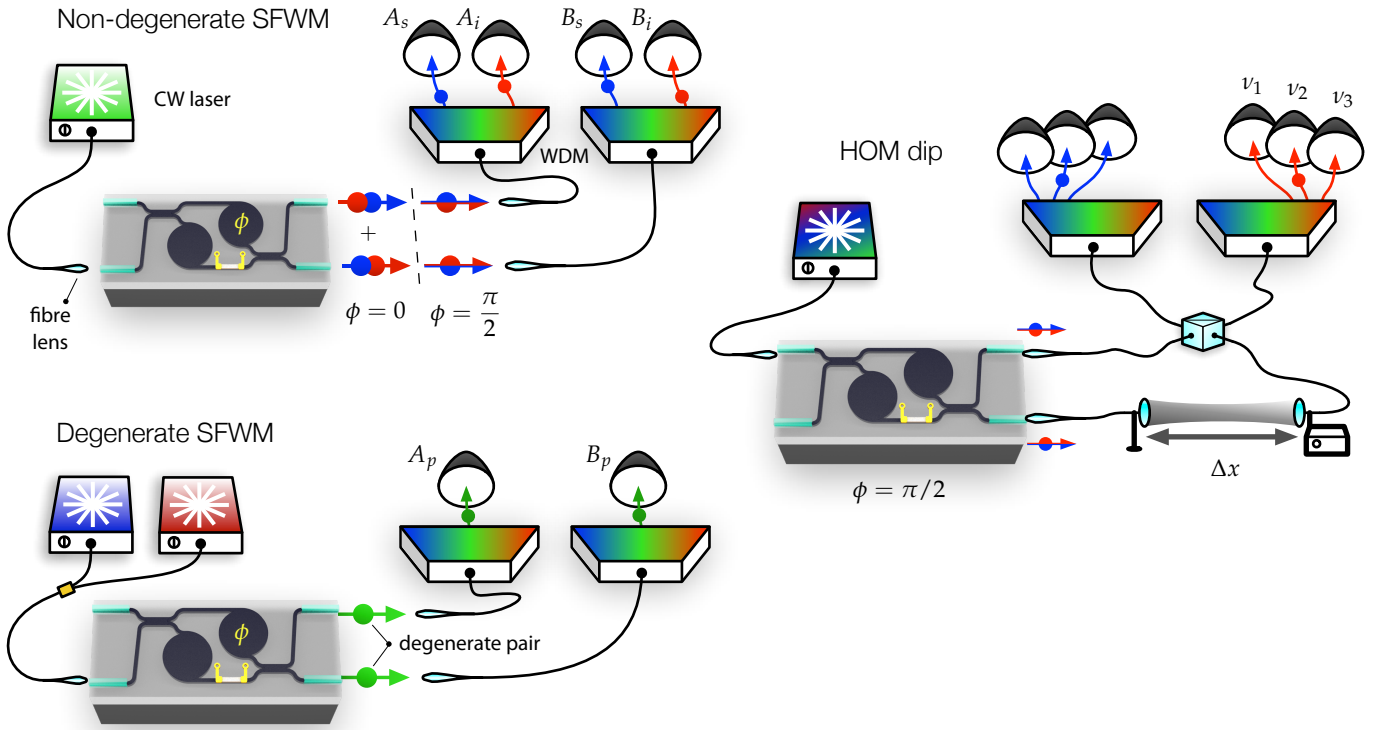
Pairs at the output, on the other hand, are generated by a pump which is being steered by ϕ . They can’t contribute to splitting measurements because those measurements look for one photon in *both* A and B , whereas output-generated pairs necessarily have both photons in *either* A or B . In bunching measurements, however, output-generated pairs behave much the same as their input-generated counterparts—when the pump power in an output peaks, the expected pair rate peaks also. That happens at $\phi = 2m\pi$ and $\phi = (2m+1)\pi$, for A and B respectively.

SFWM is a coherent process, in which interference effects can be very important. The above simple model, though it captures the bulk of the effect, it rests solely on incoherent probabilities. A fully *coherent* model, which accounts for the input, output, and source lengths (L_{in} , L_{out} , and L_s), like that developed in §E.2 is necessary to describe the data completely. From EQS. E.20, the probability to measure each rate is

$$\Pi_{\text{split}}^{A \times B} = |\gamma P \Theta(L_s + L_{\text{in}}) \sin \phi/2|^2 \quad (3.12a)$$

$$\Pi_{\text{bunch}}^{A \times A} = |\gamma P \Theta(L_{\text{in}} + L_{\text{out}} - (L_s + L_{\text{in}} + L_{\text{out}}) \cos \phi)/2|^2 \quad (3.12b)$$

$$\Pi_{\text{bunch}}^{B \times B} = |\gamma P \Theta(L_{\text{in}} + L_{\text{out}} + (L_s + L_{\text{in}} + L_{\text{out}}) \cos \phi)/2|^2. \quad (3.12c)$$



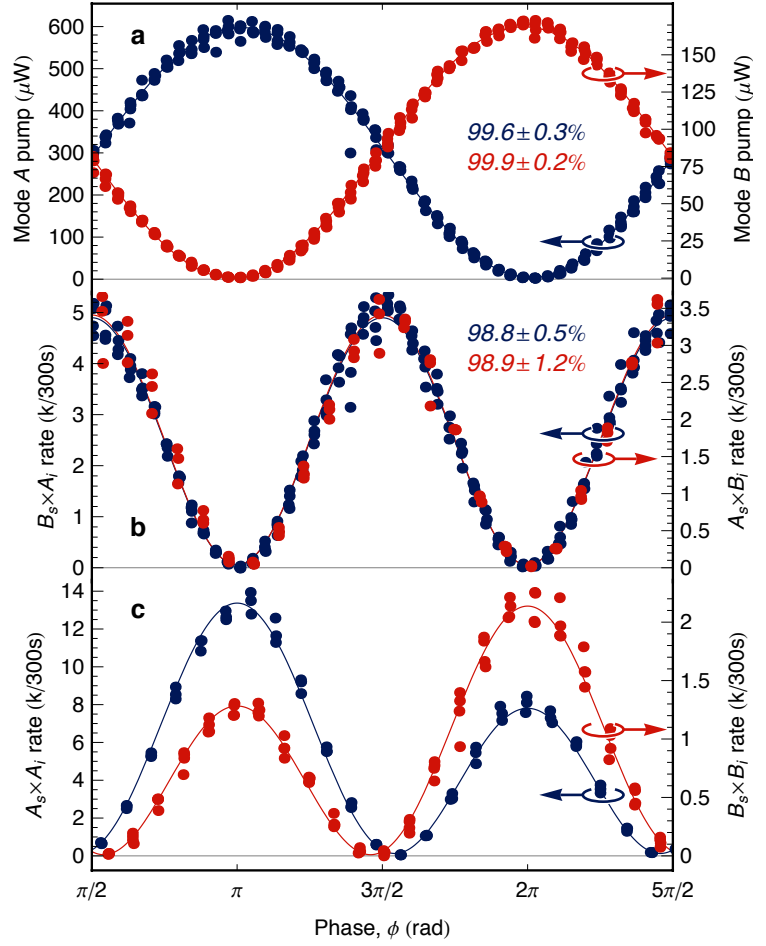
§3.3 RESULTS

As the first showcase silicon quantum photonic technology, the results of this experiment were designed to highlight the quality of silicon SFWM photons, and the variety of new techniques unlocked by this technology. Measurements of quantum interference were key to this argument, both on-chip—in the form of $\frac{\lambda}{2}$ -like fringes—and off-chip—as Hong-Ou-Mandel interference dips. We further showed that both these measurements could run on *degenerate* (time-reversed) SFWM, as degenerate photons have traditionally been preferred by the community.

3.3.1 On-chip interference fringes

Quantum interference on-chip is encoded in the probabilities to split and bunch at the device's outputs (Π_{split} and Π_{bunch} respectively) as the phase ϕ is rotated. This strongly contrasts with the classical interference which the bright pump field experiences. In the first measurement, we generated non-degenerate photon pairs, and measured them with the pictured apparatus. Silica arrayed-waveguide gratings (AWG) with a 200-GHz channel spacing were used to both clean up the input pump, and to separate that pump from the signal and idler photons at the output. All experiments in this chapter were pumped with a very coherent continuous-wave tuneable external-cavity diode laser, amplified to about 100 mW by an erbium-doped fibre amplifier (EDFA). After filtering by two fibre Bragg gratings (out-of-band suppression > 50 dB), launched power was at most 30 mW. I'll label the various coincidences between detectors A_s , A_i , B_s , B_i using a multiplication sign, which is suggestive of the AND operation of a coincidence count.

FIG. 3.2: On-chip quantum and classical interference measurements, varying the internal phase ϕ . **a.** Transmission of the pump laser: classical interference. **b.** Measured rates of signal-idler splitting between modes A and B . **c.** Measured rates of signal-idler bunching, with signal and idler both detected in mode A or B . Asymmetry arises from SFWM noise in the input and output waveguides. Coincidence data have accidental coincidences subtracted.



We pumped at 1549.6 nm ($\nu_p = 193.47$ THz) and collected signal and idler photons at $\nu_s, \nu_i = \nu_p \pm 400$ GHz (two AWG channels pump-detuned) in a bandwidth $\Delta\nu_c \approx 100$ GHz. We measured coincidences $A_s \times B_i$ and $B_s \times A_i$ for Π_{split} , and coincidences $A_s \times A_i$ and $B_s \times B_i$ for Π_{bunch} . The usual classical behaviour is shown in **FIG. 3.2a**. This contrasts strongly with the splitting and bunching statistics which are shown in **FIGS. 3.2b** and **c**, respectively. Both the Π_{split} and Π_{bunch} fringes showed $\frac{\lambda}{2}$ -like behaviour—a signature of path-entangled two-photon states. We observed high-quality interference in both classical and quantum measurements.

Visibility is a key metric for any interference fringe. Interference results in the cancellation of (classical) fields and (quantum) events which would be expected to happen in the absence of coherence. Where interference cancels one field or event, it also constructively boosts another. For this reason, the ratio between the “height” of a fringe, and its minimum is an indicator of interference quality. The visibility is defined as

$$V \equiv \frac{N_{\max} - N_{\min}}{N_{\max}} \quad (3.13)$$

I will use visibility exclusively as a metric of interference quality, but note that there exists a very similar alternative metric: the contrast, which has an added N_{\max} in the denominator. In the above, N_{\max} and N_{\min} are the biggest and smallest count values registered in a given interference fringe. In HOM dip measurements, N_{\max} is by convention taken as the classical coincidence rate (as in [EQ. 3.13](#)). In classical measurements, N_{\max} and N_{\min} are normally the biggest and smallest measured op-

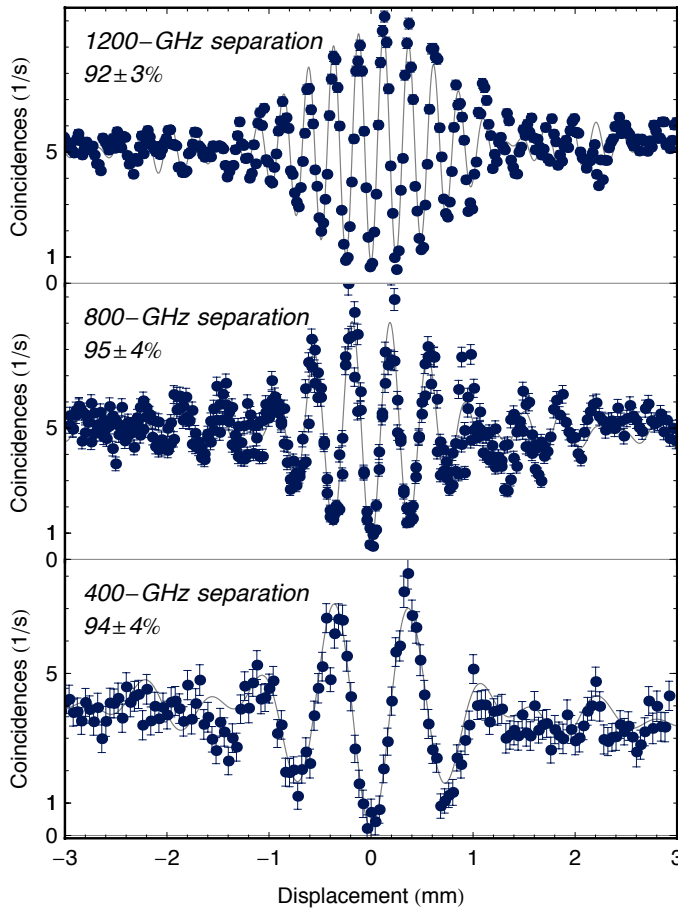


FIG. 3.3: Off-chip Hong-Ou-Mandel quantum interference measurements of $|split\rangle$. Beating in each fringe is due to signal-idler detuning, determined by separation between filtered signal and idler bands (labelled, in frequency units). Coincidence data have accidental coincidences subtracted. Error bars are Poissonian, based on raw coincidences.

tical power values. Visibility runs from 0 to 100%, with higher numbers indicating better interference.

According to the naïve model of [EQ. 3.10](#), the splitting rate should follow $\Pi_{\text{split}} \propto \sin^2 \phi$. This model seems to work well, with the data exhibiting visibility $99.1 \pm 0.5\%$ for $A_i \times B_s$, and $98.8 \pm 1.2\%$ for $A_s \times B_i$ ([FIG. 3.2b](#)). Remember that the model of [EQ. 3.12a](#)—corrected for spurious pairs in the access waveguides—*also* predicts a $\sin^2 \phi$ dependence.

Our two models make different predictions for *bunched* light, however: the naïve [EQ. 3.10](#) predicts a *symmetric* $\cos^2 \phi$ fringe, while the corrected [EQS. 3.12b,c](#) predict a more complicated *asymmetric* behaviour. To your great surprise, we find that the bunching fringes are strongly asymmetric, as shown in [FIG. 3.2c](#). The model is in excellent agreement with the bunching data, supporting our hypothesis of spurious generation. We extracted the spurious pair rate from the data, and found that these pairs accounted for a small fraction of the total, estimating that effectively $(L_{\text{in}} + L_{\text{out}})^2 / L_s^2 \approx 2.5\%$ for $\Pi_{\text{bunch}}^{A \times A}$, and 2.1% for $\Pi_{\text{bunch}}^{B \times B}$. The relevant lengths are fixed by the design of the chip as $(L_{\text{in}} + L_{\text{out}})^2 / L_s^2 = 2.0\%$, in close agreement with the estimates from Π_{bunch} .

3.3.2 Off-chip Hong-Ou-Mandel dips

Next, we show how our $|split\rangle$ pairs could be used externally, and explore the colour entanglement present in $|split\rangle$. This colour entanglement allows a bi-colour, split

pair to behave like a monochrome pair. To test this, we put split pairs, generated by our chip, through the simplest off-chip interferometer—a single beamsplitter—in a series of Hong-Ou-Mandel-type⁷ measurements.

We set $\phi = \pi/2$, such that the device produced $|split\rangle$ (EQ. 3.8), and measured HOM dips for various signal-idler detunings, $|\nu_s - \nu_i|$. One photon went to a tunable delay line, and the other went through a polarisation controller; hence the optical polarisation of the pair could be precisely matched, and we could make them variably distinguishable in arrival time only. We interfered the pairs on a fibre beamsplitter ($R = 50.2\%$), and recorded coincidences while varying the arrival time τ (via a free-space displacement, $x = \tau/c$).

In SE.3, I calculate the shape of the HOM dip for the case at hand: two photons, each with square lineshape, bandwidth $\Delta\nu_c$ (dictated by the filters), and mutually detuned by $|\nu_s - \nu_i|$. EQ. E.29 gives the resulting coincidence probability*:

$$\Pi_{\text{HOM}} = \frac{1}{2} \left(1 - V \text{sinc}(2\pi\Delta\nu_c\tau) \cos(2\pi(\nu_s - \nu_i)\tau) \right). \quad (3.14)$$

The sinc envelope is due to the square photon lineshape, and the signal-idler detuning causes the cosine modulation—a beating between the two frequencies, which manifests itself in the quantum interference. The beating surprised us, but we later discovered that it's a 30-year-old phenomenon. It was first observed by Hong, Ou, and Mandel in 1988⁸, then by Rarity and Tapster in 1990⁹, and more recently heralded as ‘discrete colour entanglement’ by Ramelow et al. in 2009¹⁰ (in contrast with the ‘continuous’ colour entanglement of the joint spectrum¹¹). EQ. 3.14 also shows how we define the visibility for these unconventional fringes.

Hong-Ou-Mandel interferograms are shown in FIG. 3.3. As predicted by EQ. 3.14, the two-colour $|split\rangle$ state exhibited strong temporal beating. As we tuned $|\nu_s - \nu_i| \rightarrow 0$, the beat frequency decreased inline with EQ. 3.14. Off-chip HOM interference visibilities for each value of $|\nu_s - \nu_i|$ (subscripted in GHz) were measured: $V_{1200} = 94 \pm 4\%$, $V_{800} = 95 \pm 4\%$, and $V_{400} = 92 \pm 3\%$. These results show that this device would perform well as an on-chip two-photon source, and indeed we use it for just that, later in the two experiments of CH. 5.

3.3.3 Production and interference of degenerate pairs

All previously mentioned measurements utilised the usual non-degenerate pairs from SFWM. Here, we use *degenerate* SFWM to produce degenerate photons (see §3.1.2). This process requires a two-frequency pump: we used $\nu_p = \nu_s \pm 1400$ GHz, accomplished by the addition of a second tuneable pump laser. One AWG at the input and one at the output provided pump-rejection filtering. Due to the increased detuning between the pump, signal, and idler, this reduced filtering proved sufficient. We measured a surprisingly high > 90 dB suppression from each (Opneti) AWG—much greater than the 45 dB quoted by the manufacturer. The collection bandwidth was $\Delta\nu_c = 120$ GHz. In this configuration, we observed on-chip quantum interference with $V = 100.0 \pm 0.4$, and an off-chip HOM dip with $V = 95 \pm 4\%$ (FIG. 3.4). The dip was free from beating, as expected.

*Conditional on a pair being generated, and it surviving to cause both detectors to click.

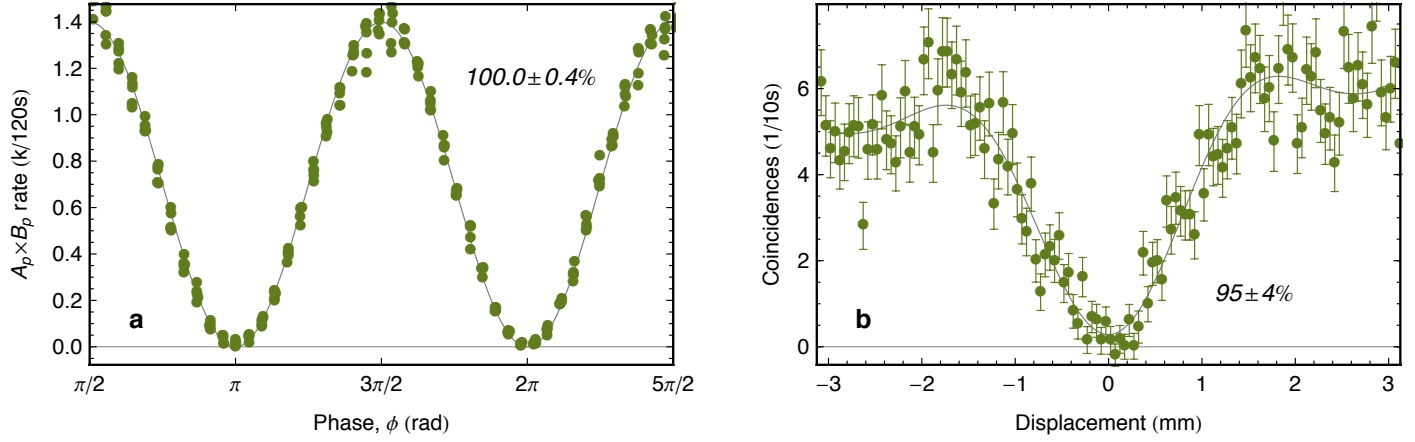


FIG. 3.4: Quantum interference between *degenerate* photon pairs. Measured rates are shown. **a.** On-chip interference measuring photon splitting (cf. [FIG. 3.2b](#)). **b.** Off-chip Hong-Ou-Mandel interference (cf. [FIG. 3.3](#)).

3.3.4 Brightness

Despite their demonstrably excellent indistinguishability, these on-chip sources were not bright. To extract the single-source pair generation rate, we examined an isolated spiralled waveguide, identical to those we used in our device. We found a generation rate of $22 \pm 3 \text{ Hz/GHz/mW}^2$ for non-degenerate pairs, and a similar $20 \pm 5 \text{ Hz/GHz/mW}^2$ for degenerate pairs*. These values are referenced to the *launched* power. Corresponding coincidence-to-accidental ratios were 290, and 45, at 100 kHz generation rates. Using non-degenerate SFWM data and [EQ. 2.10](#), we extracted the channel efficiencies as $\eta_s = -24.2 \text{ dB}$ and $\eta_i = -25.5 \text{ dB}$, which agree with the measured device insertion loss, filtering losses, and detection efficiency, leaving a combined MMI and facet loss of 7.3 dB, with which the above values can be adjusted to obtain the *coupled* power. These numbers, together with the 5.2-mm source length, allow us to calculate

$$\gamma = \eta \sqrt{X} / L = \begin{cases} 167 \pm 21/\text{Wm} & (\text{non-degenerate}) \\ 161 \pm 25/\text{Wm} & (\text{degenerate}) \end{cases} \quad (3.15)$$

where $X = \{22 \pm 3, 20 \pm 5\} \text{ Hz/GHz/mW}^2$ for the two processes, $\eta = -7.2 \text{ dB}$ accounts for the difference between launched and coupled power ($\pm 10\%$), and $L = 5.2 \pm 0.1 \text{ mm}$ is the spiral length. Note that in practice the degenerate rate is reduced by a factor 1/4, due to its dependence on $(P/2)^2$, as discussed in [§3.1.2](#).

§3.4 DISCUSSION

The fraction of pairs generated in the input and output waveguides is related to the ratio $(L_{\text{in}} + L_{\text{out}})^2 / L_s^2$. This ratio is of considerable importance—it directly de-

*In wavelength units: $2.7 \pm 0.4 \text{ kHz/nm/mW}^2$, and $2.5 \pm 0.6 \text{ kHz/nm/mW}^2$ (a factor of c/v^2 separates them).

termines the amount of $|bunch\rangle$ contamination when the device is configured to produce only $|split\rangle$. It could be reduced by: minimising L_{in} and L_{out} ; by modifying the waveguide geometry outside the source regions to increase the effective mode area¹², or to reduce the overlap with silicon using a slot (eg. 13) or sub-wavelength grating¹⁴ waveguide; or by moving to brighter resonant (**Ch. 4**) or slow-light¹⁵ sources. Since the $|bunch\rangle$ state can split on a beamsplitter (depending on the path-length), it can cause coincidences inside the HOM dip. In this experiment, spurious pairs limited the maximum observable dip visibility to $V < 98\%$.

Entangled states are produced by this device. The device's two output states, $|bunch\rangle$ and $|split\rangle$, defined in [EQ. 3.8](#), can be written in terms of path-frequency qubits, using the mapping of [EQ. 1.7](#). They are two of the maximally entangled Bell states ([§1.1.4](#)):

$$|split\rangle = \frac{|01\rangle + |10\rangle}{\sqrt{2}} = |\Psi^+\rangle \quad |bunch\rangle = \frac{|00\rangle - |11\rangle}{\sqrt{2}} = |\Phi^-\rangle, \quad (3.16)$$

where the two qubits are the signal and idler photons, and the states $|0\rangle$ and $|1\rangle$ describe a photon occupying mode a or b , respectively. This type of entanglement, with two photons in a superposition of orthogonal frequencies, has been labelled 'discrete colour entanglement'¹⁰, and is an entanglement resource like any other. In this experiment, we did not deeply probe this entanglement, we only used it for the cheap trick of splitting up the two photons. In the next experiment, [Exp. 2](#), we examine this source of entanglement closely.

We used two 'time-reversed' processes—SFWM, and HOM interference—to show that we can deterministically separate co-propagating photon pairs in a silicon photonic device. This required the combination of several optical elements on-chip—leveraging both linear and nonlinear quantum optics—and ultimately resulted in the most functionally integrated quantum photonic device at the time. In the next chapter, I take this one step further, and address some of the shortcomings of this experiment: poor brightness, limited access to internal states, and limited evidence of entanglement.



ACKNOWLEDGEMENTS

This experiment was a strong collaboration between myself and Dr. Damien Bonneau. Damien deserves particular credit for developing the quantitative model for spurious SFWM emission (though the hypothesis was mine), and for the model of the HOM dip shape. The device was fabricated at Toshiba Japan by Kazuya Ohira, Nobuo Suzuki, Haruhiko Yoshida, Norio Iizuka, and Mizunori Ezaki. Our superconducting detector system was designed, built and maintained by Dr. Michael Tanner, and Dr. Chandra Natarajan, in the group of Prof. Robert Hadfield, originally at Herriot-Watt University and now at the University of Glasgow. I presented this work at CLEO Europe, 2013 (ref. 16). This work is published in ref. 1.

REFERENCES

- [1] Silverstone, J. W. *et al.* On-chip quantum interference between silicon photon-pair sources. *Nature Photonics* **8**, 104–108 (2014). ⟨55, 66⟩
- [2] Jin, H. *et al.* On-Chip Generation and Manipulation of Entangled Photons Based on Reconfigurable Lithium-Niobate Waveguide Circuits. *Physical Review Letters* **113**, 103601 (2014). ⟨55⟩
- [3] Ollslager, L. *et al.* Silicon-on-insulator integrated source of polarization-entangled photons **38**, 1960–1962 (2013). ⟨55⟩
- [4] In a cut-back measurement, the loss of different waveguide lengths is used to extract the effect of length on loss—the propagation loss. So called due to its use in fibre optics, whereby an engineer would repeatedly cut the fibre to determine its propagation loss. ⟨57⟩
- [5] Teich, M. *et al.* Two-photon interference in a Mach-Zehnder interferometer. *Physical Review Letters* **65**, 1348–1351 (1990). ⟨59⟩
- [6] Matthews, J. C. F., Politi, A., Stefanov, A. e. & O'Brien, J. L. Manipulation of multiphoton entanglement in waveguide quantum circuits. *Nature Photonics* **3**, 346–350 (2009). ⟨59⟩
- [7] Hong, C., Ou, Z. & Mandel, L. Measurement of subpicosecond time intervals between two photons by interference. *Physical Review Letters* **59**, 2044–2046 (1987). ⟨63⟩
- [8] Ou, Z. Y., Mandel, L. & Mandel, L. Observation of spatial quantum beating with separated photodetectors. *Physical review letters* (1988). ⟨63⟩
- [9] Rarity, J. & Tapster, P. Experimental violation of Bell's inequality based on phase and momentum. *Physical Review Letters* **64**, 2495–2498 (1990). ⟨63⟩
- [10] Ramelow, S., Ratschbacher, L., Fedrizzi, A. & Langford, N. K. Discrete Tunable Color Entanglement. *Physical Review Letters* **103**, 253601 (2009). ⟨63, 65⟩
- [11] Law, C. K., Walmsley, I. A. & Eberly, J. H. Continuous Frequency Entanglement: Effective Finite Hilbert Space and Entropy Control. *Physical Review Letters* **84**, 5304–5307 (2000). ⟨63⟩
- [12] Clemmen, S. *et al.* Continuous wave photon pair generation in silicon-on-insulator waveguides and ring resonators. *Optics Express* **17**, 16558–16570 (2009). ⟨65⟩
- [13] Zhang, H. *et al.* CMOS-Compatible Fabrication of Silicon-Based Sub-100-nm Slot Waveguide With Efficient Channel-Slot Coupler. *Photonics Technology Letters, IEEE* **24**, 10–12 (2012). ⟨65⟩
- [14] Bock, P. J. *et al.* Subwavelength grating periodic structures in silicon-on-insulator: a new type of microphotonic waveguide. *Optics Express* **18**, 20251–20262 (2010). ⟨65⟩
- [15] Xiong, C. *et al.* Slow-light enhanced correlated photon pair generation in a silicon photonic crystal waveguide. *Optics Letters* **36**, 3413–3415 (2011). ⟨65⟩
- [16] Silverstone, J. W. *et al.* Monolithic generation and manipulation of nondegenerate photon pairs within a silicon-on-insulator quantum photonic circuit. In *Conference on Lasers and Electro-Optics - International Quantum Electronics Conference, IA_6_6-1* (Optical Society of America, Munich, 2013). ⟨66⟩

Chapter 4

Experiment 2

Qubit entanglement & resonant photons

In [Exp. 1](#) I introduced a new device, which I claimed ❶ produced entanglement, and ❷ leveraged that entanglement to perform a useful function—the deterministic splitting of photon pairs. In this chapter, I describe an experiment which makes this entanglement explicit, and showcases some novel new technology in the process. This experiment was published in *Nature Communications* in 2015 (ref. 1).

§4.1 EXPERIMENT

The experimental device is pictured in [FIG. 4.1](#). As in [Exp. 1](#), at the core of the device are two SFGM sources, pumped by one laser, with pump light distributed by a beamsplitter. Unlike the device of [Exp. 1](#): the sources are now formed of microring resonators; the beamsplitter is now an evanescent coupler; the pump laser is now pulsed; and the interferometer containing the sources is not closed (yet). We've broken into the time-reversed HOM interferometer, so we can examine what's inside. The remainder of the device performs this examination. Add-drop microring demultiplexers separate the signal-idler pairs by frequency, and each photon is coherently analysed by a Mach-Zehnder interferometer. The evolution of the light through the device is detailed in [§F.1](#).

In a perfect world, the state inside the time-reversed HOM interferometer should be a maximally entangled Bell-type state in the qubit basis ([EQ. F.10](#)),

$$\frac{|0\rangle_s|0\rangle_i + e^{i\Theta}|1\rangle_s|1\rangle_i}{\sqrt{2}}, \quad (4.1)$$

where Θ is the intrinsic phase difference accumulated by the two photons at the analysis stage, and signal and idler photons in two paths form the two qubits*. We seek to probe the internal state of the device, and see whether it really is entangled—and if so, by how much. In doing so, we will measure the overlap between SFGM

*With $|0\rangle_m \equiv |1_a 0_b\rangle_m$, $|1\rangle_m \equiv |0_a 1_b\rangle_m$, $m \in \{s, i\}$, as in [EQ. 1.7](#).

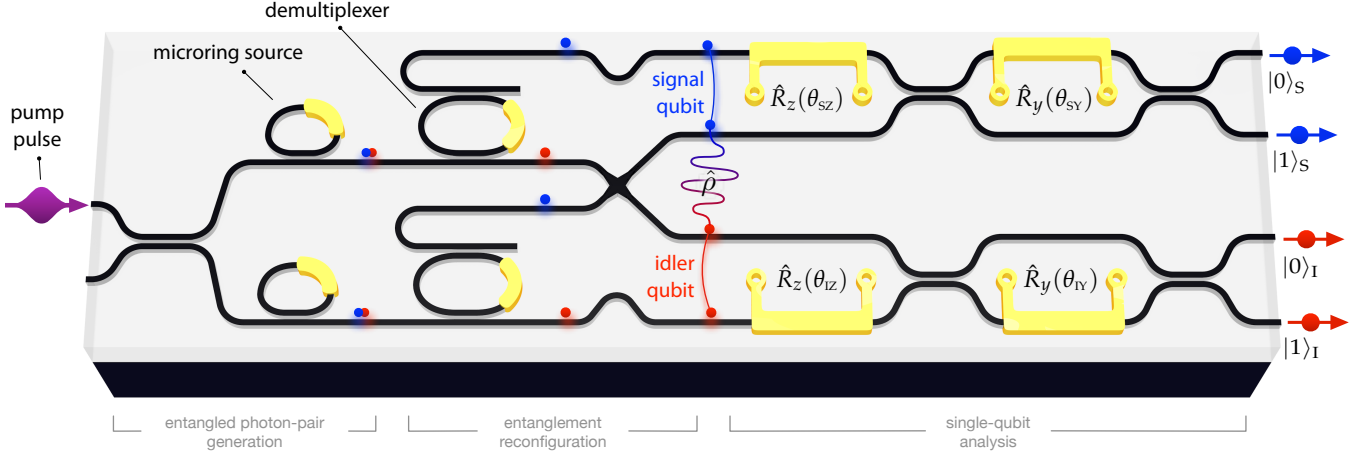


FIG. 4.1: Schematic layout of the device. A picosecond pump pulse is coupled into the silicon chip where it generates a superposition of photon pairs via spontaneous four-wave mixing. This superposition is separated into signal (blue) and idler (red) path qubits, which are analysed by two Mach-Zehnder interferometers. Thermo-optic phase shifters are shown in yellow. Photons at the output are separated from residual pump by fibre wavelength-division multiplexers (not shown) and collected by single-photon detectors.

pairs from two spectrally structured, resonant sources. Finally, these sources, pumped by short pulses, are predicted to produce *separable* photon pairs², and we want evidence of this.

4.1.1 Device operation

Each pair is produced in a superposition of being generated in the top and bottom ring sources simultaneously, as in [EXP. 1](#). This two-photon-in-four-mode superposition is mapped into entanglement between two path qubits by two frequency demultiplexers. These were add-drop ring resonators ([§1.3.2](#)), which exhibited a selectivity of 22 dB, a bandwidth of 35 GHz, and a negligible loss. Their 640-GHz FSR was designed to select the signal photon and maximally reject the idler (see peaks in [FIG. 4.3b](#)). Finally, the frequency demultiplexed waveguides are rearranged, grouping signal and idler modes together.

In [§F.1](#), I compute the photonic evolution through the device. Written in the form of a density matrix, and in terms of the experimental parameters β , σ , and Θ , the resulting qubit-basis state is

$$\begin{aligned} \hat{\rho}_{\text{th}} = & |00\rangle\langle 00| \cdot \beta \\ & + |11\rangle\langle 11| \cdot (1 - \beta) \\ & + |00\rangle\langle 11| \cdot e^{-i\Theta} \sqrt{\beta} \sqrt{1 - \beta} \cdot \sigma \\ & + |11\rangle\langle 00| \cdot e^{+i\Theta} \sqrt{\beta} \sqrt{1 - \beta} \cdot \sigma^* \end{aligned} \quad (4.2)$$

where the balance β describes the relative brightness of the two sources, Θ accumulates the intrinsic total phase between the two qubits, and the overlap σ quantifies the spectral indistinguishability of the two sources ([Eqs. F.6, F.7, F.12](#)). Experimentally, we control the balance β by adjusting the tuning of the filters (at the expense of spectral overlap), and the overlap σ by tuning the two ring sources. If the flux

from the two sources is identical ($\beta = 1/2$) and their joint spectra are identical ($\sigma = 1$) then $\hat{\rho}_{\text{th}}$ matches the maximally entangled state of [EQ. 4.1](#). If $\beta \in \{0, 1\}$ then $\hat{\rho}_{\text{th}}$ is separable; if $\sigma < 1$ then $\hat{\rho}_{\text{th}}$ is mixed, with a minimum purity of $\mathcal{P} = 0.5$ occurring when $\sigma = 0$.

The on-chip state is analysed by two Mach-Zehnder interferometers (MZI). These interferometers, shown in [FIG. 4.1](#), implement \hat{R}_z and \hat{R}_y rotations by angles θ_{SY} , θ_{IZ} , θ_{SY} , and θ_{IY} on the signal (S) and idler (I) qubits, respectively ([§1.1.1](#)). These rotations allow arbitrary single-qubit measurements on the generated two-qubit state.

Device details

We pumped on resonance with the cavity at ν_p , and collected signal and idler photons from adjacent cavity resonances, one free spectral range (FSR) away, at $\nu_{s,i} = \nu_p \pm 800 \text{ GHz}$. The cavity linewidth was $\Delta\nu = 21 \text{ GHz}$. Source resonances cause the highlighted dips in the transmission spectrum of [FIG. 4.3a](#); the peaks in that spectrum are due to the signal-idler demultiplexers. Our pump laser produced $\Delta t = 10.8 \text{ ps}$ pulses, with a 40 GHz linewidth, at a rate of $f = 51 \text{ MHz}$. In our measurements, an average pump power of $150 \mu\text{W}$ (253 mW peak) was delivered, leading to $|\xi|^2 = \{0.06, 0.09\}$ pairs per pulse for the top and bottom sources. The device had a total fibre-to-fibre loss of -16 dB^* . This loss resulted in measured rates around 30 Hz , with a CAR around 10. The efficiency imbalance between the two sources was somewhat compensated by the measured reflectivity of the first coupler, $\eta = 54\%$, leading to an overall source balance of $\beta = 43\%$. Photons were counted using two 25%-efficient avalanche photodiodes, gated on each laser pulse.

Physically, the device was constructed as follows. All layers were patterned using electron beam lithography. Waveguides had a cross-section of $500 \times 220 \mu\text{m}^2$. Evanescent couplers, with 300-nm gaps, were used throughout ([§1.3.2](#)). Waveguides were over-clad with a 900-nm layer of silica. Onto this, heaters and electrical traces were patterned via a lift-off technique on respectively 50-nm film nickel-chromium, and 200-nm gold layers. Heaters exhibited resistance between 1.9 and $2.8 \text{ k}\Omega$, with some variation between straights and rings. Spot-size converters were used to couple the chip to fibre, with $2 \times 1.5 \mu\text{m}^2$ SU8 polymer waveguides, and lensed fibres with a spot-size of $2.5 \mu\text{m}$.

Calibration

Before we could use the rotations $\hat{R}_y(\theta_{\text{SY}})$, $\hat{R}_y(\theta_{\text{IY}})$, $\hat{R}_z(\theta_{\text{SZ}})$, and $\hat{R}_z(\theta_{\text{IZ}})$ to analyse the on-chip light, they required phase-voltage calibration. We injected laser light into the device and recorded the output power P from each interferometer as a function of its two phases, obtaining $P(\theta_{\text{SY}}, \theta_{\text{SZ}})$ and $P(\theta_{\text{IY}}, \theta_{\text{IZ}})$. We fit this data with the following model of the double interferometer (including the first coupler), to obtain the various coupler reflectivities and phase-voltage relationships. For the signal qubit,

$$P(\theta_{\text{SY}}, \theta_{\text{SZ}}) \propto |\mathbf{E}_{\text{out}}^\dagger \cdot \hat{U}_{\text{BS}}(\eta_{y1}) \cdot \hat{U}_{\text{PS}}(\theta_{\text{SY}}) \cdot \hat{U}_{\text{BS}}(\eta_{y0}) \cdot \hat{U}_{\text{PS}}(\theta_{\text{SZ}}) \cdot \hat{U}_{\text{BS}}(\eta_p) \cdot \mathbf{E}_{\text{in}}|^2, \quad (4.3)$$

*Measured by launching 1 mW, summing the output powers, and normalising.

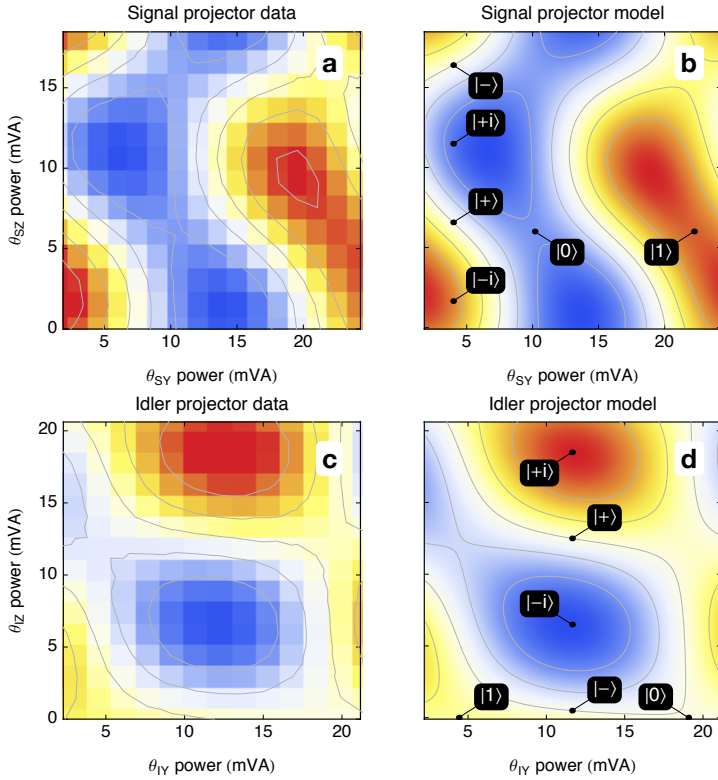


FIG. 4.2: Bright light calibration data (**a** and **c**) and models (**b** and **d**) for signal (**a** and **b**) and idler (**c** and **d**) qubit analysis interferometers. Optimal locations of single-qubit tomographic projectors are extracted from each model, and marked.

with \hat{U}_{BS} and \hat{U}_{PS} from [EQ. 1.10](#), and where \mathbf{E} are the two-mode input and output electric field vectors. This method is unable to determine the absolute values of θ_{SZ} and θ_{IZ} , so we defined these phases relatively (with the difference being lumped into Θ). These data and resulting models are plotted in [FIG. 4.2](#) for the two analysis stages. We used the resulting models to control the on-chip phase shifters, as required by each part of the experiment.

§4.2 RESULTS

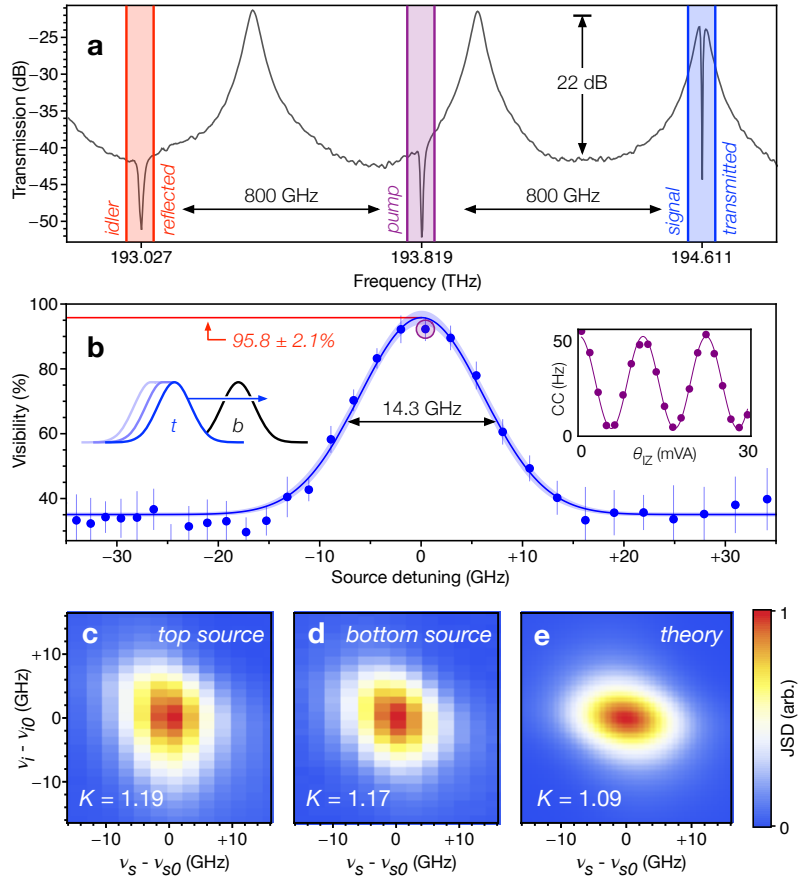
4.2.1 Resonant source overlap

Interference between photons from different sources requires those photons to be indistinguishable in all degrees of freedom, but spectral indistinguishability poses a particular challenge. We refer to this spectral indistinguishability as the overlap, σ , which runs from $\sigma = 0$ for fully distinguishable photon pairs to $\sigma = 1$ for indistinguishable ones. We explored the overlap between the two resonant sources by interfering the signal-idler superposition on the ‘idler’ interferometer, and spectrally tuning one source resonance over the other.

We thermally tuned the resonances of the top source ring across those of the bottom one, while interfering their pairs on the bottom MZI, $\hat{R}_y(\theta_{IY} = \frac{\pi}{2})$ (see [FIG. 4.1](#)). To allow both signal and idler photons to reach this MZI, we detuned both demultiplexers to remove them from the light path. Both signal and idler photons were then routed downwards. Finally, we measured coincidences* while varying

*Measuring across the bottom two output ports, labelled $|0\rangle_i$ and $|1\rangle_i$ in [FIG. 4.1](#).

FIG. 4.3: Spectral characteristics of the experiment. **a**, Spectral layout of source (dips) and demultiplexer (peaks) resonances in the central telecommunications band. Source free spectral range is 800 GHz, to match the 200 GHz ITU grid. **b**, Two-photon fringe visibility measured as a function of top-to-bottom source detuning, as the top resonances were scanned over the stationary bottom resonances. Inset: representative two-photon fringe corresponding to peak visibility value (highlighted). The residual visibility is due to interference between pairs generated outside the resonators. Error bars represent three standard errors of each sinusoidal regression. Shaded region on fit represents one standard deviation in visibility. Measured joint spectral density profiles for the top (**c**), and bottom (**d**) microring sources, as well as from a model based on the linear resonator characteristics (**e**).



θ_{IZ} , making fringes. An example fringe is shown inset to **FIG. 4.3b**. The visibility of these fringes reflect σ . We extracted the visibility of each fringe, and these visibility data are plotted versus the source detuning in **FIG. 4.3b**.

The observed fringes are like those collected in **EXP. 1** (cf. **FIG. 3.2**), but the resonant sources in this experiment were much brighter. If we account for the source imbalance, and for multi-pair events, the maximum ($\sigma = 1$) observable visibility is $V < 96.0\%$. When the sources were tuned, we observed a peak visibility of $V = 95.8 \pm 2.1\%$. This corresponds to a near-perfect overlap of $\sigma = 0.99 \pm 0.04$, when accounting for a pair generation probability of $|\xi|^2 = 0.075$ (an average of the measured values). These estimates were obtained by modifying the state produced by one of the sources: a modified squeezed vacuum (**EQ. D.8**), with a simplified joint spectrum,

$$|\xi\rangle'_{II} = \sqrt{1 - |\zeta|^2} \sum_{p=0}^{\infty} (-\zeta)^p (\sigma |p_s p_i\rangle + \sqrt{1 - \sigma^2} |p_{s'} p_{i'}\rangle). \quad (4.4)$$

The overlap between **EQ. 4.4** and the usual squeezed vacuum—which contains only frequencies s and i —is σ , by design. Simulations of fringes between these two partially-overlapped sources $|\xi\rangle_{II} \otimes |\xi\rangle'_{II}$ yielded the corrected values for σ . In low power, and with perfect balance, $V = 2\sigma/(1 + \sigma)$. Plots of visibility versus overlap and squeezing are shown in **FIG. 4.4**.

The interference peak is like a cross-correlation between the frequency spectra of the two sources. It can help us understand the sources' spectral shapes. The peak in **FIG. 4.3b** had a width of 14.3 GHz, indicating an emission linewidth

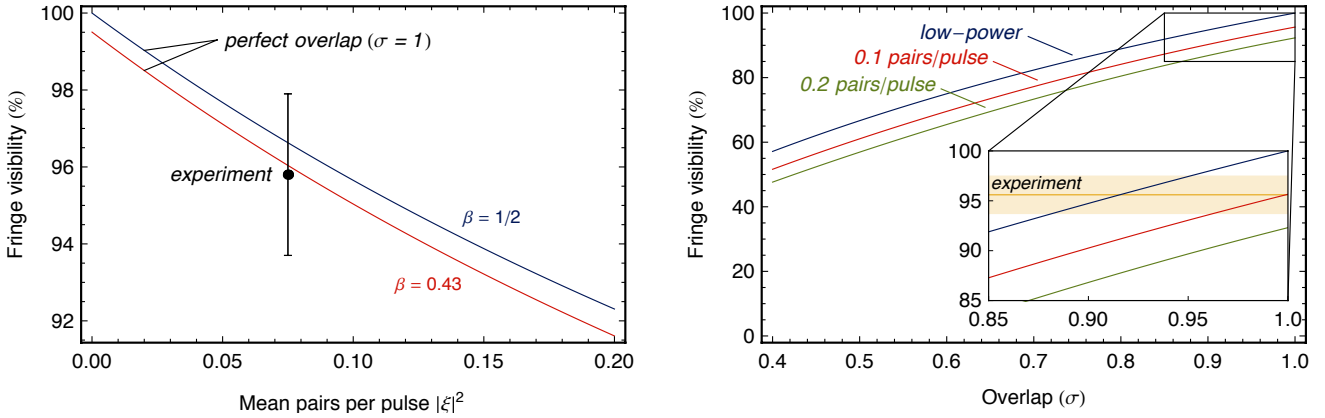


FIG. 4.4: Maximum fringe visibility versus pair generation probability (left). Visibility versus overlap for several values of squeezing (right). Both plots show the high level of overlap indicated by FIG. 4.3b. See §E.2 for additional discussion.

of 28.6 GHz, somewhat broader than the cold cavity linewidth, $\Delta\nu = 21.0$ GHz. Stochastic processes—such as laser power jitter, electrical control jitter, or intra-cavity SPM³—could cause this broadening, and would explain the peak’s Gaussian (not Lorentzian) lineshape.

When the two sources were completely detuned, the visibility reached a floor of 37%, caused by interference with broadband pairs from the non-resonant parts of the device. This visibility indicates that the spectral brightness of the bus waveguide was 1% of that of the tuned microring. The on-chip demultiplexers greatly suppress this waveguide-generated flux, so it does not significantly affect later measurements. Above all, these data prove that ring resonator SFWM sources are bright, and can be made highly indistinguishable.

4.2.2 Joint spectra

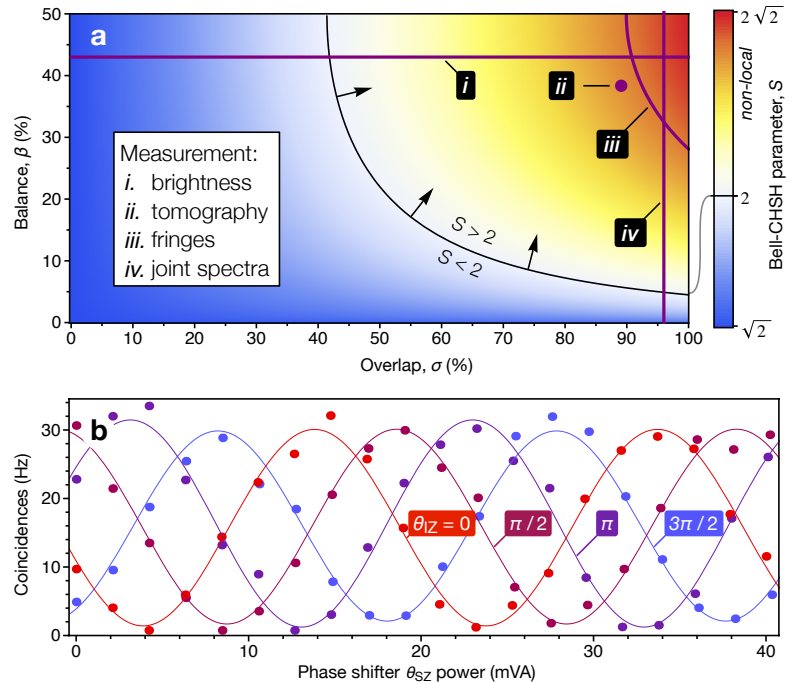
By pumping the source cavities with spectrally broad pulses, we relax the energy and momentum requirements of the SFWM process. The emitted signal and idler photons then naturally and independently take on the structure of the cavity enhancement, which has been predicted to improve their spectral separability². To quantify this, we measured the source joint spectral density (JSD) using *stimulated* four-wave mixing, via stimulated emission tomography^{4,5} (§2.3).

A narrow linewidth seed laser was swept across one resonance of each ring, and the stimulated FWM was collected by a spectrometer. The seed field was provided by an amplified tuneable laser with 10 kHz linewidth and a 600 MHz repeatability⁶. We reduced the launched seed power until no evidence of seed-induced optical bistability (§1.3.3) remained. The stimulated FWM signal was collected by a spectrometer with a 6-GHz resolution⁶.

Measured JSD profiles of the top and bottom sources are shown in FIGS. 4.3c,d, exhibiting $\sigma = 0.962$. Residual spectral entanglement is quantified by the Schmidt number K (§2.3). Since we only access the *magnitude* of the joint spectrum, we can put a lower bound on K . We measured $K > 1.19$ for the top source, and $K > 1.17$ for the bottom source, where $K = 1$ represents perfect spectral separability.

We used the transmission spectrum of each source resonator to inform a model

FIG. 4.5: Summary of measurements of Bell-CHSH inequality violation. **a**, Map showing violation S as a function of balance β and overlap σ , with listing of measurement results overlaid. When $S > 2$, the Bell-CHSH inequality is violated. By measuring: (i) the brightness of each source, we can estimate the balance β ; (ii) the quantum state, we can estimate both the balance β and the overlap σ ; (iii) correlated fringes, we directly estimate $S(\beta, \sigma)$; and (iv) the overlap between measured joint spectra, we obtain σ . Measurement (iv) naturally excludes multi-photon contamination, while measurements (i–iii) include it: these consequently result in lower values of σ . **b**, Fringes generated by \hat{R}_z rotations on signal and idler qubits, allowing a direct measurement of CHSH S parameter (denoted measurement (iii) in part **a**).



for the SFWM. This model^{2,7} takes in the cavity response, the pump lineshape, and the waveguide dispersion and provides a predicted JSD. **FIG. 4.3e** shows this prediction. Additionally, **FIG. 4.3e** reflects the resolution of our apparatus by including a Gaussian convolution—the spectrometer (low-resolution) measured the signal channel, while the laser (high-resolution) scanned the idler. The relative narrowness of the prediction as compared to the measured values (**FIGS. 4.3c,d**) could be due to the same stochastic broadening observed in the overlap measurement (**§4.2.1**).

4.2.3 Bell inequality violation

A well known test of quantum mechanical non-locality, as well as a very strict indicator of the entanglement present between two particles, is based on the formulation of Bell's original inequality due to Clauser, Horne, Shimony and Holt (CHSH). In this test, a parameter S —whose value indicates the presence of non-locality—is estimated based on a series of independent measurements on each particle⁸. Classically, the following inequality holds:

$$S \equiv |E(\mathbf{a}, \mathbf{b}) + E(\mathbf{a}', \mathbf{b}) + E(\mathbf{a}, \mathbf{b}') - E(\mathbf{a}', \mathbf{b}')| \leq 2. \quad (4.5)$$

where \mathbf{a} , \mathbf{a}' , \mathbf{b} , and \mathbf{b}' are independently chosen measurements on one of the two particles, and E represents the expectation value of their measurement. Truly quantum, non-local states can violate **EQ. 4.5**: S is actually bounded by $S < 2\sqrt{2}$ ^{8,9}. Furthermore, the *amount* of violation very strictly quantifies the particles' entanglement¹⁰.

Here, particles a and b are *qubits*, and their observables \mathbf{a} and \mathbf{b} are vectors on the Bloch sphere (**FIG. 1.3**). A measurement in the x -direction is a measurement of \hat{X} , and the same is true for (y, \hat{Y}) and (z, \hat{Z}) . A general measurement, projecting

on $\mathbf{a} = (x, y, z)$, can be written in spherical coordinates* as,

$$\begin{aligned}\hat{O}(\mathbf{a}) \equiv \mathbf{a} \cdot (\hat{\mathbf{X}}, \hat{\mathbf{Y}}, \hat{\mathbf{Z}}) &= \hat{X}x + \hat{Y}y + \hat{Z}z \\ &= \hat{X}\sin(\theta)\cos(\phi) + \hat{Y}\sin(\theta)\sin(\phi) + \hat{Z}\cos(\theta).\end{aligned}\tag{4.6}$$

$\hat{O}(\mathbf{a})$ is Hermitian, and represents a single-qubit observable which projects onto \mathbf{a} . We can write $E(\mathbf{a}, \mathbf{b})$ in terms of $\hat{O}(\mathbf{a})$ and $\hat{O}(\mathbf{b})$ and the spherical coordinates:

$$E(\mathbf{a}, \mathbf{b}) = \langle \hat{O}(\mathbf{a}) \otimes \hat{O}(\mathbf{b}) \rangle = \begin{cases} \langle \psi | \hat{O}(\mathbf{a}) \otimes \hat{O}(\mathbf{b}) | \psi \rangle & \text{pure state } |\psi\rangle \\ \text{Tr}\{\hat{\rho} \cdot \hat{O}(\mathbf{a}) \otimes \hat{O}(\mathbf{b})\} & \text{general state } \hat{\rho}, \end{cases}\tag{4.7}$$

where for the general state, we used Born's rule (EQ. 1.3). Later, in §4.2.4, we will use EQS. 4.7, 4.6, and 4.5 to compute S for various reconstructed states $\hat{\rho}_{\text{ex}}$.

At the edge of the chip, we measure the qubits with the operator $|00\rangle\langle 00|$. To project from $|0\rangle$ onto some state with Bloch spherical coordinates $\mathbf{a} = (\theta, \phi)$, we apply the rotation sequence $\hat{R}_z(\phi)\hat{R}_y(\theta)|0\rangle$. Thus, to project a qubit $|\psi\rangle$ onto $|0\rangle$, we must apply these rotations in reverse: $|\langle 0|\hat{R}_y(\theta)\hat{R}_z(\phi)|\psi\rangle|^2 = \langle \psi | \hat{O}(\mathbf{a}) | \psi \rangle$. The expectation values of a two-qubit $|\psi\rangle$ are then

$$E(\mathbf{s}, \mathbf{i}) = |\langle 00 | \hat{R}_y(\theta_{SY})\hat{R}_z(\theta_{SZ}) \otimes \hat{R}_y(\theta_{IY})\hat{R}_z(\theta_{IZ}) | \psi \rangle|^2.\tag{4.8}$$

which can be obtained by configuring the on-chip phases and measuring coincidences. This method is not restricted to measuring CHSH violations—it's a general prescription for measuring the on-chip state.

Now that we've made S concrete, we can explicitly calculate the value which results from $\hat{\rho}_{\text{th}}$ of EQ. 4.2, and quantify how the violation depends on the balance and source overlap (see §F.3):

$$S = \sqrt{2}(1 + 2\sigma\sqrt{\beta}\sqrt{1 - \beta}).\tag{4.9}$$

This is maximised, as expected, when $\sigma = 1$ and $\beta = 1/2$. EQ. 4.9 is plotted as a heat map in FIG. 4.5a, showing the entanglement implied by each part of this experiment.

One manifestation of the entanglement in our on-chip state (EQ. 4.2) is the non-local phase factor, Θ . As a result of this factor, \hat{R}_z rotations on each qubit cannot be observed independently: each equally contributes to the non-local phase. Experiencing this spooky behaviour in the lab was a highlight of my PhD. We configured the signal and idler \hat{R}_y rotations to mix the two modes of each qubit ($\theta_{SY} = \theta_{IY} = \pi/2$), then manipulated both θ_{SZ} and θ_{IZ} . We observed coincidence fringes with the non-local phase $\Theta = \theta_{SZ} + \theta_{IZ}$, shown in FIG. 4.5b. These fringes have mean visibility $V = 94.7 \pm 1.0\%$, consistent with a CHSH violation $S = 2.686 \pm 0.026$. This violates the inequality EQ. 4.5 by 83% and 26 standard deviations.

4.2.4 Tomography

Quantum state tomography is the process of experimentally estimating the state of a quantum system from the results of a set of measurements on it¹¹. This measurement set is informationally complete—"its statistics determine completely the

*Where θ and ϕ are the polar and azimuthal angles, respectively.

quantum state on which the measurement is carried out”¹². A state of q qubits has 2^{2q} degrees of freedom (**SB.4.1**), so for two qubits, our set needs at least 16 measurements to be informationally complete.

Early experiments used the *exactly complete* scheme of 16 measurements¹³, but this practice has been superseded by so-called ‘over-complete’ measurements¹⁴. The advantage of these is clear. Tomography is an exercise in multi-dimensional regression, or curve-fitting. Given a set of measurements, what model best describes the data? Relying on the complete measurement set amounts to fitting two points with a line—a clear *faux pas*. With only two points, we have no information about our measurement *apparatus*—is one measurement an outlier? Is one of our measurement settings out of calibration? With 16 measurements, we just don’t know. In this experiment, we used a set of 36 measurements, composed of a six-sided ‘cube,’ inscribed into the Bloch sphere of each qubit. The corresponding observables are are

$$\{\hat{O}_i\} = \left[|0\rangle\langle 0|, |1\rangle\langle 1|, |+\rangle\langle +|, |-\rangle\langle -|, |+i\rangle\langle +i|, |-i\rangle\langle -i| \right]^{\otimes 2}. \quad (4.10)$$

These observables are projectors—they project $\hat{\rho}_{\text{ex}}$ onto a given state, measuring their overlap. For example, a measurement of the projector $|++\rangle\langle ++|$ on $\hat{\rho}_{\text{th}}$ (**EQ. 4.2**), via Born’s rule (**EQ. 1.3**) gives

$$\text{Tr}\{\hat{\rho}_{\text{th}} \cdot |++\rangle\langle ++|\} = \frac{1}{4}(1 + 2\sigma\sqrt{\beta}\sqrt{1-\beta}\cos\Theta), \quad (4.11)$$

which—since Θ is double the applied phase—produces the time-reversed HOM fringes of **EXP. 1**. Notice that their visibility is unit when the source overlap and balance is perfect ($\sigma = 1, \beta = 1/2$).

Ideally, we’d like to make measurements which are evenly distributed throughout the state’s Hilbert space¹², but this would require *arbitrary* rotations on the state. In linear optics, we can only do arbitrary rotations on single-qubits, so we use a measurement set which is at least homogeneous in the space of separable measurements (**EQ. 4.10**).

Model states

So, each tomographic set constitutes 36 estimates of how $\hat{\rho}_{\text{ex}}$ behaves in different situations (**EQ. 4.10**). We could fit these data by assuming that $\hat{\rho}_{\text{ex}}$ looks just like $\hat{\rho}_{\text{th}}$ (**EQ. 4.2**), but this could blind us to other effects. What we do instead is use a model for a *general* state.

The Cholesky decomposition tells us that any Hermitian, positive-semidefinite matrix—like our $\hat{\rho}_{\text{ex}}$ —can be written as $\hat{\tau}\hat{\tau}^\dagger$, where $\hat{\tau}$ is lower triangular (see **SB.4.3**). Since, as discussed, our two-qubit state has 16 degrees of freedom, the 4 diagonal elements of τ can be real (the remaining 6 sub-diagonal elements are complex; $4 + 2(6) = 16$). To ensure $\hat{\rho}_{\text{ex}}$ is normalised, in practice we take

$$\hat{\rho}_{\text{ex}}(\hat{\tau}) = \frac{\hat{\tau}\hat{\tau}^\dagger}{\text{Tr}(\hat{\tau}\hat{\tau}^\dagger)}. \quad (4.12)$$

We then search for the state $\hat{\rho}_{\text{ex}}$ which best describes the data by minimising the sum squared of the error (just like in a regression). This is known as the constrained

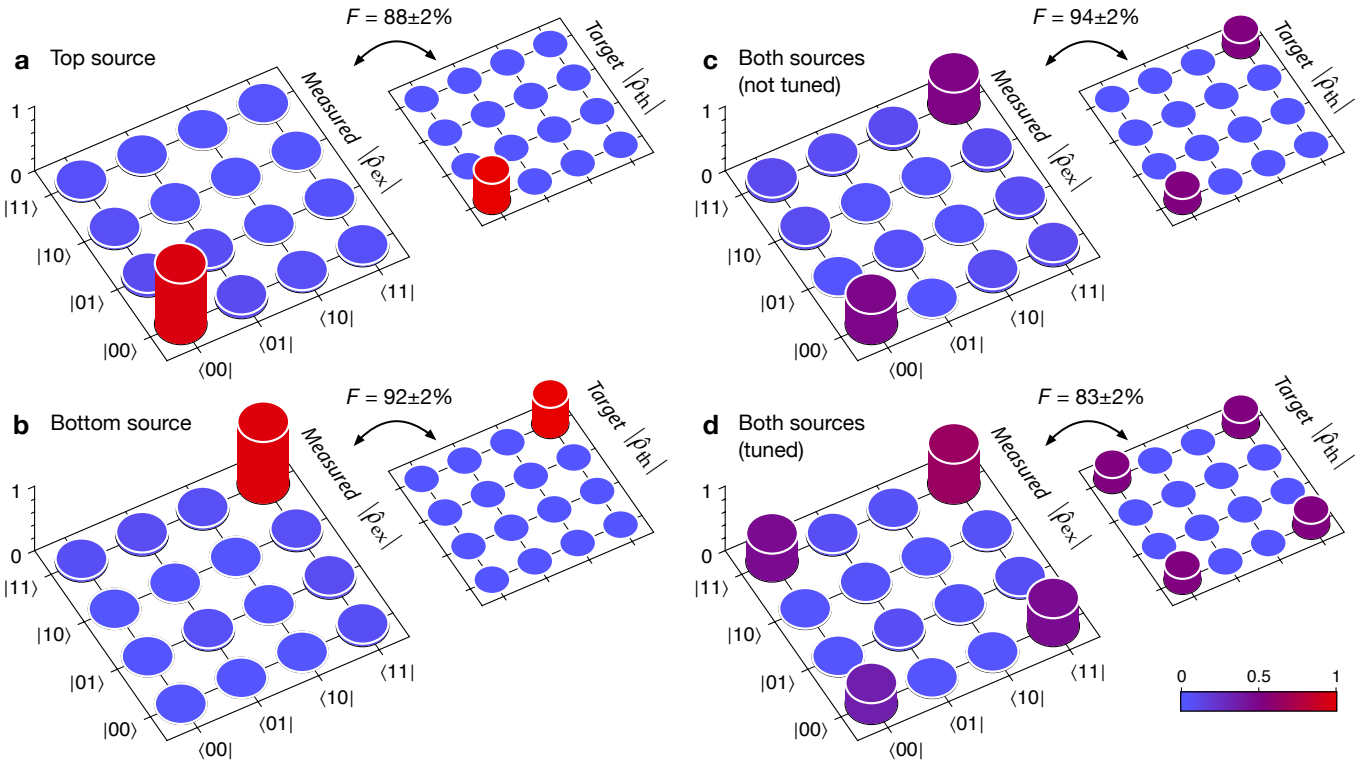


FIG. 4.6: Measured and target states for various device configurations. Configuration: **a**, top source only (bottom source detuned); **b**, bottom source only (top source detuned); **c**, both sources tuned but not overlapped, showing mixture; **d**, both sources tuned and overlapped, showing entanglement.

least-squares estimator*. If we define Π_i as the measurement result from the projection \hat{O}_i (EQ. 4.10), then the problem can be stated as

$$\hat{\tau} = \arg \min_{\hat{\tau}} \left\{ \sum_i |\Pi_i - \text{Tr}\{\hat{\rho}_{\text{ex}}(\hat{\tau}) \cdot \hat{O}_i\}|^2 \right\} \quad (4.13)$$

from which we can immediately obtain $\hat{\rho}_{\text{ex}}$, via EQ. 4.12. The experimentally obtained probabilities Π_i are derived from net coincidence counts X via

$$\Pi_i = \frac{X_i}{(4/N) \sum_i X_i}, \quad (4.14)$$

where $N = 36$ is the number of measurements in the set. The factor 4 arises from the fact that the result of four orthogonal projections on two qubits must be normalised (since there can *only* be four such projectors). With EQ. 4.14, the tomography process is now fully specified.

Measurements

We produced a series of on-chip states by using different configurations of source and filter tuning:

*In the presence of Gaussian noise on the data, the CLS estimator is equivalent to the more common maximum likelihood estimator. CLS is more robust to high-noise measurements, however, as it doesn't blow up for measurement results near zero.

- ❶ Separable states ($\beta \in \{0, 1\}$),
- ❷ Mixed states ($\beta = 1/2, \sigma = 0$)
- ❸ Entangled states ($\beta = 1/2, \sigma = 1$)

Manipulating both the source balance (β) and spectral overlap (σ), we observed changes in the resulting state in agreement with the predictions $\hat{\rho}_{\text{th}}$ of [EQ. 4.2](#). To compare the resulting estimates $\hat{\rho}_{\text{ex}}$ with the various predictions $\hat{\rho}_{\text{th}}$, we use the fidelity,

$$F = \text{Tr} \left\{ \sqrt{\sqrt{\hat{\rho}_{\text{ex}}} \cdot \hat{\rho}_{\text{th}} \cdot \sqrt{\hat{\rho}_{\text{ex}}}} \right\}^2, \quad \text{with} \quad \sqrt{\hat{\rho}_{\text{ex}}} = \hat{\tau}. \quad (4.15)$$

Fidelity is a measure of the distance between two states: $F = 1$ if they're identical, and $F = 0$ if they're orthogonal.

To prepare separable states ❶, we pumped either the top or the bottom source (by detuning the other one) and tuned its corresponding demultiplexer. Reconstructed states for tuned top and bottom sources are shown in [FIG. 4.6a](#) and [4.6b](#). These exhibit peaks in the pure, separable $|00\rangle$ and $|11\rangle$ components, as expected. We compute corresponding fidelities of $88 \pm 2\%$ and $92 \pm 2\%$.

Next, we pumped both sources, but didn't tune them to overlap. The reconstructed $\hat{\rho}_{\text{ex}}$ is shown in [FIG. 4.6c](#). It shows amplitude in both the $|00\rangle\langle 00|$ and $|11\rangle\langle 11|$ components—but not the coherence terms, $|00\rangle\langle 11|$ and $|11\rangle\langle 00|$ —making it a mixed state ❷. Optically, this is because photons produced in the top and bottom sources are different frequencies, and so don't interfere at the analysis interferometers. Indeed, the estimated state is mixed, with a purity of 0.49 ± 0.01 . Since this state is incoherent, we were able to use the filter lineshapes to balance the source brightness, achieving $\beta = 0.49$.

Finally, we tuned all four microrings to overlap, and measured the highly entangled state of [FIG. 4.6d](#), in which both sources are producing photons, and are mutually coherent ❸. We evaluated the Bell-CHSH S parameter for this state as $S = 2.692 \pm 0.018$. This violates the inequality [EQ. 4.5](#) by 83% and 38 standard deviations. It agrees nicely with our estimation based on correlated fringes ([FIG. 4.5b](#)).

Experimental uncertainty in each Π_i of [EQ. 4.13](#) was estimated from the residuals of several coincidence fringes, via [EQ. 4.14](#). We took this data and generated 500 mock experiments around each measurement set, sampling from the distribution we found from the fringes. We reconstructed the state for each of the 500, and found the distribution—and uncertainty—of each figure of merit (fidelity, S , etc.). This procedure is identical to that used in ref. [15](#).

§4.3 DISCUSSION

This device is the first to both generate entangled light *and* analyse it on-chip—a milestone in the evolution of quantum photonics. It was purpose-built to resolve the question, raised in [CH. 3](#), about the nature of the light produced by two coherently pumped sources: it's entangled. On-chip photon pairs easily passed the strictest test of entanglement—the Bell-CHSH test—expressing near-maximal quantum correlations. [FIG. 4.5a](#) summarises the Bell inequality violation implied by each measurement in this chapter; all measurements point to a very strong violation.

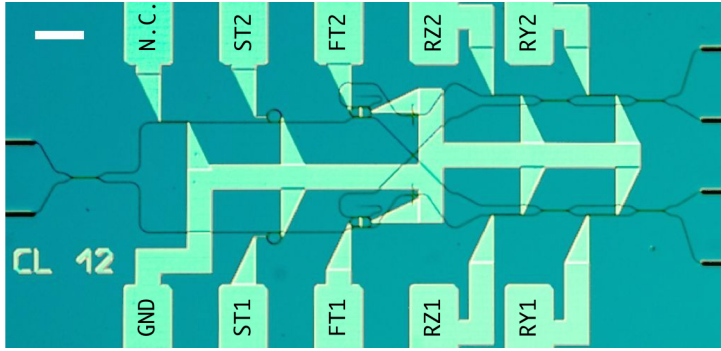


FIG. 4.7: Optical micrograph of the device studied in this chapter. A 100- μm scale bar is shown. Electrical connections are indicated: GND, ground; ST1 and ST2, source resonator tuning; FT1 and FT2, demultiplexer tuning; RZ1 and RZ2, qubit z-rotations; RY1 and RY2, qubit y-rotations; N.C., not connected, was used as the sense port for the crosstalk compensation ([§F4](#)).

New technology was needed to reveal this on-chip entanglement. Our experiment is among the first to leverage on-chip frequency-selective elements^{[16,17](#)}, and, furthermore, it does so in a phase-stable way, faithfully preserving entanglement. Our compact resonant demultiplexers performed acceptably, but the sharp phase response* in the pass-band of resonant demultiplexers like these have made *non-resonant* structures the weapon of choice going forward. Non-resonant structures (such as arrayed-waveguide gratings^{[16](#)}, waveguide Bragg gratings^{[17](#)}, or asymmetric Mach-Zehnder interferometers^{[18](#)}) lack this sharp phase response, tend to have lower loss, and are easier to fabricate. Moreover, they suffer no extra nonlinear effects, such as optical bistability ([§1.3.3](#)).

Resonant SFWM sources, in contrast with resonant demultiplexers, hold much promise. They can provide the spectral brightness needed to overcome SFWM generated elsewhere in a silicon quantum photonic device—we observed an order of magnitude less background SFWM than in [EXP. 1](#), in an even larger device. We showed in [§4.2.1](#) that they can also meet the second requirement of a photon-pair source: indistinguishability. We were able to overlap resonant photon pairs to a very high degree, a degree which—in the presence of multi-pair emission—was indistinguishable from unity. Finally, we were the first to apply the new stimulated emission tomography method to a resonant SFWM source. In fact, we were nearly the first team to measure the joint spectrum of a silicon source by *any* method; the first report, using conventional methods, was released only five months prior^{[19](#)}.

4.3.1 Source of entanglement

Entanglement is a property which arises in only very specific circumstances. In the single-pair regime, the squeezed state produced by each source is only slightly entangled (see [§D.4](#)). Since $\hat{\rho}_{\text{th}}$ is just a product of squeezed states, it should have no more entanglement than its constituent parts. So where does its (nearly maximal) entanglement come from?

In our derivation of $\hat{\rho}_{\text{th}}$ ([§F.1](#)), and indeed in our experiments, we *post-select* on measuring a coincidence—we ignore the very large vacuum part of the state. You can easily imagine that if we *could* measure vacuum at each laser clock, we would measure an awful lot of vacuum, and the correlations between signal and idler clicks would be drowned out. It's only once we ignore this vacuum that we see the strong correlations between photons.

*This phase response is a product of the Kramers-Kronig relations. See [FIG. C.3](#).

It would be surprising if any two naturally probabilistic sources—anywhere in the universe—pumped in phase, were intrinsically entangled. The Bell-type entanglement generated in this experiment—and, indeed, in any down-conversion-based entanglement scheme—is a product of our post-selection. However, its humble origin makes this entanglement no less real or potent.

Post-selection is the beating heart of linear quantum optics—it allows us to build entanglement *without interaction*. This insight lead Knill, Laflamme, and Milburn to their revolutionary discovery²⁰: “...passive linear optics does not involve particle interactions other than those imposed by statistics and can be understood in terms of classical wave mechanics. **There is, however, a hidden nonlinearity in LOQC (in the photo-detectors)** and our techniques effectively transfer this nonlinearity to the bosonic qubits, thus enabling universal quantum computation.”



ACKNOWLEDGEMENTS

Quantum state tomography and the Bell-CHSH test were implemented in collaboration with Mr. Raffaele Santagati. The joint spectral model of SFWM in a ring resonator is due to Dr. Damien Bonneau, adapted from the framework developed by Dr. Lukas Helt and Prof. John Sipe at the University of Toronto. Mr. Luka Milic helped with the JSD measurement. I'd like to thank Dr. Jake Kennard for stimulating discussions on the origins of entanglement in optics. The device was fabricated by Dr. Michael Strain in the group of Dr. Marc Sorel, at the University of Glasgow. I presented this work at CLEO:2014 (ref. 21). This work is published in Nature Communications (ref. 1).

REFERENCES

- [1] Silverstone, J. W. *et al.* Qubit entanglement between ring-resonator photon-pair sources on a silicon chip. *Nature Communications* **6**, 1–7 (2015). [\(67, 80\)](#)
- [2] Helt, L. G., Sipe, J. E., Yang, Z. & Liscidini, M. Spontaneous four-wave mixing in microring resonators. *Optics Letters* **35**, 3006–3008 (2010). [\(68, 72, 73\)](#)
- [3] Bell, B., McMillan, A., McCutcheon, W. & Rarity, J. On the effects of self- and cross-phase modulation on photon purity for four-wave mixing photon-pair sources. *arXiv.org* (2015). [1504.03776](#). [\(72\)](#)
- [4] Liscidini, M., Liscidini, M. & Sipe, J. E. Stimulated Emission Tomography. *Physical Review Letters* **111**, 193602 (2013). [\(72\)](#)
- [5] Eckstein, A. *et al.* High-resolution spectral characterization of two photon states via classical measurements. *Laser & Photonics Reviews* n/a–n/a (2014). [\(72\)](#)
- [6] For the stimulated emission tomography, we swept a Photoneics Tunics Plus tuneable laser (10 kHz linewidth, 600 MHz repeatability), and collected the emission with an Anritsu MS9740A optical spectrum analyser (6 GHz resolution). [\(72\)](#)
- [7] Bonneau, D. *Integrated quantum photonics at telecommunication wavelength in silicon-on-insulator and lithium niobate platforms*. Ph.D. thesis, Bristol (2013). [\(73\)](#)
- [8] Aspect, A., Aspect, A., Grangier, P., Grangier, P. & Roger, G. Experimental realization of Einstein-Podolsky-Rosen-Bohm Gedankenexperiment: a new violation of Bell's inequalities. *Physical review letters* (1982). [\(73\)](#)
- [9] Clauser, J., Horne, M., Shimony, A. & Holt, R. Proposed Experiment to Test Local Hidden-Variable Theories. *Physical Review Letters* **23**, 880–884 (1969). [\(73\)](#)
- [10] Bartkiewicz, K. *et al.* Entanglement estimation from Bell inequality violation. *Physical Review A* **quant-ph**, 052105 (2013). [\(73\)](#)
- [11] Leonhardt, U. & Leonhardt, U. Quantum-State Tomography and Discrete Wigner Function. *Physical Review Letters* **74**, 4101–4105 (1995). [\(74\)](#)
- [12] Renes, J. M., Blume-Kohout, R., Scott, A. J. & Caves, C. M. Symmetric informationally complete quantum measurements. *Journal of Mathematical Physics* **45**, 2171–2180 (2004). [\(75\)](#)
- [13] James, D. F. V., Kwiat, P. G., Munro, W. J. & White, A. G. Measurement of qubits. *Physical Review A* (2001). [\(75\)](#)
- [14] de Burgh, M., Langford, N., Doherty, A. & Gilchrist, A. Choice of measurement sets in qubit tomography. *Physical Review A* **78**, 052122 (2008). [\(75\)](#)
- [15] Shadbolt, P. J. *et al.* Generating, manipulating and measuring entanglement and mixture with a reconfigurable photonic circuit. *Nature Photonics* **6**, 45–49 (2012). [\(77\)](#)
- [16] Matsuda, N. *et al.* On-chip generation and demultiplexing of quantum correlated photons using a silicon-silica monolithic photonic integration platform. *Optics Express* **22**, 22831–22840 (2014). [\(78\)](#)
- [17] Harris, N. C. *et al.* Integrated Source of Spectrally Filtered Correlated Photons for Large-Scale Quantum Photonic Systems. *Physical Review X* **4**, 041047 (2014). [\(78\)](#)
- [18] Horst, F. *et al.* Cascaded Mach-Zehnder wavelength filters in silicon photonics for low loss and flat pass-band WDM (de-)multiplexing. *Optics Express* **21**, 11652–11658 (2013). [\(78\)](#)
- [19] Kumar, R., Ong, J. R., Savanier, M. & Mookherjea, S. Controlling the spectrum of photons generated on a silicon nanophotonic chip. *Nature Communications* **5**, 5489 (2014). [\(78\)](#)
- [20] Knill, E., Laflamme, R. & Milburn, G. J. A scheme for efficient quantum computation with linear optics. *Nature* **409**, 46–52 (2001). [\(79\)](#)
- [21] Santagati, R. *et al.* On-chip generation and analysis of maximal path-frequency entanglement. In *Conference on Lasers and Electro-Optics: Quantum Electronics and Laser Science - Fundamental Science*, paper FM1A.5 (San Jose, 2014). [\(80\)](#)

Chapter 5

Experiments 3 & 4

Two-qubit quantum logic

We have seen how the light emitted from synchronously pumped photon-pair sources is entangled ([Exp. 2](#)). We have also seen how erasing the path information from that state symmetrises it, making non-degenerate pairs mimic degenerate ones ([Exp. 1](#)). We have talked about how quantum gates in optics can be implemented via post-selection ([§1.1.3](#)). In this chapter we will explore how these ideas can be combined, and used to perform basic quantum information tasks with on-chip-generated quantum light, for the first time.

§5.1 BACKGROUND

5.1.1 Split pairs are indistinguishable

As we claimed—then experimentally tested—in [Exp. 1](#), split pairs from a time-reversed Hong-Ou-Mandel (RHOM) source precisely mimic monochrome photon pairs in any external interferometer. This a surprising result. The signal and idler photons which compose each split pair are strictly orthogonal in frequency—they could not interfere classically. Their *entanglement* enables this mimicry.

Beamsplitter

To demystify this effect, let's examine how a split pair behaves on a beamsplitter, in a HOM-dip configuration. Through a symmetric beamsplitter ([Eq. 1.10](#)) a signal photon in mode a and an idler photon in mode b evolve as:

$$\begin{aligned} a_s^\dagger b_i^\dagger &\rightarrow \frac{1}{2}(a_s^\dagger + ib_s^\dagger)(ia_i^\dagger + b_i^\dagger)|\mathbf{0}\rangle \\ &= \frac{1}{2}(ia_s^\dagger a_i^\dagger + a_s^\dagger b_i^\dagger - b_s^\dagger a_i^\dagger + ib_s^\dagger b_i^\dagger)|\mathbf{0}\rangle \end{aligned} \tag{5.1}$$

and similarly, if we swap the modes into which we inject each photon,

$$b_s^\dagger a_i^\dagger \rightarrow \frac{1}{2}(ia_s^\dagger a_i^\dagger - a_s^\dagger b_i^\dagger + b_s^\dagger a_i^\dagger + ib_s^\dagger b_i^\dagger)|\mathbf{0}\rangle. \tag{5.2}$$

In both cases, the two photons bunch and split randomly, as expected—they don't see each other. *However*, quantum mechanics is linear, so if we instead inject $|split\rangle$,

which is the sum of these two input cases, the result is the sum of the two outputs:

$$\begin{aligned}
|split\rangle &= \frac{1}{\sqrt{2}}(a_s^\dagger b_i^\dagger + b_s^\dagger a_i^\dagger)|0\rangle \\
&= \frac{1}{2\sqrt{2}}((ia_s^\dagger a_i^\dagger + a_s^\dagger b_i^\dagger) - (b_s^\dagger a_i^\dagger + ib_s^\dagger b_i^\dagger) + (ia_s^\dagger a_i^\dagger - a_s^\dagger b_i^\dagger) + (b_s^\dagger a_i^\dagger + ib_s^\dagger b_i^\dagger))|0\rangle \\
&= \frac{i}{\sqrt{2}}(a_s^\dagger a_i^\dagger + b_s^\dagger b_i^\dagger)|0\rangle.
\end{aligned} \tag{5.3}$$

This is the usual quantum interference result—the photons only bunch at the output, and no a - b coincidences occur. It happens because the various output configurations are indistinguishable, so they coherently interfere—the highlighted components cancel, and prevent splitting at the output. The zero-delay points in [FIG. 3.3](#) show exactly this behaviour.

Arbitrary interferometer

So $|split\rangle$ behaves like $|11\rangle$ in the specific case of a beamsplitter, but this is also true for a general interferometer. Following ref. 1, we can show that the frequency-entangled $|split\rangle$ state ([EQ. 3.8](#)) has the same behaviour as a monochromatic separable state. See [SE.4](#) for full calculations. Written with signal and idler modes denoted a and b , and the input spatial mode in subscript*, the two states are:

$$|separable\rangle \equiv |11\rangle = a_p^\dagger a_q^\dagger |0\rangle, \tag{5.4a}$$

$$|split\rangle \equiv \frac{1}{\sqrt{2}}(|1001\rangle + |0110\rangle) = \frac{1}{\sqrt{2}}(a_p^\dagger b_q^\dagger + a_q^\dagger b_p^\dagger) |0\rangle. \tag{5.4b}$$

A general N -mode linear optical network is encoded in a unitary \hat{U} . It has elements $U_{i,j}$ with $i, j \in [1, N]$. The two states evolve through \hat{U} as ([EQ. E.31](#))

$$|separable\rangle \rightarrow \sum_i \sum_{j < i} (U_{i,p} U_{j,q} + U_{j,p} U_{i,q}) a_i^\dagger a_j^\dagger |0\rangle + \sum_i U_{i,p} U_{i,q} (a_i^\dagger)^2 |0\rangle \tag{5.5a}$$

$$|split\rangle \rightarrow \sum_i \sum_{j < i} (U_{i,p} U_{j,q} + U_{j,p} U_{i,q}) \left[\frac{a_i^\dagger b_j^\dagger + a_j^\dagger b_i^\dagger}{\sqrt{2}} \right] |0\rangle + \sum_i U_{i,p} U_{i,q} \sqrt{2} (a_i^\dagger b_i^\dagger) |0\rangle. \tag{5.5b}$$

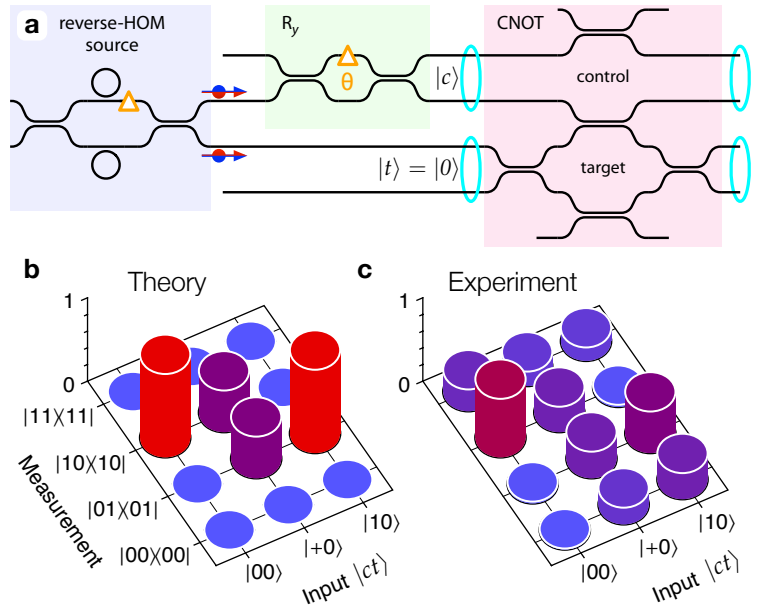
In both cases then, the chance to measure photons in modes i and j , provided our detectors don't distinguish between signal and idler frequencies, is the same:

$$P_{i,j} = |U_{i,p} U_{j,q} + U_{j,p} U_{i,q}|^2 \quad P_{i,i} = 2 |U_{i,p} U_{i,q}|^2. \tag{5.6}$$

If only one signal-idler configuration is measured, then the split state probabilities of [EQ. 5.6](#) suffer a post-selection penalty of $1/2$.

*We require $p \neq q$ since we're talking about the $split$ states. [EQ. 5.4](#) isn't normalised if $p = q$.

FIG. 5.1: Device of [Exp. 3](#) integrating a photon-pair source and an optical quantum gate for the first time. **a**, Device schematic. **b**, **c**, Expected and measured truth tables (computational basis measurements).



Experiment 3: Source & entangling gate

SFWM sources do not readily produce photon pairs in separate modes, unlike bulk SPDC sources. Leveraging the time-reversed HOM effect, however, we can make this happen ([CH. 3](#)). Additionally, we saw in [§5.1.1](#) how *non-degenerate* photons from an RHOM source mimic truly degenerate pairs. Non-degenerate pairs use the more efficient forwards SFWM process, and additionally require only one pump laser, making them practically simpler to produce. The time is ripe, then, to combine these effects, and build devices which use photons generated on chip to power quantum information experiments.

Here, I present the first chip-scale device to integrate a source of quantum light with an optical quantum gate. This work was presented at Frontiers in Optics in 2013². Several issues hindered the device's performance, however, and the experiment ultimately failed to meet expectations. Despite this, valuable lessons were learned, and these helped tremendously in the long run. Chronologically, this experiment preceded [Exp. 2](#).

§5.2 OPERATION

5.2.1 Ideal operation

The experiment is pictured in [FIG. 5.1a](#). It directly implements the idea of combining on-chip-generated photon pairs with a quantum gate. An RHOM source (with ring resonators) produces the state $|split\rangle$, and feeds these photons into the control and target qubits of a post-selected CNOT gate (refs. 3,4, [§1.1.3](#), and [§B.7.2](#)). To probe states outside the computational basis (00, 01, 10, 11), we added a y -rotation on the control qubit $|c\rangle$, while the target qubit $|t\rangle$ was kept fixed:

$$|c\rangle = \hat{R}_y(\theta)|1\rangle = \cos \frac{\theta}{2}|0\rangle - \sin \frac{\theta}{2}|1\rangle, \quad |t\rangle = |0\rangle. \quad (5.7)$$

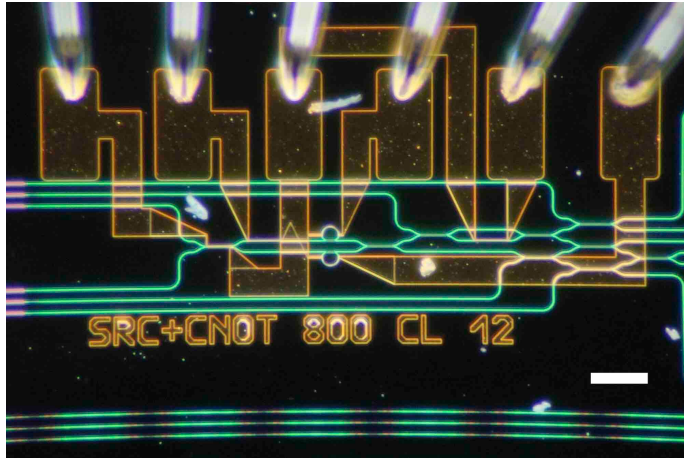


FIG. 5.2: Optical micrograph of the device of [Exp. 3](#), with pump input to one of centre waveguides at right, and qubit output from the four centre waveguides at right. A 100 μm scale bar is shown.

The output state from the post-selected CNOT, then is

$$|ct\rangle \rightarrow \cos \frac{\theta}{2} |01\rangle - \sin \frac{\theta}{2} |10\rangle = \begin{cases} |01\rangle & \theta = 0 \\ |\Phi^-\rangle & \theta = \pi/2 \\ |10\rangle & \theta = \pi. \end{cases} \quad (5.8)$$

So the device (in principle) produces an entangled state when $\theta = \pi/2$. Unfortunately, one lesson learned from this device was the need for analysis interferometers—we could only measure the output in the computational basis, and had no way of knowing its coherence properties. Measuring in the computational basis, then, we would expect:

$$\Pi_{00} = \Pi_{11} = 0, \quad \text{and} \quad \Pi_{01} = 1 - \Pi_{10} = \cos^2(\theta/2). \quad (5.9)$$

Following Boolean nomenclature, this ideal ‘truth table’ is shown in [FIG. 5.1b](#), for $\theta \in \{0, \pi/2, \pi\}$.

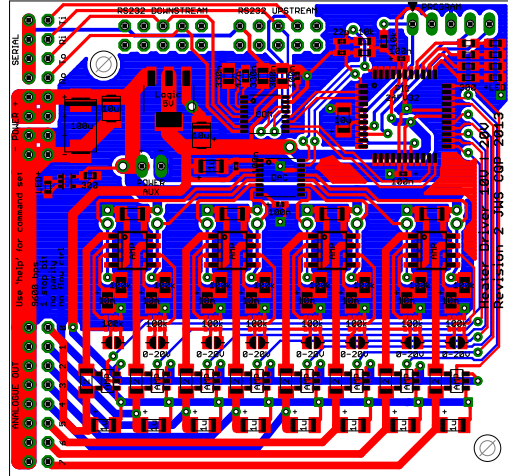
5.2.2 Actual operation

The experiment looks—at least in principle—fair. We must simply rotate the control qubit using θ , and collect computational basis measurements. The omission of an analysis stage was a design oversight, but not a fatal one. However, as I have alluded to, this experiment foundered under the vast weight of practicality.

Having only four electrical degrees of freedom (θ , the RHOM phase, and a tuner for each ring), we controlled the device in the same manner as we did in [Exp. 1](#)—with stand-alone electrical power supplies. We had only one programmable supply, so we swapped this back and forth between the two phase shifters when we needed to collect fringes. The other power supplies were controlled the old-fashioned way—with a volume knob. Since, in principle, the experiment only called for one degree of freedom to be actively manipulated (θ), this was OK.

I calibrated the device and collected the normalised data of [FIG. 5.1c](#). Comparing [FIGS. 5.1b](#) and [5.1c](#), it’s evident that something inside the device was not right. Upon further investigation, I found that the closed CNOT interferometer wasn’t phase-balanced. If it were balanced, bright light injected in one of the ports of the

FIG. 5.3: First deployed revision of my ‘heater driver’ board. It interfaces eight 12-bit voltage sources with a computer, via RS-232. It contains sophisticated over-voltage and over-current protections. At the time of writing, this device is in widespread use throughout the Bristol group.



target qubit would emerge entirely from the opposite output port ($|0\rangle \leftrightarrow |1\rangle$). Instead, roughly 70% did this, and the remaining 30% leaked out from the wrong port. Coupler reflectivity also affected performance: I measured 60% reflectivity on the ‘33%’ couplers, and 41% on the ‘50%’ ones. Finally, I discovered significant electrical crosstalk between the microring sources, and the frequently-adjusted phase shifters. This lead to different source overlaps at different values of θ . All these factors will have contributed to the behaviour observed in [FIG. 5.1c](#).

Three long months of experimentation, and two devices later, the manual power supply sealed this experiment’s fate. Eventually, swapping power supplies, and manually controlling voltages lead to a catastrophic heater failure on both copies of the device.

§5.3 LESSONS

The failure of this experiment was particularly instructive. Since it occurred before [EXP. 2](#), several of these solutions were implemented there. The remainder are taken up by the next experiment, this one’s true successor, [EXP. 4](#).

① Electronic control

Poor control over the device’s electrical degrees of freedom ultimately caused this experiment to fail. In particular, the voltage sources we were using exhibited significant over-shoot problems, and had insufficient protections. Also, as devices become more electrically sophisticated, stacking up PSUs is not a scalable solution.

Commercial solutions for multi-port electrical control are either expensive, or insufficiently powerful. Following this experiment, I spent some time coming up with a scalable solution. The circuit board layout of the first version of my ‘heater driver’ is pictured in [FIG. 5.3](#). This hardware was used in [EXP. 2](#) and [EXP. 4](#). It is also becoming important to other work (e.g. ref. 5).

② Crosstalk

Silicon ring resonators shift by 70 pm, or about half a resonant linewidth, per Kelvin change in temperature. A typical heater ([§1.3.2](#)) achieves about 5 K/mW, so a half-linewidth shift requires a change in heater power of only 200 μ W. Electrical and thermal crosstalk meant that the device’s resonators tended to drift, depending on the phase required elsewhere.

To circumvent this in [Exp. 2](#), I implemented a negative-feedback loop to control the voltage of the on-chip common ground. This worked well, but required a spare connection to the on-chip ground for sensing. See [§F.4](#) for details.

③ Avoid moving fibres

To access all the computational basis measurements, we had to move the output lensed fibres. This made the normalisation of the resulting coincidence counts into probabilities challenging. In the next experiment, we circumvent this by including a MZI at the output of each qubit, which allows us to examine each of the qubits’ two output modes by simply changing the interferometer’s phase.

④ Truth table versus density matrix

If we had had access to coherent measurements in this experiment, we would have gained significantly more information about the device’s operation and its output state. We could have determined whether our CNOT gate was modifying the state’s entanglement. Incidentally, coherent measurements would have alleviated the previous fibre-movement-related problem as well.

⑤ Closed CNOT versus open CSIGN

A random phase inside the closed CNOT interferometer caused much grief here. To avoid this phase, the next experiment uses the equivalent—but interferometrically open—CSIGN entangling gate. The CSIGN gate is also structurally simpler than the CNOT, having two fewer beamsplitters.

⑥ Filtering: ease versus efficiency

This was the last experiment in which we used fibre Bragg gratings (FBG) for pump cleaning and rejection. FBGs offer lower loss, at the expense of lower rejection. They also degrade under visible light. Accordingly, in subsequent experiments we exclusively use AWG input and output filters, which are pre-aligned and accomplish all necessary filtering in one optical element.

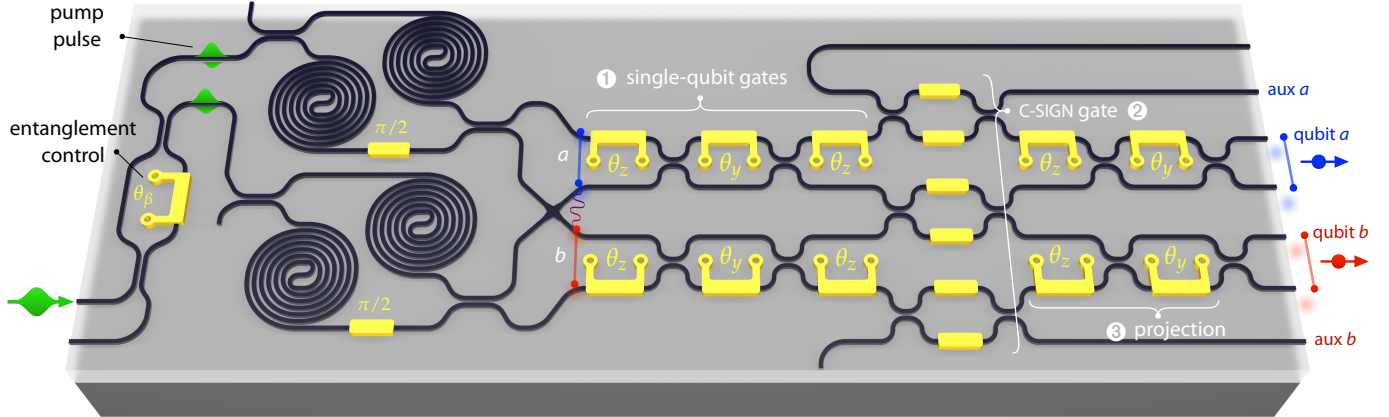


FIG. 5.4: Schematic of the [Exp. 4](#) device. It produces two variably entangled qubits, and can arbitrarily entangle (or disentangle) them. Numbered labels are referred to in the main text.

Experiment 4: Disentanglement

The last experiment ([Exp. 3](#)) was ambitious: it combined an on-chip source of separable photonic qubits with a quantum logic gate, and used the interference between resonant SFWM sources, all for the first time. In this final experiment we act on the lessons of [Exp. 3](#), and take these ideas one step further, but this time with more success.

Entanglement forms the basis for many quantum information advantages, and is essential for the non-classical behaviour in these systems⁶. The ability to entangle and disentangle a quantum state forms the basis of the well known quantum phase estimation algorithm⁷, which itself is at the heart of Shor’s quantum algorithm for factoring numbers⁸. The ability to coherently create and destroy entanglement is thus a key requirement for any integrated quantum device, composed of photons or otherwise.

Disentangling a pair of quantum bits requires the application of a two-qubit gate. If those qubits are stored in photons, then a (post-selected) two-qubit gate requires those photons to interfere quantum mechanically—they must be indistinguishable. In this experiment, I show how an on-chip state of *entangled* qubits, comprised of indistinguishable photons, can be produced using non-degenerate photon pairs. The photons’ indistinguishability is confirmed by their interference inside a two-qubit optical quantum gate. After [Exp. 3](#), this is the second time a two-qubit gate has been applied to an on-chip-generated state of photonic qubits.

§5.4 DESIGN

I showed in [Exp. 2](#) how on-chip phase-stable photon-pair sources can be used to produce path entanglement. The resulting photons in that experiment were strictly distinguishable in frequency, however. Here, I show a new source design which can produce two-qubit states with *any* level of entanglement, composed of photons which are non-degenerate but indistinguishable.

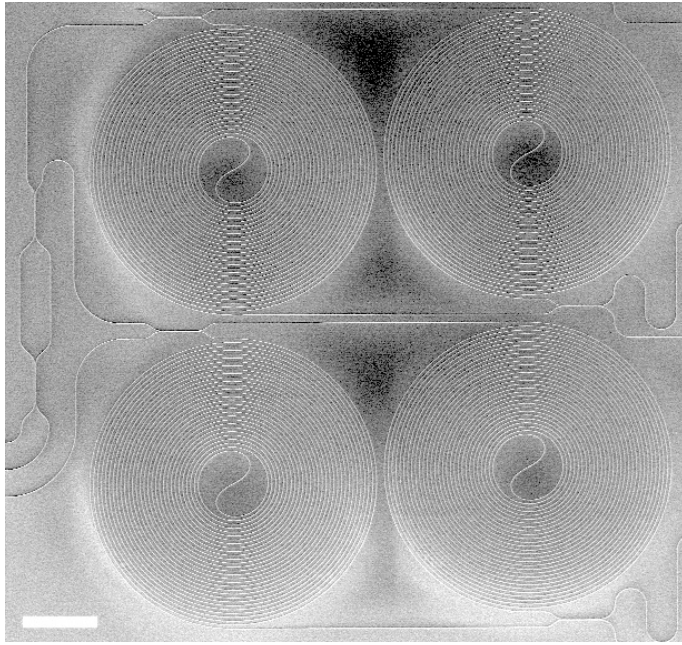


FIG. 5.5: A scanning electron micrograph taken during fabrication of the spiralled sources used in **EXP. 4**. A 100- μm scale bar is shown. Microscopy credit: Michael Strain.

5.4.1 Source

Two entangled qubits were sourced from a pair of reversed-HOM structures, as shown schematically in **FIG. 5.4**. I showed in **S5.1.1** that non-degenerate pairs from these structures behave as if they were degenerate; this applies to all photon pairs in this experiment, so I will use the simpler degenerate notation from now on, referring to this type of pair as ‘pseudo-degenerate’. Each RHOM structure, with its internal phase set to $\pi/2$, produces pseudo-degenerate photons in two modes,

$$|\text{RHOM}\rangle = |\mathbf{0}\rangle + \xi|\mathbf{1}\rangle. \quad (5.10)$$

As in previous experiments, the vacuum here composes the bulk of the state, with $\xi \ll 1$. Occasionally a pair is produced, and each photon of that pair emerges in a different mode. Since our two RHOM sources are independent, their joint state is just a tensor product:

$$|\text{RHOM}_t\rangle \otimes |\text{RHOM}_b\rangle = |\mathbf{0}\rangle + \xi_t|\mathbf{1100}\rangle + \xi_b|\mathbf{0011}\rangle + \mathcal{O}(\xi_t\xi_b), \quad (5.11)$$

where t and b indicate top and bottom RHOM sources, respectively. We can immediately see that **EQ. 5.11**, when post-selected on coincidences and pumped weakly ($\xi_t\xi_b \ll \xi$), will produce the same flavour of entanglement as in **EXP. 1** and **EXP. 2**. Performing this post-selection, neglecting higher-order terms, and swapping the middle two modes (see **FIG. 5.4**), we obtain the source’s qubit output state,

$$|\psi_{\text{src}}\rangle = \xi_t|\mathbf{1010}\rangle + \xi_b|\mathbf{0101}\rangle = \xi_t|\mathbf{00}\rangle + \xi_b|\mathbf{11}\rangle. \quad (5.12)$$

The *entanglement* between the two qubits can be controlled by adjusting the squeezing of the two sources, ξ_t and ξ_b : when either squeeze parameter is zero, the state is separable, and when $|\xi_t| = |\xi_b|$, it’s maximally entangled.

The level of squeezing depends on the pumping power. Since we’re expressly dealing with weak squeezing, we can use a simple description for the squeeze parameters: $\xi_i \propto P_i$ (with $i \in \{t, b\}$; **EQ. 2.5**, **TABLE 2.1c**). Cleverly, the device includes

a mechanism to vary the power delivered to each source, via the phase shifter θ_β (see [FIG. 5.4](#)). Using θ_β , the power delivered to the top (t) and bottom (b) source is

$$P_t = P_0 \sin^2(\theta_\beta/2) \quad P_b = P_0 \cos^2(\theta_\beta/2), \quad (5.13)$$

for a total pump power of P_0 . Thus, the normalised state from the source, as a function of θ_β , is

$$|\psi_{\text{src}}\rangle = \frac{\sin^2(\theta_\beta/2) |00\rangle + \cos^2(\theta_\beta/2) |11\rangle}{N} \quad (5.14)$$

with normalisation factor* N , which depends on θ_β . As with the source in [EXP. 2](#), $|\psi_{\text{src}}\rangle$ is in the family of maximally entangled Bell states ([§1.1.4](#)) when $\theta_\beta = \pi/2$; it is separable when $\theta_\beta \in \{0, \pi\}$.

5.4.2 Quantum logic

After the source, the device's remaining interferometers form a two qubit quantum circuit. This circuit contains: ① an arbitrary rotation on each qubit ([§1.1.1](#)); ② an on-off-switchable two-qubit CSIGN gate; and ③ a final rotation on each qubit to allow arbitrary projective measurements. These elements are indicated on [FIG. 5.4](#).

Arbitrary single-qubit rotations are implemented by a MZI (\hat{R}_y) bracketed by phase shifters (\hat{R}_z), with the ensemble producing a single-qubit rotation[†]

$$\hat{R}_z(\theta_{z2}) \cdot \hat{R}_y(\theta_y) \cdot \hat{R}_z(\theta_{z1}), \quad (5.15)$$

where θ_{z1} is the first phase shifter the photon sees, and θ_{z2} is the last one, with θ_y bracketed by two symmetric beamsplitters (see [FIGS. 5.4](#), and [1.4](#)).

The two-qubit switchable CSIGN gate³ is the same one described in [§1.1.3](#), with an MZI in place of each asymmetric beamsplitter. Note that an MZI composed of *symmetric* beamsplitters acts as a single *asymmetric* beamsplitter, with reflectivity $\eta = \sin^2(\theta/2)$. The operation of this post-selected gate is detailed in [§B.7.2](#). The vacuum modes of this gate give us access to useful auxiliary outputs inside the interferometer; these are marked on the right side of [FIG. 5.4](#).

Finally, single-qubit projective measurements are implemented in the same way as in [EXP. 2](#), allowing a tomographic reconstruction of the on-chip state. These measurements use the final two \hat{R}_z and \hat{R}_y rotations on each qubit. Notice as well that we can use the single-qubit rotations (①), and the auxiliary outputs to tomographically reconstruct the state directly from the source.

5.4.3 Device structure

The device has fabrication technology in common with the devices of both [EXP. 2](#) and [EXP. 3](#). It was manufactured using electron-beam lithography on a silicon-on-insulator wafer with a 220-nm slab. Its strip waveguides are 500-nm wide. Each of its four photon-pair sources is a 22 mm spiral of this waveguide; an electron micrograph of these spirals is shown in [FIG. 5.5](#). The sixteen electrical degrees of

*With $N = \sqrt{\sin^4(\theta_\beta/2) + \cos^4(\theta_\beta/2)}$.

[†]This is the same as [EQ. B.28](#), with $\alpha = \frac{i}{2}(\theta_{z1} + \theta_y + \theta_{z2} + \pi)$, $\beta = -\theta_{z2}$, $\gamma = \theta_y$, and $\delta = -\theta_{z1}$.

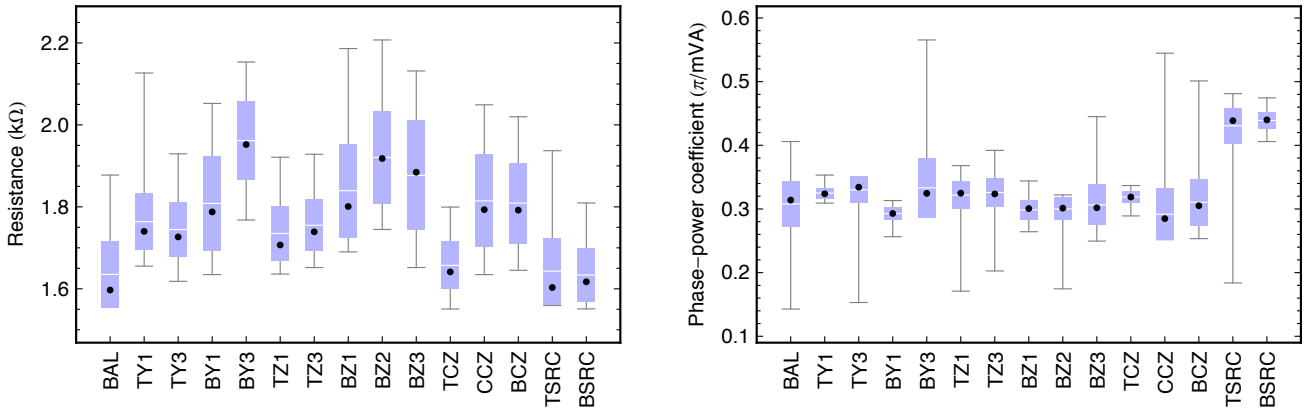


FIG. 5.6: Phase shifter statistical parameters over the five-month span of the experiment. The resistance (left) and phase-power coefficient (right) of each phase shifter were calibrated frequently, and the mean (white line), median (black dot), standard deviation (coloured box), and extrema (grey bars) describe their distributions. No significant drift in either coefficient was observed, so the measurements are taken to be independent. Phase shifter TZ2 failed, and is omitted. Source heaters TSRC and BSRC have a curved geometry, different to the others. All other heaters were $54\ \mu\text{m}$ long, $0.9\ \mu\text{m}$ wide, and $0.2\ \mu\text{m}$ thick nickel-chromium, separated from the waveguide by $0.9\ \mu\text{m}$, and connected via gold traces.

freedom (phase shifters) are again controlled thermally, using two copies of the control electronics developed following [Exp. 3](#) (shown in [FIG. 5.3](#)). Finally, spot-size converters coupled pump light and single photons on and off the chip.

§5.5 RESULTS

5.5.1 Source performance

First, we commissioned the device's two RHOM photon-pair sources. Neither source exhibited the very high visibility quantum interference observed in [Exp. 1](#), but both performed acceptably: we observed 96.5% and 84.3% photon splitting probability for the top and bottom sources, respectively ([FIG. 5.7](#)). Each visibility is affected by deviations from $\eta = 50\%$ in the input evanescent coupler, and by

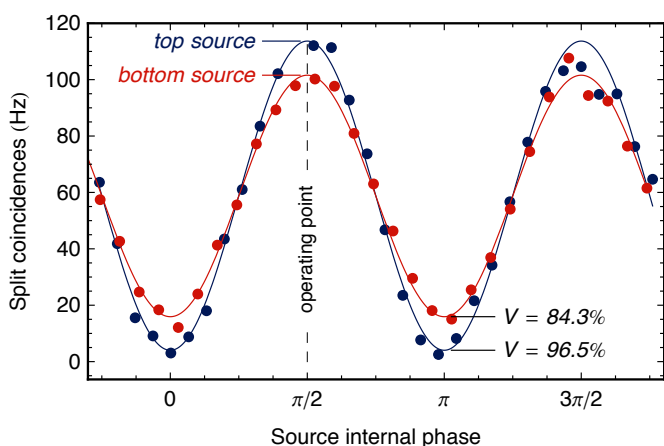
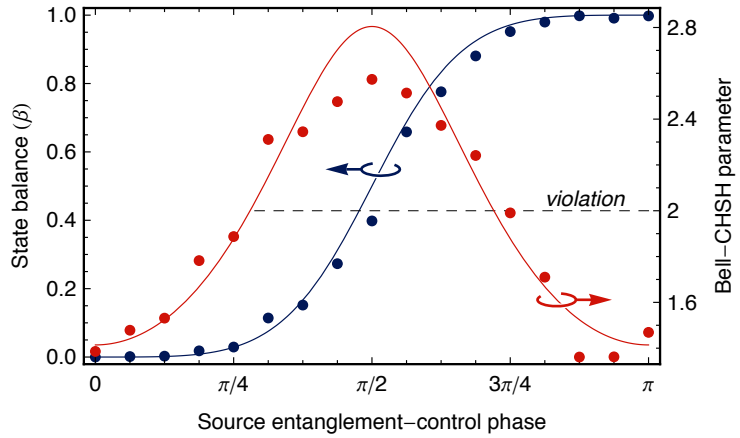


FIG. 5.7: Splitting fringes produced the top and bottom time-reversed HOM sources. Visibilities V are indicated. Each is configured to produce split pairs, at $\pi/2$.

FIG. 5.8: Effect of the entanglement-control phase on the state’s balance, and Bell-CHSH violation. The balance β closely follows a model quadratic SFGM power dependence (see CH. 2) superimposed as a line. The Bell-CHSH parameter S (see §4.2.3) violates the classical bound $|S| < 2$ for a wide range of phase values.



differences in brightness between the two interfering spiralled sources. Generation in the input and output waveguides also has a small effect. Assuming that the reduced visibility is due solely to input coupler imbalance, these values are consistent with reflectivities of $\eta_{\text{top}} \approx 40\%$ and $\eta_{\text{bot}} \approx 30\%$, for the two sources.

Initial measurements of the spectral brightness of the lumped RHOM sources indicate an (input-power-referenced) efficiency of $300 \pm 100 \text{ Hz/GHz/mW}^2$. This rough value compares favourably with the 22 Hz/GHz/mW^2 produced in EXP. 1 (§3.3.4), considering the $\times 4.4$ increase in source length here, and the L^2 dependence of bandwidth-limited SFGM (§2.2). After escaping the device’s 30 dB insertion loss, surviving photons yielded measured coincidence rates of up to 50 Hz.

Using the on-chip analysers, we could measure the balance β in the sourced entangled state: $|\psi_{\text{src}}\rangle = \sqrt{\beta}|00\rangle + \sqrt{1-\beta}|11\rangle$, where β is the fraction of all pairs generated in the top RHOM source*. These data are shown on the left axis of FIG. 5.8. They agree well with the model of EQ. 5.14, with $\beta = \sin^4(\theta_\beta/2)/N^2$, where θ_β is the source entanglement-control phase, which controls the pump delivered to each of the two sources (see EQ. 5.13, FIG. 5.4). We also monitored the entanglement present between the two qubits as the balance was varied, again using the CHSH parameter as an entanglement metric (§4.2.3); these values are shown on the right axis of FIG. 5.8. As expected, the entanglement peaks when $\beta = 1/2$ and returns to its separable state value of $\sqrt{2} \approx 1.4$ when $\beta \in \{0, 1\}$. The quantum state tomography used to obtain these values is described in the next section.

5.5.2 Tomography

We configured the chip to perform several representative functions, resulting in corresponding output states. These states were reconstructed via an over-complete quantum state tomography identical to that used in CH. 4. Direct measurements on the source were implemented using the single-qubit-rotation interferometers (❶), with coincidences collected between the auxiliary ports of each qubit (see note 9; FIG. 5.4). Measurements which included the switchable CSIGN gate were implemented by the final ‘projection’ interferometers on each qubit (❷, FIG. 5.4).

In each measurement configuration—direct, or through the gate—we examined

*Compare this to Eqs. 5.14, 4.2. The balance β is the same as in EXP. 2 (see EQ. F6).

states with nominal balances of $\beta = 1/2$ and $\beta = 1$, which are respectively entangled and separable. In the through-the-gate measurements, we examined the effect of turning the gate on and off. Measurements from these configurations are shown in [FIG. 5.9](#), alongside the quantum circuit representation of each. Note that, since the CSIGN gate acts on the *phase* of the qubits' joint state, we must consider the gate's action on the *argument* of the resulting density matrices. For this reason, I show both $|\hat{\rho}|$ and $\arg[\hat{\rho}]$ for the measurements involving the active gate ([FIGS. 5.9e,f](#)), rather than just the magnitude as in the other measurements.

TABLE 5.1: Figures of merit for the states produced in [EXP. 4](#). \mathcal{P} , the purity; K , the Schmidt number; and $|S|$, the CHSH parameter.

Estimated state	Fig.	\mathcal{P}	K	$ S $
Separable source (11) direct	5.9b	1.00	1.00	1.44
Separable source (11) transmitted	5.9d	0.97	1.02	1.57
Separable source (00) direct	...	1.00	1.01	1.57
Separable source (00) transmitted	...	0.95	1.03	1.44
Entangled source direct	5.9a	0.88	1.92	2.59
Entangled source transmitted	5.9c	0.85	1.95	2.57
Entangling gate	5.9f	0.88	1.69	2.49
Disentangling gate	5.9e	0.92	1.15	1.97

Figures of merit for the various measurements are shown in [TABLE 5.1](#): purity, \mathcal{P} ; Schmidt number, K ; and CHSH parameter, $|S|$. Ideally, all states would be pure ($\mathcal{P} \approx 1$); separable states would have $K \approx 1$, and $|S| \approx \sqrt{2} \approx 1.41$; and maximally entangled states would have $K \approx 2$, and $|S| \approx 2\sqrt{2} \approx 2.83$. The source performed very well, with direct measurements on separable and entangled configurations aligning closely with these targets. Measurements looking through the 'off' gate preserved this performance. When the gate was 'on', it qualitatively produced the desired effects—entangling a separable state, and disentangling an entangled state. However, neither its entanglement nor its disentanglement were maximal, with $K = 1.69 < 2$, and $K = 1.15 > 1$, respectively. All states were quite pure.

§5.6 DISCUSSION

This experiment relied strongly on a sophisticated semi-automatic calibration procedure (see note 10). Due to the significant insertion loss, integration times on the order of 10 s were needed, leading to 10-minute tomographic reconstructions. Though these were faster than in the other experiments of this thesis, the added complexity of this device (16 DOFs) meant that a brute force strategy for finding the correct operating point was not possible. The same finger-type electrical probes were used as before, but this time their unstable contact resistance meant the device needed full recalibration at least once per day (see right side of [FIG. 5.6](#)). This was somewhat eased by the automated calibration procedure¹⁰. When feedback on the single-photon behaviour was necessary, however, brute force parameter searches were still needed—the source parameter θ_β , and the CSIGN reflectivities were optimised for each relevant measurement.

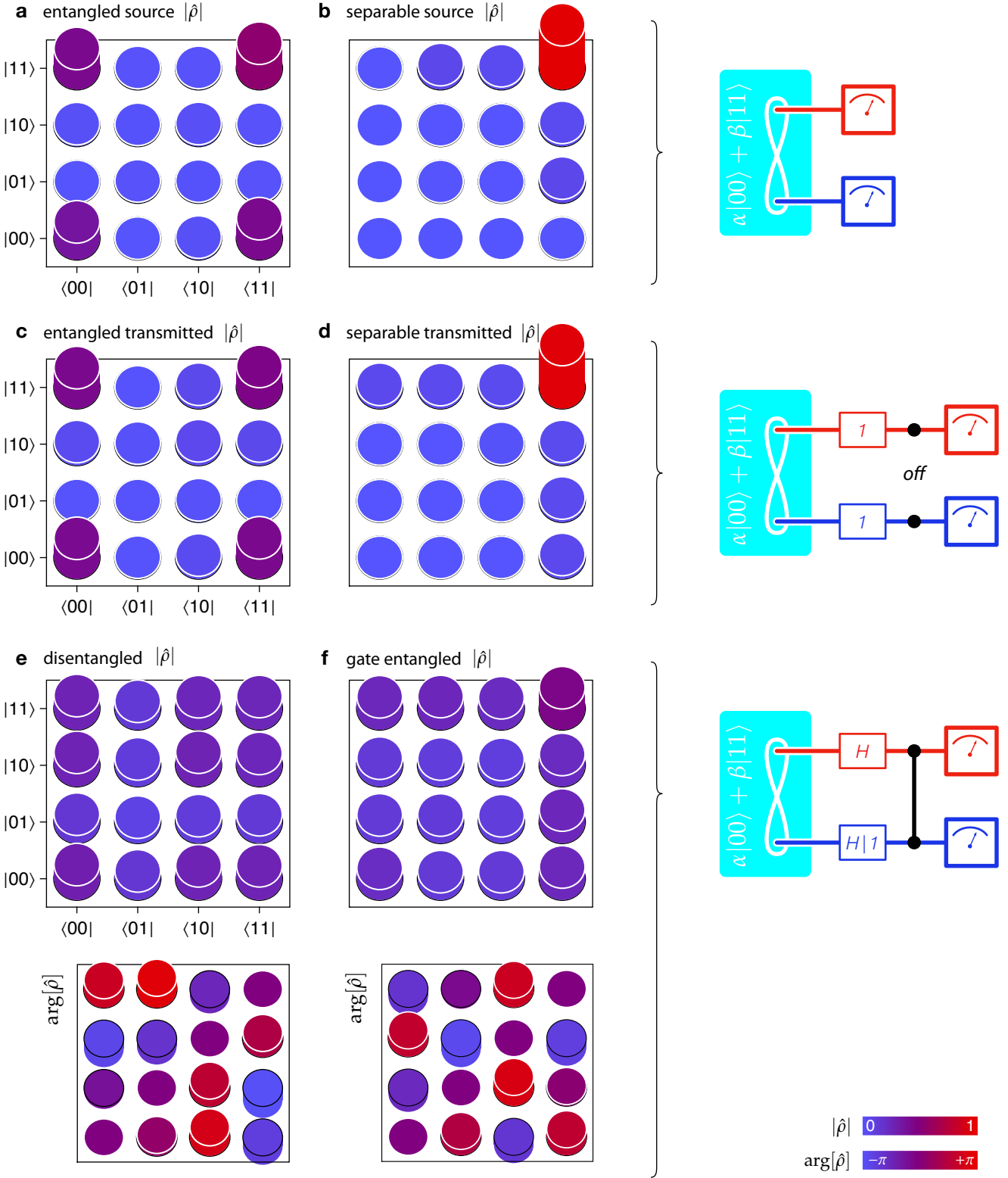


FIG. 5.9: Estimated states for various configurations of the device's variably entangled two-qubit source, and on-off CSIGN gate. Density matrices are shown in modulus. **a, b**, Entangled and separable states measured directly from the source (via auxiliary outputs); and **c, d**, the same states transmitted through the *off* CSIGN gate. **e, f**, Entangled and separable states (rotated to the x -basis by Hadamard gates) which are respectively disentangled and entangled, as evidenced by their phases, shown below. Colour codes are shown for both modulus and phase matrices.

Source performance was generally very good: the two-qubit source was able to produce both separable and entangled two-qubit states with high fidelity. For the direct measurements on the source output state, we were able to simply fix the intra-source phases ($\pi/2$) and optimise θ_β for the desired output state. The resulting performance validates the use of non-degenerate photon pairs to produce indistinguishable qubits, and encourages the use of this configuration in future experiments.

Compared to the source, the post-selected CSIGN gate performed less well. Two factors were to blame: the gate's post-selection meant that the coincidence rate through the active gate was reduced by a factor of 9, slowing optimisation; and the gate has effectively three degrees of freedom affecting its performance, each of which required careful tuning¹¹. Together, these difficulties meant that the gate's operation couldn't be finely tuned, though I'm confident that with more stability, or faster collection (lower loss), this could be overcome.

Ultimately, to scale up these devices, unconditional electro-optic stability is needed. Good electrical connections are a low-hanging fruit in this area: robust, metallurgical electrical joints (via wire-bonding and soldering) will add considerable stability, without needing sweeping architectural changes. Looking even further afield, integrated control electronics will remove the need for these connections altogether, though they will likely bring their own suite of challenges.

Finally, the straight-waveguide sources used in this experiment require significant spectral filtering before becoming spectrally separable (§2.1). Such sources have been shown to interfere in a heralded configuration¹², but this interferability comes at the cost of brightness, via filtering. Bright, separable multi-pair sources must be naturally separable and un-filtered, as those in Exp. 2. Future multi-pair devices will thus have to tune and overlap several such spectrally structured sources. A strong motivator for the straight-waveguide sources in this two-photon experiment was its lack of tuning; this decision seems justified, in light of the excellent observed source performance.

Irrespective of source separability, the core effect behind this entanglement generation scheme—photon-number post-selection—is unlikely to scale to systems of more than one pair. Altogether new approaches will be needed to realise entanglement between multiple photon pairs, but these innovations will necessarily take us closer to large-scale quantum-enhanced devices, powered by photons.



ACKNOWLEDGEMENTS

Quantum circuit design and application were done in collaboration with Mr. Raffaele Santagati. My split-versus-separable statistics derivation follows and somewhat expands upon one by Dr. Damien Bonneau. In **EXP. 3**, we used the same detector system as in **EXP. 1**, built by the group of Prof. Robert Hadfield. In **EXP. 4** we use an improved version of this system, incorporating high-efficiency NbTiN nanowires¹³ fabricated and characterised by the groups of Dr. Masahide Sasaki (NICT Koganei) and Dr. Hirotaka Terai (NICT Kobe), including Dr. Shigehito Miki, Dr. Taro Yamashita, and Dr. Mikio Fujiwara. The devices of both **EXP. 3** and **EXP. 4** were fabricated by Dr. Michael Strain in the group of Dr. Marc Sorel, at the University of Glasgow. **EXP. 3** was presented at FiO in 2013 (ref. 2); and **EXP. 4** was presented at CLEO Europe and IPR, by Raffaele and myself, respectively, in 2015 (refs. 14 and 15).

REFERENCES

- [1] Matthews, J. C. F. *et al.* Observing fermionic statistics with photons in arbitrary processes. *Scientific Reports* **3**, 1539 (2013). [\(82\)](#)
- [2] Silverstone, J. W. *et al.* Silicon Quantum Photonic Circuits for On-chip Qubit Generation, Manipulation and Logic Operations. In *Frontiers in Optics 2013* (2013), FW4C.5 (Optical Society of America, Miami, 2013). [\(83, 95\)](#)
- [3] Ralph, T. C., Langford, N. K., Bell, T. B. & White, A. G. Linear optical controlled-NOT gate in the coincidence basis. *Physical Review A* **65** (2002). [\(83, 89\)](#)
- [4] Hofmann, H. F. & Takeuchi, S. Quantum phase gate for photonic qubits using only beam splitters and postselection. *Physical Review A* **66**, 024308 (2002). [\(83\)](#)
- [5] Carolan, J. *et al.* Universal linear optics. *Science* **349**, 711–716 (2015). [\(85\)](#)
- [6] We are starting to understand that ‘quantum discord’ is more fundamental than entanglement, but this is an active topic of research. See ref. 16. Entanglement is widely understood to enable the quantum advantages which we know of today. [\(87\)](#)
- [7] Ralph, T. C. Calculating unknown eigenvalues with a quantum algorithm. *Nature Photonics* **7**, 223–228 (2013). [\(87\)](#)
- [8] Politi, A., Matthews, J. C. F. & O’Brien, J. L. Shor’s quantum factoring algorithm on a photonic chip. *Science* **325**, 1221–1221 (2009). [\(87\)](#)
- [9] For the direct measurements on the source, the top and bottom interferometers of the CSIGN gate were configured as crossers (i.e. with 0 internal phase). This way, we could make projective measurements on $|01\rangle\langle 01|$, rotated by the first set of single-qubit interferometers. [\(91\)](#)
- [10] The semi-automatic calibration procedure was as follows. Control over the device’s phase shifters, and feedback via two photodiodes, was dynamically passed into Mathematica. There, bright light fringes on various phases were collected, and fit sinusoidally to obtain the phase-power relationship (right side, **FIG. 5.6**) and phase offset of each heater. Various optical inputs and outputs were used to isolate each DOF on the chip, and these were configured by manually moving the input and output fibres. [\(92\)](#)
- [11] Note that making the gate *inactive* was considerably easier, as transmission through the auxiliary ports could be simply minimised (so fixing two DOFs), and the photon pair rate could avoid the $1/9$ brightness reduction imposed by the *active* gate. [\(94\)](#)
- [12] Harada, K.-i. *et al.* Indistinguishable photon pair generation using two independent silicon wire waveguides. *New Journal of Physics* **13**, 065005 (2011). [\(94\)](#)
- [13] Miki, S., Yamashita, T., Terai, H. & Wang, Z. High performance fiber-coupled NbTiN superconducting nanowire single photon detectors with Gifford-McMahon cryocooler. *Optics Express* **21**, 10208–10214 (2013). [\(95\)](#)
- [14] Santagati, R. *et al.* Quantum phase estimation algorithm on a reconfigurable silicon photonic chip. In *Conference on Lasers and Electro-Optics - International Quantum Electronics Conference*, JSV-4.1 THU (Munich, 2015). [\(95\)](#)
- [15] Silverstone, J. W. *et al.* Photonic qubit entanglement and processing in silicon waveguides. *Advanced Photonics 2015* (2015), paper IS4A.5 IS4A.5 (2015). [\(95\)](#)
- [16] Datta, A., Shaji, A. & Caves, C. M. Quantum Discord and the Power of One Qubit. *Physical Review Letters* **100**, 050502 (2008). [\(95\)](#)

Chapter 6

Conclusion

The story of quantum optics—and entanglement—in silicon is an unfinished one. Indeed, it has only just begun. In this final chapter, I want to look forward, to where the twists and turns of plot might take us, but first I'll look back on the small part of this story of which I've been part.

§6.1 RETROSPECTIVE

The scene, when I started my PhD in 2011, was set. As I showed in §1.2, LOQC has three core technological requirements: a source of single-photons, linear optics to manipulate those photons, and detectors to see what they did. 2011 was the year when these three pieces fell into place for on-chip quantum optics. A long campaign of silicon SFWM development^{1–5} culminated in 2011 with the demonstration of heralded quantum interference between two silicon photon-pair sources⁵. By that time, the team in Bristol had shown that silica- and lithium-niobate-waveguide interferometers could execute linear optical operations with very high fidelity⁶ and speed⁷, respectively. And, finally, in 2011, two teams—in Eindhoven, and at NIST—completed the puzzle by demonstrating gallium arsenide⁸ and laser-written⁹ waveguide-coupled superconducting single-photon detectors*.

The experiments and devices which I have described in this thesis take some of the first steps to unifying these technological achievements in one photonic material system. In particular, they coherently combine the linear optics of glass waveguides with the photon-pair sources of silicon. Together, they comprise a detailed study of **entangled light in silicon waveguides**: its coherent generation between silicon photon-pair sources, and its manipulation in path, frequency, and by post-selection.

§6.2 UN-FINISHED BUSINESS

I'd like to say that we left no stone unturned and no experiment untested in our quest to unify sources and linear optics in silicon, but I would be lying. This

*Historical note: ‘superconducting single-photon detector’ was the name given by Gol’tsman to his superconducting *nanowire* single-photon detector¹⁰. This nomenclature lingers today. Here, though, I use the term in the most general sense.

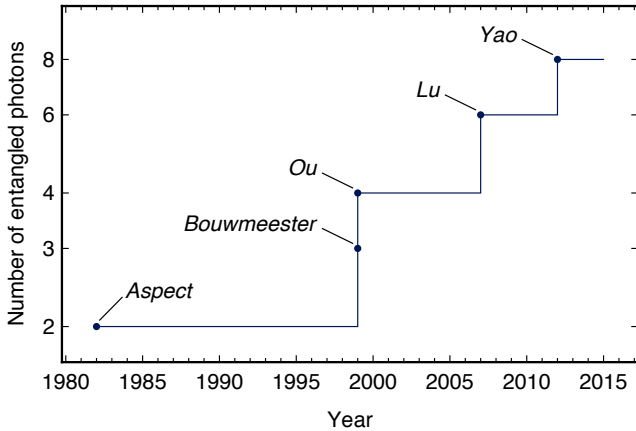


FIG. 6.1: Progress in the generation and measurement of entangled photons. To my knowledge, this trend was first plotted by Prof. Mark Thompson. The trend indicates a photon-number doubling every 15 years, or about 4.7% compounded interest per year. Logarithmic scale. First authors label each advancement: see refs. 17–21.

system—slowly reconfigurable silicon interferometers, operated at room temperature and in the near infrared—remains a useful testbed for a number of further advances.

The first necessary advance, possible with current technology, is to breach the multi-pair barrier. Heralded interference between two pairs generated on the same chip must be demonstrated, as proof of photon-pair separability (§2.1). In contrast with the current state-of-the-art⁵, future experiments: should interfere photons from two sources on the same chip; should not use strong filtering* to achieve separability; and, importantly, should show a high visibility of quantum interference[†].

The near infrared offers high-quality tuneable lasers and spectrometers. These can be leveraged towards the first heralded pair source with integrated pump-rejection filters. In the near term, having integrated pump-rejection filters means that many pair sources can be combined on-chip—in an expansion of EXP. 4—to generate large entangled states without the need for off-chip optics. Integrated pump-rejection filters will become *essential*, however, when parametric photon-pair sources are to be integrated with single-photon detectors. Work towards such filters is ongoing^{11–13}.

One last direction in which current technology can make headway is in that of unexplored higher dimensions. All the experiments of this thesis dealt with simple path *qubits*—with four modes containing two photons. Small-footprint silicon optics are ideal for expanding the photonic Hilbert space into many more modes. In this way, we can build systems of multiple—perhaps up to ten—qubits, stored in just two photons, with each photon spread over $2^{n/2}$ modes (where n is the number of qubits being emulated). This approach has been extensively used in bulk quantum optics (e.g. refs. 14–16), but it could be taken much further by dense, phase-stable, integrated devices.

*By ‘filtering’, I mean filtering which shapes the photons’ joint spectrum. Demultiplexing and pump-suppression filters don’t do this.

[†]Harada et al. were able to obtain 73% raw visibility; they attribute this low value to leaked pump photons, and residual frequency distinguishability due to their relatively narrow-band pump.

6.2.1 Barriers to further progress

What constitutes progress? We could directly benchmark ourselves against the requirements for LOQC, listed in §1.2.1. However, today our quantum photonic largesse is limited entirely by how many entangled photons we can produce. Humanity’s progress in generating larger and larger entangled states of light is plotted in FIG. 6.1. That plot indicates a slow—but exponential—upward trend*, with a yearly growth of about 4.7%. At this rate, we would expect to see the first reliable ten-entangled-photon experiment sometime in 2018. As with Moore’s law, though, this rate will be boosted by new technologies coming online; simple SPDC has been the technological driver behind growth to date. What emerging technology will feed the next photon-number growth spurt, and what’s preventing silicon from being part of it?

In CH. 2, I described the *multiplexing* of probabilistic photon-pair sources, to achieve on-demand or higher-flux single-photon sources. This is a promising technique to leverage SPDC and SFWM sources further, potentially allowing a speed-up in our march to larger entangled states. Multiplexing photon-pair sources requires essentially five things[†]:

- ❶ Photon-pair sources which are separable and heralded;
- ❷ Pump-rejection filters with low loss;
- ❸ Single-photon detectors with low latency;
- ❹ Optical switches which are fast and low-loss;
- ❺ Feed-forward from detection to switching with low latency.

The question then is how many of the above criteria are satisfied by existing, room temperature, silicon photonics technology?

The separability requirement of ❶ is satisfied, but cross-two-photon absorption (XTPA, §1.3.3) fundamentally limits heralding efficiency. I show in §D.5 the degree to which this is the case. For a silicon waveguide source producing a modest 0.1 pairs per pump pulse, XTPA fundamentally limits the heralding efficiency to about 85%. This means that 15% of the time, when a photon is heralded, it is found to be mysteriously absent, having been lost *inside* the source. With any luck, the pump-rejection criterion, ❷, will be satisfied in the near future, with some effort already exerted^{11–13}.

Room-temperature waveguide-integrated single-photon detectors have not yet been demonstrated, but their cryogenic counterparts show exceptionally high levels of performance. For this reason, it is likely that future devices will reside inside cryostats, to satisfy the detection criterion ❸. Single photon detectors based on superconducting nanowires⁸ (SNSPD) show particular promise of high speed, high efficiency²², and high yield²³, by leveraging the strong confinement and high-quality top surface of silicon strip waveguides.

Silicon photonics offers carrier-based modulators sufficient for high-bandwidth classical communication²⁴, but these are typically very lossy, so cannot satisfy ❹. Micro- and nano-electromechanical switches^{25–29} have low loss and can operate at

*This trend was first noticed by my advisor, Mark Thompson.

[†]The careful reader will notice that these criteria are nearly identical to those for LOQC, in §1.2.1.

low temperature, but are not very fast. Electro-optic modulators are possible in strained silicon^{30–32}, or in heterostructures^{33–36}, offering low loss and high-speed, at the expense of a large footprint.

We can be optimistic, however, that silicon photonics in any form can accommodate either front- or back-end integrated electronics, for implementing the feed-forward control required by ❸. CMOS electronics can be modified to work at cryogenic temperatures^{37–39}, and superconducting electronics^{40,41} could serve a naturally complementary role.

§6.3 UN-STARTED BUSINESS

It should be clear, from the discussion thus far, that if we are to make future-proof integrated quantum optics, then dramatic technological changes are required. Two challenges come to the fore: the integration of detectors, and the banishment of parasitic two-photon absorption.

6.3.1 Cold silicon quantum photonics

It is increasingly likely that the future of LOQC will be cold. There has been no demonstration of a waveguide-coupled detector operating at room-temperature. Operating around 2 K, SNSPDs have recently been developed¹⁰. They realise near-ideal detection characteristics in a very simple package, requiring only a single patterning step (albeit a high-resolution one). A modest exploration of superconducting materials has been carried out with them. Devices have primarily employed thin films of polycrystalline NbN^{10,42,43}, but interest has moved to the amorphous WSi^{44–46}, MoSi^{47,48}, and MoGe⁴⁹ superconductors, which allow higher yield*. Detectors, primarily of NbN, have been coupled to waveguides of various materials^{8,22,23,43,46}. These devices use the intimacy between guided mode and nanowire to allow for very short meanders—increasing yield—while maintaining near-unit absorption in the near-infrared. An alternate route to yield, using fabrication on a membrane and a transfer technique, has been shown to allow high-yield detectors made of NbN²³.

Superconducting detectors present a devil’s bargain: they offer everything you could want in a detector, with the only caveat being that *everything else must work at cryogenic temperatures*. This caveat quickly rules out the thermal tuners used in this thesis; it also rules out silicon’s carrier-based modulators. It requires careful accounting for system energy budgets. Packaging and testing must adapt—no more rigs with unlimited access and control. Doubtless, the unforeseen and unforeseeable effects are legion.

More pragmatically, silicon quantum photonics at low temperatures may hold several advantages. Compact integrated optics can be readily fit into the confines of a cryostat, in contrast with bulk- or fibre-optic systems. Nonlinear optical effects are largely temperature-independent: $\chi^{(3)}$ effects work nearly as well at low temperature⁵⁰. SFWM photon-pair sources, as well as XPM and FWM, will continue to work, though TPA’s dark cloud lingers. The thermal-expansion-based strain-

*Due to larger hot-spots (so wider wires), and more uniform films.

ing, used to produce $\chi^{(2)}$ in silicon³⁰, could benefit from the larger deposition-to-operation temperature difference; $\chi^{(2)}$ electro-optic modulators could be invaluable for low-temperature switching. Control electronics—both semiconductor and superconductor—are feasible at low temperatures. Semiconductor electronics will benefit from increased carrier mobility, provided sufficient carrier densities are not ‘frozen out’. Finally, the effort expended to make silicon photonics *athermal* would be unnecessary: silicon’s low-temperature thermo-optic coefficient is 1/10 000th of its room-temperature value^{50,51}.

Cold silicon quantum photonics certainly presents challenges, but it comes with benefits too. The biggest prize of all, though, is access—enabled by *integrated* single-photon detection—to previously unimaginable system architectures. Multiplexing, as we know it, is only the first of these architectural shifts. Regardless whether we choose to go the *cold* route or not, our greatest future challenges and greatest future triumphs can only be unknown unknowns⁵². Only time and effort can vindicate our choice.

6.3.2 Banishing nonlinear absorption, forever

Two-photon absorption dominates discussions of nonlinear optics in silicon. TPA is occasionally useful (e.g. refs. 53,54), but is more often problematic. When we want to use the Kerr effect directly—via SPM, XPM, or FWM—the presence of nonlinear loss fundamentally reduces efficiency. In the case of SFWM, this translates to a fundamental reduction in *heralding* efficiency, which will become intolerable as time goes on ([§6.2.1](#)). In addition to improving heralding, banishing TPA will yield several corollary benefits in techniques which will become feasible: XPM all-optical switches^{54,55}; FWM frequency-conversion^{56,57}; Raman lasing⁵⁸; and FWM and Raman parametric amplification^{59–61}.

TPA is intrinsic, and eliminating it will require significant changes to our optics. The so-called nonlinear figure of merit (FOM) tries to quantify how ‘good’ a material is for $\chi^{(3)}$ nonlinear optical applications, in the presence of TPA⁶²:

$$\text{FOM} \equiv \frac{1}{\lambda} \frac{n_2}{\alpha_2}. \quad (6.1)$$

This FOM doesn’t account for the *strength* of the nonlinearity, so it tells us nothing about the geometry or feasibility of resulting devices, but it’s useful nonetheless. Figures of merit and waveguide nonlinear parameters (γ , [EQ. 1.39](#)) for some candidate systems are listed in [TABLE 6.1](#). The possibilities are largely CMOS-compatible*. All represent a complete or near-complete elimination of TPA, at the cost of size, manufacturing complexity, or optical frequency.

A shift to longer wavelengths, nearer silicon’s two-photon bandgap (2.2 μm), represents the simplest change in materials (i.e. none). This approach maintains a high nonlinearity, while almost completely eliminating nonlinear absorption⁷¹, allowing silicon to keep its nonlinear-optical crown⁷². Complexity is shifted entirely to the optics: new pump sources, and detectors must be developed to operate at

*Meaning that materials and processes could, in principle, be integrated with a CMOS process flow. Obviously significant effort would be required to do so, and a case-by-case economics would be necessary. For further commentary, see ref. 63.

TABLE 6.1: Candidate low-TPA materials and their nonlinear parameters. Silicon and silica fibre are included for reference. Unless otherwise noted: $\lambda = 1.55 \mu\text{m}$, $T \approx 300 \text{ K}$, and silicon is crystalline. γ and FOM are defined in [Eqs. 1.39](#) and [6.1](#), respectively.

Material	Waveguide		FOM	$\gamma (\text{W}^{-1} \text{m}^{-1})$	Reference
SiO_2	fibre		10	0.002	64
Si_3N_4	strip	$\alpha_2 \approx 0$	$\gg 1$	1.2	65
Si:polymer	slot	DDMEBT	> 5	104	64
a-Si:H	strip	TM pol.	5	140	54,66
Si	strip	$\lambda = 2.0 \mu\text{m}$	4	100	67,68
Si	strip	$\lambda = 1.55 \mu\text{m}$	0.5	220	Tab. 1.1
AlGaAs	rib		10	516	69,70

these longer wavelengths. What makes this approach credible are recent developments on both fronts: high-powered thulium- and holmium-doped fibre lasers are becoming available⁷³, and measurements on the amorphous superconductors are showing sensitivity to long wavelengths^{74–76}. Indeed, SNSPDs were first developed to detect millimetre-wave signals⁷⁷. Provided the optical challenges can be met, the long-wave option is the easiest to implement.

Hydrogen-terminated amorphous silicon (a-Si:H) provides the benefit of three-dimensional flexibility—it can be freely deposited to construct multi-layered and multi-tiered structures. With well-controlled fabrication, this flexibility could be a strong advantage, but could otherwise introduce additional uncertainty into waveguide optical and geometrical properties. a-Si:H offers good nonlinearity and a large reduction in TPA at $1.55 \mu\text{m}$ (0.8 eV), having a bandgap of about 1.7 eV. However, its lack of crystal structure also permits wide-band Raman scattering—and in-band single-photon noise^{78,79}—in contrast with crystalline silicon ([§1.3.3](#)). Low temperatures will suppress this Raman scattering, however. Amorphous silicon shows promise.

Silicon nitride (Si_3N_4) is deposited in thin layers as an insulator in CMOS electronics. It is the sole dielectric in my list of candidates, and has a relatively small index, around⁸⁰ 2.0, which leads to relatively large $20 \mu\text{m}$ bend radii⁶⁵. Nitride's dielectric nature means it suffers absolutely no nonlinear loss at terrestrial intensities; experimentalists regularly inject watts of pump power (e.g. [81](#)), which are often necessary due to its small nonlinearity. Switching in silicon nitride could be accomplished all-optically, but this is the only option. Owing to its depositability, nitride could underpin the same three-dimensional photonics as amorphous silicon: its faults can be curtailed by further integration.

Neither of the final two candidates—slot-waveguide-integrated polymers, and AlGaAs—are CMOS-compatible, but they have some interesting features. The slot-waveguide method allows the straightforward combination of any $\chi^{(3)}$ or $\chi^{(2)}$ nonlinear polymer with silicon waveguides, and so offers considerable design flexibility. Slot waveguide propagation loss will always be greater than that of an equivalent strip waveguide. The polymers in this approach may limit manufacturing flexibility in temperature. AlGaAs is a direct-bandgap semiconductor, which readily forms junctions with GaAs, enabling electrically pumped on-chip light sources.

It has a strong $\chi^{(3)}$ and suffers little nonlinear absorption. Moreover, it has a useful $\chi^{(2)}$ nonlinearity, which has been used both for electro-optic modulation⁸², and for photon-pair generation⁸³.

§6.4 PROSPECTIVE

Photons and optics are not the only way to control quantum information—several other scalable frontrunners are vying for the prize. Silicon underpins many of these: phosphorous-in-silicon has produced the longest coherence times of any qubit⁸⁴; vacancies in silicon carbide, and silicon-vacancies in diamond, can not only act as single-photon sources^{85,86}, but as spin-qubits too^{87,88}; even superconducting qubits based on silicon have been proposed⁸⁹. Silicon—which enabled the first computing revolution—is certain to lie at the scalable core of the next one.

Photonic quantum information was—and often is—viewed as a toy system, to be discarded when ‘real’ matter qubits materialise. Though linear optics needs colossal overhead to achieve quantum computation, this overhead lies on a bedrock of a *millenium* of human experience, intuition, and innovation in the manipulation and understanding of light. Regardless which technology ends up processing quantum information, photons and optics are unique in their ability to transmit it. Whether playing a supporting role, giving matter qubits wings, or down by the metal, crunching the numbers, entangled light has a bright future in silicon waveguides.



REFERENCES

- [1] Lin, Q. & Agrawal, G. P. Silicon waveguides for creating quantum-correlated photon pairs. *Optics Letters* **31**, 3140 (2006). [\(97\)](#)
- [2] Sharping, J. E. *et al.* Generation of correlated photons in nanoscale silicon waveguides. *Optics Express* **14**, 12388–12393 (2006). [\(97\)](#)
- [3] Harada, K.-i. *et al.* Generation of high-purity entangled photon pairs using silicon wire waveguide. *Optics Express* **16**, 20368–20373 (2008). [\(97\)](#)
- [4] Clemmen, S. *et al.* Continuous wave photon pair generation in silicon-on-insulator waveguides and ring resonators. *Optics Express* **17**, 16558–16570 (2009). [\(97\)](#)
- [5] Harada, K.-i. *et al.* Indistinguishable photon pair generation using two independent silicon wire waveguides. *New Journal of Physics* **13**, 065005 (2011). [\(97, 98\)](#)
- [6] Laing, A. *et al.* High-fidelity operation of quantum photonic circuits. *Applied Physics Letters* **97** (2010). [\(97\)](#)
- [7] Bonneau, D. *et al.* Fast Path and Polarization Manipulation of Telecom Wavelength Single Photons in Lithium Niobate Waveguide Devices. *Physical Review Letters* **108**, 053601 (2012). [\(97\)](#)
- [8] Sprengers, J. P. *et al.* Waveguide superconducting single-photon detectors for integrated quantum photonic circuits. *Applied Physics Letters* **99**, 181110–181110 (2011). [\(97, 99, 100\)](#)
- [9] Gerrits, T. *et al.* On-chip, photon-number-resolving, telecommunication-band detectors for scalable photonic information processing. *Physical Review A* **84**, 060301 (2011). [\(97\)](#)
- [10] Gol'tsman, G. N. *et al.* Picosecond superconducting single-photon optical detector. *Applied Physics Letters* **79**, 705–707 (2001). [\(97, 100\)](#)
- [11] Harris, N. C. *et al.* Integrated Source of Spectrally Filtered Correlated Photons for Large-Scale Quantum Photonic Systems. *Physical Review X* **4**, 041047 (2014). [\(98, 99\)](#)
- [12] Ong, J. R., Kumar, R. & Mookherjea, S. Ultra-High-Contrast and Tunable-Bandwidth Filter Using Cascaded High-Order Silicon Microring Filters. *Photonics Technology Letters, IEEE* **25**, 1543–1546 (2013). [\(98, 99\)](#)
- [13] Matsuda, N. *et al.* On-chip generation and demultiplexing of quantum correlated photons using a silicon-silica monolithic photonic integration platform. *Optics Express* **22**, 22831–22840 (2014). [\(98, 99\)](#)
- [14] Chen, K. *et al.* Experimental Realization of One-Way Quantum Computing with Two-Photon Four-Qubit Cluster States. *Physical Review Letters* **99**, 120503 (2007). [\(98\)](#)
- [15] Vallone, G., Donati, G., Bruno, N., Chiuri, A. & Mataloni, P. Experimental realization of the Deutsch-Jozsa algorithm with a six-qubit cluster state. *Physical Review A* **81** (2010). [\(98\)](#)
- [16] Zhou, X.-Q. *et al.* Adding control to arbitrary unknown quantum operations. *Nature Communications* **2** (2011). [\(98\)](#)
- [17] Aspect, A., Aspect, A., Grangier, P., Grangier, P. & Roger, G. Experimental realization of Einstein-Podolsky-Rosen-Bohm Gedankenexperiment: a new violation of Bell's inequalities. *Physical review letters* (1982). [\(98\)](#)
- [18] Bouwmeester, D., Pan, J.-W., Daniell, M., Weinfurter, H. & Zeilinger, A. Observation of Three-Photon Greenberger-Horne-Zeilinger Entanglement. *Physical Review Letters* **82**, 1345–1349 (1999). [\(98\)](#)
- [19] Ou, Z. Y., Rhee, J. K. & Wang, L. J. Observation of Four-Photon Interference with a Beam Splitter by Pulsed Parametric Down-Conversion. *Physical Review Letters* **83**, 959–962 (1999). [\(98\)](#)
- [20] Lu, C.-Y. *et al.* Experimental entanglement of six photons in graph states. *Nature* **3**, 91–95 (2007). [\(98\)](#)
- [21] Yao, X.-C. *et al.* Observation of eight-photon entanglement. *Nature Photonics* **6**, 225–228 (2012). [\(98\)](#)
- [22] Pernice, W. H. P. *et al.* High-speed and high-efficiency travelling wave single-photon detectors embedded in nanophotonic circuits. *Nature Communications* **3**, 1325 (2012). [\(99, 100\)](#)
- [23] Najafi, F. *et al.* On-chip detection of non-classical light by scalable integration of single-photon detectors. *Nature Communications* **6**, 5873 (2015). [\(99, 100\)](#)
- [24] Reed, G. T., Mashanovich, G., Gardes, F. Y. & Thomson, D. J. Silicon optical modulators. *Nature Photonics* **4**, 518–526 (2010). [\(99\)](#)
- [25] Kauppinen, L. J. *et al.* Micromechanically tuned ring resonator in silicon on insulator. *Optics Letters* **36**, 1047 (2011). [\(99\)](#)
- [26] Van Acoleyen, K. *et al.* Ultracompact Phase Modulator Based on a Cascade of NEMS-Operated Slot Waveguides Fabricated in Silicon-on-Insulator. *Photonics Journal, IEEE* **4**, 779–788 (2012). [\(99\)](#)
- [27] Poot, M. Broadband nanoelectromechanical phase shifting of light on a chip. *Applied Physics Letters* **104**, 061101 (2014). [\(99\)](#)
- [28] Han, S. *et al.* Large-scale silicon photonic switches with movable directional couplers. *Optica* **2**, 370–375 (2015). [\(99\)](#)
- [29] Seok, T. J., Quack, N., Han, S. & Wu, M. C. 50x50 Digital Silicon Photonic Switches with MEMS-Actuated Adiabatic Couplers. *Optical Fiber Communication Conference* (2015) M2B.4 (2015). [\(99\)](#)
- [30] Jacobsen, R. S. *et al.* Strained silicon as a new electro-optic material. *Nature* **441**, 199–202 (2006). [\(100, 101\)](#)
- [31] Fage-Pedersen, J., Frandsen, L. H., Lavrinenko, A. V. & Borel, P. I. A Linear Electrooptic Effect in Silicon, Induced by Use of Strain. In *3rd IEEE International Conference on Group IV Photonics, 2006.*, 37–39 (IEEE, 2006). [\(100\)](#)
- [32] Chmielak, B. *et al.* Pockels effect based fully integrated, strained silicon electro-optic modulator. *Optics Express* **19**, 17212–17219 (2011). [\(100\)](#)
- [33] Abel, S. *et al.* A strong electro-optically active lead-free ferroelectric integrated on silicon. *Nature Communications* **4**, 1671 (2013). [\(100\)](#)

- [34] Abel, S. *et al.* Electro-Optical Active Barium Titanate Thin Films in Silicon Photonics Devices. *Advanced Photonics* 2013 IW4A.5 (2013). ⟨100⟩
- [35] Xiong, C. *et al.* Active Silicon Integrated Nanophotonics: Ferroelectric BaTiO₃ Devices. *Nano Letters* 140205130629005 (2014). ⟨100⟩
- [36] Fathpour, J. C. S. Mid-infrared integrated waveguide modulators based on silicon-on-lithium-niobate photonics. *Optica* 1, 350–355 (2014). ⟨100⟩
- [37] Ekanayake, S. R., Lehmann, T., Dzurak, A. S., Clark, R. G. & Brawley, A. Characterization of SOS-CMOS FETs at Low Temperatures for the Design of Integrated Circuits for Quantum Bit Control and Readout. *Electron Devices, IEEE Transactions on* 57, 539–547 (2010). ⟨100⟩
- [38] Nagata, H. *et al.* Development of Cryogenic Readout Electronics for Far-Infrared Astronomical Focal Plane Array. *IEICE Transactions on Communications* E94-B, 2952–2960 (2011). ⟨100⟩
- [39] Lengeler, B. Semiconductor devices suitable for use in cryogenic environments. *Cryogenics* (1974). ⟨100⟩
- [40] Likharev, K. K. & Semenov, V. K. RSFQ logic/memory family: a new Josephson-junction technology for sub-terahertz-clock-frequency digital systems 1, 3–28 (1991). ⟨100⟩
- [41] Yamashita, T., Miki, S., Terai, H., Makise, K. & Wang, Z. Crosstalk-free operation of multielement superconducting nanowire single-photon detector array integrated with single-flux-quantum circuit in a 0.1 W Gifford-McMahon cryocooler. *Optics Letters* 37, 2982–2984 (2012). ⟨100⟩
- [42] Heath, R. M. *et al.* Nanoantenna Enhancement for Telecom-Wavelength Superconducting Single Photon Detectors. *Nano Letters* 15, 819–822 (2015). ⟨100⟩
- [43] Rath, P. *et al.* Superconducting single photon detectors integrated with diamond nanophotonic circuits. *arXiv.org* (2015). 1505.04251. ⟨100⟩
- [44] Marsili, F. *et al.* Detecting single infrared photons with 93% system efficiency. *Nature Photonics* 7, 210–214 (2013). ⟨100⟩
- [45] Verma, V. B. *et al.* High-efficiency WSi superconducting nanowire single-photon detectors operating at 2.5 ÅLK. *Applied Physics Letters* 105, 122601 (2014). ⟨100⟩
- [46] Beyer, A. *et al.* Waveguide-Coupled Superconducting Nanowire Single-Photon Detectors. *CLEO: 2015 STh1I.2* (2015). ⟨100⟩
- [47] Verma, V. B. *et al.* High-efficiency superconducting nanowire single-photon detectors fabricated from MoSi thin-films. *arXiv.org* (2015). 1504.02793. ⟨100⟩
- [48] Korneeva, Y. P. *et al.* Superconducting single-photon detector made of MoSi film. *Superconductor Science and Technology* 27, 095012 (2014). ⟨100⟩
- [49] Verma, V. B. *et al.* Superconducting nanowire single photon detectors fabricated from an amorphous Mo0.75Ge0.25 thin film. *Applied Physics Letters* 105, 022602 (2014). ⟨100⟩
- [50] Sun, X., Zhang, X., Schuck, C. & Tang, H. X. Nonlinear optical effects of ultrahigh-Q silicon photonic nanocavities immersed in superfluid helium. *Scientific Reports* 3 (2013). ⟨100, 101⟩
- [51] Komma, J., Schwarz, C., Hofmann, G., Heinert, D. & Nawrodt, R. Thermo-optic coefficient of silicon at 1550 nm and cryogenic temperatures. *Applied Physics Letters* 101, 041905 (2012). ⟨101⟩
- [52] http://en.wikipedia.org/wiki/There_are_known_knowns. ⟨101⟩
- [53] Tanabe, T., Notomi, M., Mitsugi, S., Shinya, A. & Kuromochi, E. All-optical switches on a silicon chip realized using photonic crystal nanocavities. *Applied Physics Letters* 87, 151112 (2005). ⟨101⟩
- [54] Pelc, J. S. *et al.* Picosecond all-optical switching in hydrogenated amorphous silicon microring resonators. *Optics Express* (2014). ⟨101, 102⟩
- [55] Rambo, T. M., McCusker, K. T., Huang, Y.-P. & Kumar, P. Low-loss all-optical quantum switching. In *2013 IEEE Photonics Society Summer Topical Meeting Series*, WD2.3 (IEEE, 2013). ⟨101⟩
- [56] Caspani, L. *et al.* Optical frequency conversion in integrated devices. *Journal of the Optical Society of America B-Optical Physics* 28, A67 (2011). ⟨101⟩
- [57] Turner, A. C., Foster, M. A., Gaeta, A. L. & Lipson, M. Ultra-low power parametric frequency conversion in a silicon microring resonator. *Optics Express* 16, 4881–4887 (2008). ⟨101⟩
- [58] Rong, H. *et al.* An all-silicon Raman laser. *Nature* 433, 292–294 (2005). ⟨101⟩
- [59] Liu, X., Osgood, R. M., Vlasov, Y. A. & Green, W. M. J. Mid-infrared optical parametric amplifier using silicon nanophotonic waveguides. *Nature Photonics* 4, 557–560 (2010). ⟨101⟩
- [60] Foster, M. A. *et al.* Broad-band optical parametric gain on a silicon photonic chip. *Nature* 441, 960–963 (2006). ⟨101⟩
- [61] Espinola, R., Dadap, J., Richard Osgood, J., McNab, S. & Vlasov, Y. Raman amplification in ultrasmall silicon-on-insulator wire waveguides. *Optics Express* 12, 3713–3718 (2004). ⟨101⟩
- [62] Leuthold, J., Koos, C. & Freude, W. Nonlinear silicon photonics. *Nature Photonics* 4, 535–544 (2010). ⟨101⟩
- [63] Baehr-Jones, T. *et al.* Myths and rumours of silicon photonics. *Nature Photonics* 6, 206–208 (2012). ⟨101⟩
- [64] Leuthold, J. *et al.* Silicon Organic Hybrid Technology—A Platform for Practical Nonlinear Optics. *Proceedings of the IEEE* 97, 1304–1316 (2009). ⟨102⟩
- [65] Moss, D. J., Morandotti, R., Gaeta, A. L. & Lipson, M. New CMOS-compatible platforms based on silicon nitride and Hydex for nonlinear optics. *Nature Photonics* 7, 597–607 (2013). ⟨102⟩
- [66] Grillet, C. *et al.* Amorphous silicon nanowires combining high nonlinearity, FOM and optical stability. *Optics Express* 20, 22609–22615 (2012). ⟨102⟩
- [67] Gholami, F. *et al.* Third-order nonlinearity in silicon beyond 2350 nm. *Applied Physics Letters* 99, 081102 (2011). ⟨102⟩

- [68] Zlatanovic, S. *et al.* Mid-infrared wavelength conversion in silicon waveguides using ultracompact telecom-band-derived pump source. *Nature Photonics* **4**, 561–564 (2010). [\(102\)](#)
- [69] Aitchison, J. S., Hutchings, D. C., Kang, J. U., Stegeman, G. I. & Villeneuve, A. The nonlinear optical properties of AlGaAs at the half band gap. *IEEE Journal of Quantum Electronics* **33**, 341–348 (1997). [\(102\)](#)
- [70] Lacava, C., Pusino, V., Minzioni, P., Sorel, M. & Cristiani, I. Nonlinear properties of AlGaAs waveguides in continuous wave operation regime. *Optics Express* **22**, 5291–5298 (2014). [\(102\)](#)
- [71] Wang, T. *et al.* Multi-photon absorption and third-order nonlinearity in silicon at mid-infrared wavelengths. *Optics Express* **21**, 32192–32198 (2013). [\(101\)](#)
- [72] Jalali, B. Silicon photonics: Nonlinear optics in the mid-infrared. *Nature Photonics* **4**, 506–508 (2010). [\(101\)](#)
- [73] Geng, J. & Jiang, S. Fiber Lasers: The 2 μm Market Heats Up. *Optics and Photonics News* **25**, 34–41 (2014). [\(102\)](#)
- [74] Marsili, F. *et al.* Mid-Infrared Single-Photon Detection with Tungsten Silicide Superconducting Nanowires. *CLEO: 2013* (2013), paper CTu1H.1 CTu1H.1 (2013). [\(102\)](#)
- [75] Baek, B., Lita, A. E., Verma, V. & Nam, S. W. Superconducting a-W \times Si 1 \times nanowire single-photon detector with saturated internal quantum efficiency from visible to 1850 nm. *Applied Physics Letters* **98**, 251105 (2011). [\(102\)](#)
- [76] Korneeva, Y. *et al.* New Generation of Nanowire NbN Superconducting Single-Photon Detector for Mid-Infrared. *IEEE Transactions on Applied Superconductivity* **21**, 323–326 (2011). [\(102\)](#)
- [77] Gershenzon, E. M. *et al.* Millimeter and submillimeter range mixer based on electron heating of superconducting films in the resistive state. *Superconductivity* **3**, 1583–1597 (1990). [\(102\)](#)
- [78] Wang, K.-Y. *et al.* Multichannel photon-pair generation using hydrogenated amorphous silicon waveguides **39**, 914–917 (2014). [\(102\)](#)
- [79] Clemmen, S. *et al.* Generation of correlated photons in hydrogenated amorphous-silicon waveguides. *Optics Letters* **35**, 3483–3485 (2010). [\(102\)](#)
- [80] Ikeda, K., Saperstein, R. E., Alic, N. & Fainman, Y. Thermal and Kerr nonlinear properties of plasma-deposited silicon nitride / silicon dioxide waveguides. *Optics Express* **16**, 12987–12994 (2008). [\(102\)](#)
- [81] Herr, T. *et al.* Universal formation dynamics and noise of Kerr-frequency combs in microresonators. *Nature Photonics* **6**, 480–487 (2012). [\(102\)](#)
- [82] Spickermann, R., Sakamoto, S. R., Peters, M. G. & Dagli, N. GaAs/AlGaAs travelling wave electro-optic modulator with an electrical bandwidth >40 GHz. *Electronics Letters* **32**, 1095–1096 (1996). [\(103\)](#)
- [83] Orioux, A. *et al.* Direct Bell States Generation on a III-V Semiconductor Chip at Room Temperature. *Physical Review Letters* **110**, 160502 (2013). [\(103\)](#)
- [84] Muhonen, J. T. *et al.* Storing quantum information for 30 seconds in a nanoelectronic device. *Nature Nanotechnology* **9**, 986–991 (2014). [\(103\)](#)
- [85] Widmann, M. *et al.* Coherent control of single spins in silicon carbide at room temperature. *Nature materials* **14**, 164–168 (2015). [\(103\)](#)
- [86] Sipahigil, A. *et al.* Indistinguishable Photons from Separated Silicon-Vacancy Centers in Diamond. *Physical Review Letters* **113**, 113602 (2014). [\(103\)](#)
- [87] Christle, D. J. *et al.* Isolated electron spins in silicon carbide with millisecond coherence times. *Nature materials* **14**, 160–163 (2015). [\(103\)](#)
- [88] Rogers, L. J. *et al.* All-Optical Initialization, Readout, and Coherent Preparation of Single Silicon-Vacancy Spins in Diamond. *Physical Review Letters* **113**, 263602 (2014). [\(103\)](#)
- [89] Shim, Y.-P. & Tahan, C. Bottom-up superconducting and Josephson junction devices inside a group-IV semiconductor. *Nature Communications* **5** (2014). [\(103\)](#)

Appendices

Appendix A

List of symbols

Conventions

of the order of x	$\mathcal{O}(x)$...
power	P	...
probability	Π	...
time	t, τ	...
length	L	...
efficiency (transmission)	η	...

Quantum

state vector	$ \psi\rangle$...
density matrix (state)	$\hat{\rho}$	$ \psi\rangle\langle\psi $
fidelity	F	$ \langle\psi \phi\rangle ^2, \text{Tr}^2\sqrt{\sqrt{\hat{\rho}_1} \cdot \hat{\rho} \cdot \sqrt{\hat{\rho}_1}}$
purity	\mathcal{P}	$\text{Tr}\{\hat{\rho}^2\}$
CHSH parameter	S	...

Nonlinear optics

two-photon absorption coefficient	α_2	$[\text{m W}^{-1}]$
nonlinear parameter	γ	$[\text{W}^{-1} \text{m}^{-1}]$
nonlinear refractive index	n_2	$12\pi^2\chi^{(3)}/n^2$
effective mode area	A	...
second-order susceptibility	$\chi^{(2)}$	$[\text{m V}^{-1}]$
third-order susceptibility	$\chi^{(3)}$	$[\text{m}^2 \text{V}^{-2}]$
free-carrier absorption cross-section	σ_c	...
free-carrier lifetime	τ_c	...
free-carrier density	N_c	...
cross-TPA transmission	η_{XTPA}	...
free-carrier transmission	η_{FCA}	...
effective length	L_{eff}	$(1 - e^{\alpha L})/\alpha$
parametric gain	g	...
momentum mismatch	Δk	...

Fundamental constants

Planck constant	h	$6.626 \times 10^{-34} \text{ J s}$
reduced Planck constant	\hbar	$h/2\pi = 1.055 \times 10^{-34} \text{ J s}$
speed of light in vacuum	c	$2.998 \times 10^8 \text{ m s}^{-1}$

Coincidence measurements

total coincidence count	X	...
accidental coincidence count	X_{acc}	...
net coincidence count	X_{net}	$X - X_{\text{acc}}$
singles count	C	...

Joint spectra

Schmidt number	K	$1/\mathcal{P}(\hat{\rho}_{\text{sub}})$
joint spectral amplitude	J	...

Resonators

free spectral range (FSR)	ν_0	$n_g L/c$
round-trip time	T_0	$1/\nu_0$
self-coupling parameter (reflection)	r	...
cross-coupling parameter (transmission)	t, κ	$\sqrt{1 - r^2}$
photon lifetime	τ	...
quality factor	Q	$\omega\tau$
field enhancement	F	...

Electrodynamics

electric permittivity of free space	ϵ_0	$1/\mu_0 c^2$
electric permittivity	ϵ	...
magnetic permeability of free space	μ_0	$4\pi \times 10^{-7}$
electric susceptibility	χ	$\epsilon/\epsilon_0 - 1$
speed of light in vacuum	c	$1/\sqrt{\mu_0 \epsilon_0}$
refractive index	n	$\sqrt{\epsilon\mu/\epsilon_0\mu_0} \sim \sqrt{\epsilon/\epsilon_0}$, $\sqrt{\chi + 1}$
effective index	n_{eff}	...
effective index	n_g	$n - \lambda_0 (\text{d}n/\text{d}\lambda_0)$
vacuum wavelength	λ	...
vacuum wavenumber	k_0	$2\pi/\lambda, \omega/c$
wavenumber	k	$2\pi/\lambda_m, nk_0$
propagation constant	β	$n_{\text{eff}} k_0$
higher-order dispersion	β_i	$\text{d}^i k / \text{d}\omega^i$
dispersion parameter	D	$-2\pi\nu^2\beta_2/c$
frequency	ν	...
angular frequency	ω	$2\pi\nu, k_0 c$
electric field	E	...
electric displacement field	D	$\epsilon_0 E + P$
magnetic field	B	$\mu_0 H$

Appendix B

Quantum

§B.1 QUANTUM STATES

The state of a quantum system is written in terms of a state vector, $|m\rangle$. The set of states which the system can occupy form a vector space, known as the state's Hilbert space. The Hermitian conjugate ([§B.4.1](#)) of a state $|m\rangle$ is written as $\langle m|$.

B.1.1 Pure states

A pure quantum state is represented by a set of complex numbers $\{a_m\}$, which each describe the probability amplitude of a given system state $|m\rangle$. From here on, I'll assume the $|m\rangle$ are orthogonal, i.e. $\langle m|n\rangle = \delta_{m,n}$. In general, a system represented by $|\psi\rangle$ may be in a *superposition* of its possible states. We can write this as a sum:

$$|\psi\rangle = \sum_m a_m |m\rangle. \quad (\text{B.1})$$

The probability to find a system described by $|\psi\rangle$ in the m^{th} state is

$$\Pi_m = \langle m|\psi\rangle\langle\psi|m\rangle = |\langle m|\psi\rangle|^2 = |a_m|^2. \quad (\text{B.2})$$

Since the probability to find it in *any* state is 1, the state must be *normalised*:

$$\sum_m |a_m|^2 = 1. \quad (\text{B.3})$$

B.1.2 Mixed states

In general, a system may not be in a *coherent* superposition of its states, but a mixture. This means that some information about the state of the system is unknown to us, so we can just assign a probability distribution to the possible outcomes. By representing states as *density matrices* we can smoothly vary the coherence. A density matrix $\hat{\rho}$, which is in the state $|m\rangle$ with probability Π_m , is written as

$$\hat{\rho} \equiv \sum_m \Pi_m |m\rangle\langle m|. \quad (\text{B.4})$$

The probability to find a system represented by $\hat{\rho}$ in a state $|m\rangle$ is, via Born's rule, is

$$\Pi_m = \text{Tr}\{\hat{\rho} \cdot |m\rangle\langle m|\}. \quad (\text{B.5})$$

The purity, which measures how coherent a state is, is defined for a state $\hat{\rho}$ as $\mathcal{P} \equiv \text{Tr}\{\hat{\rho} \cdot \hat{\rho}\}$.

§B.2 DIRAC MATRIX NOTATION

Matrices—especially sparse ones—can be conveniently represented in Dirac notation, in terms of their bases. A d -dimensional unitary operator \hat{U} which takes $|\psi_i\rangle \rightarrow |\phi_i\rangle$, for d orthogonal $|\psi_i\rangle^*$, can be represented as

$$\hat{U} = \sum_{i=1}^d |\psi_i\rangle\langle\phi_i| \quad (\text{B.6})$$

A few common examples are listed below. (see [Eqs. 1.16, 1.17](#)):

$$\text{CNOT} \equiv |00\rangle\langle 00| + |01\rangle\langle 01| + |10\rangle\langle 11| + |11\rangle\langle 10| \quad (\text{B.7a})$$

$$\text{CSIGN} \equiv |00\rangle\langle 00| + |01\rangle\langle 01| + |10\rangle\langle 10| - |11\rangle\langle 11| \quad (\text{B.7b})$$

$$\hat{I} \equiv \sum_{i=1}^d |i\rangle\langle i| \quad (\text{B.7c})$$

$$\hat{X} \equiv |0\rangle\langle 1| + |1\rangle\langle 0| \quad (\text{B.7d})$$

$$\hat{Y} \equiv |+i\rangle\langle -i| + |-i\rangle\langle +i| = |0\rangle\langle 1| + |1\rangle\langle 0| \quad (\text{B.7e})$$

$$\hat{Z} \equiv |+\rangle\langle -| + |-\rangle\langle +| = |0\rangle\langle 0| - |1\rangle\langle 1| \quad (\text{B.7f})$$

§B.3 FIELD QUANTISATION

Closely following reference ¹, I will quantise the field inside a single longitudinal mode of a perfect resonator with dimensions $w \times h \times l$, where all dimensions tend to infinity. The mode propagates in the z direction is characterised by a wave vector k , which satisfies the resonant condition of the cavity ($k = \pi m/l$) at a frequency $\omega = kc$. The electric field in the cavity is x -polarised, forcing the magnetic field to lie along the y axis. At the walls of the cavity ($z = 0$ and $z = l$) the electric field is zero. We choose an electric field (satisfying Maxwell's equations) of the form

$$E_x(z, t) = \sqrt{\frac{2\omega^2}{whl\epsilon_0}} q(t) \sin kz \quad (\text{B.8})$$

where $q(t)$ has dimensions of length, and will become the harmonic oscillator's canonical position. By Faraday's Law ($\nabla \times \mathbf{B} = c^{-2} \dot{\mathbf{E}}$), the non-zero magnetic field component is

$$B_y(z, t) = \frac{1}{kc^2} \sqrt{\frac{2\omega^2}{whl\epsilon_0}} \dot{q}(t) \cos kz. \quad (\text{B.9})$$

Our strategy now is to compute the total energy of the system (i.e. the energy inside the resonator) and equate this with the Hamiltonian. Then we can use the correspondence principle to obtain the quantum dynamics. The total energy, H

¹The rows and columns of a d -dimensional unitary matrix form an orthonormal basis for a d -dimensional space, so we can be sure that the behaviour of d orthonormal states evolved by \hat{U} fully determines \hat{U} .

then is

$$\begin{aligned}
H &= \frac{1}{2} \iiint \left(\epsilon_0 \mathbf{E} \cdot \mathbf{E} + \frac{1}{\mu_0} \mathbf{B} \cdot \mathbf{B} \right) dx dy dz = \frac{wh}{2} \int \left(\epsilon_0 E_x^2 + \frac{1}{\mu_0} B_y^2 \right) dz \\
&= \frac{wh}{2} \int \left(\frac{2\omega^2}{whl} q^2 \sin^2 kz + \frac{1}{k^2 c^2} \frac{2\omega^2}{whl} \dot{q}^2 \cos^2 kz \right) dz \\
&= \frac{1}{l} \int (\omega^2 q^2 \sin^2 kz + \dot{q}^2 \cos^2 kz) dz \\
&= \frac{1}{l} \int_{z=0}^l \left(\omega^2 q^2 \left(\frac{1 - \cos 2kz}{2} \right) + \dot{q}^2 \left(\frac{1 + \cos 2kz}{2} \right) \right) dz \\
&= \frac{1}{2l} \left(\omega^2 q^2 \left(1 - \frac{\sin 2kz}{2k} \right) + \dot{q}^2 \left(1 + \frac{\sin 2kz}{2k} \right) \right) \Big|_{z=0}^l = \frac{1}{2} (\omega^2 q^2 + \dot{q}^2)
\end{aligned} \tag{B.10}$$

which is the energy of a harmonic oscillator with unit mass and position $q(t)$. In the second-last line, we use the fact that $kl = \pi m$ for $m \in \mathbb{Z}$, so $\sin(2\pi m) = 0$. We now replace the classical Hamiltonian H , canonical position q , and canonical momentum $p = \dot{q}$ with their quantum counterparts \hat{H} , \hat{q} , and \hat{p} , yielding the standard harmonic oscillator result:

$$\hat{H} = \frac{1}{2} (\omega^2 \hat{q}^2 + \hat{p}^2). \tag{B.11}$$

The canonical position and momentum satisfy the canonical commutation relation:

$$\hat{q}\hat{p} - \hat{p}\hat{q} = i\hbar \tag{B.12}$$

At this point, we can cheat and guess the ladder operators (creation and annihilation operators) of the oscillator (field):

$$\begin{aligned}
\hat{a} &\equiv \frac{1}{\sqrt{2\hbar\omega}} (\omega\hat{q} + i\hat{p}) \\
\hat{a}^\dagger &\equiv \frac{1}{\sqrt{2\hbar\omega}} (\omega\hat{q} - i\hat{p})
\end{aligned} \tag{B.13}$$

with the commutation relation

$$\begin{aligned}
\hat{a}\hat{a}^\dagger - \hat{a}^\dagger\hat{a} &= \frac{1}{2\hbar\omega} \left[(\omega\hat{q} + i\hat{p})(\omega\hat{q} - i\hat{p}) - (\omega\hat{q} - i\hat{p})(\omega\hat{q} + i\hat{p}) \right] \\
&= \frac{1}{2\hbar\omega} \left[(\omega^2 \hat{q}^2 - i\omega\hat{q}\hat{p} + i\omega\hat{p}\hat{q} + \hat{p}^2) - (\omega^2 \hat{q}^2 + i\omega\hat{q}\hat{p} - i\omega\hat{p}\hat{q} + \hat{p}^2) \right] \\
&= \frac{1}{2\hbar\omega} \left[-2i\omega\hat{q}\hat{p} + 2i\omega\hat{p}\hat{q} \right] \\
&= \frac{-i}{\hbar} [\hat{q}\hat{p} - \hat{p}\hat{q}] \\
&= 1.
\end{aligned} \tag{B.14}$$

We can manipulate the ladder operators,

$$\begin{aligned}
\hat{a}^\dagger\hat{a} &= \frac{1}{2\hbar\omega} (\omega^2 \hat{q}^2 + \hat{p}^2 + i\omega\hat{q}\hat{p} - i\omega\hat{p}\hat{q}) \\
&= \frac{1}{2\hbar\omega} (\omega^2 \hat{q}^2 + \hat{p}^2 + i\omega [\hat{q}\hat{p} - \hat{p}\hat{q}]) \\
&= \frac{1}{2\hbar\omega} (\omega^2 \hat{q}^2 + \hat{p}^2 + i\omega [i\hbar]) \\
&= \frac{1}{2\hbar\omega} (\omega^2 \hat{q}^2 + \hat{p}^2 - \hbar\omega)
\end{aligned} \tag{B.15}$$

so the Hamiltonian becomes

$$\hat{H} = \frac{1}{2}(\omega^2 \hat{q}^2 + \hat{p}^2) = \hbar\omega \left(\hat{a}^\dagger \hat{a} + \frac{1}{2} \right) \quad (\text{B.16})$$

as expected. We can check that \hat{H} is Hermitian, i.e. $\hat{H} = \hat{H}^\dagger$:

$$\begin{aligned} \hat{H}^\dagger &= \hbar\omega \left(\hat{a}^\dagger \hat{a} + \frac{1}{2} \right)^\dagger \\ &= \hbar\omega \left([\hat{a}^\dagger \hat{a}]^\dagger + \frac{1}{2} \right) \\ &= \hbar\omega \left(\hat{a}^\dagger \hat{a}^\dagger + \frac{1}{2} \right) \\ &= \hbar\omega \left(\hat{a}^\dagger \hat{a} + \frac{1}{2} \right) = \hat{H} \end{aligned} \quad (\text{B.17})$$

which relies on the identity of the Hermitian conjugate, $[AB]^\dagger = B^\dagger A^\dagger$.

We can now confirm the operation of our ladder operators by rewriting the Schrödinger equation in terms of them, then applying them in turn, and observing the change in the Hamiltonian's energy eigenvalue.

$$\hat{H}|\psi\rangle = \hbar\omega \left(\hat{a}^\dagger \hat{a} + \frac{1}{2} \right) |\psi\rangle = E|\psi\rangle. \quad (\text{B.18})$$

First, we apply the annihilation operator \hat{a} to both sides, and suggestively write $|\psi\rangle$ as the energy eigenstate $|n\rangle$ with eigenvalue E_n :

$$\begin{aligned} \hbar\omega \left(\hat{a} \hat{a}^\dagger \hat{a} + \frac{\hat{a}}{2} \right) |n\rangle &= E_n \hat{a} |n\rangle \\ \hbar\omega \left([\hat{a}^\dagger \hat{a} + 1] \hat{a} + \frac{\hat{a}}{2} \right) |n\rangle &= E_n \hat{a} |n\rangle \\ \hbar\omega \left(\hat{a}^\dagger \hat{a} + \frac{1}{2} + 1 \right) \hat{a} |n\rangle &= E_n \hat{a} |n\rangle \\ \hbar\omega \left(\hat{a}^\dagger \hat{a} + \frac{1}{2} \right) \hat{a} |n\rangle + \hbar\omega \hat{a} |n\rangle &= E_n \hat{a} |n\rangle \\ \hbar\omega \left(\hat{a}^\dagger \hat{a} + \frac{1}{2} \right) \hat{a} |n\rangle &= (E_n - \hbar\omega) \hat{a} |n\rangle. \end{aligned} \quad (\text{B.19})$$

So the state $\hat{a}|n\rangle$ has an energy one quantum less than the state $|n\rangle$ —the operator \hat{a} annihilates a photon from the field. Following a similar prescription for \hat{a}^\dagger , we find

$$\hbar\omega \left(\hat{a}^\dagger \hat{a} + \frac{1}{2} \right) \hat{a}^\dagger |n\rangle = (E_n + \hbar\omega) \hat{a}^\dagger |n\rangle \quad (\text{B.20})$$

or in other words, the operator \hat{a}^\dagger creates a photon in the field.

It turns out that this result generalises for multi-mode fields, in any polarisation state. As long as we don't care about the form of the energy eigenstates $|n\rangle$, then these other situations are treated identically. At this point, I'll stop our derivation and refer to the literature for the remaining properties of the creation and annihilation operators, which, together with a summary of our findings above, are shown in **TABLE B.1**.

§B.4 PROPERTIES OF MATRICES

B.4.1 Hermitian matrices

\hat{H} is Hermitian if and only if $\hat{H} = \hat{H}^\dagger$. For a Hermitian \hat{H} ,

$$\langle a | (\hat{H}|b) \rangle = (\langle a | \hat{H}^\dagger) |b\rangle, \quad \rightarrow \quad \langle a | \hat{H}^\dagger |a\rangle = \langle a | \hat{H} |a\rangle \quad \rightarrow \quad \langle a | \hat{H} |a\rangle \in \mathbb{R} \quad (\text{B.21})$$

and all eigenvalues of \hat{H} are real. In this way, Hermitian matrices or operators represent physical observables (energy, position, momentum, etc.). The Hermitian conjugate (a.k.a. Hermitian adjoint, adjoint, conjugate transpose) is defined as

$$(\hat{A}^\dagger)_{i,j} = (\hat{A}_{j,i})^*, \quad \text{with} \quad (\hat{A}^\dagger)^\dagger = \hat{A}, \quad (\hat{A}\hat{B})^\dagger = \hat{B}^\dagger\hat{A}^\dagger, \quad \text{and} \quad |a\rangle^\dagger = \langle a|. \quad (\text{B.22})$$

Any matrix \hat{A} can be written in terms of matrices \hat{H}_1 and \hat{H}_2 , which are both Hermitian, $\hat{A} = \hat{H}_1 + i\hat{H}_2$, and any matrix can be made Hermitian by adding it to its own Hermitian conjugate, $\hat{H} = \hat{A} + \hat{A}^\dagger$. A matrix \hat{A} is Hermitian if any of the following are true:

- ① $\langle x | \hat{A} |x\rangle$ is real, for any $|x\rangle$.
- ② \hat{A} has only real eigenvalues.
- ③ $\hat{S}^\dagger \hat{A} \hat{S}$ is Hermitian, for any matrix \hat{S} in the same space as \hat{A} .

The eigenvectors of a Hermitian matrix \hat{H} form a unitary matrix \hat{U} which diagonalises it:

$$\hat{U}^\dagger \hat{H} \hat{U} = \hat{D}(\lambda_i), \quad (\text{B.23})$$

where $\hat{D}(\lambda_i)$ is a diagonal matrix composed of the (real) eigenvalues λ_i of \hat{H} .

Degrees of freedom

A Hermitian matrix \hat{H} with d dimensions has at most $N_\lambda = d$ unique eigenvalues, and associated orthogonal eigenvectors. The eigenvectors, apart from their association, have no dependence on the eigenvalues, and together the eigenvalues and eigenvectors completely specify \hat{H} . How many degrees of freedom (independent real parameters) does \hat{H} have? The first *complex* eigenvector is normalised, but otherwise completely free: it has $2(d - 1)$ degrees of freedom. The second must be orthogonal to the first, so it has $d - 2$. Thus, continuing the recursion, the total number of degrees of freedom N of \hat{H} is,

$$N = N_\lambda + \sum_{i=1}^d 2(i - 1) = (d) + \left(2\frac{d^2 + d}{2} - d\right) = d^2. \quad (\text{B.24})$$

If \hat{H} is in the space of *qubits*, then for q such qubits, $d = 2^q$, and $N = 2^{2q}$, which grows rather rapidly.

B.4.2 Unitary matrices

A matrix \hat{U} is unitary if $\hat{U}^\dagger \hat{U} = \hat{I}$. Unitary matrices are ‘normal,’ so obey $UU^\dagger = \hat{U}^\dagger \hat{U} = I$. Together, these properties imply that unitary matrices preserve inner products:

$$\langle \hat{U}w | \hat{U}v \rangle = \langle w | \hat{U}^\dagger | \hat{U}v \rangle = \langle w | \hat{U}^\dagger \hat{U} | v \rangle = \langle w | \hat{I} | v \rangle = \langle w | v \rangle. \quad (\text{B.25})$$

Thus, a unitary operator or matrix \hat{U} is one which, when applied to a vector $|x\rangle$, changes only its direction, not its magnitude.

$$U|x\rangle = |y\rangle, \quad \|x\| = \|y\| \quad (\text{B.26})$$

For a certain angle θ , the eigenvalues of \hat{U} all have length 1, as

$$\hat{U}|x\rangle = e^{i\theta}|x\rangle. \quad (\text{B.27})$$

Any 2×2 unitary matrix \hat{U} may be written in the following form²

$$\hat{U} = e^{i\alpha} \begin{bmatrix} e^{i(-\beta/2-\delta/2)} \cos \frac{\gamma}{2} & e^{i(-\beta/2+\delta/2)} \sin \frac{\gamma}{2} \\ e^{i(+\beta/2-\delta/2)} \sin \frac{\gamma}{2} & -e^{i(+\beta/2+\delta/2)} \cos \frac{\gamma}{2} \end{bmatrix}, \quad (\text{B.28})$$

for real numbers α, β, γ , and δ .

Unitary property	Implication	Hamiltonian property	Implication
Unitary	$\hat{U}^\dagger \hat{U} = \hat{I}$	Hermitian	$\hat{H}^\dagger = \hat{H}$
Normal	$\hat{U}^\dagger \hat{U} = \hat{U} \hat{U}^\dagger$	Normal	$\hat{H}^\dagger \hat{H} = \hat{H} \hat{H}^\dagger$
Invertible	$\hat{U}^\dagger = \hat{U}^{-1}$	Energy eigenvalues	$\hat{H} \psi\rangle = E \psi\rangle$
Unit eigenvalues	$ \lambda ^2 = 1$		$E \in \mathbb{R}$
Length-preserving	$\langle \hat{U}\psi \rangle = \langle \psi \rangle$	Composable	$\hat{H} = \hat{H}_0 + \hat{H}_1$

B.4.3 Density matrices

The density matrix $\hat{\rho}$ is a special Hermitian matrix, which is also positive-semidefinite (defined shortly). For $\hat{\rho}$ to be physical (i.e. describe a physical system), it must have two properties, simply stated,

$$\begin{aligned} \textcircled{1} \quad & \text{Tr}(\hat{\rho}) = 1 \\ \textcircled{2} \quad & \lambda_i \geq 0, \forall i. \end{aligned} \quad (\text{B.29})$$

Property **1** represents normalisation, and **2** (where λ_i is an eigenvalue of $\hat{\rho}$) is called positivity*, and is the same as requiring that probabilities be non-negative.

Density matrices evolve under a unitary \hat{U} via

$$\hat{\rho} \rightarrow \hat{U}\hat{\rho}\hat{U}^\dagger, \quad (\text{B.30})$$

and as we already discussed, a Hermitian matrix like $\hat{\rho}$ is diagonalised by a unitary matrix (EQ. B.23). Thus, there exists some unitary which makes $\hat{\rho}$ diagonal. When this happens, we can just read out the eigenvalues of $\hat{\rho}$ from its diagonal, and these eigenvalues are *also* the probabilities of finding $\hat{\rho}$ in its various basis states. Since probabilities must be positive, $\hat{\rho}$'s eigenvalues must also be positive, and so **2** is proven. Another way to see this is presented in ref. 3.

Since $\hat{\rho}$ is positive-semidefinite, it admits a Cholesky decomposition, whereby it can be broken into two lower-triangular matrices, $\hat{\tau}$:

$$\hat{\rho} = \hat{\tau} \cdot \hat{\tau}^\dagger. \quad (\text{B.31})$$

If the diagonal elements of $\hat{\tau}$ are strictly real, EQ. B.31 still holds.

*The terms ‘positive’ and ‘positive-semidefinite’ are interchangeable.

The partial trace

For a state $\hat{\rho}_{AB}$ which describes two subsystems A and B , we can compute the state of each of the two subsystems *when the other is ignored*. This is accomplished via the partial trace. Denote the independent descriptions of A and B as $\hat{\rho}_A$ and $\hat{\rho}_B$. The partial trace accomplishes the following operation:

$$\hat{\rho}_A = \text{Tr}_B(\hat{\rho}_{AB}) \quad \hat{\rho}_B = \text{Tr}_A(\hat{\rho}_{AB}). \quad (\text{B.32})$$

If subsystem B has basis states $\{|b_i\rangle\}$ then the partial trace over B can be written as

$$\hat{\rho}_A = \sum_i \langle b_i | \hat{\rho}_{AB} | b_i \rangle. \quad (\text{B.33})$$

For example, if A and B are qubits, then $\{|b_i\rangle\} = \{|0_B\rangle, |1_B\rangle\}$ (with the subscripts emphasising that we're discussing states of qubit B , only) and

$$\hat{\rho}_A = \langle 0_B | \hat{\rho}_{AB} | 0_B \rangle + \langle 1_B | \hat{\rho}_{AB} | 1_B \rangle. \quad (\text{B.34})$$

If the two qubits are in a Bell state, $\hat{\rho}_{AB} = |\Phi^+\rangle\langle\Phi^+|$, then

$$\begin{aligned} \hat{\rho}_{AB} &= \frac{1}{2} \left(|00\rangle\langle 00| + |11\rangle\langle 11| + |00\rangle\langle 11| + |11\rangle\langle 00| \right) \\ &= \frac{1}{2} \left(|0_A\rangle\langle 0_A| |0_B\rangle\langle 0_B| + |1_A\rangle\langle 1_A| |1_B\rangle\langle 1_B| \right. \\ &\quad \left. + |0_A\rangle\langle 1_A| |0_B\rangle\langle 1_B| + |1_A\rangle\langle 0_A| |1_B\rangle\langle 0_B| \right) \end{aligned} \quad (\text{B.35})$$

so the state of A alone is

$$\begin{aligned} \hat{\rho}_A &= \langle 0_B | \hat{\rho}_{AB} | 0_B \rangle + \langle 1_B | \hat{\rho}_{AB} | 1_B \rangle \\ &= \frac{1}{2} \left[|0_A\rangle\langle 0_A| + |1_A\rangle\langle 1_A| \right], \end{aligned} \quad (\text{B.36})$$

which is completely mixed, as expected from half a maximally entangled state.

B.4.4 Schmidt number

The Schmidt number K reflects the amount of entanglement in a pure state, or the amount of mixture in mixed state. For a bi-photon, K can be determined from the purity of one photon when the other is ignored (i.e. traced over; $K \equiv 1/\mathcal{P}$). For two photons, a signal (s) and an idler (i), in a joint state with complex amplitude* given by $J_{s,i}$,

$$|\psi_{s,i}\rangle \equiv \sum_s \sum_i J_{s,i} |s\rangle |i\rangle, \quad (\text{B.37})$$

which has density matrix

$$\begin{aligned} \hat{\rho}_{s,i} &\equiv |\psi_{s,i}\rangle\langle\psi_{s,i}| = \left(\sum_s \sum_i J_{s,i} |s\rangle |i\rangle \right) \otimes \left(\sum_s \sum_i J_{s,i}^* \langle s | \langle i | \right) \\ &= \sum_{s,i} \sum_{s',i'} J_{s,i} J_{s',i'}^* |s\rangle\langle s'| \otimes |i\rangle\langle i'|. \end{aligned} \quad (\text{B.38})$$

*Modeled on the joint spectrum, $J_{s,i} = J(\nu_s, \nu_i)$.

TABLE B.1: Properties of the creation and annihilation operators.

Property	Expression
Commutation relation	$aa^\dagger - a^\dagger a = 1$
Creation	$a^\dagger n\rangle = \sqrt{n+1} n+1\rangle$
Annihilation	$a n\rangle = \sqrt{n} n-1\rangle$
Normalisation	$ n\rangle = \frac{(a^\dagger)^n}{\sqrt{n!}} 0\rangle$
Time dependence	$a^\dagger(t) = a^\dagger(0)e^{i\omega t}$
Time dependence	$a(t) = a(0)e^{-i\omega t}$
Number operator	$a^\dagger a n\rangle = n n\rangle$

So, if we (arbitrarily) trace out the idler, the signal's reduced density matrix is

$$\begin{aligned}\hat{\rho}_s &\equiv \text{Tr}_i(\hat{\rho}_{s,i}) = \sum_{s,i} \sum_{s',i'} J_{s,i} J_{s',i'}^* |s\rangle\langle s'| \cdot \text{Tr}(|i\rangle\langle i'|) \\ &= \sum_{s,i} \sum_{s',i'} J_{s,i} J_{s',i'}^* |s\rangle\langle s'| \cdot \delta(i, i') \\ &= \sum_{s,i} \sum_{s'} J_{s,i} J_{s,i}^* |s\rangle\langle s'|.\end{aligned}\quad (\text{B.39})$$

We want to know its purity, so we must calculate

$$\begin{aligned}\hat{\rho}_s \cdot \hat{\rho}_s &= \left(\sum_{s,i} \sum_{s'} J_{s,i} J_{s',i}^* |s\rangle\langle s'| \right) \cdot \left(\sum_{s,i} \sum_{s'} J_{s,i} J_{s',i}^* |s\rangle\langle s'| \right) \\ &= \sum_{s,i,s'} \sum_{\sigma,\iota,\sigma'} J_{s,i} J_{s',i}^* J_{\sigma,\iota} J_{\sigma',\iota}^* |s\rangle\langle s'| \langle \sigma' | \sigma' | \\ &= \sum_{s,i,s'} \sum_{\sigma,\iota,\sigma'} J_{s,i} J_{s',i}^* J_{\sigma,\iota} J_{\sigma',\iota}^* |s\rangle\langle \sigma' | \cdot \delta(s', \sigma) \\ &= \sum_{s,i,s',\iota,\sigma'} J_{s,i} J_{s',i}^* J_{s',\iota} J_{\sigma',\iota}^* |s\rangle\langle \sigma' |,\end{aligned}\quad (\text{B.40})$$

then the purity gives us K , via⁴

$\frac{1}{K} = \mathcal{P}(\hat{\rho}_s) \equiv \text{Tr}(\hat{\rho}_s \hat{\rho}_s) = \sum_{s,i,s',\iota} J_{s,i} J_{s',i}^* J_{s',\iota} J_{s,\iota}^*$

(B.41)

§B.5 CREATION AND ANNIHILATION OPERATORS

B.5.1 Properties

Some common properties of creation and annihilation operators are listed in **TABLE B.1**.

B.5.2 Operator evolution (Heisenberg picture)

In the so called Heisenberg picture of quantum mechanics, the evolution of a quantum system is lumped into the evolution of an operator on a fixed initial state. This way of describing the evolution of single photons is useful and intuitive in the context of creation operators operating on the vacuum.

Here, I'll derive in general terms how we can use the evolution of creation operators to describe the evolution of single photons through quantum photonic networks.

Let's assume we have a set of N modes with associated annihilation (field) operators for the inputs $\{a_0, a_1 \dots a_N\}$ and outputs $\{b_0, b_1 \dots b_N\}$ which evolve according to a single-photon unitary operator \hat{U} which takes inputs to outputs, and is equivalent to the unitary scattering matrix which acts on the classical electric field*:

$$\begin{bmatrix} E'_0 \\ \vdots \\ E'_N \end{bmatrix} = \hat{U} \begin{bmatrix} E_0 \\ \vdots \\ E_N \end{bmatrix} \longrightarrow \begin{bmatrix} b_0 \\ \vdots \\ b_N \end{bmatrix} = \hat{U} \begin{bmatrix} a_0 \\ \vdots \\ a_N \end{bmatrix} \quad (\text{B.42})$$

To obtain the rule for transforming input creation operators (a_i^\dagger) to output creation operators (b_i^\dagger), we must solve [EQ. B.42](#) for the $\{a_i^\dagger\}$. Using the invertibility property of unitary matrices ($\hat{U}^{-1} = \hat{U}^\dagger$), the distributive property of the Hermitian conjugate ($(AB)^\dagger = B^\dagger A^\dagger$), and conjugating both sides to obtain relationships for the *creation* operators. Starting with [EQ. B.42](#) and condensing the notation,

$$\begin{aligned} \mathbf{b} &= \hat{U}\mathbf{a} \\ \hat{U}^{-1}\mathbf{b} &= \mathbf{a} \\ \hat{U}^\dagger\mathbf{b} &= \mathbf{a} \\ (\hat{U}^\dagger\mathbf{b})^\dagger &= \mathbf{a}^\dagger \\ \mathbf{b}^\dagger\hat{U} &= \mathbf{a}^\dagger \\ \left[b_0^\dagger \dots b_N^\dagger \right] \hat{U} &= \left[a_0^\dagger \dots a_N^\dagger \right] \end{aligned} \quad (\text{B.43})$$

Thus, the transformation of creation operators proceeds *backwards in time* compared to classical electric fields, and this makes sense considering that a^\dagger is just time-reversed a , which evolves classically according to the quantisation rule. Since we usually right-multiply matrices by vectors, [EQ. B.43](#) may be clearer as:

$$\hat{U}^T \begin{bmatrix} b_0^\dagger \\ \vdots \\ b_N^\dagger \end{bmatrix} = \begin{bmatrix} a_0^\dagger \\ \vdots \\ a_N^\dagger \end{bmatrix} \quad \text{or} \quad a_i^\dagger = \sum_j U_{j,i} b_j^\dagger. \quad (\text{B.44})$$

So a state $|\psi_{\text{in}}\rangle$ encoded in the coefficients A_i evolves according to [EQ. B.44](#) as

$$|\psi_{\text{in}}\rangle \equiv \sum_i A_i a_i^\dagger |\mathbf{0}\rangle \rightarrow \sum_i \sum_j A_i U_{j,i} b_j^\dagger |\mathbf{0}\rangle = |\psi_{\text{out}}\rangle. \quad (\text{B.45})$$

§B.6 HAMILTONIANS & UNITARY EVOLUTION

The results in this section can be found in any introductory quantum mechanics book (e.g. [5,6](#)). The Hamiltonian \hat{H} of a quantum system describes the dynamics of that system via the Schrödinger equation:

$$i\hbar \frac{d}{dt} |\psi(t)\rangle = \hat{H} |\psi(t)\rangle \quad (\text{B.46})$$

*The transfer matrix for the electric field is normally referred to as \hat{S} . I'll keep it as \hat{U} here to emphasise its unitarity, and to keep with the quantum optical literature.

from which follows the general solution (with normalisation constant A)

$$|\psi(t)\rangle = A \exp\left(-\frac{it}{\hbar}\hat{H}\right). \quad (\text{B.47})$$

We can postulate the existence of an operator \hat{U}_{01} which evolves the state from a starting time t_0 to a later time t_1 ,

$$\begin{aligned} \hat{U}_{01}|\psi(t_0)\rangle &= |\psi(t_1)\rangle \\ \hat{U}_{01}A \exp\left(-\frac{it_0}{\hbar}\hat{H}\right) &= A \exp\left(-\frac{it_1}{\hbar}\hat{H}\right) \\ \hat{U}_{01} &= \exp\left(\frac{i(t_0 - t_1)}{\hbar}\hat{H}\right) \end{aligned} \quad (\text{B.48})$$

where on the last line we have used the Baker-Campbell-Hausdorff formula, and the fact that an operator (\hat{H}) commutes with itself. For example, in optics, $t_1 - t_0$ might be the time to traverse an optical path length of interaction, $t \approx L/n_g c$. For convenience, and without loss of generality, we imagine evolution beginning at $t_0 = 0$, and define

$$\hat{U} \equiv \exp\left(-\frac{it}{\hbar}\hat{H}\right) \quad (\text{B.49})$$

B.6.1 Evolution of a photon in a single mode

A photon in a single mode evolves according to the vacuum Hamiltonian of [EQ. B.16](#). We can shift up our energy reference such that the zero-point energy is our new zero point—i.e. $\hat{H} = \hat{H}_{\text{vac}} + \hat{H}_{\text{ZPE}}$. It varies in time according to [EQ. B.49](#), with unitary

$$\hat{U}_{\text{vac}} = e^{-i\omega t(\hat{a}^\dagger \hat{a})} = \sum_{n=0}^{\infty} \frac{(-i\omega t)^n}{n!} (\hat{a}^\dagger \hat{a})^n \quad (\text{B.50})$$

The initial state of such a photon is $|\psi_0\rangle \equiv |1\rangle$. The final state of the photon is then $|\psi_1\rangle \equiv \hat{U}_{\text{vac}}|\psi_0\rangle$. We can use the number operator property of the ladder operators ([TABLE B.1](#)) to find:

$$|\psi_1\rangle = \sum_{n=0}^{\infty} \frac{(-i\omega t)^n}{n!} (\hat{a}^\dagger \hat{a})^n |1\rangle = \sum_{n=0}^{\infty} \frac{(-i\omega t)^n}{n!} (1)^n |1\rangle = e^{-i\omega t} |1\rangle. \quad (\text{B.51})$$

Thus, in a time t , a photon in a single mode acquires a phase of ωt , as expected.

§B.7 OPTICAL ENTANGLING GATES

In this section I discuss the operation of two methods of entangling two photons. The first is mostly pedagogical, and depends on a strong photon-photon nonlinearity. The second is of practical relevance, and relies on post-selection.

B.7.1 Cross-phase modulation

Here, I will show how the $\chi^{(3)}$ cross-phase modulation (XPM) effect can be used to implement an interaction and an entangling operation. See [§1.1.3](#) for discussion.

Applying the XPM Hamiltonian⁷ [EQ. 1.19](#) (see also [§D.1](#)) for an interaction time t , we obtain the unitary

$$\begin{aligned}\hat{U}_{\text{XPM}} &= \exp\left(-i\frac{t}{\hbar}\hat{H}_{\text{XPM}}\right) \\ &= \exp\left[\underbrace{-i2\Phi_1(a^\dagger ab^\dagger b)}_{\hat{x}}\right].\end{aligned}\tag{B.52}$$

Using the results of [TABLE B.1](#), we can see that $a^\dagger a|1\rangle = a^\dagger|0\rangle = |1\rangle$, so we can evaluate

$$\hat{x}|11\rangle = -i2\Phi_1|11\rangle\tag{B.53}$$

and

$$\hat{x}^n|11\rangle = (-i2\Phi_1)^n|11\rangle.\tag{B.54}$$

Now we can evaluate $\hat{U}_{\text{XPM}}|11\rangle$ via the matrix exponential

$$\begin{aligned}\hat{U}_{\text{XPM}}|11\rangle &= \left(\sum_{n=0}^{\infty} \frac{\hat{x}^n}{n!}\right)|11\rangle = \sum_{n=0}^{\infty} \frac{\hat{x}^n|11\rangle}{n!} \\ &= \sum_{n=0}^{\infty} \frac{(-i2\Phi_1)^n|11\rangle}{n!} = \left(\sum_{n=0}^{\infty} \frac{(-i2\Phi_1)^n}{n!}\right)|11\rangle \\ \hat{U}_{\text{XPM}}|11\rangle &= e^{-i2\Phi_1}|11\rangle\end{aligned}\tag{B.55}$$

Travelling the same route with the simpler $|10\rangle$ input state:

$$\hat{x}|01\rangle = \hat{x}^n|01\rangle = 0$$

$$\begin{aligned}\hat{U}_{\text{XPM}}|01\rangle &= \sum_{n=0}^{\infty} \frac{x^n|11\rangle}{n!} \\ &= |01\rangle + \sum_{n=1}^{\infty} \frac{x^n|11\rangle}{n!} \\ &= |01\rangle,\end{aligned}\tag{B.56}$$

and by symmetry, $\hat{U}_{\text{XPM}}|10\rangle = |10\rangle$. Finally, since $\hat{U}|0\rangle = |0\rangle$ for all \hat{U} , $\hat{U}_{\text{XPM}}|00\rangle = |00\rangle$. Thus, if we choose $\Phi_1 = \pi/2$, we find that XPM has the maximally entangling unitary map

$$\hat{U}_{\text{XPM}} = |00\rangle\langle 00| + |01\rangle\langle 01| + |10\rangle\langle 10| - |11\rangle\langle 11|.\tag{B.57}$$

Φ is known as the nonlinear phase shift, and is given (classically) by $\Phi = \gamma PL$, where γ is the nonlinear parameter, P is the pump power, and L is the interaction length. Since our ‘pump’ is a single photon, $P \approx \hbar\omega c/\Lambda$, where Λ is the coherence length of the pump photon. In the presence of loss, the asymptotic maximum effective length is $L_{\max} = 1/\alpha$. Then $\Phi_1 = \gamma\hbar\omega cL_{\max}/\Lambda$. For a silicon waveguide, as detailed in [TABLE 1.3](#), with a 100- μm long pump photon, this works out to about 2 microradians.

B.7.2 The post-selected CSIGN gate

Here I derive the behaviour and discuss the operation of this important interferometer. For discussion, see [§1.1.3](#).

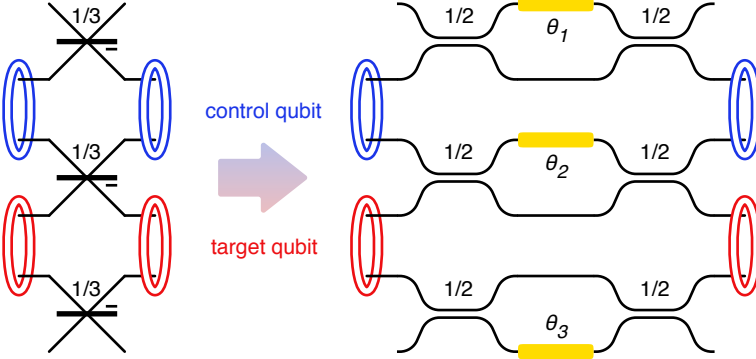


FIG. B.1: The post-selected controlled-Z gate, and the reconfigurable integrated implementation discussed here. Reproduced from [FIG. 1.6](#) for convenience.

The two-qubit CNOT or controlled-NOT gate performs a bit-flip operation (\hat{X}) on its target qubit when its control qubit is in the $|1\rangle$ state, and does nothing otherwise. Likewise, a CSIGN gate performs a sign-flip (\hat{Z}) on its target qubit when its control qubit is $|1\rangle$. The CSIGN, like the CNOT, is also maximally entangling, but entangles a different set of product states, namely those on the equator of the Bloch Sphere. The CSIGN is defined as

$$\text{CSIGN} \equiv |00\rangle\langle 00| + |01\rangle\langle 01| + |10\rangle\langle 10| - |11\rangle\langle 11|. \quad (\text{B.58})$$

The linear optical implementation of the CSIGN is simpler than that of the CNOT, so this gate is preferable. My design replaces the $1/3$ -beamsplitters by on-chip Mach-Zehnder interferometers, such that the effective reflectivity can be varied (see [FIG. B.1](#)). In this way, the $1/3$ operating point can be precisely met (via tuning) and the gate can be reconfigured to the identity (by setting $\theta_i = \pi$).

Let's piece together the qubit-basis operation performed by our on-chip CSIGN gate, as a function of the three interferometer settings, θ_1 , θ_2 , and θ_3 . Each column of the operator's matrix is the output state obtained for each of the four computational basis inputs: $|00\rangle$, $|01\rangle$, $|10\rangle$, and $|11\rangle$. We will examine these in turn.

Since each mode's path passes through an on-chip Mach-Zehnder interferometer, we must know what operation these perform. A Mach-Zehnder interferometer with balanced symmetric couplers, and a phase shifter in the top arm performs the operation

$$\hat{U}_{\text{MZI}} = e^{i\frac{\theta+\pi}{2}} \begin{pmatrix} \sin(\theta/2) & \cos(\theta/2) \\ \cos(\theta/2) & -\sin(\theta/2) \end{pmatrix} \equiv \begin{pmatrix} r & t \\ t & -r \end{pmatrix}. \quad (\text{B.59})$$

Non-interfering configurations

Starting with the qubit state $|00\rangle$, we first translate into creation operators on modes a through d , then evolve those operators through the interferometers.

$$\begin{aligned} |00\rangle &= |010100\rangle = a^\dagger c^\dagger |000000\rangle \\ |\psi_{00}\rangle &= (r_1 r_2 a^\dagger c^\dagger - r_1 t_2 a^\dagger b^\dagger - t_1 r_2 c^\dagger v_t^\dagger + t_1 t_2 b^\dagger v_t^\dagger) |000000\rangle \\ &= r_1 r_2 |010100\rangle - r_1 t_2 |011000\rangle - t_1 r_2 |100100\rangle + t_1 t_2 |101000\rangle. \end{aligned} \quad (\text{B.60})$$

We can now post-select on the qubit basis: i.e. exactly one photon must be in either mode of each qubit. Formally, we will apply the post-selection operator

$\hat{P} = |00\rangle\langle 010100| + |01\rangle\langle 010010| + |10\rangle\langle 001100| + |11\rangle\langle 001010|$ to obtain the $|00\rangle$ column of the on-chip CSIGN operator \hat{C} :

$$\hat{P}|\psi_{00}\rangle = r_1 r_2 |00\rangle. \quad (\text{B.61})$$

Expanding r_1 and r_2 , according to our MZI definition (EQ. B.59), the first column has one element, whose value is

$$\boxed{\hat{P}|\psi_{00}\rangle = + \sin(\theta_1/2) \sin(\theta_2/2) |00\rangle.} \quad (\text{B.62})$$

Similarly, the $|01\rangle$ and $|11\rangle$ columns are, respectively

$$\boxed{\hat{P}|\psi_{01}\rangle = + \sin(\theta_1/2) \sin(\theta_3/2) |01\rangle} \quad (\text{B.63})$$

$$\boxed{\hat{P}|\psi_{11}\rangle = - \sin(\theta_2/2) \sin(\theta_3/2) |11\rangle,} \quad (\text{B.64})$$

where $\hat{P}|\psi_{11}\rangle$ accumulates a minus sign from the reflection of the oppositely oriented interferometers (θ_2 and θ_3 in FIG. B.1) in the $|11\rangle$ configuration.

Interfering configuration

When the input state is $|10\rangle$, the photons composing the two qubits meet at the central interferometer (with phase θ_2) and undergo Hong-Ou-Mandel-type quantum interference. It is this interference which allows the scheme to work, and for this reason we must treat this case separately.

Considering two photons meeting on a MZI

$$\begin{aligned} |10\rangle &= |001100\rangle = b^\dagger c^\dagger |000000\rangle \\ |\psi_{10}\rangle &= (r_2 b^\dagger + t_2 c^\dagger)(t_2 b^\dagger - r_2 c^\dagger) |000000\rangle \\ &= (r_2 t_2 b^{\dagger 2} + t_2 r_2 c^{\dagger 2} + (t_2^2 - r_2^2)b^\dagger c^\dagger) |000000\rangle \\ &= \sqrt{2}r_2 t_2 |002000\rangle + \sqrt{2}t_2 r_2 |000200\rangle + (t_2^2 - r_2^2) |001100\rangle, \end{aligned} \quad (\text{B.65})$$

which, after post-selection, leads to

$$\boxed{\begin{aligned} \hat{P}|\psi_{10}\rangle &= (t_2^2 - r_2^2) |10\rangle \\ &= (\cos^2(\theta_2/2) - \sin^2(\theta_2/2)) |10\rangle = \cos \theta_2 |10\rangle. \end{aligned}} \quad (\text{B.66})$$

Operator

Joining the columns in EQ. B.62, EQ. B.63, EQ. B.66, and EQ. B.64, we obtain the complete matrix for the on-chip CSIGN operator with variable reflectivities.

$$\hat{C} = \begin{pmatrix} +r_1 r_2 & 0 & 0 & 0 \\ 0 & +r_1 r_3 & 0 & 0 \\ 0 & 0 & (t_2^2 - r_2^2) & 0 \\ 0 & 0 & 0 & -r_2 r_3 \end{pmatrix} \quad (\text{B.67})$$

$$\boxed{\begin{aligned} \hat{C} &= \sin\left(\frac{\theta_1}{2}\right) \sin\left(\frac{\theta_2}{2}\right) |00\rangle\langle 00| + \sin\left(\frac{\theta_1}{2}\right) \sin\left(\frac{\theta_3}{2}\right) |01\rangle\langle 01| \\ &\quad + \cos(\theta_2) |10\rangle\langle 10| - \sin\left(\frac{\theta_2}{2}\right) \sin\left(\frac{\theta_3}{2}\right) |11\rangle\langle 11| \end{aligned}} \quad (\text{B.68})$$

For the special case of $\theta_1 = \theta_2 = \theta_3 = \arccos(1/3)$, whereby we use the original $1/3$ reflectivity, we recover the (post-selected) CSIGN operation,

$$\hat{C}|_{1/3} = \frac{1}{3}(|00\rangle\langle 00| + |01\rangle\langle 01| + |10\rangle\langle 10| - |11\rangle\langle 11|) = \frac{\text{CSIGN}}{3}, \quad (\text{B.69})$$

which succeeds $1/9$ of the time, as expected.

Unitarity

The operation described by [EQ. B.68](#) is not in general unitary (or even scaled-unitary). In cases when an operator is non-unitary we cannot use it to handle quantum information. In the case here, most of the $\{\theta_1, \theta_2, \theta_3\}$ space describes operators which apply different loss to qubits in the $|0\rangle$ state and the $|1\rangle$ state, meaning that different states are associated with different success probabilities, and consequently that the success or failure of the gate gives us some information about what that input state was: the gate performs a measurement on the state. For \hat{C} to be unitary:

$$\begin{aligned} \hat{C}^\dagger \hat{C} &= \sin^2\left(\frac{\theta_1}{2}\right) \sin^2\left(\frac{\theta_2}{2}\right) |00\rangle\langle 00| + \sin^2\left(\frac{\theta_1}{2}\right) \sin^2\left(\frac{\theta_3}{2}\right) |01\rangle\langle 01| \\ &\quad + \cos^2(\theta_2) |10\rangle\langle 10| + \sin^2\left(\frac{\theta_2}{2}\right) \sin^2\left(\frac{\theta_3}{2}\right) |11\rangle\langle 11| \quad (\text{B.70}) \\ &= s\hat{I} = s|00\rangle\langle 00| + s|01\rangle\langle 01| + s|10\rangle\langle 10| + s|11\rangle\langle 11| \end{aligned}$$

so all of the following must be simultaneously satisfied for a certain unknown scalar $s \leq 1$:

$$\sin^2\left(\frac{\theta_1}{2}\right) \sin^2\left(\frac{\theta_2}{2}\right) = s \quad (\text{B.71a})$$

$$\sin^2\left(\frac{\theta_1}{2}\right) \sin^2\left(\frac{\theta_3}{2}\right) = s \quad (\text{B.71b})$$

$$\cos^2(\theta_2) = s \quad (\text{B.71c})$$

$$\sin^2\left(\frac{\theta_2}{2}\right) \sin^2\left(\frac{\theta_3}{2}\right) = s. \quad (\text{B.71d})$$

From [EQ. B.71a](#) and b, we see that $\theta_2 = \theta_3$, and from [EQ. B.71b](#) and d, we see that $\theta_1 = \theta_2$, so $\theta \equiv \theta_1 = \theta_2 = \theta_3$. Then [EQ. B.71c](#) reads

$$\begin{aligned} \cos^2(\theta) &= \sin^4\left(\frac{\theta}{2}\right) \\ &= \left(\sin^2\left(\frac{\theta}{2}\right)\right)^2 \\ &= \left(\frac{1 - \cos \theta}{2}\right)^2 \\ &= \frac{1}{4} - \frac{1}{2} \cos \theta + \frac{1}{4} \cos^2 \theta. \end{aligned} \quad (\text{B.72})$$

so we must solve the quadratic equation $0 = -\frac{3}{4}x^2 - \frac{1}{2}x + \frac{1}{4}$ for $x = \cos \theta$:

$$\cos \theta = \frac{\frac{1}{2} \pm \sqrt{\frac{1}{4} + \frac{3}{4}}}{-\frac{3}{2}} = -\frac{1 \pm 2}{3} = \{-1, 1/3\}. \quad (\text{B.73})$$

Therefore, the only unitary configurations of the gate are when $\theta_1 = \theta_2 = \theta_3 = \pi$ ($\hat{C} = \hat{I}$) and when $\theta_1 = \theta_2 = \theta_3 = \arccos(1/3)$ ($\hat{C} = \text{CSIGN}/3$).

- [1] Gerry, C. C. & Knight, P. L. *Introductory Quantum Optics*. (Cambridge University Press, Cambridge, UK, 2005), first edn. [⟨112⟩](#)
- [2] See Eqs. 4.11, 4.12 of ref. [6](#). [⟨116⟩](#)
- [3] James, D. F. V., Kwiat, P. G., Munro, W. J. & White, A. G. Measurement of qubits. *Physical Review A* (2001). [⟨116⟩](#)
- [4] Eberly, J. H. Schmidt analysis of pure-state entanglement. *Laser Physics* **16**, 921–926 (2006). [⟨118⟩](#)
- [5] Griffiths, D. J. *Introduction to quantum mechanics* (Addison-Wesley, Reed College, 2005), second edn. [⟨119⟩](#)
- [6] Nielsen, M. A. & Chuang, I. L. *Quantum computation and quantum information* (Cambridge Univ. Press, Cambridge, 2010), 10th anniversary edn. [⟨119, 125⟩](#)
- [7] Kok, P. Effects of self-phase-modulation on weak nonlinear optical quantum gates. *Physical Review A* **77**, 013808 (2008). [⟨121⟩](#)

Appendix C

Optics

§C.1 ELECTROMAGNETIC WAVE EQUATION

Starting with Maxwell's equations in matter:

$$\nabla \cdot \mathbf{D} = \rho \quad (\text{C.1a})$$

$$\nabla \cdot \mathbf{B} = 0 \quad (\text{C.1b})$$

$$\nabla \times \mathbf{E} = -\dot{\mathbf{B}} \quad (\text{C.1c})$$

$$\nabla \times \mathbf{H} = +\dot{\mathbf{D}} + \mathbf{J} \quad (\text{C.1d})$$

Assume neutral, insulating materials, such that there's no free charge ($\rho = 0$) or current ($\mathbf{J} = 0$). This assumption is valid in semiconductors when the photons energy is less than the band gap energy. We will further assume that the material is non-magnetic, such that $\mathbf{B} = \mu_0 \mathbf{H}$. [EQS. C.1](#) then become

$$\nabla \cdot \mathbf{D} = 0 \quad (\text{C.2a})$$

$$\nabla \cdot \mathbf{B} = 0 \quad (\text{C.2b})$$

$$\nabla \times \mathbf{E} = -\dot{\mathbf{B}} \quad (\text{C.2c})$$

$$\nabla \times \mathbf{B} = \mu_0 \dot{\mathbf{D}} \quad (\text{C.2d})$$

Following the standard treatment [1-3](#), we take the curl of the electric field curl equation [EQ. C.2c](#), and substitute for $\nabla \times \mathbf{B}$ using the time derivative of Ampere's law [EQ. C.2d](#).

$$\nabla \times (\nabla \times \mathbf{E}) = -\nabla \times \dot{\mathbf{B}} = -\mu_0 \ddot{\mathbf{D}} \quad (\text{C.3})$$

Then we can use the identity $\nabla \times \nabla \times \mathbf{E} = \nabla(\nabla \cdot \mathbf{E}) - \nabla^2 \mathbf{E}$ (and assume that the first term either vanishes, or can be safely neglected, such as when $\rho = 0$) and the constitutive relation $\mathbf{D} = \epsilon_0 \mathbf{E} + \mathbf{P}$ to obtain*

$$\nabla^2 \mathbf{E} = \mu_0 \epsilon_0 \ddot{\mathbf{E}} + \mu_0 \dot{\mathbf{P}} \quad (\text{C.4})$$

C.1.1 Linear media

To obtain the linear wave equation, we simply assume that the material polarisation is proportional to the electric field, $\mathbf{P} = \epsilon_0 \chi \mathbf{E}$. Since $\epsilon \equiv \epsilon_0(1 + \chi)$, we can simplify

*See equation 2.1.11 of [1](#) or equation 2.26 of [2](#)

EQ. C.4 to its familiar form

$$\begin{aligned}\nabla^2 \mathbf{E} &= \mu_0 \epsilon_0 \ddot{\mathbf{E}} + \mu_0 \ddot{\mathbf{P}} \\ &= \mu_0 \epsilon_0 \ddot{\mathbf{E}} + \mu_0 (\epsilon_0 \chi \ddot{\mathbf{E}}) \\ &= \mu_0 \epsilon_0 (1 + \chi) \ddot{\mathbf{E}} \\ &= \mu_0 \epsilon \ddot{\mathbf{E}}\end{aligned}\tag{C.5}$$

which is the canonical vector wave equation.

Similarly, we can use **Eqs. C.2c,d** in the opposite order, and obtain the wave equation in terms of the magnetic field:

$$\nabla^2 \mathbf{B} = \mu_0 \epsilon \ddot{\mathbf{B}}.\tag{C.6}$$

C.1.2 Nonlinear media

In nonlinear media, we cannot in general assume a particular form (or even time response) of the material polarisation $\mathbf{P}(t, \mathbf{E})$, but if we assume an instantaneous Kerr nonlinearity, as is the case in silicon, we can get somewhere. These assumptions translate to a polarisation which responds instantaneously to the electric field with non-zero first and third orders:

$$\mathbf{P} = \epsilon_0 (\chi^{(1)} \mathbf{E} + \chi^{(3)} \mathbf{E}^3).\tag{C.7}$$

Now we can

$$\begin{aligned}\nabla^2 \mathbf{E} &= \mu_0 \epsilon_0 \ddot{\mathbf{E}} + \mu_0 \ddot{\mathbf{P}} \\ &= \mu_0 \epsilon_0 \ddot{\mathbf{E}} + \mu_0 \epsilon_0 (\chi^{(1)} \ddot{\mathbf{E}} + \chi^{(3)} \frac{\partial^2 (\mathbf{E}^3)}{\partial t^2}) \\ &= \mu_0 \epsilon \ddot{\mathbf{E}} + \mu_0 \epsilon_0 (\chi^{(3)} (6 \dot{\mathbf{E}}^2 \mathbf{E} + 3 \mathbf{E}^2 \ddot{\mathbf{E}})).\end{aligned}\tag{C.8}$$

Note that $\epsilon_0 = \epsilon / n^2$, and $n_2 = 12\pi^2 \chi^{(3)} / n^2$, so we can simplify **EQ. C.8** to

$$\begin{aligned}\nabla^2 \mathbf{E} &= \mu_0 \epsilon \ddot{\mathbf{E}} + \mu_0 \epsilon \left(\frac{3 \chi^{(3)}}{n^2} (2 \dot{\mathbf{E}}^2 \mathbf{E} + \mathbf{E}^2 \ddot{\mathbf{E}}) \right) \\ &= \mu_0 \epsilon \ddot{\mathbf{E}} + \mu_0 \epsilon \left(\frac{n_2}{4\pi^2} (2 \dot{\mathbf{E}}^2 \mathbf{E} + \mathbf{E}^2 \ddot{\mathbf{E}}) \right) \\ &= \underbrace{\mu_0 \epsilon \left(1 + \frac{n_2}{4\pi^2} E^2 \right) \ddot{\mathbf{E}}}_{\text{Nonlinear propagation}} + \underbrace{\mu_0 \epsilon \left(\frac{n_2}{2\pi^2} \dot{\mathbf{E}}^2 \mathbf{E} \right)}_{\text{Nonlinear absorption}}\end{aligned}\tag{C.9}$$

§C.2 WAVEGUIDES

C.2.1 Two-dimensional confinement

Starting from the wave equation in linear media (**§C.1.1**) with $\mathbf{F} \in \{\mathbf{E}, \mathbf{B}\}$

$$\nabla^2 \mathbf{F} = \mu_0 \epsilon \ddot{\mathbf{F}},\tag{C.10}$$

we insert harmonic solutions, propagating in z and not changing transverse shape: $\mathbf{F} = \mathcal{F}(x, y) e^{i\beta z - i\omega t}$.

In cartesian coordinates,

$$\nabla^2 \mathbf{A} = x \nabla^2 (\mathbf{A} \cdot \mathbf{x}) + y \nabla^2 (\mathbf{A} \cdot \mathbf{y}) + z \nabla^2 (\mathbf{A} \cdot \mathbf{z}),\tag{C.11}$$

so we can evaluate

$$\nabla^2 \mathbf{F} = \nabla^2 (\mathcal{F}(x, y) e^{i\beta z - i\omega t}) = \nabla^2 \mathcal{F} e^{i\beta z - i\omega t} - \beta^2 \mathcal{F} e^{i\beta z - i\omega t}. \quad (\text{C.12})$$

The time derivative in [EQ. C.10](#) is

$$\ddot{\mathbf{F}} = \frac{\partial^2}{\partial t^2} (\mathcal{F} e^{i\beta z - i\omega t}) = -\omega^2 \mathcal{F} e^{i\beta z - i\omega t} \quad (\text{C.13})$$

Finally then, without specifying the direction of \mathcal{F} , we can insert [Eqs. C.12](#) and [C.13](#) back into [EQ. C.10](#), noting that $\mu_0 \epsilon = n^2/c^2$, and $k \equiv n\omega/c$, to obtain

$$\begin{aligned} (\nabla^2 \mathcal{F} e^{i\beta z - i\omega t} - \beta^2 \mathcal{F} e^{i\beta z - i\omega t}) &= \mu_0 \epsilon (-\omega^2 \mathcal{F} e^{i\beta z - i\omega t}) \\ \nabla^2 \mathcal{F} - \beta^2 \mathcal{F} &= -\frac{n^2}{c^2} \omega^2 \mathcal{F} \\ \nabla^2 \mathcal{F} - \beta^2 \mathcal{F} &= -k^2 \mathcal{F} \end{aligned} \quad (\text{C.14})$$

$$\boxed{\nabla^2 \mathcal{F} = (\beta^2 - k^2) \mathcal{F}}, \quad (\text{C.15})$$

the vector Helmholtz equation for transverse waves. To find the modes of a waveguide, [EQ. C.15](#) must be solved for its eigenvalue ($\beta^2 - k^2$) throughout all space, without forgetting that $k = nk_0$ depends on the local refractive index (which is likely not constant, if it's a good waveguide).

C.2.2 One-dimensional confinement

In this appendix, I will solve for the modes and propagation constants for a one-dimensional slab waveguide. For discussion, see [§1.3.1](#).

We will search for a mode propagating in the $+z$ direction, TE polarised along x , such that

$$\mathbf{E}(\mathbf{r}, t) = \mathcal{E}_x(y) e^{i\beta z - i\omega t} \mathbf{x}. \quad (\text{C.16})$$

Our task is to determine the eigenmode \mathcal{E}_x (the transverse electric field amplitude) and the eigenvalue β (the complex propagation constant). We will insert [EQ. C.16](#) into the wave equation [EQ. C.5](#) from [§C.1](#) to obtain the eigenvalue equation. First let's compute the vector Laplacian,

$$\begin{aligned} \nabla^2 \mathbf{E} &= \nabla^2 (\mathbf{E} \cdot \mathbf{x}) \mathbf{x} + \underbrace{\nabla^2 (\mathbf{E} \cdot \mathbf{y})}_{0} \mathbf{y} + \underbrace{\nabla^2 (\mathbf{E} \cdot \mathbf{z})}_{0} \mathbf{z} \\ &= \left(\underbrace{\frac{\partial^2}{\partial x^2} (\mathbf{E} \cdot \mathbf{x})}_{0} + \frac{\partial^2}{\partial y^2} (\mathbf{E} \cdot \mathbf{x}) + \frac{\partial^2}{\partial z^2} (\mathbf{E} \cdot \mathbf{x}) \right) \mathbf{x} \\ &= \left(\frac{\partial^2}{\partial y^2} (\mathcal{E}_x(y) e^{i\beta z - i\omega t}) + \frac{\partial^2}{\partial z^2} (\mathcal{E}_x(y) e^{i\beta z - i\omega t}) + 0 \right) \mathbf{x} \\ &= e^{i\beta z - i\omega t} (\mathcal{E}_x'' - \beta^2 \mathcal{E}_x) \mathbf{x}, \end{aligned} \quad (\text{C.17})$$

and the second time derivative, $\ddot{\mathbf{E}} = -\mathcal{E}_x \omega^2 e^{i\beta z - i\omega t} \mathbf{x}$. We can then combine the two sides of [EQ. C.5](#) to find the eigenvalue equation

$$\mathcal{E}_x'' + (n^2 k_0^2 - \beta^2) \mathcal{E}_x = 0 \quad (\text{C.18})$$

where we defined $n^2/c^2 = \mu_0\epsilon$ and used $k_0 = \omega/c$. Compare this with the full transverse version [EQ. C.15](#). This index n is the *material* index, corresponding to the material in which [EQ. C.18](#) is being evaluated: n_{top} for the top cladding, n_{core} for the core, and n_{bot} for the bottom cladding. [EQ. C.18](#) is the homogeneous Helmholtz equation with eigenvalue $\kappa^2 \equiv n^2 k_0^2 - \beta^2$. The electric field curl equation ([EQ. C.2c](#)) reads

$$i\beta E_x \mathbf{y} + \frac{\partial E_x}{\partial y} \mathbf{z} = -i\omega B_y \mathbf{y} - i\omega B_z \mathbf{z} \quad (\text{C.19})$$

and since \mathbf{B} is continuous across the interfaces, we know that E_x and E'_x are also continuous. Our task is to solve the boundary value problem of [EQ. C.18](#) while enforcing the boundary conditions for the two dielectric interfaces—the transverse electric field must be smooth. Defining the top interface at $y = t$ and the bottom at $y = 0$, the boundary conditions are:

$$\lim_{y \rightarrow 0^+} \mathbf{E}(y) \cdot \mathbf{x} = \lim_{y \rightarrow 0^-} \mathbf{E}(y) \cdot \mathbf{x} \quad (\text{C.20a})$$

$$\lim_{y \rightarrow 0^+} \mathbf{E}'(y) \cdot \mathbf{x} = \lim_{y \rightarrow 0^-} \mathbf{E}'(y) \cdot \mathbf{x} \quad (\text{C.20b})$$

$$\lim_{y \rightarrow t^+} \mathbf{E}(y) \cdot \mathbf{x} = \lim_{y \rightarrow t^-} \mathbf{E}(y) \cdot \mathbf{x} \quad (\text{C.20c})$$

$$\lim_{y \rightarrow t^+} \mathbf{E}'(y) \cdot \mathbf{x} = \lim_{y \rightarrow t^-} \mathbf{E}'(y) \cdot \mathbf{x}. \quad (\text{C.20d})$$

If the field is guided, we obtain two additional conditions as $y \rightarrow \pm\infty$. Thus, the field decays exponentially in the top and bottom cladding, and oscillates in the core. Our piecewise general expression for \mathcal{E}_x then reads

$$\mathcal{E}_x(y) = \begin{cases} B_t e^{-\kappa_t y}, & t < y \\ A_c e^{i\kappa_c y} + B_c e^{-i\kappa_c y}, & 0 < y < t \\ A_b e^{\kappa_b y}, & y < 0 \end{cases} \quad (\text{C.21})$$

Here, to satisfy [EQ. C.18](#), we have defined the quantities

$$\kappa_t = \sqrt{\beta^2 - n_t^2 k_0^2} \quad \kappa_c = \sqrt{n_c^2 k_0^2 - \beta^2} \quad \kappa_b = \sqrt{\beta^2 - n_b^2 k_0^2}. \quad (\text{C.22})$$

The boundary conditions ([EQS. C.20a–d](#)) now read

$$A_c + B_c = A_b \quad (\text{C.23a})$$

$$i\kappa_c(A_c - B_c) = \kappa_b A_b \quad (\text{C.23b})$$

$$B_t e^{-\kappa_t t} = A_c e^{i\kappa_c t} + B_c e^{-i\kappa_c t} \quad (\text{C.23c})$$

$$-\kappa_t B_t e^{-\kappa_t t} = i\kappa_c(A_c e^{i\kappa_c t} - B_c e^{-i\kappa_c t}). \quad (\text{C.23d})$$

Eliminating A_b from [EQ. C.20b](#) using [EQ. C.20a](#), eliminating $B_t e^{-\kappa t}$ from [EQ. C.20d](#) using [EQ. C.20c](#), then combining these to eliminate A_c and B_c , we arrive at the eigenvalue equation for β :

$$e^{-2i\kappa_c t} = \left(\frac{\kappa_c - i\kappa_b}{\kappa_c + i\kappa_b} \right) \left(\frac{\kappa_c - i\kappa_t}{\kappa_c + i\kappa_t} \right) \quad (\text{C.24})$$

Using the identity $\frac{i}{2} \log(\frac{1-iz}{1+iz}) = \arctan z + j\pi$, for $j \in \mathbb{Z}$, this can be rewritten in the standard form^{[3,4](#)}:

$$\kappa_c t + j\pi = \arctan\left(\frac{\kappa_b}{\kappa_c}\right) + \arctan\left(\frac{\kappa_t}{\kappa_c}\right).$$

(C.25)

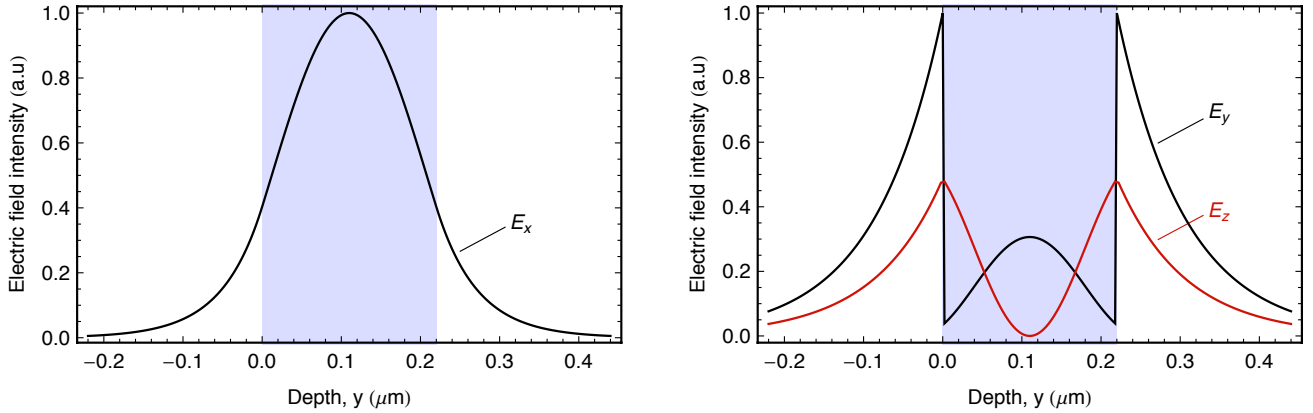


FIG. C.1: The fundamental guided TE (left, $n_{\text{eff}} = 2.83$) and TM (right, $n_{\text{eff}} = 2.07$) modes of a 220- μm -thick silicon slab embedded in silica. No higher order modes propagate. In the TM case, both non-zero electric fields are shown.

Given top, bottom, and core refractive indices (n_t , n_b , n_c), the slab thickness (t), and the wavelength ($\lambda = k_0/2\pi$), we can solve [EQ. C.25](#) for the m^{th} mode, then use [EQ. C.21](#) and [EQ. C.22](#) to obtain the mode profile $\mathcal{E}_x(y)$. As an example, the fundamental—and only—guided TE mode of a 220- μm -thick silicon slab is shown in [FIG. C.1](#).

TM slab modes are obtained by a similar process, but instead of the boundary conditions [EQS. C.20a-d](#), we find a discontinuity at the two interfaces, since the perpendicular *displacement field* (D) is continuous at the interface. Both TE and TM have continuous electric field first derivatives, since the material is taken as non-magnetic. Analogous to how the TE mode has only the electric y -component non-zero, the TM mode has only the magnetic y -component non-zero, and the electric field has non-zero x and z components.

We can solve the magnetic wave equation in the same way, defining the magnetic field as:

$$\mathbf{B}(\mathbf{r}, t) = \mathcal{B}_x(y)e^{i\beta z - i\omega t}\mathbf{x}, \quad (\text{C.26})$$

then enforcing boundary conditions at the interfaces. The magnetic field curl equation ([EQ. C.2d](#)) reads

$$i\beta B_x \mathbf{y} + \frac{\partial B_x}{\partial y} \mathbf{z} = -i\omega \mu_0 D_y \mathbf{y} + -i\omega \frac{n^2}{c^2} E_z \mathbf{z} \quad (\text{C.27})$$

and since D_y is continuous across the interfaces, so is B_x ; however, B'_x has a discontinuity, as it depends on n^{-2} . We now must solve the boundary value problem satisfying [EQ. C.6](#) with the above conditions at each interface. Omitting the details, we arrive at the TM eigenvalue equation:

$$\kappa_c t + j\pi = \arctan\left(\frac{n_c^2 \kappa_b}{n_b^2 \kappa_c}\right) + \arctan\left(\frac{n_c^2 \kappa_t}{n_t^2 \kappa_c}\right). \quad (\text{C.28})$$

§C.3 EVANESCENT COUPLERS

In this section, I use coupled-mode theory to model the effect of directional evanescent coupling between waveguides—i.e. an *evanescent coupler*. See [§1.3.2](#) for dis-

cussion. For co-propagating fields, the coupled mode approximation⁵ takes the field in the one waveguide (b) as a perturbation on the polarisation of the other waveguide (a). I'll assume the medium remains linear in the electric fields of both waveguides, such that the two fields are coupled together through the medium⁵:

$$\begin{aligned}\mathbf{P}_a &= \epsilon_0(\chi\mathbf{E}_a + \chi_{ab}\mathbf{E}_b) \\ \mathbf{P}_b &= \epsilon_0(\chi\mathbf{E}_b + \chi_{ab}\mathbf{E}_a).\end{aligned}\quad (\text{C.29})$$

We can write [EQ. C.5](#) as a set of two equations, one for each mode, inserting the expressions for the coupled polarisation ([EQ. C.29](#)), and letting $E_i \equiv \mathbf{E}_i \cdot \mathbf{x}$

$$\nabla^2 \mathbf{E} = \mu_0 \epsilon_0 \ddot{\mathbf{E}} + \mu_0 \ddot{\mathbf{P}} \rightarrow \begin{cases} \frac{\partial^2 E_a}{\partial z^2} = \mu_0 \epsilon \ddot{E}_a + \mu_0 \epsilon_0 \chi_{ba} \ddot{E}_b \\ \frac{\partial^2 E_b}{\partial z^2} = \mu_0 \epsilon \ddot{E}_b + \mu_0 \epsilon_0 \chi_{ab} \ddot{E}_a \end{cases} \quad (\text{C.30})$$

As an example, if we assume phase-matched travelling-wave solutions $E_a(z, t) = \mathcal{E}_a(z) \exp(i\beta z \pm i\omega t)$ and $E_b(z, t) = \mathcal{E}_b(z) \exp(i\beta z \pm i\omega t)$ (with $\beta \equiv \beta_a = \beta_b$), and evaluate the product rule on the LHS of [EQ. C.30](#), and the time derivatives on the RHS,

$$\frac{\partial^2 E}{\partial z^2} = \frac{\partial^2}{\partial z^2} (\mathcal{E} \exp(i\beta z \pm i\omega t)) = \exp(i\beta z \pm i\omega t) \left(\frac{\partial^2 \mathcal{E}}{\partial z^2} + 2i\beta \frac{\partial \mathcal{E}}{\partial z} - \beta^2 \mathcal{E} \right) \quad (\text{C.31})$$

$$\frac{\partial^2 E}{\partial t^2} = \frac{\partial^2}{\partial t^2} (\mathcal{E} \exp(i\beta z \pm i\omega t)) = \exp(i\beta z \pm i\omega t) (-\omega^2 \mathcal{E}). \quad (\text{C.32})$$

then, rewriting [EQ. C.30](#), and treating the case where $\beta = \omega/v$, in which the two waveguides are balanced and have (identical) normal dispersion, we find

$$\begin{aligned}\frac{\partial^2 \mathcal{E}_a}{\partial z^2} + 2i\frac{\omega}{v} \frac{\partial \mathcal{E}_a}{\partial z} &= -\chi_{ab} \frac{\omega^2}{c^2} \mathcal{E}_b \\ \frac{\partial^2 \mathcal{E}_b}{\partial z^2} + 2i\frac{\omega}{v} \frac{\partial \mathcal{E}_b}{\partial z} &= -\chi_{ab} \frac{\omega^2}{c^2} \mathcal{E}_a.\end{aligned}\quad (\text{C.33})$$

These become the usual coupled mode equations if we assume a slowly varying envelope and consequently neglect the second derivative term⁵. Solving [EQ. C.33](#) using the boundary conditions $\mathcal{E}_a(0) = 1$ and $\mathcal{E}_b(0) = \mathcal{E}'_a(0) = \mathcal{E}'_b(0) = 0$,

$$\begin{aligned}\mathcal{E}_a(z) &= \frac{e^{-i\beta z}}{2} \left\{ \cos(zk_0 n_+) + \cos(zk_0 n_-) + i \left(\frac{nn_-}{n_-^2} \sin(zk_0 n_+) + \frac{nn_+}{n_-^2} \sin(zk_0 n_-) \right) \right\} \\ \mathcal{E}_b(z) &= \frac{e^{-i\beta z}}{2} \left\{ \cos(zk_0 n_+) - \cos(zk_0 n_-) + i \left(\frac{nn_-}{n_-^2} \sin(zk_0 n_+) - \frac{nn_+}{n_-^2} \sin(zk_0 n_-) \right) \right\}\end{aligned}\quad (\text{C.34})$$

where $n_{\pm} \equiv \sqrt{\chi \pm \chi_{ab} + 1}$. The approximate form, assuming a slowly varying envelope, and allowing $\mathcal{E}_a(0)$ and $\mathcal{E}_b(0)$ to be free, is more informative:

$$\mathcal{E}_a(z) \approx \mathcal{E}_a(0) \cos\left(z \frac{k_0 \chi_{ab}}{2n}\right) + i \mathcal{E}_b(0) \sin\left(z \frac{k_0 \chi_{ab}}{2n}\right) \quad (\text{C.35a})$$

$$\mathcal{E}_b(z) \approx i \mathcal{E}_a(0) \sin\left(z \frac{k_0 \chi_{ab}}{2n}\right) + \mathcal{E}_b(0) \cos\left(z \frac{k_0 \chi_{ab}}{2n}\right) \quad (\text{C.35b})$$

and nicely shows the oscillating power balance between the two waveguides, as well as the $\pi/2$ phase shift which is acquired by the transmitted field. Here, n is the effective refractive index of the fundamental mode of the two (identical) waveguides. The critical length of the coupler (i.e. when the power in waveguide a returns to its original value) is

$$z_{\text{crit}} = \frac{2n\pi}{\chi_{ab}k_0} = \frac{n\lambda}{\chi_{ab}} \quad (\text{C.36})$$

which can be compared to the standard result⁴ in terms of the *coupling coefficient* κ as:

$$z_{\text{crit}} = \frac{\pi}{\kappa} \quad (\text{C.37})$$

so we can identify $2n/\chi_{ab}k_0 = 1/\kappa$ and $\kappa = \chi_{ab}k_0/2n$.

Eq. C.35 also gives us directly the scattering matrix of the evanescent coupler:

$$\hat{U}_{\text{EC}} = \begin{pmatrix} \cos(\pi z/z_{\text{crit}}) & i \sin(\pi z/z_{\text{crit}}) \\ i \sin(\pi z/z_{\text{crit}}) & \cos(\pi z/z_{\text{crit}}) \end{pmatrix}. \quad (\text{C.38})$$

We can identify the reflectivity $\eta = \cos^2(\pi z/z_{\text{crit}})$, so to get a $\eta = 50\%$ beamsplitter, we need $z = z_{\text{crit}}/4$.

§C.4 RING RESONANCE

This section runs through the calculation to obtain the pertinent parameters of a ring resonance. Discussion is in §1.3.2.

The equations relating the four frequency-domain* complex field amplitudes (loosely termed 'fields') in the ring resonator are as follows. The evanescent coupler (reflectivity $\eta = r^2 = 1 - t^2$, with r and t real) relates the fields inside and outside the loop,

$$\begin{aligned} E_l &= rE'_l + itE \\ E' &= itE'_l + rE \end{aligned} \quad (\text{C.39})$$

and propagation through the loop decreases the field amplitude by η and adds a phase ϕ (both real quantities),

$$E'_l = E_l \eta e^{i\phi}. \quad (\text{C.40})$$

This phase ϕ depends on the wavelength of the incident light λ and the optical path length of the ring, nL , where n is the refractive index (n_{eff} in a waveguide) and L is the geometric length,

$$\phi = kL = 2\pi \frac{nL}{\lambda} = 2\pi\nu \frac{nL}{c} = \omega \frac{nL}{c}. \quad (\text{C.41})$$

The factor η is the round-trip loss of the *field*, such that the circulating power is reduced by a factor of η^2 after one round trip. We can solve for the three unknown quantities: the fields at the beginning and end of the loop, E_l , E'_l ; and the field at the output, E' :

$$E_l = E \frac{it}{r\eta e^{i\phi} - 1} \quad (\text{C.42a})$$

*A time-domain model is also possible. See for example 6.

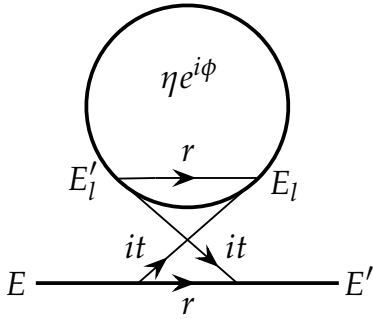
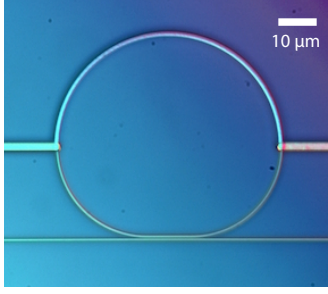


FIG. C.2: Optical micrograph of a microring resonator, and diagram labelling fields and relationships for the ring resonator model of §C.4.

$$E'_l = \eta e^{i\phi} E_l \quad (\text{C.42b})$$

$$E' = E \frac{r - \eta e^{i\phi}}{r \eta e^{i\phi} - 1} \quad (\text{C.42c})$$

or, in terms of intensity, where $P \equiv |E|^2$:

$$P_l \equiv |E_l|^2 = P \frac{t^2}{1 + r^2 \eta^2 - 2r\eta \cos \phi} \quad (\text{C.43a})$$

$$P'_l \equiv |E'_l|^2 = \eta^2 |E_l|^2 \quad (\text{C.43b})$$

$$P' \equiv |E'|^2 = P \frac{r^2 + \eta^2 - 2r\eta \cos \phi}{1 + r^2 \eta^2 - 2r\eta \cos \phi}. \quad (\text{C.43c})$$

We can quantify the effect of the resonator on the field using the field enhancement factor, F , defined below. Assuming we are close to a resonance ($\phi \rightarrow 0$), the lineshape is Lorentzian, and

$$F \equiv \left| \frac{E_l}{E} \right| = \left| \frac{it}{r \eta e^{i\phi} - 1} \right| \approx \sqrt{\frac{1 - r^2}{(1 - r\eta)^2 + r\eta\phi^2}} \quad (\text{C.44})$$

is known as the field enhancement factor and is useful for treating light-matter interactions. It represents the resonant scaling of the intra-cavity field as compared to the field outside the resonator.

On resonance ($\phi = 2m\pi, m \in \mathbb{Z}$), **Eqs. C.43a–c** become

$$P_l = P \frac{t^2}{(1 - r\eta)^2} \quad (\text{C.45a})$$

$$P'_l = \eta^2 P_l \quad (\text{C.45b})$$

$$P' = P \frac{(r - \eta)^2}{(1 - r\eta)^2}, \quad (\text{C.45c})$$

and the critical coupling condition can be seen, when $r = \eta$, in which $|E'|^2$ (**Eq. C.45c**) becomes zero—i.e. no light is transmitted past the resonator, and all incident light is coupled inside and absorbed or scattered.

The m^{th} resonance (reading from **Eq. C.41**) occurs at

$$k_m = \frac{2m\pi}{L} \quad \nu_m = \frac{mc}{n(\nu_m)L} \quad (\text{C.46})$$

Evidently resonances occur evenly distributed in wavevector, with a pitch of $2\pi/L$. The free spectral range (FSR, ν_0) of the resonator is the distance between resonances

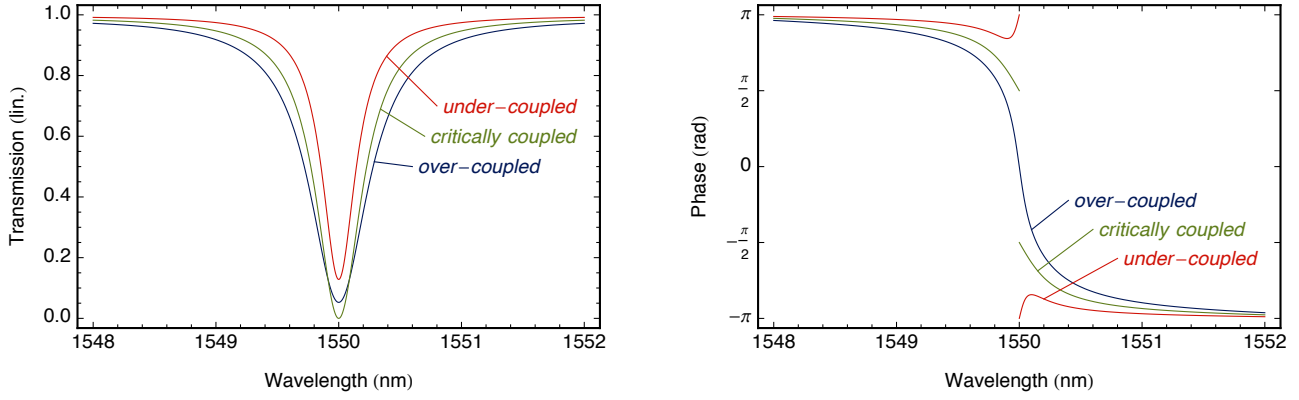


FIG. C.3: Power (left) and phase (right) spectra of a ring resonance in the three coupling regimes. Round-trip transmission $\eta = 0.8$ and $n_g L = 40 \mu\text{m}$. From [EQ. C.42c](#), $|E'(\lambda)|$ and $\arg\{E'(\lambda)\}$.

in either wavelength or frequency, and is also the inverse of the cavity round-trip time T_0 . For high-order resonances ($m \gg 1$) the FSR in frequency units is given by

$$\nu_0 \equiv \frac{c}{n_g L} \equiv \frac{1}{T_0} \quad (\text{C.47})$$

where n_g is the group index ([EQ. 1.27](#)) and L is the cavity length.

The linewidth is the FWHM of any of the [Eqs. C.45](#). Looking at [EQ. C.43a](#) and [EQ. C.45a](#), we want to find the ϕ which makes the off-resonance response half as big as the on-resonance one. In other words, we want to find the $\phi_{1/2}$ which solves

$$\frac{P_l(\phi_{1/2})}{P_l(0)} = \frac{P'_l(\phi_{1/2})}{P'_l(0)} = \frac{P'(\phi_{1/2})}{P'(0)} = \frac{1 + r^2\eta^2 - 2r\eta}{1 + r^2\eta^2 - 2r\eta \cos \phi_{1/2}} = \frac{1}{2} \quad (\text{C.48})$$

If $\phi_{1/2}$ is small, then $\cos \phi_{1/2} = 1 - \phi_{1/2}^2/2$ and [EQ. C.48](#) becomes

$$\phi_{1/2} = \pm \frac{1 - r\eta}{\sqrt{r\eta}}. \quad (\text{C.49})$$

So the phase required to cover the FWHM is $2|\phi_{1/2}|$ or

$$2|\phi_{1/2}| = 2\pi\Delta\nu \frac{nL}{c} \rightarrow \Delta\nu = \frac{|\phi_{1/2}|c}{\pi nL} = \frac{c}{\pi nL} \frac{1 - r\eta}{\sqrt{r\eta}} \quad (\text{C.50a})$$

$$2|\phi_{1/2}| \approx 2\pi\Delta\lambda \frac{nL}{\lambda^2} \rightarrow \Delta\lambda \approx 2|\phi_{1/2}| \frac{\lambda^2}{2\pi nL} = \frac{\lambda^2}{\pi nL} \frac{1 - r\eta}{\sqrt{r\eta}} \quad (\text{C.50b})$$

where $\Delta\nu$ and $\Delta\lambda$ are the FWHM in frequency and wavelength, respectively. [Eqs. C.50](#) are valid only if the linewidth is small; if not, then [EQ. C.48](#) must be used. [EQ. C.50b](#) assumes that $\Delta\lambda \ll \lambda$.

Two other figures of merit are often used to describe resonator performance. The quality factor Q describes the sharpness of a cavity resonance, where

$$Q \equiv \frac{\nu}{\Delta\nu} = \frac{\lambda}{\Delta\lambda}. \quad (\text{C.51})$$

For a resonator which is critically coupled ($r = \eta$), low loss ($\eta \approx 1$), and on resonance, the field enhancement factor (Eq. C.44) can be conveniently recast in terms of Q and the resonance order m :

$$F = \frac{1}{t} \approx \sqrt{\frac{Q\nu_0}{\pi\nu}} \approx \sqrt{\frac{Q}{\pi m}}. \quad (\text{C.52})$$

Finally, the amount of light scattered by the cavity on resonance is measured by the cavity's extinction, which is given in decibels as

$$20 \left(\log_{10} |r - \eta| - \log_{10} |1 - r\eta| \right) \text{ dB} \quad (\text{C.53})$$

Reference 7 contains many detailed considerations of ring resonators, as well as their geometries in various material systems.

§C.5 QUANTUM DESCRIPTION OF LASER LIGHT

The coherent state is a quantum description of a bright light with Poissonian photon statistics, like a laser. It is a very useful tool when describing joint systems of bright and quantum light, as is the case in parametric processes like SFWM (§D). Some properties of the coherent state are listed in TABLE C.1

TABLE C.1: Properties of the coherent state $|\alpha\rangle$ from ref. 8.

Property	Value
Definition	$ \alpha\rangle \equiv e^{- \alpha ^2/2} \sum_{n=0}^{\infty} \alpha^n n\rangle / \sqrt{n!}$
Mean photon number	$\langle \alpha a^\dagger a \alpha \rangle = \alpha ^2$
Eigenstate (right)	$a \alpha\rangle = \alpha \alpha\rangle$
Eigenstate (left)	$\langle \alpha a^\dagger = \alpha^* \langle \alpha $
Displacement operator	$\hat{D}(\alpha) \equiv \exp(\alpha a^\dagger - \alpha^* a)$ $\hat{D}(\alpha) 0\rangle = \alpha\rangle$

C.5.1 Bright light on a beamsplitter

When a coherent state is presented at one input of a symmetric beamsplitter, the state of light evolves as follows. Starting with a coherent state of $|\alpha|^2$ photons in mode b ,

$$|\alpha\rangle \equiv \hat{D}(\alpha)|0\rangle \equiv \exp(\alpha b^\dagger - \alpha^* b) |0\rangle \quad (\text{C.54})$$

we pass through the beamsplitter (between modes b and d), whereby $b \rightarrow \sqrt{\eta}b - i\sqrt{1-\eta}d$, and $b^\dagger \rightarrow \sqrt{\eta}b^\dagger + i\sqrt{1-\eta}d^\dagger$, for a reflectivity $\eta \in [0, 1]$. Thus,

$$\begin{aligned} |\alpha\rangle &\rightarrow e^{\alpha(\sqrt{\eta}b^\dagger + i\sqrt{1-\eta}d^\dagger) - \alpha^*(\sqrt{\eta}b - i\sqrt{1-\eta}d)} |0_b 0_d\rangle \\ &= e^{(\alpha\sqrt{\eta}b^\dagger - [\alpha\sqrt{\eta}]^*b) + ([i\alpha\sqrt{1-\eta}]d^\dagger - [i\alpha\sqrt{1-\eta}]^*d)} |0_b 0_d\rangle \\ &= e^{[\alpha\sqrt{\eta}]b^\dagger - [\alpha\sqrt{\eta}]^*b} e^{[i\alpha\sqrt{1-\eta}]d^\dagger - [i\alpha\sqrt{1-\eta}]^*d} |0_b 0_d\rangle \\ &= |\alpha\sqrt{\eta}\rangle_b |i\alpha\sqrt{1-\eta}\rangle_d \end{aligned} \quad (\text{C.55})$$

which is the quantum description of a laser splitting on a beamsplitter.

- [1] Boyd, R. W. *Nonlinear optics* (Elsevier, Burlington, MA, 2008), third edn. [\(127\)](#)
- [2] Klingshirn, C. F. *Semiconductor Optics* (Springer Berlin Heidelberg, Berlin, Heidelberg, 2005), second edn. [\(127\)](#)
- [3] Reed, G. T. & Knights, A. P. *Silicon Photonics. An Introduction* (John Wiley & Sons, Ltd, Chichester, UK, 2004). [\(127, 130\)](#)
- [4] Lifante, G. *Integrated Photonics. Fundamentals* (John Wiley & Sons, Ltd, Chichester, UK, 2003). [\(130, 133\)](#)
- [5] Yariv, A. Coupled-mode theory for guided-wave optics. *IEEE Journal of Quantum Electronics* **9**, 919–933 (1973). [\(132\)](#)
- [6] Little, B. E., Chu, S. T., Haus, H. A., Foresi, J. & Laine, J. P. Microring resonator channel dropping filters. *Journal of Lightwave Technology* **15**, 998–1005 (1997). [\(133\)](#)
- [7] Rabus, D. G. *Integrated Ring Resonators* (Springer, Berlin Heidelberg New York, 2007). [\(136\)](#)
- [8] Gerry, C. C. & Knight, P. L. *Introductory Quantum Optics*. (Cambridge University Press, Cambridge, UK, 2005), first edn. [\(136\)](#)

Appendix D

Spontaneous four-wave mixing

This appendix contains derivations related to photon-pair generation by spontaneous four-wave mixing. For discussion in the main text, see §2.2.

§D.1 HAMILTONIAN

The FWM Hamiltonian is not widely published, and where it is, little heed is paid to its dimensions¹. Here, I combine results from various authors to obtain the correct interaction picture Hamiltonian for SFWM. I will make the parametric approximation, such that the pump remains undepleted. The general $\chi^{(3)}$ interaction Hamiltonian is of the form

$$\begin{aligned} \hat{H} = & +\mathcal{E}_1 a_1^\dagger a_2 a_3 a_4^\dagger + \mathcal{E}_1^* a_1 a_2^\dagger a_3^\dagger a_4 + \mathcal{E}_2 a_1^\dagger a_2 a_3^\dagger a_4 + \mathcal{E}_2^* a_1 a_2^\dagger a_3 a_4^\dagger \\ & + \mathcal{E}_3 a_1^\dagger a_2^\dagger a_3 a_4 + \mathcal{E}_3^* a_1 a_2 a_3^\dagger a_4^\dagger + \mathcal{E}_4 a_1 a_2^\dagger a_3^\dagger a_4^\dagger + \mathcal{E}_4^* a_1^\dagger a_2 a_3 a_4 \\ & + \mathcal{E}_5 a_1^\dagger a_2 a_3^\dagger a_4^\dagger + \mathcal{E}_5^* a_1 a_2^\dagger a_3 a_4 + \mathcal{E}_6 a_1^\dagger a_2^\dagger a_3 a_4^\dagger + \mathcal{E}_6^* a_1 a_2 a_3^\dagger a_4 \\ & + \mathcal{E}_7 a_1^\dagger a_2^\dagger a_3^\dagger a_4 + \mathcal{E}_7^* a_1 a_2 a_3 a_4^\dagger \end{aligned} \quad (\text{D.1})$$

If we provide a bright pump field in modes 2 and 3 (such that pairs are produced in modes 1 and 4), then the first two terms of EQ. D.1 contribute to four-wave mixing. The other terms are variously third-harmonic generation, SPM, XPM, and other configurations of FWM, depending on the degeneracy of the four modes². We can safely assume that the contributions from these other terms are very small. Since the pump is very bright, we assume the effect of a single a^\dagger is negligible, such that $a|\alpha\rangle = a^\dagger|\alpha\rangle = |\alpha\rangle$ (see TABLE C.1). This constitutes the so-called *parametric approximation* and leads to a pair generation Hamiltonian which has the pump power as a parameter—hence ‘parametric’.

Formalising the parametric pair-generation Hamiltonian, we presuppose an interaction strength $\hbar\Omega = \mathcal{E}_1\alpha^2$ (which depends on the pump power, $P = |\alpha|^2 \frac{\hbar\omega}{\Delta t}$) with modes 2 and 3 containing the pump fields and modes 1 and 4 (renamed a and b) containing our signal and idler photons. These assumptions lead to the pair generation Hamiltonian

$$\boxed{\hat{H} = \hbar\Omega a^\dagger b^\dagger + \hbar\Omega^* ab} \quad (\text{D.2})$$

In the limit of a weak interaction ($\hbar\Omega \ll 1$) we can apply \hat{H} for a time t as $\hat{U} \equiv \exp(-\frac{i\hbar}{\hbar}\hat{H}t)$ and expand the matrix exponential to first order (weak interaction) such

that

$$\begin{aligned}\hat{U} &\approx \hat{I} - it(\Omega a^\dagger b^\dagger + \Omega^* ab) + \mathcal{O}(\hbar^2 \Omega^2) \\ &= \hat{I} - (i\Omega t)a^\dagger b^\dagger + (i\Omega t)^* ab + \mathcal{O}(\hbar^2 \Omega^2) \\ &= \hat{I} - \xi a^\dagger b^\dagger + \xi^* ab + \mathcal{O}(\hbar^2 \Omega^2),\end{aligned}\quad (\text{D.3})$$

where I defined $\xi \equiv i\Omega t$. The probability to obtain a pair from vacuum in the small-signal regime* is then

$$|\langle 11 | \hat{U} | 00 \rangle|^2 = |\langle 11 | \{ |00\rangle - \xi |11\rangle \}|^2 = |\xi|^2. \quad (\text{D.4})$$

In practice, ‘small-signal’ means $|\xi|^2 \ll 0.1$. This approximation is lifted in §D.2.1. We can now take our definition of $|\xi|^2 = |\Omega t|^2$, and work backwards to obtain Ω and the closed form of our Hamiltonian, EQ. D.2. Remember that Ω depends on *two* pump photons (α^2). This means that $\arg(\xi) = 2\arg(\alpha)$ — ξ has twice the phase of the pump. In TABLE 2.1 I’ve collected various derived values of pair probabilities $|\xi|^2$ from the literature, which describe both straight waveguides and ring resonators.

In the simplest case of TABLE 2.1a, where $|\xi|^2 \approx \gamma^2 P^2 L^2$, we can assume that the interaction happens over a length $L = ct$, so that $|\Omega| = |\xi|/t = \gamma P c$ and the SFWM hamiltonian becomes

$$\hat{H} = \hbar c P \gamma \left(e^{-i\arg(\xi)} a^\dagger b^\dagger + e^{+i\arg(\xi)} ab \right). \quad (\text{D.5})$$

§D.2 SQUEEZED VACUUM

D.2.1 Two-mode squeezing

The non-degenerate SFWM process has the phenomenological Hamiltonian given in EQ. D.2. The first term of which converts pump-mode photons to signal and idler photon pairs, and the second term converts them back again. The interaction frequency Ω , and in turn the small-signal generation probability $|\xi|^2$, determines the strength of the process, and can be found, for several situations, in TABLE 2.1. The unitary time evolution operator which results from \hat{H} is

$$\hat{U} \equiv \exp\left(-\frac{it}{\hbar} \hat{H}\right) = \exp\left(-\xi a_s^\dagger a_i^\dagger + \xi^* a_s a_i\right). \quad (\text{D.6})$$

We can compare EQ. D.6 with the two-mode squeezing operator³,

$$\hat{S}_{II}(\xi) \equiv \exp\left(\xi^* ab - \xi a^\dagger b^\dagger\right). \quad (\text{D.7})$$

Now we can immediately use the properties of \hat{S}_{II} to identify the result of operating SFWM on vacuum with the *two-mode squeezed vacuum*⁴:

$$\begin{aligned}|\xi\rangle_{II} &\equiv \hat{S}_{II}(\xi)|0,0\rangle_{s,i} \\ &= \left[\sqrt{1 - |\xi|^2} \sum_{p=0}^{\infty} \frac{(-\xi)^p}{p!} (a_s^\dagger a_i^\dagger)^p \right] |0,0\rangle_{s,i} \\ &= \sqrt{1 - |\xi|^2} \sum_{p=0}^{\infty} (-\xi)^p |p\rangle_s |p\rangle_i\end{aligned}\quad (\text{D.8})$$

*In the literature, this quantity is often $|\beta|^2$; I prefer to reserve that symbol, and use $|\xi|^2$ instead.

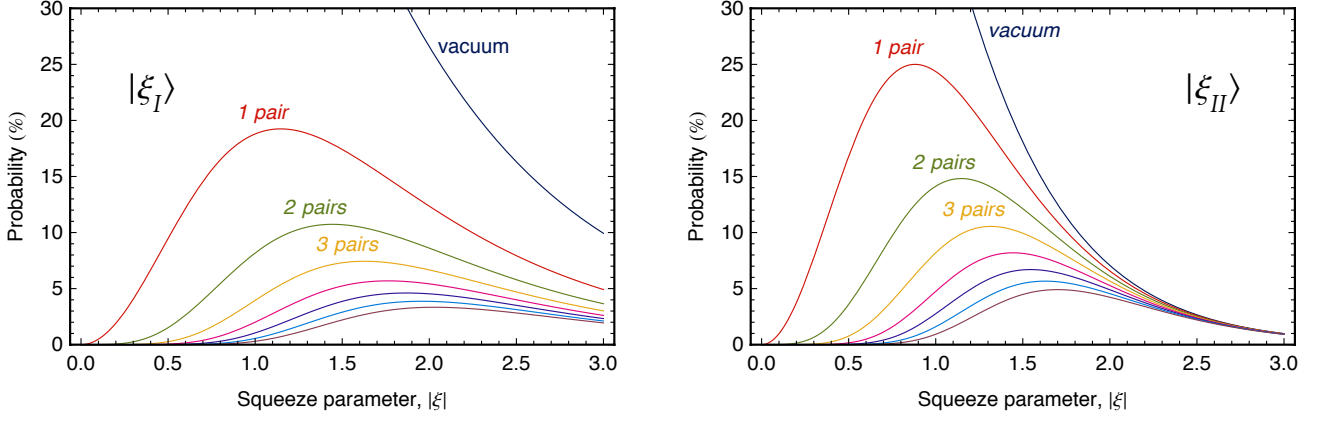


FIG. D.1: Single (left, $|\xi\rangle_I$) and two (right, $|\xi\rangle_{II}$) mode squeezed vacuum pair generation probabilities versus squeeze parameter. The single mode squeeze parameter is $|\xi| \propto \sqrt{P_0 P_1}$, while the two mode version is $|\xi| \propto P$. Most photon-pair sources produce $|\xi\rangle_{II}$.

with $\zeta = e^{i\arg(\xi)} \tanh|\xi|$. The parameter ξ is referred to as the *squeeze parameter*, and is unbounded. It determines the probability of generating one or more photon pairs (see FIG. D.1). Note that $\zeta \approx \xi$ if the squeezing is small ($\zeta < 0.25$, as discussed in §D.1). In the following discussion, I will assume the pulse-duration-collection-bandwidth product is unity: $\Delta t \Delta \nu_c = 1$. See EQ. 2.2 of the main text for the full description. The probability of generating exactly p pairs is*

$$\Pi_p(\xi) \equiv (\operatorname{sech}|\xi| \times \tanh^p|\xi|)^2 \quad (\text{D.9})$$

For example, if we are targeting single-pair operation, then

$$\begin{aligned} \Pi_0(\xi) &= \operatorname{sech}^2|\xi| \\ \Pi_1(\xi) &= \operatorname{sech}^2|\xi| \times \tanh^2|\xi| \\ \Pi_{>1}(\xi) &= 1 - \Pi_0(\xi) - \Pi_1(\xi) \end{aligned} \quad (\text{D.10})$$

and we might choose to operate at $\Pi_1(\xi) = 10\%$, which, reading from FIG. D.1, is satisfied at $\xi_{10\%} \approx 0.35$ and at $\xi'_{10\%} \approx 1.75$. We may also wish to operate at the 1-pair maximum, at $\xi_{25\%} \approx 0.88$. However, it would quickly become apparent to us that there are three very different proposals: $\xi_{10\%}$ with low-noise at $\Pi_1/\Pi_{>1} = 7.9$; $\xi_{25\%}$ being brighter but with break-even noise at $\Pi_1/\Pi_{>1} = 1$; and $\xi'_{10\%}$ with deafening noise at $\Pi_1/\Pi_{>1} = 0.1$.

D.2.2 Single-mode squeezing

Above, we covered non-degenerate SFWM, in which signal and idler photons are squeezed out of the vacuum in two orthogonal (frequency) modes. *Degenerate* SFWM, in which a two-frequency pump produces pairs of photons, results in single-mode squeezing. This process is schematised in FIG. D.2b. I discuss degenerate SFWM more in §3.1.2.

*Since $\zeta = \tanh|\xi|$ and $1 - \tanh^2\xi = \operatorname{sech}^2\xi$, $\Pi_p = (1 - |\xi|^2)(|\xi|^{2p}) = (\operatorname{sech}^2\xi)(\tanh^{2p}\xi)$.

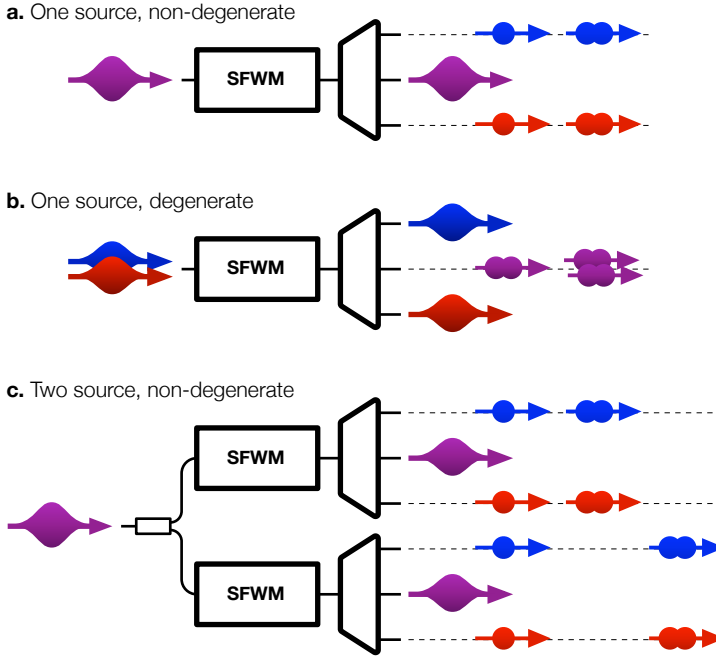


FIG. D.2: Basic configurations for SFWM sources. Signal-idler frequency non-degeneracy is shown schematically with WDMs. **a.** One pair is created in two modes from one SFWM source. **c.** Two pairs are created in the same SFWM source. **d.** Two pairs are created across two sources. In **d**, single-pair events are not shown for clarity.

The deceptively simple *single-mode* squeezing is significantly less useful for building systems than its two-mode sibling. There are three reasons for this. **1** Two pumps are needed for energy conservation, and in the case of pulsed excitation, these pumps must be synchronised inside the device; **2** these two pumps inevitably undergo non-degenerate SFWM, yielding in-band, un-filterable noise; **3** single-mode squeezing is less efficient, providing fewer pairs for more pump (see [FIG. D.1](#)) and exacerbating the noise problem. In the long term, two-mode squeezing is preferred for source heralding and multiplexing, however in the near-term, following the traditional path to higher photon numbers (pump harder, wait longer) degenerate pairs may have a role to play.

Throughout the following text, we will take similar substitutions for ξ and ζ as we did in [EQ. D.6](#) and [EQ. D.8](#), with the only exception being that two pumps are required for this scheme, so $\alpha^2 \rightarrow \alpha_0\alpha_1$. Then, proceeding, we now identify *degenerate* SFWM evolution operator with single-mode squeezing \hat{S}_I ,

$$\hat{S}_I(\xi) \equiv \exp\left(\xi^*aa - \xi a^\dagger a^\dagger\right). \quad (\text{D.11})$$

Similarly to the two-mode squeezing case, when \hat{S}_I is applied to a single-moded vacuum, *single-mode squeezed vacuum*, $|\xi\rangle_I$, results. Following a difficult derivation⁵, and again defining $\zeta = e^{i\arg(\xi)}\tanh|\xi|$,

$$\begin{aligned} |\xi\rangle_I &\equiv \hat{S}_I(\xi)|0\rangle \\ &= \sqrt{\sqrt{1 - |\zeta|^2}} \sum_{p=0}^{\infty} \frac{\sqrt{2p!}}{2^p p!} (-\zeta)^p |2p\rangle \end{aligned} \quad (\text{D.12})$$

The probability of generating the first few pairs, $|\langle 2p|\xi\rangle_I|^2$ is plotted in [FIG. D.1](#). This figure shows the lower efficiency of single-mode relative to two-mode squeezing.

§D.3 PAIRS GENERATED BY MULTIPLE SOURCES

In the case where multiple nonlinear elements are pumped coherently, as depicted in [FIG. D.2c](#), the squeezing is independent, so the resulting state of light is described by the tensor product of the two squeezed states. This tensor product can produce intuitive results whereby each source produces an independent squeezed state, but more often results in a messy superposition between photon numbers in each source. This coherent effect has been used extensively in the experiments composing this thesis. For N sources, each in one spatial mode, and sharing a pump, the resulting state is

$$|\psi_N\rangle \equiv \bigotimes_{n=0}^{N-1} |\zeta_n\rangle_T, \quad (\text{D.13})$$

where $T = II$ in the case of non-degenerate SFGM ([EQ. D.8](#)) and $T = I$ in the degenerate case ([EQ. D.12](#)). Since the majority of experiments in this thesis (and for the foreseeable future) predominantly use non-degenerate SFGM (two-mode squeezing) I will explicitly expand [EQ. D.13](#) for $T = II$. I will present a useful transformation ([EQ. D.14](#)), and tabulate some low-order pair generation coefficients ([TABLE D.1](#)).

By transforming the operator form of the two-mode squeezed vacuum ([EQ. D.8](#)) with the power series expansion for the exponential, we can rewrite the state resulting from N coherently pumped sources in terms of the number of pairs, which is of great use when truncating the infinite series, and also makes that truncation precise.

$$\begin{aligned} \bigotimes_{n=0}^{N-1} |\zeta_n\rangle_{II} &= \prod_{n=0}^{N-1} \left(\sqrt{1 - |\zeta_n|^2} \sum_{p=0}^{\infty} \frac{(-\zeta_n)^p}{p!} (a_{ni}^\dagger a_{ns}^\dagger)^p \right) |0\rangle^{\otimes N} \\ &= \prod_{n=0}^{N-1} \left(\sqrt{1 - |\zeta_n|^2} \right) \prod_{n=0}^{N-1} \exp\left(\langle 0 | -\zeta_n a_{ni}^\dagger a_{ns}^\dagger \rangle\right) |0\rangle^{\otimes N} \\ &= \prod_{n=0}^{N-1} \left(\sqrt{1 - |\zeta_n|^2} \right) \exp\left(\langle 0 | \sum_{n=0}^{N-1} -\zeta_n a_{ni}^\dagger a_{ns}^\dagger \rangle\right) |0\rangle^{\otimes N} \\ &= \prod_{n=0}^{N-1} \left(\sqrt{1 - |\zeta_n|^2} \right) \sum_{p=0}^{\infty} \frac{1}{p!} \left(- \sum_{n=0}^{N-1} \zeta_n a_{ni}^\dagger a_{ns}^\dagger \right)^p |0\rangle^{\otimes N} \end{aligned} \quad (\text{D.14})$$

Keep in mind that this expression describes the *state*. The probabilities associated with each term remain almost as simple as in the single-source case in [EQ. D.9](#), above. The probability of obtaining p pairs from a (possibly self-overlapping) subset S of N sources is just

$$\Pi_p(S) = \prod_{n=0}^{N-1} \operatorname{sech}^2 |\zeta_n| \times \prod_{n \in S} \tanh^{2p} |\zeta_n| \quad (\text{D.15})$$

as one might expect, from classical probability arguments. The quantum nature of this light shows through *only* when the coherence is probed, through interference, and consequently, this is the regime of interest to us here.

	One source	Two sources	N sources
vacuum (c_0)	$\sqrt{1 - \zeta ^2}$	$\sqrt{1 - \zeta_0 ^2} \sqrt{1 - \zeta_1 ^2}$	$\prod_{n=0}^{N-1} \sqrt{1 - \zeta_n ^2}$
one pair (c_1)	$-c_0(\zeta a_i^\dagger a_s^\dagger)$	$-c_0(\zeta_0 a_i^\dagger a_s^\dagger + \zeta_1 b_i^\dagger b_s^\dagger)$	$-c_0 \sum_{n=0}^{N-1} \zeta_n a_{ni}^\dagger a_{ns}^\dagger$
two pairs (c_2)	$c_0(\zeta a_i^\dagger a_s^\dagger)^2 / 2$	$c_0(\zeta_0 a_i^\dagger a_s^\dagger + \zeta_1 b_i^\dagger b_s^\dagger)^2 / 2$	$c_1^2 c_0^{-1} / 2$
three pairs (c_3)	$-c_0(\zeta a_i^\dagger a_s^\dagger)^3 / 6$	$-c_0(\zeta_0 a_i^\dagger a_s^\dagger + \zeta_1 b_i^\dagger b_s^\dagger)^3 / 6$	$c_1^3 c_0^{-2} / 6$
p pairs (c_p)	$c_0(-\zeta a_i^\dagger a_s^\dagger)^p / p!$	$c_0(-\zeta_0 a_i^\dagger a_s^\dagger - \zeta_1 b_i^\dagger b_s^\dagger)^p / p!$	$c_1^p c_0^{1-p} / p!$

TABLE D.1: Non-degenerate SFWM pair generation coefficients for various numbers of coherently pumped sources, for a state of the form $\sum_{p=0}^{\infty} c_p |vac\rangle$ such that each c_p represents the probability amplitude for the state containing p photon pairs. The phase and amplitude of the pump in each source mode, and the efficiency of that source, is encoded in ζ_n . To obtain the corresponding probabilities, these coefficients must be transformed using the usual $(a^\dagger)^n |0\rangle = |n\rangle / \sqrt{n!}$ rule (see **TABLE B.1**), then modulo squared.

§D.4 SQUEEZED VACUUM ENTANGLEMENT

How entangled is a two-mode squeezed vacuum? Starting from **EQ. D.8**, I'll trace out the idler (mode), and compute the purity of the signal (mode), then use this to work out the Schmidt number. Written as a density matrix, **EQ. D.8** reads

$$\hat{\rho}_{si} = |\xi_{II}\rangle\langle\xi_{II}| = (1 - |\zeta|^2) \sum_{p=0}^{\infty} \sum_{q=0}^{\infty} (-\zeta)^p (-\zeta^*)^q |p_s\rangle\langle q_s| |p_i\rangle\langle q_i|. \quad (\text{D.16})$$

Without loss of generality, we can assume that $\zeta = -\tanh(\xi)$ (i.e. $\xi \in \mathbb{R}$, $\arg(\zeta) = \pi$); then this can be written as

$$\hat{\rho}_{si} = \operatorname{sech}^2 \xi \sum_{p=0}^{\infty} \sum_{q=0}^{\infty} \tanh^{p+q} \xi |p_s\rangle\langle q_s| |p_i\rangle\langle q_i|. \quad (\text{D.17})$$

From **EQ. B.33**, the state of the signal, partially tracing out the idler is

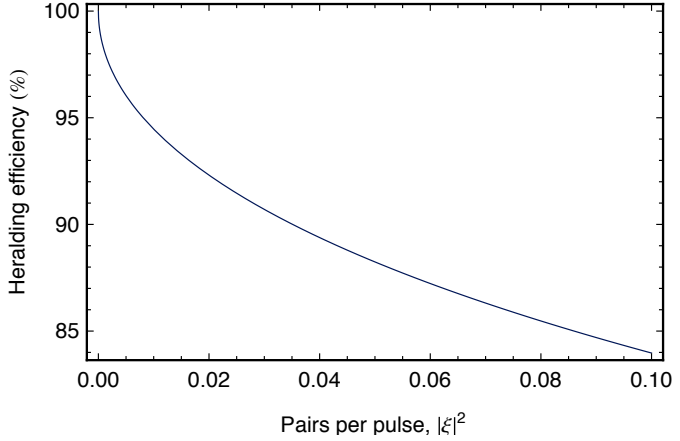
$$\hat{\rho}_s = \operatorname{Tr}_i(\hat{\rho}_{si}) = \sum_{n=0}^{\infty} \langle n_i | \hat{\rho}_{si} | n_i \rangle, \quad (\text{D.18})$$

so the partial trace selects the terms in **EQ. D.17** where $p = q$:

$$\begin{aligned} \hat{\rho}_s &= \operatorname{sech}^2 \xi \sum_{n=0}^{\infty} \langle n_i | \left(\sum_{p=0}^{\infty} \sum_{q=0}^{\infty} \tanh^{p+q} \xi |p_s\rangle\langle q_s| |p_i\rangle\langle q_i| \right) | n_i \rangle \\ &= \operatorname{sech}^2 \xi \sum_{n=0}^{\infty} \left(\sum_{p=0}^{\infty} \sum_{q=0}^{\infty} \tanh^{p+q} \xi |p_s\rangle\langle q_s| \langle n_i | p_i \rangle \langle q_i | n_i \rangle \right) \\ &= \operatorname{sech}^2 \xi \sum_{n=0}^{\infty} \sum_{p=0}^{\infty} \sum_{q=0}^{\infty} \tanh^{p+q} \xi |p_s\rangle\langle q_s| \delta_{n,p} \delta_{q,n} \\ &= \operatorname{sech}^2 \xi \sum_{n=0}^{\infty} \tanh^{2n} \xi |n_s\rangle\langle n_s|. \end{aligned} \quad (\text{D.19})$$

The purity of this is $\mathcal{P} = \operatorname{Tr}(\hat{\rho}_s^2)$. So

FIG. D.3: Heralding efficiency due to XTPA, versus a source's pair-generation probability, as described in §D.5.



$$\begin{aligned}\hat{\rho}_s^2 &= \operatorname{sech}^4 \xi \sum_{p=0}^{\infty} \sum_{q=0}^{\infty} \tanh^{2(p+q)} \xi |p_s\rangle\langle p_s| |q_s\rangle\langle q_s| \\ &= \operatorname{sech}^4 \xi \sum_{p=0}^{\infty} \tanh^{4p} \xi |p_s\rangle\langle p_s|.\end{aligned}\quad (\text{D.20})$$

Then, the trace gives the purity:

$$\mathcal{P} = \operatorname{sech}^4 \xi \sum_{p=0}^{\infty} \tanh^{4p} \xi = \frac{\operatorname{sech}^4 \xi}{1 - \tanh^4 \xi} = \operatorname{sech}(2\xi) \quad (\text{D.21})$$

For $\xi \ll 1$, $\mathcal{P} = \operatorname{sech}(2\xi) \approx 1 - 2|\xi|^2$, so $K \approx 1 + 2|\xi|^2$.

The purity is inversely related to the Schmidt number, $K \equiv 1/\mathcal{P}$ (§B.4.4), which counts the size of the superposition needed to represent the joint state $\hat{\rho}_{si}$ —here it measures the entanglement between signal and idler. When $K = 1$, the state is fully separable, and as K increases, it indicates increasing levels of entanglement. K is bounded by the dimension of the system, which for the squeezed vacuum is infinite. Thus, for a low-power limit squeeze parameter of $|\xi|^2 = 0.1$, the Schmidt number is $K \approx 1.20$, indicating that very little entanglement is present in the squeezed vacuum at experimentally relevant levels of squeezing.

§D.5 EFFECT OF XTPA ON HERALDING EFFICIENCY

As pointed out by Husko et al. in ref. 6, cross-two-photon absorption (XTPA) has a significant, negative impact on the heralding efficiency of nonlinear probabilistic sources. From EQ. 2.16, the single-photon collection efficiency due to XTPA is

$$\eta_{\text{XTPA}}(P) \equiv \frac{1}{(1 + \alpha_2 P_0 L_{\text{eff}} / A)^2}. \quad (\text{D.22})$$

We can use the low-power expression for the pair generation probability (Π_1 , EQ. 2.5), with zero momentum mismatch, to compute the power required for a certain generation probability as

$$P_{\text{targ}} = \sqrt{\Pi_1 / (\gamma^2 L_{\text{eff}}^2 \Delta t \Delta \nu_c)} \quad (\text{D.23})$$

which can then be substituted back into **EQ. D.22** to obtain the XTPA-reduced heralding efficiency for low power. This is plotted in **FIG. D.3** for the usual waveguide, as described in **TABLE 1.3**, with a $\Delta t = 10\text{ ps}$ pump pulse, and photon collection over a bandwidth of $\Delta\nu_c = 120\text{ GHz}$. Neglecting momentum mismatch makes this result valid for any length of waveguide, and so too for resonators.

- [1] See for example refs. 3,7,8. ⟨139⟩
- [2] Agrawal, G. P. *Nonlinear Fiber Optics* (Academic Press, San Diego, 2001), fourth edn. ⟨139⟩
- [3] Gerry, C. C. & Knight, P. L. *Introductory Quantum Optics*. (Cambridge University Press, Cambridge, UK, 2005), first edn. ⟨140, 146⟩
- [4] Eq 7.169 of 3. ⟨140⟩
- [5] See §7.1 of ref. 3, up to Eq. 7.68. ⟨142⟩
- [6] Husko, C. A. *et al.* Multi-photon absorption limits to heralded single photon sources. *Scientific Reports* **3** (2013). ⟨145⟩
- [7] Yang, Z. *et al.* Spontaneous parametric down-conversion in waveguides: a backward Heisenberg picture approach. *Physical Review A* (2008). ⟨146⟩
- [8] Langford, N. K. *et al.* Efficient quantum computing using coherent photon conversion. *Nature* **478**, 360–363 (2011). ⟨146⟩

Appendix E

Time-reversed Hong-Ou-Mandel interference

§E.1 TWO-PHOTONS AND BEAMSPLITTERS

This section describes the behaviour of the two-photon superpositions $|20\rangle \pm |02\rangle$ on a balanced symmetric beamsplitter (EQ. 1.10, $\eta = 1/2$). These results are used in EQS. 3.1 and 3.2, underpinning the experiment of CH. 3.

E.1.1 Degenerate pairs

The simplest case is when the pairs are degenerate (i.e. of the same time, frequency, polarisation, etc.). Though this is the less relevant case, I present it first because it's simpler.

$$\begin{aligned}
\frac{|20\rangle \pm |02\rangle}{\sqrt{2}} &= \frac{1}{2} (a^\dagger a^\dagger \pm b^\dagger b^\dagger) |00\rangle \\
&\xrightarrow{\text{BS}} \frac{1}{4} ([a^\dagger + ib^\dagger]^2 \pm [ia^\dagger + b^\dagger]^2) |00\rangle \\
&= \frac{1}{4} ([a^\dagger a^\dagger - b^\dagger b^\dagger + 2ia^\dagger b^\dagger] \pm [-a^\dagger a^\dagger + b^\dagger b^\dagger + 2ia^\dagger b^\dagger]) |00\rangle \\
&= \frac{1}{2} \left(\left[\frac{1 \mp 1}{2} \right] (a^\dagger a^\dagger - b^\dagger b^\dagger) + 2i \left[\frac{1 \pm 1}{2} \right] a^\dagger b^\dagger \right) |00\rangle \\
&= \begin{cases} ia^\dagger b^\dagger |00\rangle = i|11\rangle, \text{ if '+'}, \text{ and} \\ (a^\dagger a^\dagger - b^\dagger b^\dagger)/2 \cdot |00\rangle = (|20\rangle - |02\rangle)/2, \text{ if '-'.} \end{cases}
\end{aligned} \tag{E.1}$$

So the two superpositions behave on the beamsplitter according to

$$\frac{|20\rangle + |02\rangle}{\sqrt{2}} \xrightarrow{\text{BS}} i|11\rangle, \tag{E.2a}$$

$$\frac{|20\rangle - |02\rangle}{\sqrt{2}} \xrightarrow{\text{BS}} \frac{|20\rangle - |02\rangle}{\sqrt{2}}. \tag{E.2b}$$

These results are used in EQS. 3.1 and 3.2, underpinning the experiment of CH. 3.

E.1.2 Non-degenerate pairs

It turns out that the bunching and splitting behaviour of the previous section doesn't depend on the pairs being degenerate, as I show below.

$$\begin{aligned}
& \frac{|1_s 1_i 0_s 0_i\rangle + |0_s 0_i 1_s 1_i\rangle}{\sqrt{2}} = \\
&= \frac{1}{2} \left(a_s^\dagger a_i^\dagger \pm b_s^\dagger b_i^\dagger \right) |0000\rangle \\
&\xrightarrow{\text{BS}} \frac{1}{4} \left([a_s^\dagger + i b_s^\dagger][a_i^\dagger + i b_i^\dagger] \pm [i a_s^\dagger + b_s^\dagger][i a_i^\dagger + b_i^\dagger] \right) |0000\rangle \\
&= \frac{1}{4} \left([a_s^\dagger a_i^\dagger - b_s^\dagger b_i^\dagger + i a_s^\dagger b_i^\dagger + i a_i^\dagger b_s^\dagger] \pm [-a_s^\dagger a_i^\dagger + b_s^\dagger b_i^\dagger + i a_s^\dagger b_i^\dagger + i a_i^\dagger b_s^\dagger] \right) |0000\rangle \\
&= \frac{1}{2} \left(\left[\frac{1 \mp 1}{2} \right] (a_s^\dagger a_i^\dagger - b_s^\dagger b_i^\dagger) + i \left[\frac{1 \pm 1}{2} \right] (a_s^\dagger b_i^\dagger + a_i^\dagger b_s^\dagger) \right) |0000\rangle \\
&= \begin{cases} i(a_s^\dagger b_i^\dagger + a_i^\dagger b_s^\dagger)/2 \cdot |0000\rangle = i(|1001\rangle - |0110\rangle)/2, \text{ if '+'}, \text{ and} \\ (a_s^\dagger a_i^\dagger - b_s^\dagger b_i^\dagger)/2 \cdot |0000\rangle = (|1100\rangle - |0011\rangle)/2, \text{ if '-'}. \end{cases} \tag{E.3}
\end{aligned}$$

So the two superpositions behave on the beamsplitter according to

$$\frac{|1_s 1_i 0_s 0_i\rangle + |0_s 0_i 1_s 1_i\rangle}{\sqrt{2}} \xrightarrow{\text{BS}} i \frac{|1_s 0_i 0_s 1_i\rangle + |0_s 1_i 1_s 0_i\rangle}{\sqrt{2}} \equiv |split\rangle, \tag{E.4a}$$

$$\frac{|1_s 1_i 0_s 0_i\rangle - |0_s 0_i 1_s 1_i\rangle}{\sqrt{2}} \xrightarrow{\text{BS}} \frac{|1_s 1_i 0_s 0_i\rangle - |0_s 0_i 1_s 1_i\rangle}{\sqrt{2}} \equiv |bunch\rangle. \tag{E.4b}$$

In general,

$$\frac{|1_s 1_i 0_s 0_i\rangle + e^{i2\phi}|0_s 0_i 1_s 1_i\rangle}{\sqrt{2}} \xrightarrow{\text{BS}} e^{i\phi} (\cos \phi |split\rangle - i \sin \phi |bunch\rangle). \tag{E.5}$$

For completeness, the two split superpositions behave as

$$\frac{|1_s 0_i 0_s 1_i\rangle + |0_s 1_i 1_s 0_i\rangle}{\sqrt{2}} \xrightarrow{\text{BS}} i \frac{|1_s 1_i 0_s 0_i\rangle + |0_s 0_i 1_s 1_i\rangle}{\sqrt{2}}, \tag{E.6a}$$

$$\frac{|1_s 0_i 0_s 1_i\rangle - |0_s 1_i 1_s 0_i\rangle}{\sqrt{2}} \xrightarrow{\text{BS}} \frac{|1_s 1_i 0_s 0_i\rangle - |0_s 0_i 1_s 1_i\rangle}{\sqrt{2}}. \tag{E.6b}$$

§E.2 FINDING PAIRS IN UNEXPECTED PLACES

In this section I present a coherent model including SFWM in the input and output waveguides of the device. See §3.2.1 for discussion.

The single-waveguide state is, considering only one SFWM pair (from EQ. D.8),

$$|\xi\rangle = \hat{U}|0_s 0_i\rangle \approx (1 - \xi a_s^\dagger a_i^\dagger)|0_s 0_i\rangle, \quad \text{with } \xi = e^{i2\alpha}\gamma PL\Theta, \tag{E.7}$$

where α is the phase of the pump, \hat{U} represents SFWM, and ξ is taken from (TABLE 2.1b). The phase matching function Θ depends on length, but we will neglect this behaviour here.

The device is then broken into three lengths: the input waveguide length L_{in} (before the first coupler), the source waveguide length L_s (between the two couplers), and the output waveguide length L_{out} (after the second coupler). I'll use the same subscripts on ξ to denote these three regions.

The state after the input waveguide is

$$|\xi_{\text{in}}\rangle = (1 - \xi_{\text{in}} a_s^\dagger a_i^\dagger)|0_s 0_i\rangle \tag{E.8}$$

it passes through the first coupler

$$\begin{aligned} |\xi_{\text{in}}\rangle &\rightarrow (1 - \xi_{\text{in}}[a_s^\dagger + ib_s^\dagger][a_i^\dagger + ib_i^\dagger])|\mathbf{0}\rangle \\ &= (1 - \xi_{\text{in}}[a_s^\dagger a_i^\dagger - b_s^\dagger b_i^\dagger + ia_s^\dagger b_i^\dagger + ib_s^\dagger a_i^\dagger])|\mathbf{0}\rangle \end{aligned} \quad (\text{E.9})$$

then undergoes SFGM in both arms: $\hat{U}_A \hat{U}_B = 1 - \xi_s a_s^\dagger a_i^\dagger + \xi_s b_s^\dagger b_i^\dagger$, where we kept track of the extra phase on mode A due to the beamsplitter, and defined a multi-mode vacuum $|\mathbf{0}\rangle$. Throughout, we will keep only first order (single pair) terms. The source state is then

$$\begin{aligned} |\xi_s\rangle &= (1 - \xi_s a_s^\dagger a_i^\dagger + \xi_s b_s^\dagger b_i^\dagger)(1 - \frac{\xi_{\text{in}}}{2}[a_s^\dagger a_i^\dagger - b_s^\dagger b_i^\dagger + ia_s^\dagger b_i^\dagger + ib_s^\dagger a_i^\dagger])|\mathbf{0}\rangle \\ &= (1 - \xi_s a_s^\dagger a_i^\dagger + \xi_s b_s^\dagger b_i^\dagger - \frac{\xi_{\text{in}}}{2}[a_s^\dagger a_i^\dagger - b_s^\dagger b_i^\dagger + ia_s^\dagger b_i^\dagger + ib_s^\dagger a_i^\dagger])|\mathbf{0}\rangle, \end{aligned} \quad (\text{E.10})$$

which can be grouped into superpositions which we can apply our directional coupler rules upon ([EQS. E.4](#), [EQ. E.5](#), [EQS. E.6](#)), as

$$|\xi_s\rangle = (1 - \xi_s(a_s^\dagger a_i^\dagger - b_s^\dagger b_i^\dagger) - \frac{\xi_{\text{in}}}{2}[(a_s^\dagger a_i^\dagger - b_s^\dagger b_i^\dagger) + i(a_s^\dagger b_i^\dagger + b_s^\dagger a_i^\dagger)])|\mathbf{0}\rangle, \quad (\text{E.11})$$

but first we apply the phase $a^\dagger \rightarrow e^{i\phi} a^\dagger$:

$$|\xi_s\rangle \xrightarrow{\phi} (1 - \xi_s(e^{i2\phi} a_s^\dagger a_i^\dagger - b_s^\dagger b_i^\dagger) - \frac{\xi_{\text{in}}}{2}[(e^{i2\phi} a_s^\dagger a_i^\dagger - b_s^\dagger b_i^\dagger) + ie^{i\phi}(a_s^\dagger b_i^\dagger + b_s^\dagger a_i^\dagger)])|\mathbf{0}\rangle. \quad (\text{E.12})$$

Now we can apply the beamsplitter transformations, for convenience using [EQS. E.4](#), [EQ. E.5](#), and [EQS. E.6](#). Define the split and bunch operators* $\hat{A}_{\text{split}}^\pm = a_s^\dagger b_i^\dagger \pm b_s^\dagger a_i^\dagger$ and $\hat{A}_{\text{bunch}}^\pm \equiv a_s^\dagger a_i^\dagger \pm b_s^\dagger b_i^\dagger$, so that (summarising [EQ. E.5](#) and [EQ. E.6a](#))

$$\begin{aligned} a_s^\dagger a_i^\dagger - e^{i2\phi} b_s^\dagger b_i^\dagger &\xrightarrow{\text{BS}} -e^{i\phi}(\sin \phi \hat{A}_{\text{split}}^+ - \cos \phi \hat{A}_{\text{bunch}}^-) \\ a_s^\dagger b_i^\dagger + b_s^\dagger a_i^\dagger &\xrightarrow{\text{BS}} i \hat{A}_{\text{bunch}}^+ \end{aligned} \quad (\text{E.13})$$

then

$$\begin{aligned} |\xi_s\rangle &\xrightarrow{\text{BS}} (1 + \xi_s[e^{i\phi}(\sin \phi \hat{A}_{\text{split}}^+ - \cos \phi \hat{A}_{\text{bunch}}^-)] \\ &\quad + \frac{\xi_{\text{in}}}{2}[e^{i\phi}(\sin \phi \hat{A}_{\text{split}}^+ - \cos \phi \hat{A}_{\text{bunch}}^-) - ie^{i\phi}(i \hat{A}_{\text{bunch}}^+)])|\mathbf{0}\rangle \\ &= (1 + \xi_s e^{i\phi}[\sin \phi \hat{A}_{\text{split}}^+ - \cos \phi \hat{A}_{\text{bunch}}^-] \\ &\quad + \frac{\xi_{\text{in}}}{2}e^{i\phi}[\sin \phi \hat{A}_{\text{split}}^+ - \cos \phi \hat{A}_{\text{bunch}}^- + \hat{A}_{\text{bunch}}^+])|\mathbf{0}\rangle \end{aligned} \quad (\text{E.14})$$

Finally, SFGM occurs in the output waveguides A and B :

$$\begin{aligned} \hat{U}_A \hat{U}_B &= 1 + e^{i\phi}(\xi_{\text{out}} \sin^2(\phi/2)a_s^\dagger a_i^\dagger - \xi_{\text{out}} \cos^2(\phi/2)b_s^\dagger b_i^\dagger) \\ &= 1 + e^{i\phi}\xi_{\text{out}}(\hat{A}_{\text{bunch}}^+ - \cos \phi \hat{A}_{\text{bunch}}^-)/2, \end{aligned} \quad (\text{E.15})$$

where the sinusoids arise from the steering of the pump. Then,

$$\begin{aligned} |\xi_{\text{out}}\rangle &= (1 + \xi_s e^{i\phi}[\sin \phi \hat{A}_{\text{split}}^+ - \cos \phi \hat{A}_{\text{bunch}}^-] \\ &\quad + \xi_{\text{in}} e^{i\phi}[\sin \phi \hat{A}_{\text{split}}^+ - \cos \phi \hat{A}_{\text{bunch}}^- + \hat{A}_{\text{bunch}}^+]/2 \\ &\quad + \xi_{\text{out}} e^{i\phi}[\hat{A}_{\text{bunch}}^+ - \cos \phi \hat{A}_{\text{bunch}}^-]/2)|\mathbf{0}\rangle. \end{aligned} \quad (\text{E.16})$$

*Such that $\hat{A}_{\text{split}}^+|0000\rangle = -i\sqrt{2}|\text{split}\rangle$ and $\hat{A}_{\text{bunch}}^-|0000\rangle = \sqrt{2}|\text{bunch}\rangle$.

Now we can make the power and length dependence of ξ explicit. $\xi_{\text{in}} = \gamma P L_{\text{in}} \Theta$, $\xi_s = \gamma (P/2) L_s \Theta$, and $\xi_{\text{out}} = \gamma P L_{\text{out}} \Theta$, leaving us with

$$\begin{aligned} |\xi_{\text{out}}\rangle &= (1 + \gamma P L_s \Theta e^{i\phi} [\sin \phi \hat{A}_{\text{split}}^+ - \cos \phi \hat{A}_{\text{bunch}}^-]/2 \\ &\quad + \gamma P L_{\text{in}} \Theta e^{i\phi} [\sin \phi \hat{A}_{\text{split}}^+ - \cos \phi \hat{A}_{\text{bunch}}^- + \hat{A}_{\text{bunch}}^+]/2 \\ &\quad + \gamma P L_{\text{out}} \Theta e^{i\phi} [\hat{A}_{\text{bunch}}^+ - \cos \phi \hat{A}_{\text{bunch}}^-]/2) |0\rangle \\ &= |0\rangle + \frac{\gamma P \Theta}{2} e^{i\phi} (L_s [\sin \phi \hat{A}_{\text{split}}^+ - \cos \phi \hat{A}_{\text{bunch}}^-] \\ &\quad + L_{\text{in}} [\sin \phi \hat{A}_{\text{split}}^+ - \cos \phi \hat{A}_{\text{bunch}}^- + \hat{A}_{\text{bunch}}^+] \\ &\quad + L_{\text{out}} [\hat{A}_{\text{bunch}}^+ - \cos \phi \hat{A}_{\text{bunch}}^-]) |0\rangle. \end{aligned} \quad (\text{E.17})$$

which we can rewrite in Dirac notation, finally dropping the vacuum term, and collecting the four states:

$$\begin{aligned} |\xi_{\text{out}}\rangle &= \gamma P \Theta e^{i\phi} ((L_s + L_{\text{in}}) \sin \phi (|1001\rangle + |0110\rangle) \\ &\quad + (L_{\text{in}} + L_{\text{out}} - (L_s + L_{\text{in}} + L_{\text{out}}) \cos \phi) |1100\rangle \\ &\quad + (L_{\text{in}} + L_{\text{out}} + (L_s + L_{\text{in}} + L_{\text{out}}) \cos \phi) |0011\rangle) / 2. \end{aligned} \quad (\text{E.18})$$

So, in [EQ. E.18](#) we now have the output state, including the spurious emission from the device's input and output waveguides. Now we can calculate the probability of each of the splitting configurations ($|1001\rangle$ signal in A , and $|0110\rangle$ signal in B) and each of the bunching configurations ($|1100\rangle$ both in A , and $|0011\rangle$ both in B), via

$$\begin{aligned} \Pi_{\text{split}}^{s,i} &= \Pi_{\text{split}}^{i,s} = |\langle 1001 | \xi_{\text{out}} \rangle|^2 = |\langle 0110 | \xi_{\text{out}} \rangle|^2 \\ \Pi_{\text{bunch}}^A &= |\langle 1100 | \xi_{\text{out}} \rangle|^2 \\ \Pi_{\text{bunch}}^B &= |\langle 0011 | \xi_{\text{out}} \rangle|^2 \end{aligned} \quad (\text{E.19})$$

which work out to

$$\Pi_{\text{split}}^{s,i} = |\gamma P \Theta (L_s + L_{\text{in}}) \sin \phi / 2|^2 \quad (\text{E.20a})$$

$$\Pi_{\text{bunch}}^A = |\gamma P \Theta (L_{\text{in}} + L_{\text{out}} - (L_s + L_{\text{in}} + L_{\text{out}}) \cos \phi) / 2|^2 \quad (\text{E.20b})$$

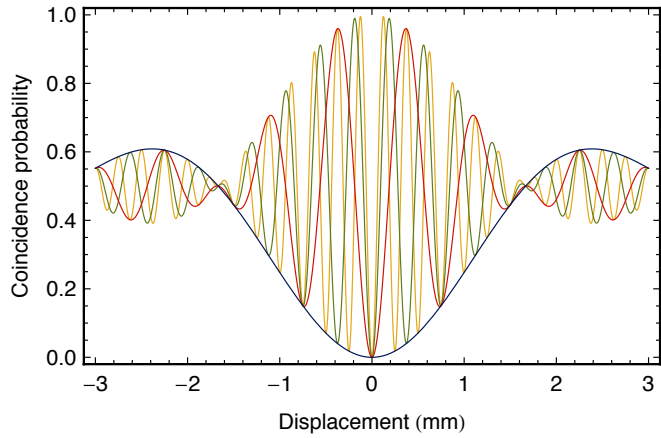
$$\Pi_{\text{bunch}}^B = |\gamma P \Theta (L_{\text{in}} + L_{\text{out}} + (L_s + L_{\text{in}} + L_{\text{out}}) \cos \phi) / 2|^2 \quad (\text{E.20c})$$

§E.3 THE HONG-OU-MANDEL DIP

No, it's not a Sino-German polka—it's the shape of the classic two-photon time-delay interferogram. See [CH. 3](#) for details of a HOM dip experiment. The shape of this fringe was well described in the original literature, so I will be working from that¹. My friend and colleague, Dr. Damien Bonneau, has also written a very detailed, first-principles derivation². Here, I will reiterate the original theory of Hong, Ou, and Mandel, with the intention of obtaining a model for the HOM dip data of [§3.3](#).

Two photons can be described in the frequency domain by their joint spectral amplitude $J(\omega_s, \omega_i)$, which encapsulates their frequency and correlations, and parametrises their joint state $|\psi_2\rangle$. Energy must be conserved between our two photons, with $2\omega_p = \omega_s + \omega_i$ (where there is some uncertainty on ω_p), so at least we expect J to be something like symmetric about a centre frequency, $\bar{\omega}_p$. This is a failing of this treatment, but everybody does it. The visibility is normally adjusted ad

FIG. E.1: Model of [EQ. E.29](#) plotted for signal-idler detunings $|\nu_s - \nu_i| = 0, 400, 800, 1200$ GHz. Compare to experimental results in [FIG. 3.3](#).



hoc. So, assuming a single-parameter joint spectrum, $J(\omega) \equiv J(\omega_p + \omega, \omega_p - \omega)$, we have the following definition of the two-photon state

$$|\psi_2\rangle \equiv \int_{\infty} J(\omega) d\omega, \quad \int_{\infty} |J(\omega)|^2 d\omega = 1. \quad (\text{E.21})$$

The time-domain photon shape $j(t)$ is given by the Fourier transform of $J(\omega)$,

$$j(t) = \frac{1}{\sqrt{2\pi}} \int_{\infty} J(\omega) e^{-i\omega t} d\omega \quad (\text{E.22})$$

Notice that we centred $J(\omega)$ around the peak in $J(\omega_s, \omega_i)$, removing any optical frequency oscillations in $j(t)$. This is important because now we will integrate $j(t)$ to obtain the coincidence probability. Also notice that, since $J(\omega)$ is normalised ([EQ. E.21](#)), $j(t)$ is too. Assuming a perfect beamsplitter ($\eta = 1/2$), the HOM modification to the coincidence probability Π_{HOM} is given by¹

$$\Pi_{\text{HOM}} = \frac{1}{4} \int_{\infty} |j(t) - j(2\tau - t)|^2 dt \quad (\text{E.23})$$

where τ is the arrival time difference between the two photons*. The total coincidence probability is the product of Π_{HOM} , the chance to generate a pair, and the two channel efficiencies. We can expand [EQ. E.23](#), and use the normalisation of $j(t)$

$$\begin{aligned} \Pi_{\text{HOM}} &= \frac{1}{4} \int_{\infty} \left(|j(t)|^2 + |j(2\tau - t)|^2 - j(t)j^*(2\tau - t) - j(2\tau - t)j^*(t) \right) dt \\ &= \frac{1}{2} - \frac{1}{4} \int_{\infty} \left(j(t)j^*(2\tau - t) + j(2\tau - t)j^*(t) \right) dt. \end{aligned} \quad (\text{E.24})$$

If $J(\omega)$ is real, then $j(t)$ is real, and

$$\Pi_{\text{HOM}} = \frac{1}{2} \left(1 - \int_{\infty} j(t)j(2\tau - t) dt \right). \quad (\text{E.25})$$

E.3.1 Application to discretely colour entangled pairs

Working from [EQ. E.25](#), with the lumped square symmetric joint spectrum, with signal-idler detuning δ and channel width $\Delta\omega$

*For the sake of clarity: one photon arrives at time t , and the other arrives at time $t - \tau$.

$$J(\omega) = \begin{cases} 1/\sqrt{2\Delta\omega}, & |\omega \pm \delta/2| < \Delta\omega/2 \\ 0, & \text{otherwise} \end{cases} \quad (\text{E.26})$$

we find the time response is

$$\begin{aligned} j(t) &= \frac{1}{\sqrt{2\pi}} \int_{-\infty}^{\infty} J(\omega) e^{-i\omega t} d\omega \\ &= \frac{1}{\sqrt{4\pi\Delta\omega}} \left(\int_{-\delta/2-\Delta\omega/2}^{-\delta/2+\Delta\omega/2} e^{-i\omega t} d\omega + \int_{+\delta/2-\Delta\omega/2}^{+\delta/2+\Delta\omega/2} e^{-i\omega t} d\omega \right) \\ &= \frac{1}{\sqrt{4\pi\Delta\omega}} \left(\frac{ie^{-i\omega t}}{t} \Big|_{-\delta/2-\Delta\omega/2}^{-\delta/2+\Delta\omega/2} + \frac{ie^{-i\omega t}}{t} \Big|_{+\delta/2-\Delta\omega/2}^{+\delta/2+\Delta\omega/2} \right) \\ &= \sqrt{\frac{\Delta\omega}{4\pi}} \frac{i}{\Delta\omega t} (e^{-i\Delta\omega t/2} - e^{+i\Delta\omega t/2}) (e^{+i\delta t/2} + e^{-i\delta t/2}) \\ &= \sqrt{\frac{\Delta\omega}{\pi}} \operatorname{sinc}\left(\frac{\Delta\omega t}{2}\right) \cos\left(\frac{\delta t}{2}\right). \end{aligned} \quad (\text{E.27})$$

Now we must evaluate [EQ. E.25](#) using our new $j(t)$. The integral is*

$$\begin{aligned} &\int_{-\infty}^{\infty} j(t) j(2\tau - t) dt \\ &= \frac{\Delta\omega}{\pi} \int \operatorname{sinc}\left(\frac{\Delta\omega t}{2}\right) \cos\left(\frac{\delta t}{2}\right) \times \operatorname{sinc}\left(\frac{\Delta\omega(2\tau - t)}{2}\right) \cos\left(\frac{\delta(2\tau - t)}{2}\right) dt \\ &= \operatorname{sinc}(\Delta\omega\tau) \cos(\delta\tau) \\ &= \operatorname{sinc}(2\pi\Delta\nu_c\tau) \cos(2\pi(\nu_s - \nu_i)\tau) \end{aligned} \quad (\text{E.28})$$

What follows is the probability to measure a coincidence when: a photon pair is put on a perfect $\eta = 1/2$ beamsplitter; one photon is delayed by τ relative to the other; the photons have a minimum square (collection) bandwidth of $\Delta\nu_c$; and share no frequency-dependent phase (i.e. no chirp).

$$\Pi_{\text{HOM}} = \frac{1}{2} \left(1 - \operatorname{sinc}(2\pi\Delta\nu_c\tau) \cos(2\pi(\nu_s - \nu_i)\tau) \right) \quad (\text{E.29})$$

[EQ. E.29](#) is plotted in [FIG. E.1](#) for 0, 400, 800, and 1200-GHz signal-idler detunings.

§E.4 MONOCHROME VERSUS SPLIT PHOTON PAIRS

Following ref. 3, I will show that the frequency-entangled $|split\rangle$ state ([EQ. 3.8](#)) has the same behaviour as a monochromatic separable state. We saw this was the case for perfectly indistinguishable photons undergoing HOM interference in [§E.3](#). Written with signal and idler modes denoted a and b , and the input spatial mode in subscript[†], the two states are:

$$|separable\rangle \equiv |11\rangle = a_p^\dagger a_q^\dagger |\mathbf{0}\rangle, \quad (\text{E.30a})$$

$$|split\rangle \equiv \frac{1}{\sqrt{2}} (|1001\rangle + |0110\rangle) = \frac{1}{\sqrt{2}} (a_p^\dagger b_q^\dagger + a_q^\dagger b_p^\dagger) |\mathbf{0}\rangle. \quad (\text{E.30b})$$

*A by-hand solution exists, but I confess that here I resorted to Mathematica.

[†]We require $p \neq q$ since we're talking about the *split* states. [EQ. E.30](#) isn't normalised if $p = q$.

A general N -mode linear optical network is encoded in a unitary \hat{U} . It has elements $U_{i,j}$ with $i, j \in [1, N]$. Our two states evolve through \hat{U} , using [EQ. B.44](#), as

$$\begin{aligned} |\text{separable}\rangle &\rightarrow \left(\sum_i U_{i,p} a_i^\dagger \right) \left(\sum_j U_{j,q} a_j^\dagger \right) |\mathbf{0}\rangle \\ &= \sum_i \sum_j U_{i,p} U_{j,q} a_i^\dagger a_j^\dagger |\mathbf{0}\rangle \\ &= \left[\sum_i \sum_{j < i} U_{i,p} U_{j,q} a_i^\dagger a_j^\dagger + \sum_i \sum_{j > i} U_{i,p} U_{j,q} a_i^\dagger a_j^\dagger + \sum_i \sum_{j=i} U_{i,p} U_{j,q} a_i^\dagger a_j^\dagger \right] |\mathbf{0}\rangle \\ &= \sum_i \sum_{j < i} (U_{i,p} U_{j,q} + U_{j,p} U_{i,q}) a_i^\dagger a_j^\dagger |\mathbf{0}\rangle + \sum_i U_{i,p} U_{i,q} (a_i^\dagger)^2 |\mathbf{0}\rangle \end{aligned} \quad (\text{E.31a})$$

$$\begin{aligned} |\text{split}\rangle &\rightarrow \frac{1}{\sqrt{2}} \left[\left(\sum_i U_{i,p} a_i^\dagger \right) \left(\sum_j U_{j,q} b_j^\dagger \right) + \left(\sum_i U_{i,q} a_i^\dagger \right) \left(\sum_j U_{j,p} b_j^\dagger \right) \right] |\mathbf{0}\rangle \\ &= \frac{1}{\sqrt{2}} \sum_i \sum_j (U_{i,p} U_{j,q} + U_{j,p} U_{i,q}) a_i^\dagger b_j^\dagger |\mathbf{0}\rangle \\ &= \frac{1}{\sqrt{2}} \left[\sum_i \sum_{j < i} (U_{i,p} U_{j,q} + U_{j,p} U_{i,q}) a_i^\dagger b_j^\dagger + \sum_i \sum_{j > i} (U_{i,p} U_{j,q} + U_{j,p} U_{i,q}) a_i^\dagger b_j^\dagger \right. \\ &\quad \left. + \sum_i \sum_{j=i} (U_{i,p} U_{j,q} + U_{j,p} U_{i,q}) a_i^\dagger b_j^\dagger \right] |\mathbf{0}\rangle \\ &= \sum_i \sum_{j < i} (U_{i,p} U_{j,q} + U_{j,p} U_{i,q}) \left[\frac{a_i^\dagger b_j^\dagger + a_j^\dagger b_i^\dagger}{\sqrt{2}} \right] |\mathbf{0}\rangle + \sum_i U_{i,p} U_{i,q} \sqrt{2} (a_i^\dagger b_i^\dagger) |\mathbf{0}\rangle. \end{aligned} \quad (\text{E.31b})$$

It's necessary to divide the states into diagonal and off-diagonal parts because $|\text{split}\rangle$ only appears in the latter. In both cases then, after injecting photons in mode p and q of \hat{U} , the chance to measure them in modes i and j is

$$P_{i,j} = |U_{i,p} U_{j,q} + U_{j,p} U_{i,q}|^2 \quad P_{i,i} = 2 |U_{i,p} U_{i,q}|^2 \quad (\text{E.32})$$

- [1] Hong, C., Ou, Z. & Mandel, L. Measurement of subpicosecond time intervals between two photons by interference. *Physical Review Letters* **59**, 2044–2046 (1987). [\(150\)](#) [\(151\)](#)
- [2] See §F.2 of ref. 4. [\(150\)](#)
- [3] Matthews, J. C. F. et al. Observing fermionic statistics with photons in arbitrary processes. *Scientific Reports* **3**, 1539 (2013). [\(152\)](#)
- [4] Bonneau, D. *Integrated quantum photonics at telecommunication wavelength in silicon-on-insulator and lithium niobate platforms*. Ph.D. thesis, Bristol (2013). [\(153\)](#)

Appendix F

Qubit entanglement from resonant sources

This appendix focusses on **Exp. 2**, but also applies to **Exp. 3** and **Exp. 4**.

§F.1 ON-CHIP STATE EVOLUTION

When a bright pump is presented at the input of the device of **Exp. 2**, the on-chip quantum state of light evolves as follows. Starting with a coherent pump state, of $|\alpha|^2$ photons in the pump mode (mode b , referring to **FIG. F.1**, and frequency p) b_p , we pass through the first coupler with reflectivity η and obtain the state (**§C.5.1**)

$$|\alpha\sqrt{\eta}\rangle_{bp}|i\alpha\sqrt{1-\eta}\rangle_{dp}. \quad (\text{F.1})$$

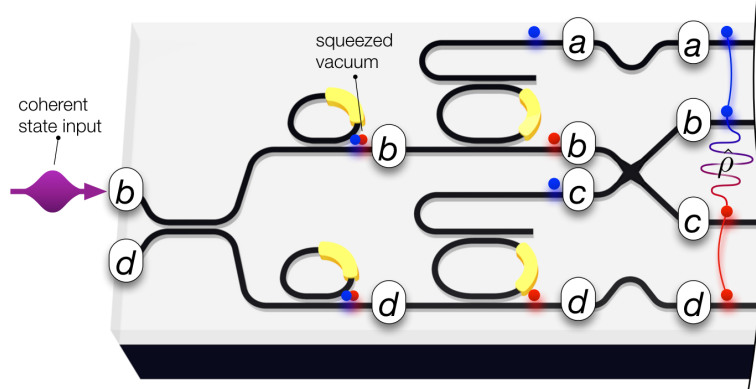
We assume the pump passes through an unknown (but fixed) intrinsic phase difference θ_0 between modes b_p and d_p :

$$|\alpha\sqrt{\eta}\rangle_{bp}|i\alpha\sqrt{1-\eta}\rangle_{dp} \rightarrow |e^{i\theta_0}\alpha\sqrt{\eta}\rangle_{bp}|i\alpha\sqrt{1-\eta}\rangle_{dp}. \quad (\text{F.2})$$

Section **D.3** tells us that for two pumped sources producing one pair each, $|\psi_s\rangle = |\xi\rangle_{II}^b \otimes |\xi\rangle_{II}^d$ (**Eqs. D.13, D.8**). Again in the *weak-pump* regime, where $\xi \ll 1$ we arrive at

$$\begin{aligned} |\psi_s\rangle &\approx \left(|0_s0_i\rangle_b - \xi_b |1_s1_i\rangle_b \right) \otimes \left(|0_s0_i\rangle_d - \xi_d |1_s1_i\rangle_d \right) \\ &= |0\rangle - \xi_d |0_s0_i\rangle_b |1_s1_i\rangle_d - \xi_b |1_s1_i\rangle_b |0_s0_i\rangle_d + \mathcal{O}(\xi_b\xi_d). \end{aligned} \quad (\text{F.3})$$

FIG. F.1: Schematic of the source and state-preparation side of the device, annotated with mode labels.



where we define the squeeze parameters for the top and bottom sources as $\xi_b \equiv ite^{i2\theta_0}\eta\xi$ and $\xi_d \equiv -t(1-\eta)\xi$, respectively, where ξ is taken from **TABLE 2.1**. This weakly pumped SFWM state is normalised in the limit of zero squeezing, and almost always gives only vacuum. Occasionally, though, a single pair is produced, and these events are what we will focus on.

Notice that **EQ. F.3** is merely a separable product of squeezed states. Since we're pumping weakly, the vacuum term dominates the pair term, and each of those squeezed states is close to separable (see **SD.4**). It would be surprising if any two naturally probabilistic sources, anywhere in the universe, pumped coherently, were intrinsically entangled. This is also not the case here. The Bell-type entanglement generated in this experiment—and, indeed, in any down-conversion-based entanglement scheme—arises from the next step, where we post-select away the vacuum component of **EQ. F.3**, and assume that the probability of multi-pair events is negligible.

Post-selecting on coincidences in our detectors (i.e. we cannot measure vacuum), and again assuming that $\xi^2 \ll \xi$, **EQ. F.3** becomes:

$$\xi_d|0_s0_i\rangle_b|1_s1_i\rangle_d + \xi_b|1_s1_i\rangle_b|0_s0_i\rangle_d. \quad (\text{F.4})$$

This differs only in a phase from the internal state of the device in **CH. 3 (EQ. 3.6)**. Frequency demultiplexers now map signal and idler modes to different paths (see **FIG. F.1**), and a waveguide crossing swaps modes b and c , taking

$$\begin{aligned} b_s &\rightarrow a_s & d_s &\rightarrow b_s \\ b_i &\rightarrow c_i & d_i &\rightarrow d_i. \end{aligned}$$

Finally, we have the state of interest, which we will call $|\phi^\pm\rangle$:

$$|\phi^\pm\rangle \equiv \xi_b|1\rangle_{as}|0\rangle_{bs}|1\rangle_{ci}|0\rangle_{di} + \xi_d|0\rangle_{as}|1\rangle_{bs}|0\rangle_{ci}|1\rangle_{di} \quad (\text{F.5})$$

Let's take a moment to reflect on the properties of $|\phi^\pm\rangle$. First, it doesn't seem normalised, since we have placed no restriction on the magnitudes of ξ_b or ξ_d . This is to be expected, since any extra normalisation is taken up by the (very large) vacuum and the (very small) multi-pair contributions, which we have omitted. To normalise $|\phi^\pm\rangle$, we define the photon flux balance between the two sources, β . It ranges from 0 to 1 when the top or bottom sources dominate, respectively, and is 1/2 when they are balanced.

$$\beta \equiv \frac{|\xi_b|^2}{|\xi_b|^2 + |\xi_d|^2} = 1 - \frac{|\xi_d|^2}{|\xi_b|^2 + |\xi_d|^2} = \frac{\gamma_b^2\eta^2}{\gamma_b^2\eta^2 + \gamma_d^2(1-\eta)^2}, \quad (\text{F.6})$$

where γ_b and γ_d are the (effective) nonlinear parameters for the two sources, including any difference in resonant field enhancement. Using this definition for β , and lumping the phases onto the bottom mode in a total internal phase Θ , we can rewrite the squeeze parameters in a clean and normalised way:

$$\xi_b \rightarrow \sqrt{\beta}, \quad \xi_d \rightarrow e^{i\Theta}\sqrt{1-\beta}, \quad \text{with} \quad \Theta \equiv \pi/2 - 2\theta_0, \quad (\text{F.7})$$

and obtain a new form of $|\phi^\pm\rangle$

$$|\phi^\pm\rangle = \sqrt{\beta}|1\rangle_{as}|0\rangle_{bs}|1\rangle_{ci}|0\rangle_{di} + e^{i\Theta}\sqrt{1-\beta}|0\rangle_{as}|1\rangle_{bs}|0\rangle_{ci}|1\rangle_{di}. \quad (\text{F.8})$$

Second, the state contains four modes with two orthogonal frequencies. Obviously, photons of different frequencies don't interfere, and so only the mode pairs (a, b) and (c, d) can. This motivates writing $|\phi^\pm\rangle$ in the qubit basis (EQ. 1.7), with the understanding that only single-qubit rotations are possible:

$$|\phi^\pm\rangle = \sqrt{\beta}|00\rangle + e^{i\Theta}\sqrt{1-\beta}|11\rangle. \quad (\text{F.9})$$

Third, $|\phi^\pm\rangle$ has a variable amount of entanglement, depending on the ratio of the two squeeze parameters. If β is either 0 or 1 (ξ_b or ξ_d is zero), $|\phi^\pm\rangle$ becomes unentangled, and takes the form $|\phi^\pm\rangle = |0101\rangle$ or $|\phi^\pm\rangle = |1010\rangle$, respectively. Conversely, if $\beta = 1/2$, then $|\phi^\pm\rangle \equiv |\phi_{\max}^\pm\rangle$ is maximally entangled, and

$$|\phi_{\max}^\pm\rangle = \frac{|00\rangle + e^{i\Theta}|11\rangle}{\sqrt{2}}, \quad (\text{F.10})$$

from which we can identify $|\phi_{\max}^\pm\rangle$ with the maximally entangled two-qubit Bell states $|\Phi^\pm\rangle$ for $\Theta = \{0, \pi\}$ (§1.1.4).

F.1.1 Imperfect overlap

In the above derivation, we assumed that photon pairs were produced into a strictly two-mode squeezed vacuum (i.e. were frequency-separable) and shared identical spectral properties. Here, we'll remove these assumptions, and treat the case of general spectral properties.

We'll expand the source efficiencies ξ to include a joint spectral component $J(\nu_s, \nu_i)$, which governs the biphotonic spectrum. This modifies the squeeze parameters as $\xi_m \rightarrow \xi_m J_m(\nu_s, \nu_i)$, with $m \in \{b, d\}$. Thus, EQ. F.5 becomes

$$|\phi^\pm\rangle \rightarrow |\phi_{io}^\pm\rangle \equiv \sum_s \sum_i \left(\xi_b J_b(\nu_s, \nu_i) |1010\rangle_{s,i} + \xi_d J_d(\nu_s, \nu_i) |0101\rangle_{s,i} \right). \quad (\text{F.11})$$

The joint spectra are normalised with respect to the signal and idler frequencies ν_s and ν_i , and the overlap σ quantifies their similarity:

$$\begin{aligned} \sum_s \sum_i |J_b(\nu_s, \nu_i)|^2 &= \sum_s \sum_i |J_d(\nu_s, \nu_i)|^2 = 1 \\ \sigma &\equiv \sum_s \sum_i J_b(\nu_s, \nu_i) \cdot J_d^*(\nu_s, \nu_i) \end{aligned} \quad (\text{F.12})$$

Here is an intricacy: we can't tell the difference between the frequencies in $\{\nu_s\}$ and $\{\nu_i\}$ since the resonator linewidths are much smaller than the collection bandwidth ($\Delta\nu \ll \Delta\nu_c$), so we must trace over them. This means we must add up all the probabilities of the indistinguishable events, and collapse our basis of all frequencies into one which contains only spatial and signal–idler information. Effectively, we can take $\sum |f|^2$ rather than $|\sum f|^2$. Thus EQ. F.5 can be written in the form of a density matrix:

$$\begin{aligned} \hat{\rho} = |\phi_{io}^\pm\rangle\langle\phi_{io}^\pm| &= |1010\rangle\langle 1010| \cdot |\xi_b|^2 \sum_s \sum_i J_b(\nu_s, \nu_i) J_b^*(\nu_s, \nu_i) \\ &\quad + |0101\rangle\langle 0101| \cdot |\xi_d|^2 \sum_s \sum_i J_d(\nu_s, \nu_i) J_d^*(\nu_s, \nu_i) \\ &\quad + |1010\rangle\langle 0101| \cdot \xi_b \xi_d^* \sum_s \sum_i J_b(\nu_s, \nu_i) J_d^*(\nu_s, \nu_i) \\ &\quad + |0101\rangle\langle 1010| \cdot \xi_b^* \xi_d \sum_s \sum_i J_d(\nu_s, \nu_i) J_b^*(\nu_s, \nu_i) \end{aligned} \quad (\text{F.13})$$

This can now be expressed using the definitions of [EQ. F.12](#) and [EQ. F.7](#) in terms of the overlap σ , balance β , and lumped internal phase Θ , and converted to the qubit basis, such that

$$\begin{aligned} \hat{\rho} = & |00\rangle\langle 00| \cdot |\xi_b|^2 &= |00\rangle\langle 00| \cdot \beta \\ & + |11\rangle\langle 11| \cdot |\xi_d|^2 &+ |11\rangle\langle 11| \cdot (1 - \beta) \\ & + |00\rangle\langle 11| \cdot \xi_b \xi_d^* \cdot \sigma &+ |00\rangle\langle 11| \cdot e^{-i\Theta} \sqrt{\beta} \sqrt{1 - \beta} \cdot \sigma \\ & + |11\rangle\langle 00| \cdot \xi_b^* \xi_d \cdot \sigma^* &+ |11\rangle\langle 00| \cdot e^{+i\Theta} \sqrt{\beta} \sqrt{1 - \beta} \cdot \sigma^* \end{aligned} \quad (\text{F.14})$$

The last equality of [EQ. F.14](#) tells us the density matrix we should expect, for source (or WDM) resonances with an imperfect overlap σ . A nice way to look at this result is in terms of the perfect, pure response, and the perfectly mixed response. In the pure case, there are maximal coherent side lobes, since the state is perfectly coherent, while in the mixed case, the energy correlations are still present, but the coherence is entirely lost. This latter case is like flipping two coins which have been glued together, while the former case represents true quantum entanglement. If it's real, the parameter σ smoothly moves the output state between these two regimes:

$$\hat{\rho} = \sigma \hat{\rho}_{\text{pure}} + (1 - \sigma) \hat{\rho}_{\text{mixed}} \quad \left\{ \begin{array}{l} \hat{\rho}_{\text{pure}} \equiv |\phi^\pm\rangle\langle\phi^\pm| \quad (\text{from } \text{EQ. F.9}) \\ \hat{\rho}_{\text{mixed}} \equiv \beta|00\rangle\langle 00| + (1 - \beta)|11\rangle\langle 11| \end{array} \right. \quad (\text{F.15})$$

§F.2 OVERLAP, VISIBILITY, AND MULTI-PAIR EVENTS

In [§4.2.1](#), we show the visibility of reverse-HOM-type fringes between our two microring sources, in the configuration of ref. 1. To convert these visibility data into overlap data (σ), additional analysis was needed. We replaced [EQ. D.8](#) for one of the sources with a new definition, which involves a coherent superposition of two frequencies: the original s and i and two new orthogonal frequencies, labelled s' and i' .

$$|\xi\rangle_{II} = \sqrt{1 - |\zeta|^2} \sum_{p=0}^{\infty} (-\zeta)^p \left(\sigma |p_s p_i\rangle + \sqrt{1 - \sigma^2} |p_{s'} p_{i'}\rangle \right) \quad (\text{F.16})$$

In this way, when $\sigma = 1$ we recover the original expression, but, when $\sigma = 0$, these new-frequency photons (at s' and i') will not interfere with those from the other source (still at the original frequencies s and i). Here, we implicitly assume that each source produces separable photon pairs—a small deviation occurs if the pairs are frequency-correlated.

The maximum achievable visibility is plotted against the pair generation probability ($|\xi|^2$ for each source) on the left side of [FIG. 4.4](#), alongside our measured result. It shows that the spectral indistinguishability of our sources is very close to unity, when a pair generation probability of 0.075 is considered. When the measured imbalance of our sources is included, the difference becomes even narrower. Using this result, we can compute the relationship between spectral overlap and visibility, while accounting for multi-pair events. This is shown on the right side of [FIG. 4.4](#). Including the source balance $\beta = 0.43$, we can estimate an experimental overlap of $\sigma = 0.99 \pm 0.08$. The overlap uncertainty is computed as $(dV/d\sigma)^{-1} \times \delta V$, where δV is the uncertainty in the visibility (0.021), and the derivative is evaluated numerically at the measured value, $V = 0.958$.

§F.3 THE BELL-CHSH TEST

To measure the CHSH parameter directly, we configured the signal and idler \hat{R}_y rotations to mix the two modes of each qubit (i.e. $\hat{R}_y(\theta_{SY}) = \hat{R}_y(\theta_{IY}) = \hat{H}$, with $\theta_{SY} = \theta_{IY} = \pi/2$), then rotated both θ_{SZ} and θ_{IZ} , to observe coincidence fringes with an entangled phase equal to $\theta_{SZ} + \theta_{IZ}$. We show below how S can be extracted from the visibility of these fringes.

First, we must obtain the expectation values of the projections along a and b from our density matrix $\hat{\rho}$. A generalised Pauli matrix, which decomposes a vector a on the Bloch Sphere into its component $\hat{\sigma}_x$, $\hat{\sigma}_y$, and $\hat{\sigma}_z$ operators, written in spherical coordinates θ and ϕ , is given by

$$\hat{O}(a) \equiv a \cdot \begin{pmatrix} \hat{\sigma}_x \\ \hat{\sigma}_y \\ \hat{\sigma}_z \end{pmatrix} = \hat{\sigma}_x \sin(\theta) \cos(\phi) + \hat{\sigma}_y \sin(\theta) \sin(\phi) + \hat{\sigma}_z \cos(\theta). \quad (\text{F.17})$$

The operator $\hat{O}(a)$ is Hermitian, and represents a single-qubit observable which projects onto a . Knowing this, we can write the vectors a and b of [EQ. 4.5](#) as expectation values of the observables \hat{O} for each of the two qubits a and b , and re-cast $E(a, b)$ in terms of the angles θ and ϕ :

$$E(a, b) = \langle \hat{O}(a) \otimes \hat{O}(b) \rangle = \begin{cases} \langle \psi | \hat{O}(a) \otimes \hat{O}(b) | \psi \rangle & \text{pure state } |\psi\rangle \\ \text{Tr}[\hat{\rho} \cdot \hat{O}(a) \otimes \hat{O}(b)] & \text{general state } \hat{\rho} \end{cases} \quad (\text{F.18})$$

$$E(a, b) \rightarrow E(\theta_a, \phi_a, \theta_b, \phi_b) = \langle \hat{O}(\theta_a, \phi_a) \otimes \hat{O}(\theta_b, \phi_b) \rangle \quad (\text{F.19})$$

The degree of violation depends strongly on one's choice of measurement bases. For our target state $|00\rangle + e^{i\Theta}|11\rangle$ the maximum violation occurs at

$$\begin{aligned} \theta_a &= 0 & \phi_a &= 0 \\ \theta_{a'} &= \pi/2 & \phi_{a'} &= 0 \\ \theta_b &= 3\pi/4 & \phi_b &= \pi - \Theta \\ \theta_{b'} &= \pi/4 & \phi_{b'} &= \pi - \Theta \end{aligned}$$

With these rotations, we can apply the test to the state [EQ. F.14](#) and obtain the following expression for the CHSH parameter

$$S = \sqrt{2} \left(1 + 2\sigma \sqrt{\beta(1-\beta)} \right) \quad (\text{F.20})$$

which, as expected, gives a maximal violation of $2\sqrt{2}$ when the overlap ($\sigma = 1$) and balance ($\beta = 1/2$) are optimised to produce a maximally entangled state. This dependence of the Bell-CHSH parameter on the source overlap and brightness balance is plotted in [FIG. 4.5](#).

To predict the effect of the overlap (σ) and balance (β) on the Bell fringe visibility ([FIG. 4.5](#) in the main text), we start with the expression for the partially mixed state given by [EQ. F.14](#), and apply the two projectors $\hat{U}_S \equiv \hat{R}_z(\theta_{SZ})\hat{R}_y(\pi/2)$ and $\hat{U}_I \equiv \hat{R}_z(\theta_{IZ})\hat{R}_y(\pi/2)$

$$\hat{U}_S = \frac{1}{\sqrt{2}} \begin{pmatrix} e^{i\theta_{SZ}} & 1 \\ e^{i\theta_{SZ}} & -1 \end{pmatrix} \quad \hat{U}_I = \frac{1}{\sqrt{2}} \begin{pmatrix} e^{i\theta_{IZ}} & 1 \\ e^{i\theta_{IZ}} & -1 \end{pmatrix} \quad (\text{F.21})$$

$$\hat{U} = \hat{U}_S \otimes \hat{U}_I = \frac{1}{2} \begin{pmatrix} e^{i(\theta_{IZ} + \theta_{SZ})} & e^{i\theta_{SZ}} & e^{i\theta_{IZ}} & 1 \\ e^{i(\theta_{IZ} + \theta_{SZ})} & e^{i\theta_{SZ}} & e^{i\theta_{IZ}} & 1 \\ e^{i(\theta_{IZ} + \theta_{SZ})} & e^{i\theta_{SZ}} & e^{i\theta_{IZ}} & 1 \\ e^{i(\theta_{IZ} + \theta_{SZ})} & e^{i\theta_{SZ}} & e^{i\theta_{IZ}} & 1 \end{pmatrix} \quad \hat{\rho} \rightarrow \hat{U}\hat{\rho}\hat{U}^\dagger \quad (\text{F.22})$$

For a Bell fringe projecting on $|00\rangle$ we expect oscillations coupled between the signal and idler Z phases, and the lumped internal phase of the state, with a visibility dependent on the overlap and balance, and indeed this is what we find. Looking at the $|00\rangle$ qubit state at the output, we predict fringes of the form

$$\Pi_{00} = \frac{1 + 2\sigma\sqrt{\beta(1 - \beta)} \cos(\Theta - \theta_{SZ} - \theta_{IZ})}{4} \quad (\text{F.23})$$

Explicitly, the Π_{00} fringe visibility has the dependency

$$V = \frac{4\sigma\sqrt{\beta(1 - \beta)}}{1 + 2\sigma\sqrt{\beta(1 - \beta)}} \quad \rightarrow \quad 2\sigma\sqrt{\beta(1 - \beta)} = \frac{V}{2 - V} \quad (\text{F.24})$$

Incidentally, the visibility of these fringes has the same dependence on σ and β as the time-reversed HOM fringes of [§4.2.1](#). Comparing this result with [EQ. F.20](#) we see immediately that the fringe visibility and the CHSH S parameter have a one-to-one correspondence:

$$S = \sqrt{2} \left(1 + \frac{V}{2 - V} \right) \quad \leftrightarrow \quad V = 2 - \frac{2\sqrt{2}}{S} \quad (\text{F.25})$$

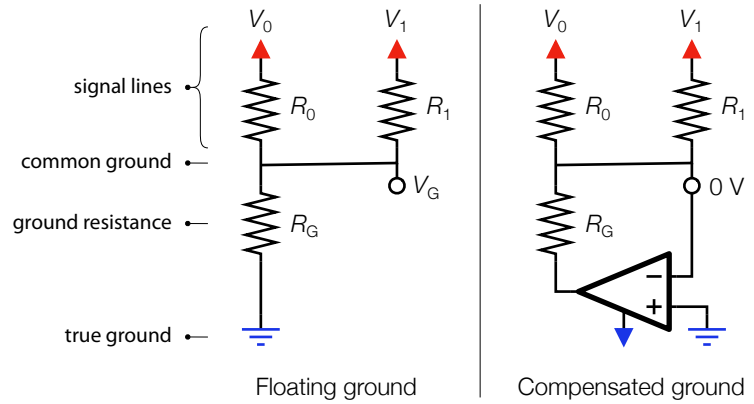
[Equation F.25](#) tells us that if we can obtain fringes with a visibility above $2 - \sqrt{2} \approx 59\%$, then the Bell-CHSH inequality will be violated. Measured fringes are plotted in [FIG. 4.5](#) of the main text, showing visibilities between 93% and 96%. Finally, according to [EQ. F.25](#), this state has an S parameter in the range from 2.64 and 2.71.

§F.4 COMMON-GROUND CROSSTALK CORRECTION

Many devices (including all in this thesis) use a common ground to reduce the required number of electrical pads, and so the designed device footprint. Fewer pads also means fewer connections (either wire-bonds or finger probes), which also increases both packaging yield and value. What's good for economy, though, is not always good for performance: common grounds introduce transconductance-type crosstalk between signal lines.

A schematic of a circuit containing two signal lines (V_0 , V_1) and a common ground (V_G) is shown in [FIG. F.2](#). The arbitrary signal voltages V_0 and V_1 modulate optical phase by driving currents I_0 and I_1 which dissipate heat in resistances R_0 and R_1 . The crosstalk arises when the current $I_0 + I_1$ passes through the small resistance R_G , which lies between the common on-chip ground, and the true ground. This current results in a voltage $V_G = (I_1 + I_0)R_G$. We can solve for the three un-

FIG. F.2: Schematic of common-ground electrical crosstalk. The effective ground voltage V_G , produced by current flowing through the small resistance R_G , depends on the signal voltages, V_0 and V_1 . Each signal voltage drives a thermo-optic phase shifter, with resistance R_0 and R_1 . A compensation scheme is shown at right.



knowns via the three nodal equations

$$\left. \begin{aligned} I_0 + I_1 &= \frac{V_G}{R_G} \\ I_0 &= \frac{V_0 - V_G}{R_0} \\ I_1 &= \frac{V_1 - V_G}{R_1} \end{aligned} \right\} \rightarrow V_G = \frac{R_G(R_1 V_0 + R_0 V_1)}{R_1 R_G + R_0 R_1 + R_0 R_G} \quad (\text{F.26})$$

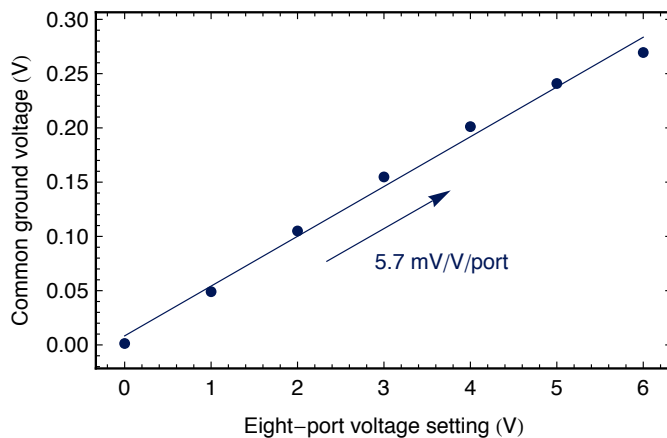
In general, for N signal lines with voltages $\{V_i\}$ and resistances $\{R_i\}$, the ground offset is

$$V_G = \left(\sum_i^N \frac{V_i}{R_i} \right) / \left(\frac{1}{R_G} + \sum_i^N \frac{1}{R_i} \right) \xrightarrow{R_i=R} \frac{\sum V_i}{R/R_G + N} \approx \frac{R_G}{R} \sum V_i \quad (\text{F.27})$$

which results in the second expression when the signal resistances are all the same (as is often the case). The effective applied voltages are then $\tilde{V}_i \equiv V_i - V_G$. So [EQ. F.27](#) tells us that the voltage crosstalk depends on the ratio of the ground resistance R_G to the signal resistances $\{R_i\}$.

In the device of [CH. 4](#), the $N = 8$ signal resistances $R_i \approx 2.2 \text{ k}\Omega$, and the ground resistance $R_G = 13 \Omega$, give a pairwise crosstalk coefficient of around 5.7 mV/V (see [FIG. F.3](#)). For example, referring again to [FIG. F.2](#), if V_1 moved up by one volt, then the voltage drop across R_0 is reduced by 5.7 mV , and V_0 is effectively reduced.

FIG. F.3: Measurement of floating-ground electrical crosstalk. V_G was measured as eight other voltages were increased. From the fit, we find a crosstalk of 5.7 mV per applied volt per port.



To correct V_G , we use a negative feedback scheme on the output common ground, with feedback through an unused port. Since the input impedance of an amplifier can be very large (easily $1\text{ M}\Omega$), we can neglect any sensing resistance, and use the sensed value to correct $V_G \rightarrow 0$, as shown on the right side of **FIG. F.2**.

- [1] Silverstone, J. W. *et al.* On-chip quantum interference between silicon photon-pair sources. *Nature Photonics* **8**, 104–108 (2014). ⟨158⟩

Index of figures and tables

Figure

- 1.1 Moore's law, 1
- 1.2 InMOS chip, 1
- 1.3 Bloch sphere, 6
- 1.4 Path qubit operations, 8
- 1.5 Linear quantum optics, 10
- 1.6 Post-selected CSIGN gate, 14
- 1.7 MBQC-LOQC stack, 15
- 1.8 Original QNIX scheme, 17
- 1.9 Fusion gate, 17
- 1.10 Waveguide types, 21
- 1.11 Strip WG geometry, 23
- 1.12 Strip WG dispersion, 24
- 1.13 Integrated optics toolbox, 25
- 1.14 Multi-mode interference, 26
- 1.15 Thermo-optic phase shifter, 27
- 1.16 Ring drop spectrum, 28
- 1.17 Fibre couplers, 29
- 1.18 Silicon bandgap and $\chi^{(3)}$, 32
- 2.1 Parametric fluorescence, 42
- 2.2 Phase matching SFWM, 44
- 2.3 Resonant SFWM example, 45
- 2.4 Coincidence measurements, 47
- 2.5 Transmission due to TPA, 49
- 2.6 SFWM power dependence, 50
- 3.1 Expt. 1 device schematic, 57
- 3.2 Two-photon fringes, 61
- 3.3 HOM dips, 62
- 3.4 Degenerate two-photon interference, 63
- 4.1 Expt. 2 device schematic, 68
- 4.2 Bright light calibration, 69
- 4.3 Spectra of resonant photon-pair sources, 70

- 4.4 Effect of multi-pair emission, 71
- 4.5 Bell-CHSH measurements, 73
- 4.6 Reconstructed states, 75
- 4.7 Expt. 2 optical micrograph, 78
- 5.1 Expt. 3 device schematic, 83
- 5.2 Optical micrograph of device, 84
- 5.3 Heater driver board, 85
- 5.4 Expt. 3 device schematic, 87
- 5.5 Electron micrograph of device, 87
- 5.6 Phase shifter statistics, 90
- 5.7 RHOM split fringes, 90
- 5.8 Source state control, 90
- 5.9 Reconstructed states, 91
- 6.1 Progress entangling photons, 98
- C.1 Slab modes, 131
- C.2 Ring resonators, 134
- C.3 Ring transmission and phase, 135
- D.1 Squeezing efficiency, 141
- D.2 Multi-source SFWM, 142
- D.3 XTPA heralding efficiency, 145
- E.1 Computed HOM dip shapes, 151
- F.1 Mode-labelled Expt. 2, 155
- F.2 Common-ground crosstalk, 160
- F.3 Crosstalk evidence, 160

Table

- 1.1 Silicon material properties, 35
- 1.2 Silica material properties, 35
- 1.3 SOI waveguide properties, 35
- 2.1 SFWM efficiency, 44
- 5.1 Preparation figures of merit, 92
- 6.1 Low-TPA materials, 102
- B.1 Ladder operators, 118
- D.1 Multi-source multi-pair SFWM coefficients, 143

Index of terms

A

accidental coincidence, 48
arrayed-waveguide grating, 60
atomic cascade, 41

B

bandgap, 35, 101, 102
beamsplitter, 11
Bell-CHSH inequality, 5, 73, 77, 159
birefringence, 20
Bloch sphere, 5, 7, 73
Boolean logic, 5
Born's rule, 7, 111
BOX, *see* buried oxide
Brillouin scattering
 stimulated, 32
buried oxide, 20

C

Cholesky decomposition, 116
CMOS-compatibility, 101
coherent state, 41, 44, 136
 properties, 136
coincidence to accidental ratio, 48
colour centre, 41
contrast, 61
controlled unitary, 12
 CPHASE, 13
 CSIGN, 13, 121
 CZ, 13, 121
 CNOT, 12
coupled-mode theory, 26, 131
creation/annihilation operator, 113, 118
cross-phase modulation, 33, 101, 120
cross-two-photon absorption, 31, 49, 99,
 145
crosstalk, 86, 160
cut-back (method), 57

D

dark counts, 48
degree of freedom, 84
density matrix, 7, 68, 111
Dirac notation, 112
dispersion, 25
dispersion parameter (D), 25
DiVincenzo criteria, 4

E

effective mode area (A), 23, 24
effective refractive index (n_{eff}), 21, 35, 41
elephant, 12
entangled states, 6, 15
 Bell, 15, 67
 cluster, 17
 graph, 15, 17
 Greenberger-Horne-Zeilinger, 15
entanglement, 7, 14
 in squeezed vacuum, 144
 origin, 78
estimator (tomography)
 constrained least-squares, 76
 maximum likelihood, 76
extinction, 136

F

FCA, *see* free-carrier absorption
FCD, *see* free-carrier dispersion
feed-forward, 11, 34, 99, 100
fibre Bragg grating, 86
fidelity, 77
field enhancement, 46
 factor, 134, 136
first quantisation, 58
Fock states, 9
four-wave mixing, 32, 33, 42, 101
free spectral range, 134

free-carrier absorption, 31, 49
free-carrier dispersion, 31
FWM, *see* four-wave mixing

G

group index n_g , 24, 25, 35
group-velocity dispersion, 25, 44

H

heralding, 14
heralding efficiency, 32, 99, 145
Hermitian conjugate, 114
Hilbert space, 111
Hong-Ou-Mandel interference, 11
dip, 12
time-reversed, 56, 75, 147

I

informationally complete
(measurement), 74
insertion loss, 58
integrated optics, 19
integrated optics devices
evanescent coupler, 25, 131, 133
grating coupler, 29
multimode interference coupler, 25
ring resonator, 28, 29
add-drop, 29, 68
critical coupling, 29
over coupling, 29
under coupling, 29
spot-size converter, 29
waveguide crossing, 28
integrated photonics, 19
intensity, 33
intensity-dependent refractive index
(n_2), 33, 35
interaction, 4, 9, 120
nonlinearity, 13

J

joint spectral amplitude, 150
joint spectrum, 46, 71, 117

K

Kerr coefficient, 33

Kerr effect, 33, 101
KLM, 4

L

large-core silicon photonics, 20
linear optical quantum computation, 4,
79, 99
measurement-based quantum
computation, 15
QNIX, 15, 17
linewidth, 135
LOQC, *see* linear optical quantum
computation

M

Mach-Zehnder interferometer, 8, 14, 59,
69
Maxwell's equations, 21, 127
MBQC, *see* linear optical quantum
computation
mixed states, 7
mixture, 7, 111
MMI, *see* integrated optics devices
mode area, 35
mode solver, 23
modulation instability, 44
momentum mismatch, 44
Moore's law, 1, 21, 99
multiplexing, 17
multiplexed source, 42, 99
MZI, *see* Mach-Zehnder interferometer

N

non-deterministic gates, 14
nonlinear figure of merit, 101
nonlinear loss, 49
nonlinear optics, 13
nonlinear parameter (γ), 33, 35, 121
nonlinear phase shift, 121
number operator, 120
number states, 9

O

optical bistability, 31
optical interconnect, 21
over-complete measurement set, 75

P

parametric approximation, 139
parametric gain, 44
partial trace, 117
path qubit, 9
Pauli matrix, 6
percolation, 18
phase matching, 42, 44
photon, 5, 9, 114
photon-pair source properties
 brightness, 43, 44
 indistinguishability, 43
 separability, 43, 45, 46, 68
photonics, 19
positivity, 116
post-selection, 13, 14, 78, 82, 121
Poynting vector, 23
probabilistic bit, 3, 7
projective measurement, 6
purity, 7, 111, 144

Q

quality factor, 135
quantisation, 9, 112
quantum circuits, 16
quantum computation, 3
 circuit model, 16
 measurement-based, 16
quantum dot, 41
quantum key distribution, 4
quantum metrology, 4
qubit, 3
 degrees of freedom, 75, 115
 dual-rail qubit, 8
 path qubit, 8
 polarisation qubit, 8
 time-bin qubit, 8
qubit basis, 9
qudit, 9, 98

R

Raman scattering
 spontaneous, 32, 102
 stimulated, 30, 32, 101
resonator types, 28
RHOM, *see* Hong-Ou-Mandel
 interference
ring resonator, 28, 45, 67, 83, 86

S

scattering matrix, 10, 26, 119, 133
Schmidt number, 15, 46, 117, 144
Schrödinger equation, 114
self-phase modulation, 101
separability, 14, 15, 98
separable states, 6
SFWM, *see* spontaneous four-wave
 mixing
silicon quantum photonics, 34
silicon-on-insulator, 20
 Smart Cut, 20
slowdown factor, 33
small-core silicon photonics, 20
SNSPD, *see* superconducting nanowire
 single-photon detector
SOI, *see* silicon-on-insulator
SPDC, *see* spontaneous parametric
 down-conversion
SPM, *see* self-phase modulation
spontaneous four-wave mixing, 42, 43
 resonant, 45
 time-reversed, 56, 141
spontaneous parametric
 down-conversion, 41, 83, 99
squeeze parameter, 44, 141
 phase of, 44, 140
stimulated emission tomography, 47
superconducting nanowire
 single-photon detector, 99, 100
switch, 99

T

thermal conductivity, 35
thermo-optic effect, 27, 35, 86
time interval analyser, 48
TPA, *see* two-photon absorption
 trace
 partial trace, 117
triangle inequality, 47
truth table, 84
two-mode squeezed vacuum, 140
 entanglement, 144
two-photon absorption, 31, 32, 35, 49,
 101

cross-, *see* cross-two-photon absorption

U

unitary, 8, 56, 115
operator, 10, 115

V

visibility, 12, 61, 63

W

waveguide, 8, 21
confinement, 20
index contrast, 20
polarisation
 TE, 22
 TM, 22
rib waveguide, 20, 21
slab waveguide, 19, 21, 22, 129
strip waveguide, 20, 21
 alternate names, 23
wavenumber (k), 20, 21, 25, 44
wavevector, *see* wavenumber (k)

X

XPM, *see* cross-phase modulation
XTPA, *see* cross-two-photon absorption

